Investigations of Reversible Thermochromic Mixtures

by

Douglas C. MacLaren

Submitted in partial fulfillment of the requirements
for the degree of Doctor of Philosophy

at

Dalhousie University
Halifax, Nova Scotia
July 2003

# Canada

DALHOUSIE UNIVERSITY

DEPARTMENT OF CHEMISTRY

The undersigned hereby certify that they have read and recommend to the Faculty of
Graduate Studies for acceptance a thesis entitled "Investigations of Reversible
Thermochromic Mixtures" by Douglas C. MacLaren in partial fulfillment for the degree
of Doctor of Philosophy.

Dated: _____ July 3, 2003 _____

External Examiner: __ ████████████████████ __

Research Supervisor: __ ████████████████████ __

Examining Committee: __ ████████████████████ __

__ ████████████████████ __

__ ████████████████████ __

Departmental Representative: __ ████████████████████ __
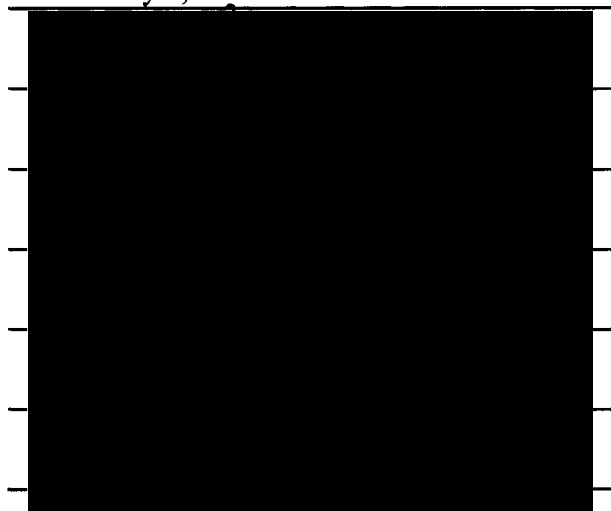
# DALHOUSIE UNIVERSITY

DATE:  July 8, 2003

AUTHOR:   Douglas C. MacLaren

TITLE:   Investigations of Reversible Thermochromic Mixtures

DEPARTMENT OR SCHOOL:   Chemistry

DEGREE:   Ph.D.          CONVOCATION:   Fall          YEAR:   2003

*For Dawn and "the Pea"*

# Table of Contents

## List of Figures

xiv

*Abstract*

Three-component organic thermochromic systems have potential applications in reversible, rewritable thermal printing. In principle, such mixtures could maintain a coloured or non-coloured state at ambient temperature depending on their thermal treatment. These systems generally consist of a functional dye (1-3 mol%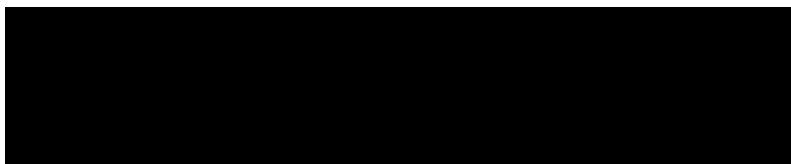), a weakly acidic colour developer (5-25 mol%), and a high-melting organic solvent (75-90 mol%). Colour development occurs at the fusion temperature of the mixture, which triggers the interaction of the dye and developer. Slow cooling of the melt results in an equilibrium state with low colour density, whereas rapid cooling of the melt results in a metastable state with high colour density. The metastable state can be decoloured by heating to an intermediate decolourisation temperature at which the coloured state becomes unstable.

Barriers to the widespread use of reversible, rewritable thermochromic materials include problems with colour contrast, colour stability, and decolourisation rates. Development is hindered by a lack of detailed knowledge of the interactions between components in these systems.

In this study the developer-dye and developer-solvent interactions were examined for an archetypal dye/developer/solvent thermochromic system. Vibrational spectroscopy, NMR, and thermal analysis were used to examine compounds formed in developer/dye and developer/solvent binary mixtures. Rewritable thermochromic properties such as metastable colour density, equilibrium colour density, and decolourisation rates were examined and discussed in terms of the thermodynamics of the developer/dye and developer/solvent interactions.

Observed thermochromic properties are shown to be strongly correlated to a competition between the dye and the solvent for interaction with the developer. Increasing the attractive interaction between the solvent and developer results in enhanced rewritable thermochromic properties.

*List of Abbreviations and Symbols*

*(In order of appearance)*

HOMO – highest occupied molecular orbital

LUMO – lowest unoccupied molecular orbital

$\Delta E$ – change in energy

$\hbar$ – Planck's constant/$2\pi$

$N$ – quantized energy level

$m_e$ – electron mass

°C – degrees Celsius

eV – electron volt

$\lambda_{max}$ – maximum absorption wavelength

PDA – polydiacetylene

TPM – triphenylmethane

CVL – crystal violet lactone, 3,3-bis($p$-N,N-dimethylaminophenyl)-6-N,N-

dimethylaminophthalide

$T$ – temperature (in Kelvin)

$T_m$ – melting temperature

$T_{fus}$ – fusion temperature

$T_d$ – decolourisation temperature

$T_{ambient}$ – ambient temperature

FD1 – 3-dibutylamino-7-(o-chloroanilino)aminofluoran

FD2 – 3-diethylamino-6-methyl-7-phenylaminofluoran

XRD – X-ray diffraction

$2\theta$ – angle of Bragg diffraction in XRD

P22 – docosylphosphonic acid

P20 – eicosylphosphonic acid

P18 – octadecylphosphonic acid

P16 – hexadecylphosphonic acid

P14 – tetradecylphosphonic acid

P12 – tetradecylphosphonic acid

P10 – decylphosphonic acid

P4 – tetraphosphonic acid

ODG - octadecylgallate

DSC – differential scanning calorimetry

LG – lauryl gallate

PG – propyl gallate

OG – octyl gallate

TD – 1-tetradecanol

HD – 1-hexadecanol

OD – 1-octadecanol

S – DSC sample chamber

R – DSC reference chamber

$\Delta T_{SR}$ – DSC temperature differential

$\dot{Q}_S$ – DSC sample power

$\dot{Q}_R$ – DSC reference power

$C_S$ –heat capacity of DSC sample

$C_R$ –heat capacity of DSC reference

$R_S$ – DSC sample thermometer resistance

$t$ – time

$dT/dt$ – rate of temperature change

$T_S$ – DSC sample temperature

$T_R$ – DSC reference temperature

$T_{ST}$ – DSC sample thermometer temperature

$T_{onset}$ – onset temperature

$\Delta_{trs}H$ – enthalpy change of transition

$\upsilon$ – vibrational frequency

$\tilde{\upsilon}$ – wavenumber

$k$ – Hooke's law force constant

$\mu_m$ – reduced mass

IR – infrared

$cm^{-1}$ – reciprocal centimetre

$I_T$ – transmitted light intensity

$I_0$ – transmitted light intensity

$\varepsilon$ – molar absorption coefficient

$c$ – molar concentration

$d$ – sample path length

$A$ – absorbance

FT – Fourier transform

$v_i$ – incident frequency

$v_m$ – scattered frequency

P – dipole moment

$\alpha_P$ – polarizability

$I_d$ – intensity of diffuse reflected light

$s_d$ – diffuse reflection coefficient

$I_{in}$ – incident diffuse light intensity

VIS – visible light spectrum

$R_\infty$ – diffuse reflectance of from an infinitely thick layer (Kubelka-Munk theory)

$\sigma_A$ – diffuse reflectance scattering coefficient

$F(R_\infty)$ – Kubelka-Munk function

$R_{\infty,STD}$ – diffuse reflectance of a highly reflecting white standard

$r_\infty$ – ratio of diffuse reflectance of from an infinitely thick layer and diffuse reflectance

of a highly reflecting white standard (Kubelka-Munk theory)

$F(r_\infty)$ – Kubelka-Munk function adjusted for $R_{\infty,STD}$

NMR – nuclear magnetic resonance

I – spin quantum number

**I** – spin quantum number vector

$I_z$ - spin quantum number vector

$m$ – magnetic quantum number

$\mu$ – magnetic moment

$\mu$ – spin quantum number vector

$\gamma$ - magnetogyric ratio

$B_0$ – applied magnetic field

$B$ – magnetic field felt by nucleus

$\sigma$ – chemical shielding constant

$\delta$ – chemical shift

*ppm* – part per million

$\Delta\delta$ - change in chemical shift

$\mu_0$ – permeability of a vacuum

MAS – magic angle spinning

RF – radiofrequency

CP – cross polarization

Å - Angstrom ($10^{-10}$ metre)

CV – crystal violet

$C_\phi$ – ispo aromatic carbon

DMSO – dimethylsulfoxide

$CDCl_3$ – deuterated chloroform

$CD_2Cl_2$ – deuterated methylene chloride

BPA – bisphenol A (2,2-bis(hydroxyphenyl)propane)

$x_i$ – mole fraction of component $i$

$pK_a$ – negative logarithm of the acid dissociation constant

$a$ – lattice parameter

$b$ – lattice paramter

$c$ – lattice paramter

$Z$ – number of atoms per unit cell

$\alpha_1$ – angle between lattice parameters $b$ and $c$

$\gamma_1$ – angle between lattice parameters $a$ and $b$

(s) – strong peak intensity

(m) – medium peak intensity

(w) – weak peak intensity

sym. – symmetric

asym. – asymmetric

$\upsilon$(C=O) – carbonyl vibration

$\upsilon$(C=C) – carbon-carbon double bond vibration

$\upsilon$(C=NR$_2$) – carbon- nitrogen double bond vibration

$\upsilon$(C-NR$_2$) – carbon-nitrogen single bond vibration

$\upsilon$(CO$^-$) – carboxylate vibration

$\gamma_{sym.}$(CO$^-$) – symmetric carboxylate wag deformation

$\beta$(C-NR$_2$) – carbon nitrogen bend

$\beta$(N$^+$C$_4$) – charged nitrogen bend

$\beta$(OH) – hydroxyl bend

$\delta$(C=NR$_2$) – carbon nitrogen double bond scissor

$\Delta\upsilon$ – change in frequency

$I_{1584}$ – vibrational peak intensity at 1584 cm$^{-1}$

$I_{1678}$ – vibrational peak intensity at 1678 cm$^{-1}$

$\alpha$ – alpha, rotational phase of 1-alcohols ($C_nH_{(2n+1)}OH$, where $n > 13$)

$\beta$ – beta, vertical low temperature phase of 1-alcohols ($C_nH_{(2n+1)}OH$, where $n > 13$)

$\gamma$ – gamma, tilted low temperature phase of 1-alcohols ($C_nH_{(2n+1)}OH$, where $n > 13$)

$S$ – entropy

$\Delta_{fus}H$ – enthalpy change of fusion

$R$ – gas constant

$\Delta T_\alpha$ – temperature range of alcohol $\alpha$-phase stability

SDBS - Integrated Spectral Database for Organic Compounds

$\alpha$-carbon – alkyl chain carbon adjacent to functional group

(G) – gauche

(T) – trans

hr – hour

Peak I – Raman peak at 1584 cm$^{-1}$ corresponding to the $\upsilon$(C=N) of ring-opened CVL

Peak II – Raman peak at 1683 cm$^{-1}$ corresponding to the $\upsilon$(C=O) of LG in (LG)$_2$•alcohol

Peak I – Raman peak at 1710 cm$^{-1}$ corresponding to the $\upsilon$(C=O) of LG (or (LG)$_2$•alcohol) interacting with free $\alpha$-alcohol

$I^I$ – intensity of Peak I

$I^{II}$ – intensity of Peak II

$I^{III}$ – intensity of Peak II

$\Delta_mH$ – melting enthalpy change

$\Delta_mS$ – melting entropy change

$\Delta_{fus}S$ – fusion entropy change

$\Delta_{mix}G$ – Gibbs energy of mixing

$\Delta_{mix}H$ – enthalpy of mixing

$\Delta_{mix}S$ – entropy of mixing

$Z$ – arbitrary thermodynamic property

$Z^{EX}$ – arbitrary excess thermodynamic property

$Z^{real}$ – observed thermodynamic property

$Z^{real}$ – ideal thermodynamic property

$G^{EX}$ – excess Gibbs energy

$H^{EX}$ – excess enthalpy

$\Delta_{mix}G^{EX}$ – excess Gibbs energy of mixing

$\Delta_{mix}H^{EX}$ – excess enthalpy of mixing

$\gamma_i$ – activity coefficient of component $i$

$P$ – pressure

$W^G$ – interaction parameter representing $\Delta_{mix}G^{EX}$

$W^H$ – interaction parameter representing $\Delta_{mix}H^{EX}$

obs. – observed

endo – endothermic

exo – exothermic

$r^2$ – statistical goodness-of-fit

*Acknowledgements*

# Chapter 1. Introduction to Thermochromism

## 1.1. Colour in Chemistry

Colour is enriches our lives and is central to chemistry. It arises from many sources and can be considered as colour by emission, absorption, and/or transmission.[1,2] The colour of matter is due to three principal factors: the spectral intensity of the incident illumination, the modification occurring as the light interacts with the chemical system, and finally the perception of this modified light by the human eye and brain.[2,3]

The simplest form of colour is black-body radiation or incandescence.[1,2] All materials absorb thermal energy and re-emit it. At sufficiently high temperatures, the radiation is in the visible region resulting in a glowing of the object.[1,2]

The electronic emission spectra of some small molecules and atoms can be in the visible range but in general, electronic energy levels are widely spaced with much higher energy than visible radiation.[2] Other sources of colour from emission are fluorescence and phosphorescence, such as from singlet-singlet and triplet-singlet relaxation in organic molecules.

Colour by transmission is pertinent to the present research. It is the colour resulting from the absorption of certain wavelengths of light. Semiconductors are characterized by a band gap between their valence and conduction bands (continua of electronic energy levels). The energy gap, or band gap, for an electron to pass from the valence band to the conduction band is often of the order of visible radiation.

The observed colour will result from the colours which are not absorbed.[1] The colour of many transition metal compounds is due in part to crystal field splitting. This effect, described by crystal field theory, arises when ligands surrounding a transition metal exert an electric field on the metal centre. When this happens the degeneracy of d electronic orbitals can be split. In many cases, electronic transitions occur in the visible frequency range.[1,2,4]

Colour centres (or F-centres) are caused by naturally occurring interstitial defects in crystals left by the migration of single charges or pairs of charges to the surface of the crystal. An electron sitting in an interstitial site has significantly lowered excitation energy, often in the visible region. Colour centres are often found in alkali halides such as fluorite ($CaF_2$ – violet), sylvite (KCl – violet) and halite (NaCl – yellow).[1,2,4,5]

Most of the colour observed in dyes and pigments is due to electronic excitation and results in the absorption of visible light by organic chromophores. The chromophore, or *colour bearer*,[2] might not necessarily absorb in the visible region; in some cases an auxochrome, or *colour increaser*,[2] attached to the chromophore can help to raise or lower the energy absorbed, placing it in the visible region. Unsaturated organic molecules characteristically absorb high-energy radiation (ultraviolet) where absorption is due to short-wavelength excitation of electrons from bonding (HOMO) to anti-bonding (LUMO) orbitals.[1,2,6-8] In a conjugated system, electron density is delocalized through the molecule's $\pi$ orbital network. The energy levels of a conjugated system can be estimated with the quantum mechanical equation for a particle in a box of length, $L$:[3,9]

$$\Delta E_N = \frac{\hbar^2 N^2}{8 m_e L^2} \quad N = 1,2,3,\ldots \qquad 1.1$$

where $\Delta E_N$ is the energy of the electronic transition, $\hbar$ is Planck's constant, $N$ is the quantized energy level, and $m_e$ is the electron's mass. The dispersion of electron density through increased conjugation lowers the energy required for HOMO-LUMO excitation into the visible region, resulting in vivid colours.[1,6-8]

## 1.2. Introduction to Thermochromism

Thermochromism is defined as a temperature-dependent alteration of the electronic absorption spectrum of a compound.[1,7,10] Although there are rare occasions where it is observed in the gas phase — e.g. the dimerization of brown $NO_2$ to form colourless $N_2O_4$ — thermochromism is primarily defined as a process occurring in the liquid and solid state.[8-11] Although reversibility is not a specific requirement for thermochromism, colour changes that occur due to events such as the thermal decomposition of compounds or the thermal destruction of colour centres in a crystal at high temperatures are not considered thermochromic.[7,8,11]

## 1.3. Inorganic Thermochromism

Many inorganic systems display thermochromism. Sources of thermochromism include changes in ligand geometry, metal coordination, solvation, band-gap, reflectance properties, and the arrangement and distribution of defects in the material.[1-5,7]

$Ag_2HgI_4$ and $Cu_2HgI_4$ are isomorphous and tetragonal, showing a first-order transition to a cubic phase at about 50 °C. These systems also undergo a gradual second-order, order-disorder transition where the silver and copper ions become mobile within the lattice, resulting in a colour change.[5] Both systems show a colour change from red to

black in the range of 25 to 75 °C.[12] This is believed to be due to a change in the reflectance spectrum of the solid resulting from the two transitions. Another example of a similar system is $HgI_2$, which changes from a red tetragonal phase to a yellow rhombic phase at 127 °C.[5] Reversible thermochromism is also observed in solution for inorganic compounds. Colour change is usually due to change in solvation, coordination number, or ligand exchange with the solvent. A commonly cited example is $CoCl_2$ in water, which is a blue solution at room temperature and a green solution at 0 °C:[5,7]

$$Co(H_2O)_6^{2+}{}_{(aq.)} + 4\ Cl^-{}_{(aq.)} \underset{-\Delta}{\overset{+\Delta}{\rightleftharpoons}} CoCl_4^{2-}{}_{(aq.)} + 6\ H_2O_{(l)} \qquad 1.2$$

$\qquad\qquad$ (green) $\qquad\qquad\qquad\qquad\qquad$ (blue)
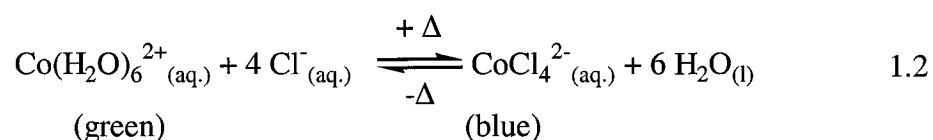
As the system is heated, the Co(II) coordination changes from octahedral to tetrahedral and the ligands exchange. This dramatically alters the crystal field about the Co(II) center and results in a colour change. $CoCl_2$ is a commonly used material in thermochromic applications.[13,14]

Since crystal field splitting is determined by the geometry and symmetry of ligands, temperature-dependent changes in geometry can result in changes in the crystal field splitting energy. For example, ruby (1% $CrO_3$/99% $Al_2O_3$) changes reversibly from red (2.20 eV) to green/gray (2.15 eV) at 450 °C due to expansion of the crystal lattice.[2]

Some organometallic compounds also show thermochromism. This can be due to changes in ligand geometry, conformational changes of ligands, or shifts in the equilibrium distribution of structures with varying coordination environments. Copper (II) bis-(N,N-diethylethylenediamine)perchlorate is brick red at room temperature and

becomes blue above 44 °C. Conformational changes of the diethylethyleneamine ligand are believed to alter the crystal field with changes in temperature.[5]

Irreversible thermochromic changes are also observed. Many of these are a result of dehydration of transition metal complexes. Loss of water results in a change in coordination of the metal center. Table 1.1 shows a selection of hydrates that change colour upon dehydration.[5]

Table 1.1. Inorganic complexes that undergo irreversible colour change because of dehydration and/or ligand exchange upon heating.[5]

| Compound | Colour change | Transition temperature/°C |
|---|---|---|
| $(NiCl_2) \cdot 6H_2O$ | Green-yellow | 200 |
| $(NiSO_4) \cdot 7H_2O$ | Green-yellow | 200 |
| $(Cu(NO_3)_2) \cdot 3H_2O$ | Blue-brown | 250 |
| $(CuC_2O_4) \cdot 5H_2O$ | Blue-black | 355 |
| $(CdC_2O_4) \cdot 3H_2O$ | White-brown | 375 |
| $(MnC_2O_4) \cdot 5H_2O$ | White-black | 400 |
| $(FeC_2O_4) \cdot 2H_2O$ | Yellow-brown | 275 |

Cobalt pentaamine chlorodichlorate, $[Co(NH_3)_5Cl]Cl_2$, goes through a series of irreversible colour changes including: pink→violet (120 °C), violet→turquoise (170 °C) and turquoise→black (230 °C). The changes are due to irreversible phase transitions that change the symmetry of the ligands. Colour associated with the highest temperature reached is retained at room temperature and gives an indication of the thermal history of the sample.[2]

## 1.4. Organic Thermochromism

Thermochromism is most common in organic compounds, of which thousands are known to display this type of behaviour. This is primarily because the conjugation of organic systems is sensitive to subtle changes in molecular environment, especially thermally induced structural changes.[8-10] There are three general mechanisms for organic thermochromism:[7] (1) structural changes not involving bond cleavage such as stereoisomerism,[7,10] cis-trans isomerization[8], or order-disorder phase transitions;[15] (2) purely physical responses to temperature such as optical interference effects as seen in liquid crystalline materials and thermochromic polymers;[16-18] (3) thermally induced reversible changes involving bond cleavage such as ring opening.[19] The third mechanism is most important to the present study.

### 1.4.1. Thermochromic Ethylenes

One of the first groups of compounds noted to be thermochromic was the thermochromic ethylenes.[10] Meyer reported thermochromism in bianthrone (Figure 1.1) in 1909 as the yellow solid melted to give a green liquid.[20] Later, in 1928, Schönberg and Schutz noted the colour change behaviour of dixanthylene (Figure 1.1), which changes from colourless in the liquid to green in the melt.[21] In 1933, Bergmann and Corte noted a similar colour change in xanthylidecanthracene (Figure 1.1).[22] At room temperature, all three structures are bent such that the two aromatic portions are facing each other. As the temperature rises, thermal expansion allows the central carbon-carbon double bond to lengthen, letting the molecule approach a more planar conformation, resulting in an increase in conjugation and lowering of the absorption energy.[8,10]

bianthrone          dixanthylene          xanthylidecanthracene
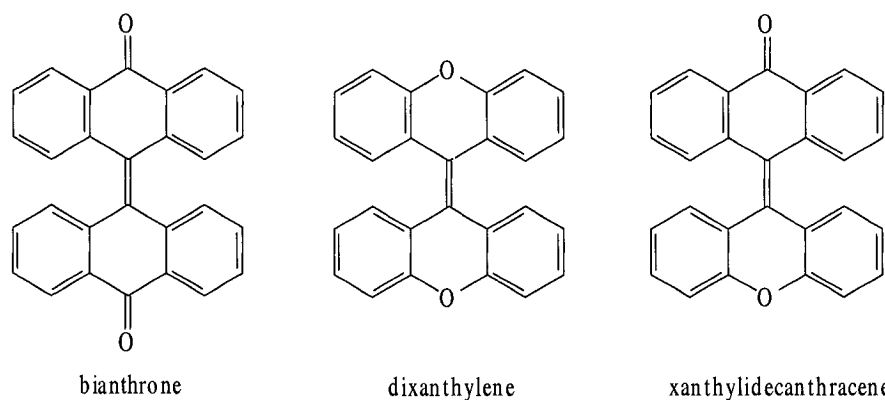
Figure 1.1. These ethylenes display thermochromism because of the temperature dependence of the molecular shape; as the temperature rises the structure becomes more planar as the central carbon-carbon double bond lengthens.[10]

### 1.4.2. Thermochromic Charge-Transfer Complexes

Charge-transfer occurs when strong electron pair donors interact with strong electron pair acceptors in close proximity.[2] For example, $p$-benzoquinone and its derivatives are known to form charge-transfer complexes with aromatic compounds.[23] Tetraisopropylbenzene and tetracyanoethylene (Figure 1.2) form a violet liquid ($\lambda_{max}$ = 500 nm) when melted together but on solidification they crystallize separately and are colourless.
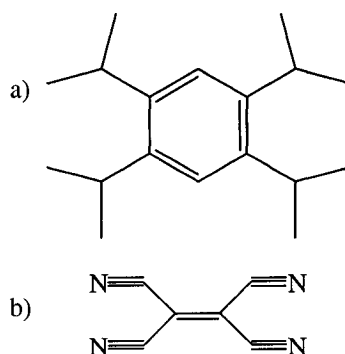


Figure 1.2. A charge transfer complex can be formed between (a) tetraisopropylbenzene and (b) tetracyanoethylene. When melted together they form a violet liquid ($\lambda_{max}$ = 500 nm) but on solidification they crystallize separately and are colourless.[2]

## 1.4.3. Thermochromic Polymers and Oligomers

Many conjugated polymers and oligomers have interesting electrical properties and are often referred to as synthetic metals.[24] Since these molecules are highly conjugated, many are susceptible to thermochromic effects. The most common polymers exhibiting thermochromism are polydiacetylenes ($[=CR_1C\equiv CCR_2=C=]_n$), polythiophenes ($[C_4HRS]_n$), and $\alpha$-conjugated polysilanes.[3,24-36]

The source of thermochromism in these polymer systems is order-disorder transitions in bulky side-chains.[33-36] Side-chains generally keep the polymer backbone in either an all-*trans* or helical configuration at room temperature. Above the thermochromic transition the side-chains effectively "melt", become disordered, and no longer hold the polymer backbone in its original position. Common configurational changes are all-*trans* to *gauche*[25,31] and rod to coil.[3,26,27,29,32]

Most polydiacetylene (PDA) derivatives such as PDA (12, 8), $R_1 = (CH_2)_{11}CH_3$ $R_1 = (CH_2)_7CH_3$, and PDA-nUPh, $R_1 = R_2 = C_6H_5\text{-NHOCO}(CH_2)_n$, are blue at room temperature and red above 70 °C.[25,28] This is due to a loss of order of the side-chains and a decrease in polymer conjugation.[28] Interaction between the disordered side-chains imposes stress on the polymer backbone disrupting conjugation as carbon-carbon single bonds rotate up to 5 degrees from planarity.[34]

Symmetrically substituted poly(di-*n*-hexylsilane) (*n*- implies normal) has an absorption maximum at a wavelength of 374 nm at room temperature corresponding to a hexagonal columnar configuration of the side-chain. The wavelength of the absorption maximum drops to 317 nm above 41 °C due to a disordering of the chains into an all-*trans* configuration.[11,29,31]

Polythiophenes are common conducting polymers and are highly conjugated when the five-membered thiophene rings are in a *trans*-planar configuration with one another.[30,35,37] Regioregular poly-3-alkylthiophenes change from red-violet to yellow reversibly when heated under a vacuum.[30] It is believed that side-chain interactions become unstable at high temperatures, causing the thienyl units to twist, resulting in a loss of conjugation.[30,37]

Thermochromic polymers are usually rigid, thermally stable, and insoluble in many solvents.[3,24] These properties make them useful for applications as sensor materials in many environments.[34,38-40]

### 1.4.4. Liquid Crystalline Materials

Liquid crystals, which also show dramatic colour changes as a function of temperature, were discovered by Reinitzer in 1888.[10] The most apparent thermochromic changes can be observed in chiral nematic or cholesteric liquid crystals, as shown in Figure 1.3.[7,18,41,42]

**(a)**



**(b)**
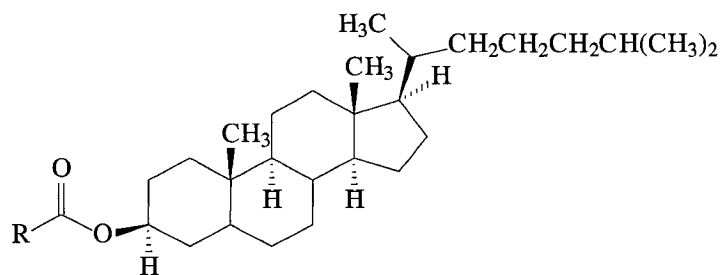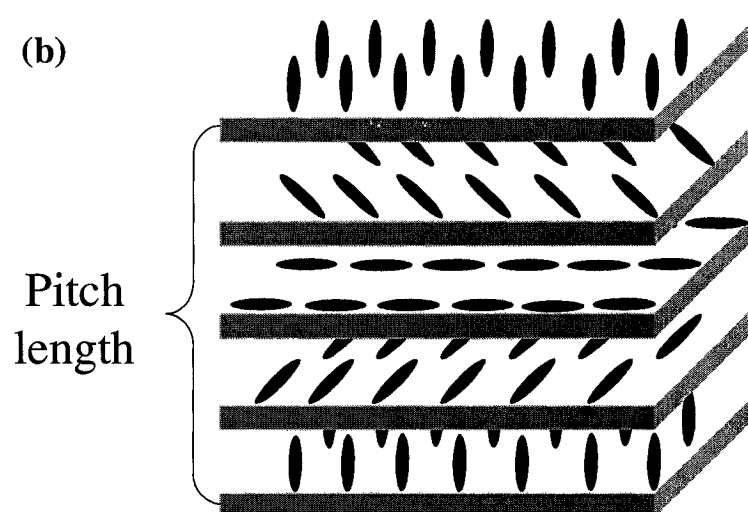


Pitch
length

Figure 1.3. Cholesteric liquid crystals can have colour associated with interference of light reflected from the layers of the same crystal orientation, separated by the pitch length. Since the pitch length of the layers is temperature-dependent, the colour observed depends on temperature. (a) Shows an example of a cholesteric liquid crystalline material. (b) The repeat distance, called the pitch length, depends critically on temperature.[1,7,41]

These materials are arranged as sheets that reflect light due to an interference effect analogous to Bragg diffraction.[1,7,18,41-44] Light of certain wavelength, reflected by the layers, constructively interferes. The repeat distance of these layers is called the pitch length and is critically dependent on temperature. These materials are red at the low-temperature range and change through yellow, green and blue as the temperature is raised.[42] The temperature range of the colour change is bounded by lower and upper

clearing temperatures; outside this range the liquid crystalline material is translucent.[42] Liquid crystalline materials can be designed to undergo thermochromic colour changes in the range of -30 ℃ to 120 ℃.[43,45,46]

### 1.4.5. Thermochromism Through Tautomerism

Most important to the present study are systems that undergo thermochromism as a direct result of thermally activated reversible molecular rearrangement. These changes are generally a result of thermal tautomerism.[7,10,19,47,48] Tautomerism, derived from the Greek word *tautos* (identical), refers to a reversible structural isomerism consisting of a series of steps including: bond cleavage, skeletal bond migration, and bond reformation. Some common examples of tautomerism include acid-base[6], keto-enol[19], and lactim-lactam[49] equilibria. Thermal tautomerism is often a result of a temperature-dependent change in the molecular environment such as solvent polarity or pH.[7,41,48]

### 1.4.5.1. Salicylideneanilines

Salicylideneanilines undergo thermochromism as a result of intramolecular proton transfer between an enol and a keto form.[47,50-52] Figure 1.4 shows the transfer of the proton from the oxygen to the nitrogen reducing the conjugation of the system and increasing the energy of the absorption maximum.[50]
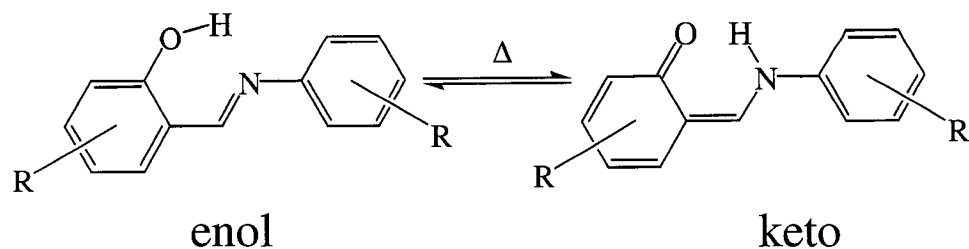
Figure 1.4. The thermally induced proton transfer from the enol to keto forms of salicylideneanilines results in less π-conjugation and a lowering of the wavelength of the absorption maximum of the molecule. In the case of salicylindeneaniline (R=H) the enol form forms a yellow solution in isopentane below –133 °C. The solution becomes colourless as the keto form predominates above –133 °C.[47]

The stability of the more conjugated enol form depends on the nature of the substituents on the aromatic rings.[47,50-52] Generally, the energy difference between the keto and enol structures is small enough to be thermally accessible at low/moderate temperatures, making them thermochromic.[47,50-52] The enol form of salicylideneaniline (R=H) is stable in isopentane below –133 °C with absorption maxima at 426 and 316 nm (yellow solution).[47] Heating the solution results in a shift to the keto form with absorption maxima of 338, 317, 300, and 270 nm at 25 °C (colourless solution).[47]

### 1.4.5.2. Spiropyrans

One of the most extensively studied thermochromic systems is the spiropyran family, characterized by two π systems linked by a tetrahedrally configured "spiro" carbon centre.[7,8,53-56] These compounds undergo reversible, thermally induced heterolytic cleavage from the spiro to a ring-opened state with an increase in absorptionwavelength maximum. The first known system of this type was di-β-napthospyran, examined by Dickinson in 1927[57], shown in Figure 1.5.
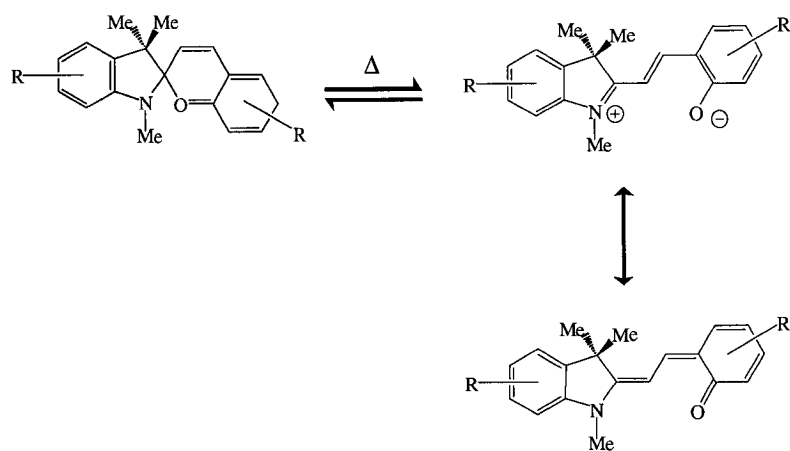
Figure 1.5. Mechanism of spiropyran ring-opening in di-β-napthospyran. Heterolytic cleavage of the spiro carbon-oxygen bond allows planarity which extends conjugation and makes the system coloured. The zwitterionic coloured structure is stabilized by a quinoid resonance structure.[55]

The enthalpy of transition to the coloured form is 12 to 25 kJ mol^{-1} with an activation barrier of about 100 kJ mol^{-1}.[54,55] Spiropyrans normally form quinoid coloured structures but strong electron-accepting substituents on the pyran moiety will stabilize a negative charge on the oxygen and allow the molecule to have zwitterionic character.[58]

### 1.4.5.3. Triphenylmethane Dyes

The phthalein derivatives of triphenylmethane (TPM) systems comprise a significant portion of the compounds known to be thermochromic. They achieve colour development through a ring-opening reaction that changes the spiro carbon centre from a tetrahedral to planar arrangement.[7,8,41,48,59,60,61] There are three main groups of TPM dyes, classified by the number and type of phenyl substituents found on the aromatic rings

attached to the central spiro carbon: (1) the malachite green series where the TPM dye has two amino substituents; (2) the roseaniline series, where the TPM dye has three amino substituents; (3) the rosalic acid series, where the TPM dye has three hydroxy substituents.[8]

When the dye molecule is opened, a tertiary carbocation, stabilized by three phenyl substituents, is formed.[7,8,41,48,59,60] The most common thermochromic TPM derivative is crystal violet lactone (CVL), a spirolactone and member of the roseaniline TPM series (Figure 1.6)[7,8,48] that undergoes an acid-induced ring-opening reaction at a pH of less than 4.[7,41,59] The term *leuco dye*, or white dye, is used to refer to the colourless, normal form of the dye.[7,41] Strictly speaking, this is an example of halochromism,[7,8,41,49] *i.e.*, a pH-dependent colour change. However, when CVL is prepared as a mixture with an electron-pair-accepting compound the *mixture* is referred to as thermochromic.[48]

An example of the ring-opening reaction of CVL in the presence of an electron pair acceptor, or acid, is shown in Figure 1.6. Conversely, thermochromic mixtures can be prepared with acidic dyes, such as phenolphthalein, that undergo ring-opening reactions in the presence of electron pair donors.[11,62]

**Leuco CVL**          **Coloured CVL**
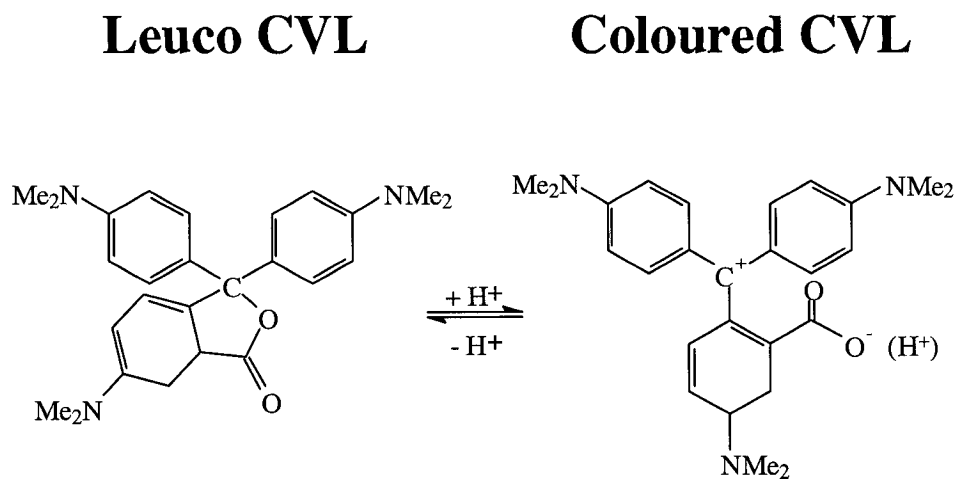


Figure 1.6. In the presence of strong electron pair acceptors, the leuco form of crystal violet lactone will open to give a planar coloured structure.[41]

### 1.4.5.4. Fluoran Dyes

Closely related to TPM derivatives are fluoran dyes.[8,48,63,64] The fluoran structure is based on that of a spirolactone but differs in that its two free phenyl rings are bridged with an oxygen to form a xanthene moiety. Examples of fluoran dyes include Eosin Y,[65,66] fluorescein,[67-69] 3-diethylamino-6-methyl-7-phenylaminofluoran (Figure 1.7),[66,70,71] and rhodamine B lactone (Figure 1.7).[65,66,72,73] Like the TPM derivatives, these systems develop colour as the result of a ring-opening reaction of the lactone moiety in the presence of an electron pair acceptor (Figure 1.7).

3-dibutylamino-7-(*o*-chloroanilino)aminofluoran

3-diethylamino-6-methyl-7-phenylaminofluoran

rhodamine B lactone
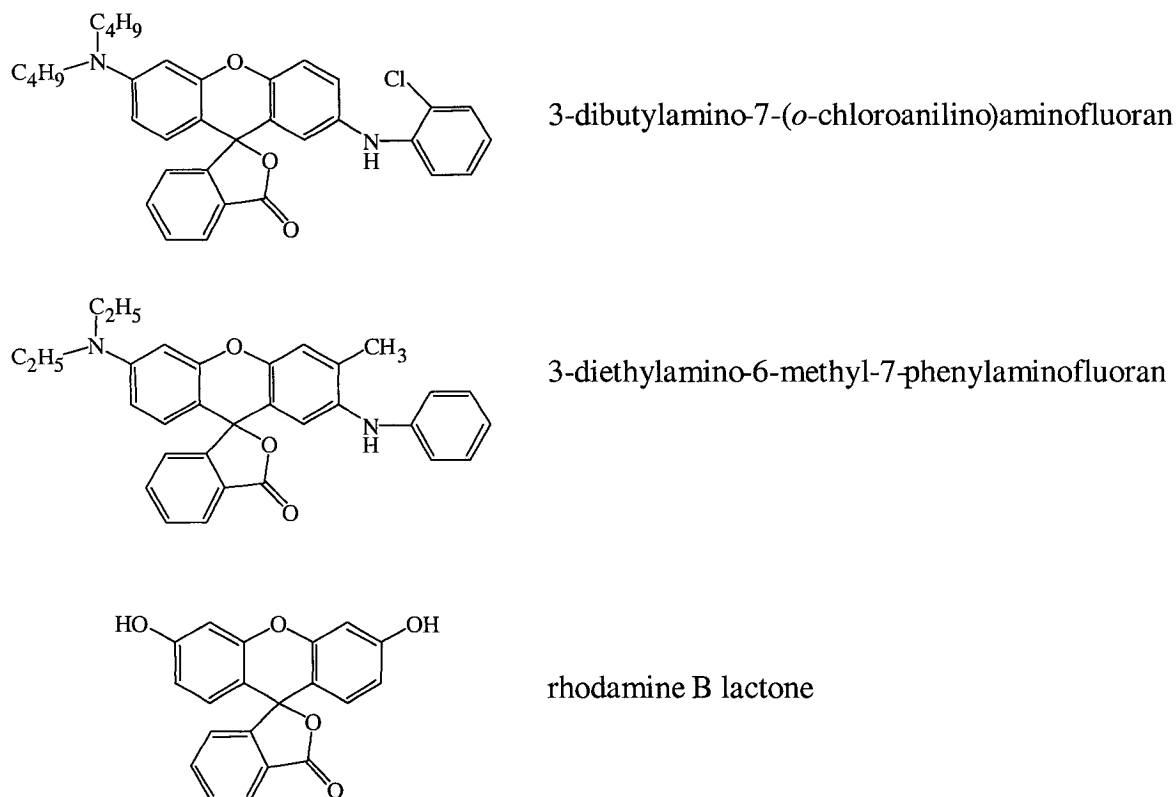
Figure 1.7. Examples of fluoran leuco dyes. These are similar to spirolactone dyes and undergo thermochromic ring-opening reactions with the same mechanism. They differ from spirolactones in that their free phenyl rings are bridged with an oxygen atom to form a xanthene moiety .[63]

## *1.5. Applications of Thermochromic Materials*

Classically, dyes have been used to colour pigments and substrates,[8] thus, the most important properties of most of dyes are high colour density and stability.[7] In recent years, a new field of dye science has developed to make use of properties of a dye other than its colouring properties.[74-76] These dyes are referred to as *functional dyes*.[7,8,41,59,77] Functional dyes display changes in their electronic absorption spectra in response to chemical and physical properties of the compounds involved. These changes are generally due to the input of small amounts of energy — *e.g.* heat, light, and electric

field.[8,74-77] Thermochromic dye systems are one sub-class of functional dyes; others include photochromic, electrochromic, piezochromic, biochromic and solvatochromic systems.[7,8,38,39,75-78] Some authors refer to these materials as 'smart' or 'intelligent' materials because the materials are able to adapt and/or respond to changes in their environment.[12,14,41,46,79]

### 1.5.1. Thermochromic Functional Materials

Thermochromic materials have been used in commercial applications since 1957, when National Cash Register patented the first process for irreversible thermal printing.[41,80] Since then thermochromic functional materials have been widely developed and used in several interesting applications.[59] Systems can be designed to undergo thermochromic changes at nearly every colour and conventionally encountered temperature. Figure 1.8 shows a flow chart outlining the variety of classes of thermochromic materials used in current applications.
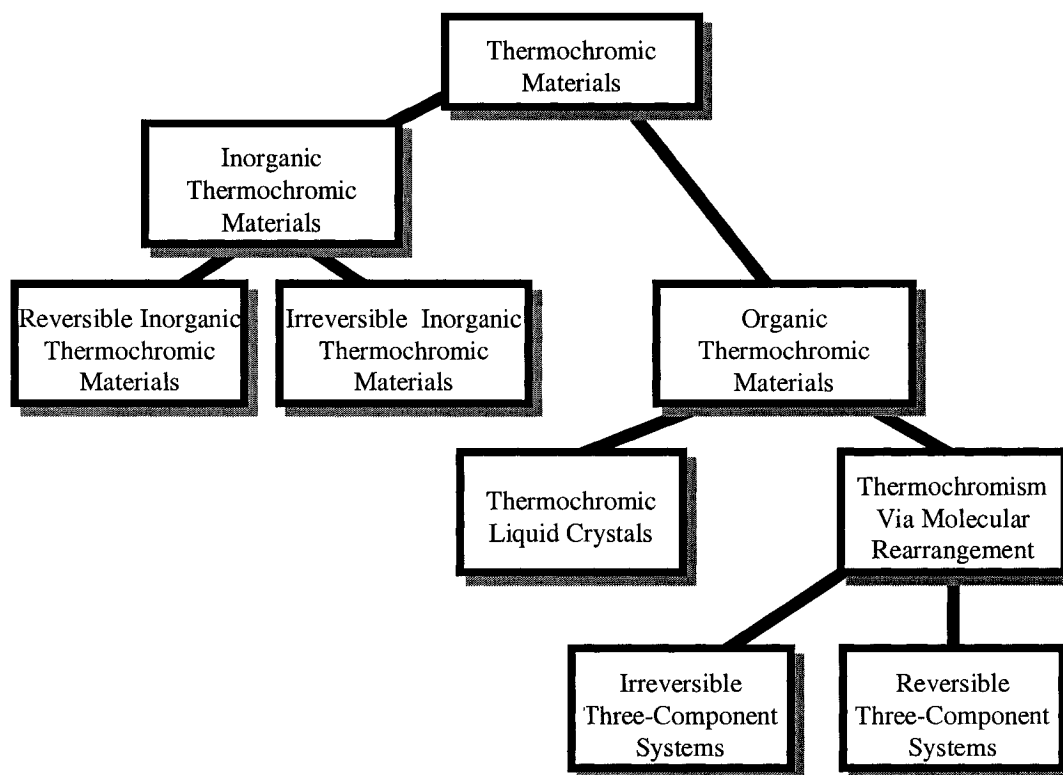
Figure 1.8. Thermochromic materials can be subdivided into various classes according to this flow chart. Most applications utilize organic thermochromic materials.

### 1.5.2. Applications of Inorganic Thermochromic Materials

Inorganic systems can be incorporated into thermochromic materials requiring much higher temperature changes than their organic counterparts.[5,7] Table 1.1 showed many irreversible thermochromic changes at temperatures in excess of 200 to 300 °C. Inorganic systems are used as pigments in thermochromic paints to indicate temperature changes on pipes or mechanical equipment. $CoCl_2$, $AgHgI_2$, and many Cu, Co and Sn complexes have been applied in thermochromic "smart" window glazings that darken at high temperatures to stabilize temperatures in greenhouses and office buildings.[12,13,81,82]

Although inorganic materials have a wider range of thermochromic temperatures, they are generally toxic, making them impractical for many applications.[59,83]

### 1.5.3. Applications of Organic Thermochromic Materials

Organic thermochromic materials are most common and widely applied. They can be divided into two major categories based on the process of colour change: thermochromic liquid crystalline materials and thermochromism via molecular rearrangement.[7,46,79]

#### 1.5.3.1. Liquid Crystalline Materials

Some of the most common thermochromic applications use liquid crystals.[41,43,45,46,84] They include several novelty applications including mood rings, 'stress testers', warning indicators, and thermometers.[7,41,43,59] Liquid crystalline systems are expensive (although newer processes allow for the production of thin-films) and do not usually undergo single colour-colour transitions.[7,41] Also, the temperature range of utility is limited, -30 to 120 °C.

#### 1.5.3.2. Thermochromism via Molecular Rearrangement

Section 1.4 outlined commonly used thermochromic leuco dyes. It was noted that a second component is generally used to aid in the thermochromic change, and thus nearly all organic thermochromic systems of this type are actually *thermochromic mixtures*.[7,48,79,83] The simplest thermochromic mixture involves the interaction of an electron pair donor, the *leuco dye*, with an electron pair acceptor, also known as the

*colour developer.*[85-88] (Colour developer will subsequently be referred to as developer.) This interaction (an example was shown in Figure 1.6) can take place in both the solid and liquid states, depending on the components chosen. In most cases, a third component, referred to as a *solvent*, is added to the dye and developer components.[7,89] Solvents can act to promote or inhibit the interaction of the dye and developer in the solid state or they can be used to solvate the dye or developer in the liquid state.[7,41]

Properties and functions of the solvent depend on the desired applications and will be discussed in a subsequent chapter. The solvent component is of great importance in the design of thermochromic mixtures because it is used in such an amount (50 to 95% by mass) that its melting temperature dictates the melting temperature of the mixture and, in many cases, the temperature of thermochromic colour change.[85-88]

For reliable and consistent application of thermochromic materials, there are two major questions that must be addressed. First, how will the dye mixture adhere to the paper, textile fibres, or plastic of the application? (The attachment of dyes to textile or paper fibres is a difficult field on its own.[7] The designer of a thermochromic mixture must consider not only the dye but also a developer and possibly a solvent.) Second, how will the components of the dye mixture be kept in intimate contact to achieve consistent colour development? To develop colour, the leuco dye and its developer must be in close contact when heat is applied. For reversible mixtures, components must remain in contact after many colour development cycles.[85-88,90-93]

Thermochromic mixtures can be microencapsulated in gum arabic, cellulose, polyurea, or polyamide shells. Although commercial microencapsulation techniques are primarily applied now in the pharmaceutical industry, they were first developed to

produce colour-forming mixtures for thermal printing applications.[7,41,46,79,84,94-96] Microencapsulation of thermochromics is most commonly achieved through three techniques: complex coacervation, salt coacervation, and interfacial polymerization.[7,41,84]

The resulting microcapsules are usually between 3 to 5 $\mu$m[84,96] but can be up to 50 $\mu$m for some thermochromic printing applications.[41,95] Microcapsules can be mixed with paints, adsorbed to textile or paper fibres, incorporated into polymers during polymerization, blended with standard acrylic printing paste for the production of inks, or spray deposited onto papers and other solid objects.[7,41,59,95]

### *1.5.3.3. Irreversible Organic Thermochromic Mixtures*

If the interaction between the basic dye and acidic developer is very strong, an irreversible thermochromic change can take place. This was the basis for the first application of organic thermochromic materials – irreversible thermal printing.[76] These mixtures can be either two-component (dye and developer) or three-component (dye, developer, and solvent). The two most common examples are carbonless copy paper and irreversible heat-writable paper.[7,10,59,97-100]

Although carbonless copy paper is not thermochromic, its chemistry is similar to irreversible heat-writable paper; both mixtures contain a leuco dye such as CVL or 2-$o$-chloroanilino-6-dibutylaminofluoran (Figure 1.7), and an acidic developer.[41,59] The underside of the top sheet of carbonless copy paper is coated with a layer of leuco dye or leuco dye/solvent mixture microencapsulated in a bead of polyurethane, gelatine, gum arabic, or polyvinyl alcohol.[7,59] The top of the bottom sheet is coated with a developer such as an acidic phenolic clay or inorganic salt.[101,102] When pressure is applied to the top

sheet the microcapsules rupture and expose the leuco dye and solvent to the acid developer, resulting in colouration.[7,59] This system is irreversible because the developers (electron pair acceptors) used form strong complexes with the leuco dye.[98-102]

In irreversible thermal printing, paper is spray coated with microcapsules containing a three-component mixture where leuco dye and developer are blended with a solvent that inhibits dye-developer interaction in the solid state.[59,79] Upon the application of heat, usually through the use of a thermal printing head, the multicomponent mixture melts and mixes resulting in an irreversible colour change. Thermal printing was popular several years ago for facsimile machine printing before the development of 'plain paper facsimile' and is still extensively used to print cash register receipts and movie theatre ticket stubs.[7,59,85-88] Irreversible mixtures also can be used in quality control for packaging or for examination of temperature control in industrial processes where exposure to undesirable temperatures results in a colour change as an indicator of the thermal history of the product.[14,79]

### 1.5.3.4. Three-Component Reversible Thermochromic Mixtures

Three-component mixtures consisting of a leuco dye, developer and solvent are the most common systems for reversible thermochromic applications.[41,83,89] Most novelty applications of thermochromism operate using this mechanism, shown in Figure 1.9.[103] The dye and the developer interact to form a coloured complex in the solid state (State A). Upon melting, $T > T_m$, the developer dissolves in the molten solvent and colour density is lost (State B). When the mixture solidifies the developer comes out of solution and interacts with the dye, reestablishing colour (State A).
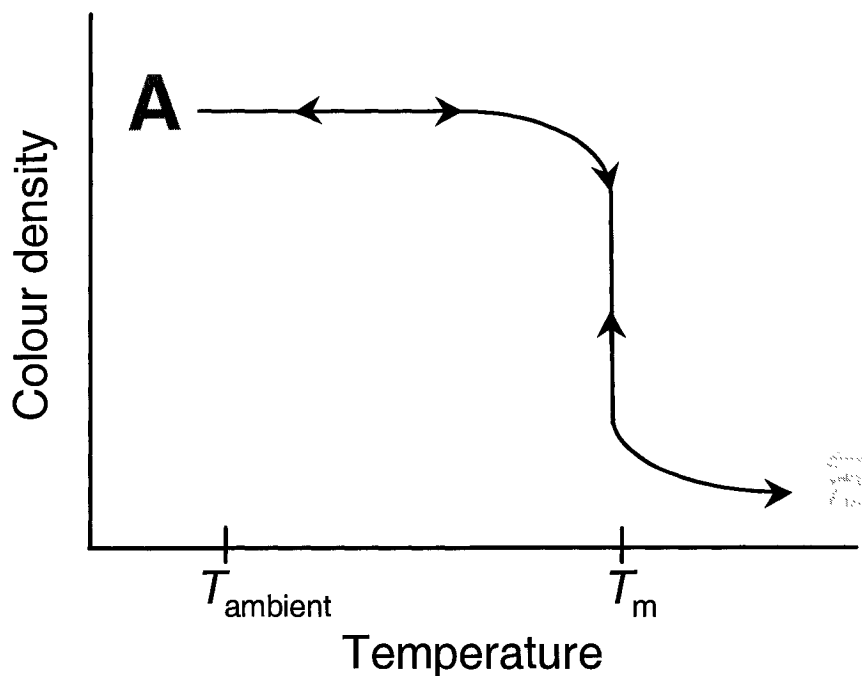
Figure 1.9. Schematic view of a three-component reversible thermochromic mixture. In State A the dye and developer interact in the solid state. Melting of the mixture at $T_m$ results in the dissolution of the developer in the solvent (State B) and loss of colour. This process is reversible.[103]

The use of a solvent makes these mixtures more manageable and easier to design, as the temperature of the thermochromic change can be altered by changing the solvent to one with a desirable melting point.[60,64,88]

This type of three-component mixture is used in thermochromic applications that are coloured at room temperature and undergo colour loss when moderate amounts of heat are applied. Subsequent cooling and solidification of the mixture results in the return of colour. Common applications are novelty papers, toys, clothing, and cutlery that change colour at human body temperature (~37 °C),[7,41,48,59,46,79,104] as shown in Figure 1.10. Cookware and cutlery that change colour at higher temperatures can be used as visible warnings of dangerous temperatures. Mixtures with low-temperature (0 to 10 °C) melting points are colourless at room temperature and are used to indicate when a

beverage, such as beer, is properly chilled (Figure 1.10).[14,104] Colour-to-colour transitions can be achieved by combining a thermochromic dye with a standard dye of a different colour. The colour of the standard dye dominates when the thermochromic dye undergoes colour loss, resulting in an apparent colour-to-colour transition.[7,104,105]
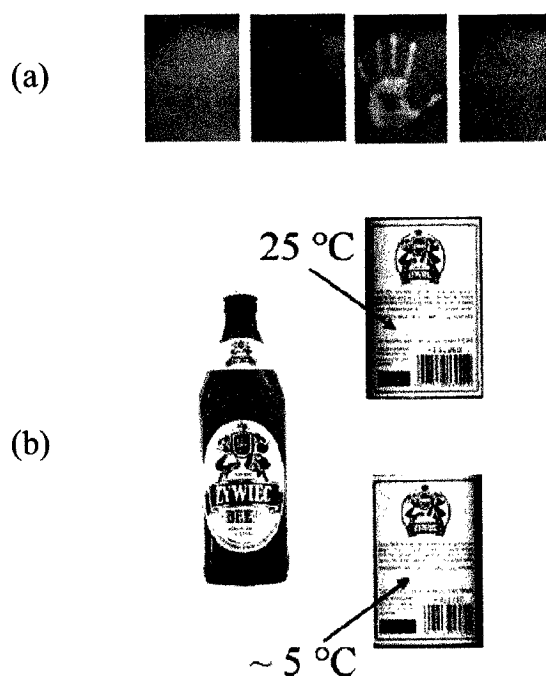


Figure 1.10. Images of common reversible thermochromic applications. (a) A novelty paper changes colour at human body temperature. (b) A reversible mixture with a low-temperature thermochromic transition can indicate when a beverage has been chilled to an appropriate temperature. The small "ŽYWIEC" logo on the bottle label is white at room temperature (25 °C) and becomes red when the bottle is chilled to 5 °C.

# Chapter 2. Rewritable Three-Component Thermochromic Mixtures

## 2.1. Rewritable Three-Component Thermochromic Mixtures

Most common reversible thermochromic mixtures are simply that, they change from a coloured to non-coloured state as the mixture changes from a solid to liquid state or *vice versa*. A specialized class of thermochromic mixtures is able to be either coloured *or* non-coloured in the solid state depending on its thermal history.[7,41,60,85-93] These mixtures will be subsequently referred to as *rewritable thermochromic mixtures* and they are the focus of the present research.

Rewritable thermochromic mixtures can, in principle, be microencapsulated and applied to media in the same manner as conventional thermochromic materials.[7,41,84] The most commonly cited application is the preparation of inks or papers treated with thermochromic microcapsules that can be printed or erased through a series of heating and cooling steps.

In recent years, people have become very conscious of natural resources; recycling of paper products is a billion dollar industry world-wide.[106] The development of rewritable thermochromic mixtures for heat writable/rewritable inks and/or printing systems could dramatically reduce the amount of paper used in the modern office.[46,59,86,88,90,106,107] Rewritable thermal printing could also have applications in other multi-use items such as telephone cards, train-tickets, security markers, and in quality control.[7,41,85-93,106-119]

## 2.2. Basic Principles of Rewritable Thermal Printing

Rewritable thermochromic mixtures use the same colour-forming components as the conventional thermochromic mixtures outlined in Chapter 1. They contain an electron-pair-accepting (basic) leuco dye and an electron-pair-donating (acidic) developer. Colour development is determined by the effective interaction between the dye and developer. In most cases a third component, called a solvent, is added to aid the transition between coloured (interacting) and non-coloured (non-interacting) dye-developer states.[83,103,112-115] In other words, the solvent can be used to modify the chemical environment of the dye and developer in the liquid and solid state.[120]

Although there are many types of rewritable thermochromic mixtures, they all have one property in common; the printing and erasing properties of the system are related to a change from a metastable to equilibrium state within the mixture.[60,64,85-88,90-93,108-119] The metastable state is generally coloured (depending on the system) and must be *long lived* at ambient temperature to ensure practical usage.[86,119] Destruction of the metastable, coloured mixture results in the formation of a non-coloured, equilibrium mixture.

### 2.2.1. General Methods of Rewritable Thermal Printing

Printing and erasing mechanisms of rewritable thermochromic mixtures are related to heat cycles, heating rates, and the relative thermodynamic stability of the phases formed.[118] The most common method for achieving rewritable thermal printing is shown schematically in Figure 2.1.
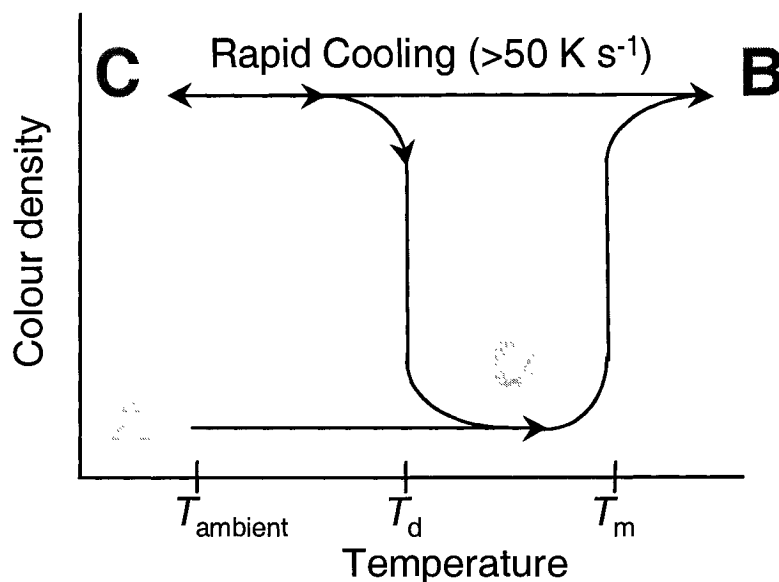
Figure 2.1. Schematic view of a three-component rewritable thermochromic mixture. At (State A) the dye and developer do not interact in the solid state. Melting of the mixture at $T_m$ results in the mixture of the developer in the molten solvent and the development of colour, (State B). Rapid quenching of the mixture ($> 50$ K s$^{-1}$) results in the formation of a metastable, but long lived, coloured state (State C). Heating of the mixture to $T$, $T_d < T < T_m$ results in the formation of the equilibrium, non-coloured, state (State D).[85,87,88]

The equilibrium solid state contains the dye and developer in a non-coloured state, shown as (State A) in Figure 2.1. Colour development occurs when the mixture is melted, resulting in the interaction of the dye and developer in the liquid mixture (State B). Rapid quenching ($>50$ K s$^{-1}$) results in the formation of a metastable, but long lived, coloured state, (State C). Heating of the mixture to $T$, such that $T_d < T < T_m$, results in the formation of the equilibrium, non-coloured, state (State D). Since the equilibrium solid state of the mixture is non-coloured, slow cooling of the molten coloured mixture results in a non-coloured solid state.[85,87,88]

This type of mixture is optimal for the development of a reversible thermal printing apparatus, shown schematically in Figure 2.2. A thermal printing head at $T_1$, $T_1 > T_m$, is used to develop colour in the mixture. Quick removal of this head achieves the

rapid       cooling rate necessary for the formation of a metastable coloured solid. The metastable coloured solid is maintained as long as the mixture temperature is kept below $T_d$, the decolourisation temperature of the mixture. A second thermal head at $T_2$, where $T_d < T_2 < T_m$, is used to decolourise the mixture to achieve erasure. The mixture remains colourless until it is reprinted at $T_1$, $T_1 > T_m$ (Figure 2.2). [87,88]
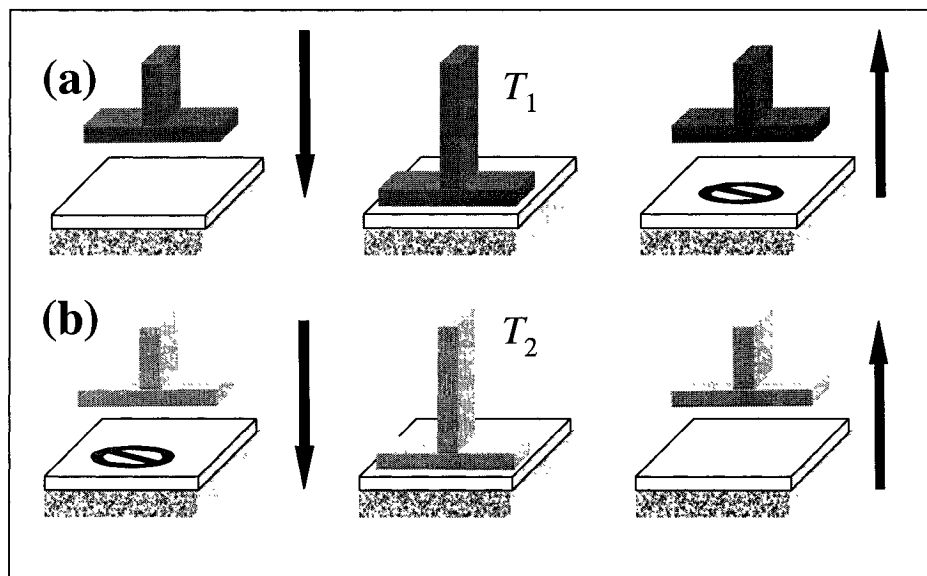


Figure 2.2. Reversible thermal printing is achieved using two thermal printing heads. (a) Application and quick removal of the first head, at $T_1$ ($T_1 > T_m$) results in metastable colour development. (b) Application of a second head at $T_2$, ($T_d < T_2 < T_m$) results in erasure of the colour.

### 2.2.2. Optimal Thermochromic Properties

Three properties are crucial for the optimization of rewritable thermochromic mixtures. First, the contrast between the coloured and non-coloured solid states of the mixture at ambient temperature must be high. This requires a combination of high colour density in the coloured solid and effective erasure to produce the non-coloured solid. Second, the rate of colour change of the solid mixture must be fast. The time required for the thermal head to cause the metastable-to-equilibrium transition should be short. Third, the metastable state must be sufficiently long lived to ensure that no significant change in

colour density occurs at ambient temperature over an extended period of time.[64,85-88,90-93,108-119]

## 2.3. Previous Experimental Work

Although there is very little information in the open literature regarding these materials, many patents have been issued in the area of rewritable thermal printing. Within the patent literature, many types of rewritable thermochromic mixtures are described containing basic leuco dyes, acidic developers, and high-melting organic solvents.

### 2.3.1. General Composition

Common leuco dyes include TPM systems such as fluorans and spirolactones. The most commonly cited examples are 3-dibutylamino-7-(o-chloroanilino)aminofluoran (FD1) (Figure 1.7) and 3,3-(p-N,N-dimethylaminophenyl)-6-N,N-dimethylaminophthalide (CVL) (Figure 1.6). In the coloured state, FD1 is a black leuco dye with absorption maxima of 446 and 586 nm[99,121] and CVL is a blue dye with an absorption maximum of 620 nm.[99,122] Since all the dyes considered in the present study are of the leuco dye type, the term *dye* will hereafter refer to leuco dye molecules.

Common developers include carboxylic acids, phosphonic acids, esters, and phenolic compounds such as alkylthiophenols, alkoxyphenols, and alkyl gallates.[60,64,85-88,90-93,108-119]

The role and structure of the solvent varies depending on the system type. Solvents are also referred to as decolouration-accelerating agents,[64] reversible materials,[86] sensitizing agents,[88] phase-separation controllers,[91] and activators.[118] Solvents range from

long-chain aliphatics such as alkanes, alcohols, and esters, to smaller globular molecules such as steroids and branched hydrocarbons.[60,64,85-88,90-93,108-119]

Component mixing ratios are similar regardless of system design. Dyes and developers make up about 5 to 20% and 10 to 50% by mass, respectively. The solvent makes up the remainder of the composition.[64,85,86,88,115]

Other minor components might be added to the final mixture to aid in the general stability of the mixture. These include many antioxidants and UV-absorbers that enhance the light stability of the dyes; these are also used in conventional, non-thermochromic, dye mixtures.[60,64,85-88,90-93,108-119] Since this study is primarily concerned with the fundamental chemistry of rewritable thermochromic mixtures, the effects of these additives will not be considered. Emphasis will be placed on the dye, developer, and solvent components exclusively.

An examination of the patent literature reveals a complicated series of studies concerned with the optimization of rewritable thermochromic properties, as outlined in the previous sections. While very few experimental data are provided, the bulk of the research appears to have been directed toward an understanding of binary metastable dye-developer complexes. While not an exhaustive review of the literature, the following section is intended to give the reader a sense of the research methods used this area and some of the problems hindering the development of rewritable thermochromic mixtures.

### 2.3.2. Binary Metastable Coloured Mixtures

Metastable coloured phases are thought to be weakly interacting complexes of dye and developer held together through intermolecular interactions such as H-bonds and van der Waals forces.[60,64,85,92,108,112,113,118] The structures of metastable phases observed

vary from featureless, amorphous mixtures to more ordered formations of dye-developer molecular aggregates.[60,64,85,92,108,112,113,118] Destruction of the metastable phase occurs above $T_d$ when developer molecules phase separate and crystallize from the coloured aggregate, resulting in loss of colour.
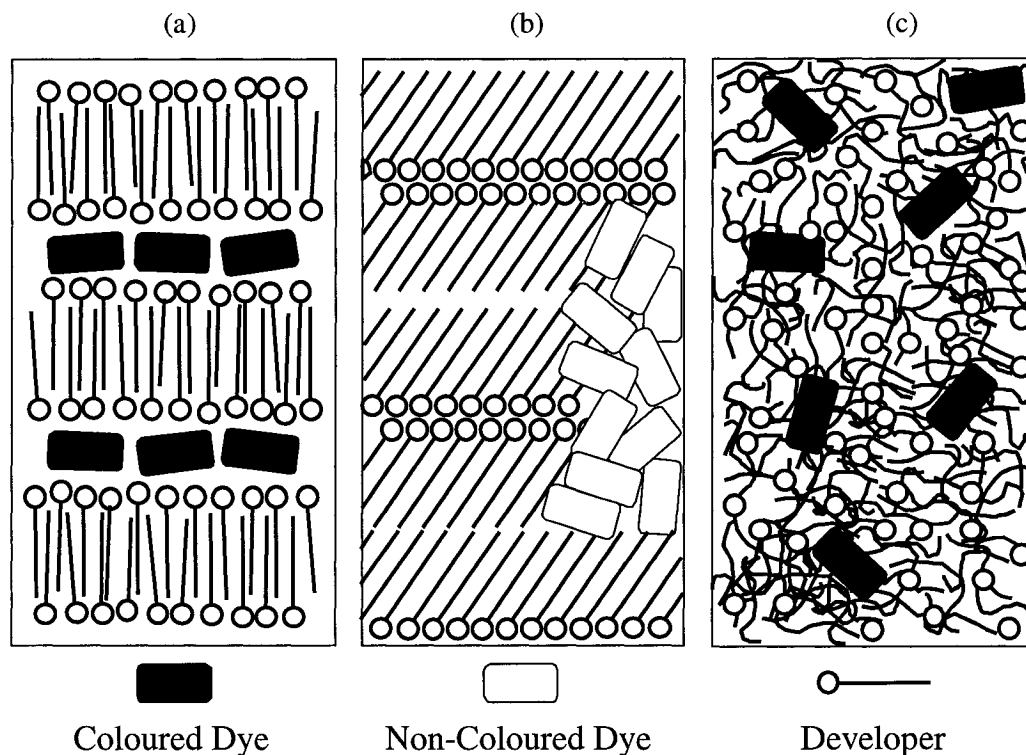


Figure 2.3. Schematic images of the two types of metastable phases thought to be formed in binary dye-developer mixtures used in rewritable thermochromic systems compared with the structure of the mixtures at equilibrium. (a) The metastable aggregate with long-range lamellar order is formed upon rapid cooling from the molten mixture and is metastable with respect to (b) a phase-separated mixture of dye and developer. (c) An amorphous metastable phase shows no long-range order and is also metastable with respect to (b) a phase-separated mixture of dye and developer. Adapted from references 61 and 92.

Figure 2.3 shows a schematic view of the two types of metastable phases commonly observed. The so-called "aggregate phases" display ordering of the developer and dye molecules into supermolecular complexes displaying lamellar features.

[60,64,85,92,108,112,113,118] Amorphous metastable phases display no long-range order and are glassy solids.

Several patents address the formation of metastable aggregate structures but specific mechanisms and detailed structures are not clear.[60,64,79,85,89,110] It is speculated that the ability to form aggregate structures is related to the carbon chain length of alkyl developers. Aggregate structures are believed to be formed by standard TPM dyes and acidic developers with long alkyl-chains (> 12 carbons) where van der Waals interactions between the chains allow the formation of large supermolecular complexes.[60,64,85,110] Long-chain alkyl groups are believed to support the formation of a metastable complex while maintaining the high degree of crystallinity in their pure state to ensure efficient phase-separation upon decolourisation.[60,64,85,92,108,112,113,118]

Many patents examine the X-ray diffraction (XRD) patterns of binary dye-developer mixtures. For example, Figure 2.4 shows the XRD patterns of rapidly cooled, coloured thermochromic mixtures consisting of 3-dibutylamino-7-(o-chloroanilino)aminofluoran (FD1) and a series of developers with an electron-pair-accepting functionality, n-alkyl phosphonic acids.[85,92]
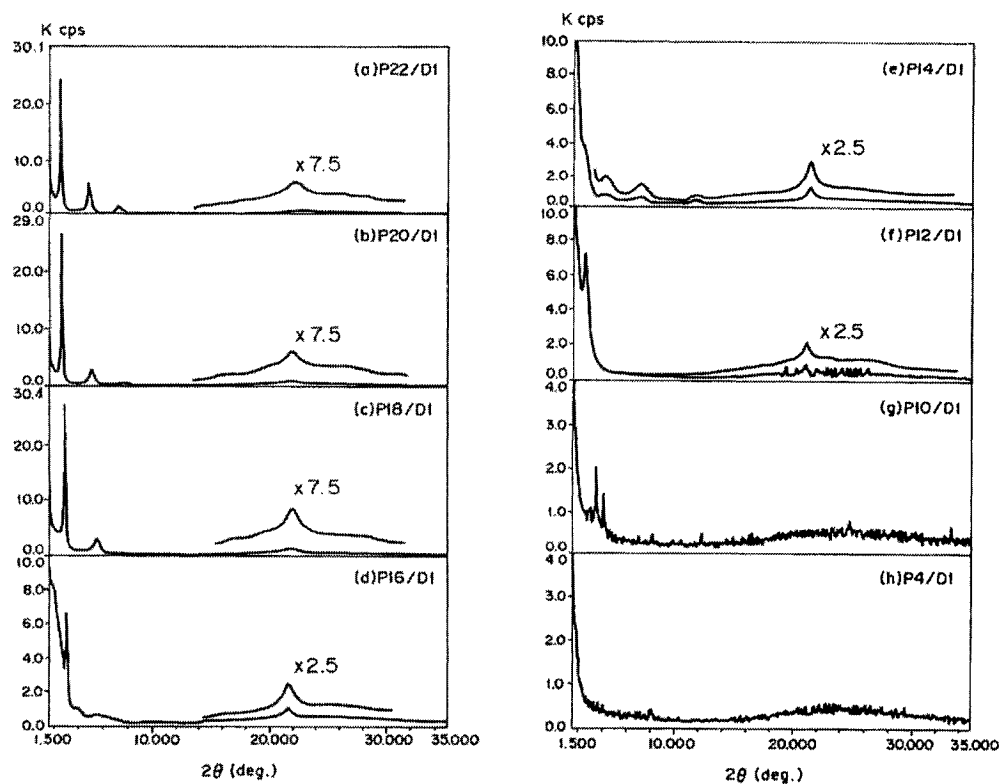
Figure 2.4. X-Ray diffraction patterns of rapidly cooled (1:5 dye-developer by mass) mixtures of 3-dibutylamino-7-(o-chloroanilino)aminofluoran (FD1) and a series of n-alkyl phosphonic acids: (a) and 1-docosylphosphonic acid (P22) (b) 1-eicosylphosphonic acid (P20) (c) 1-octadecylphosphonic acid (P18) (d) 1-hexadecylphosphonic acid (P16) (e) 1-tetradecylphosphonic acid (P14) (f) 1-dodecylphosphonic acid (P12) (g) 1-decylphosphonic acid (P10) and (h) 1-butylphosphonic acid (P4). Mixtures a) through f) are characterized by long-range lamellar order at diffraction angles of $2\theta = 1$ to 10° and aggregation of alkyl-chains at angles of $2\theta = 20$ to 25°. Phosphonic acid developers with alkyl-chains shorter than 12 carbons produce amorphous solid structures (mixtures g and h). Figure adapted from references 85 and 92.

XRD patterns show the structural changes of the mixture as the alkyl-chain length of the developer is increased. Binary mixtures containing phosphonic acids with alkyl-chain lengths greater than 12 carbons were coloured on rapid cooling and colourless on slow cooling. They displayed two major features at diffraction angles of $2\theta = 1$ to 10° and $2\theta = 20$ to 25°. Small diffraction angles are indicative of long range order[123] and the

peaks observed at $2\theta = 1$ to $10°$ are described as being due to a long-range lamellar order (*cf.* Figure 2.3) within the system.

The weak, broad peaks at diffraction angles in the region of $2\theta = 20$ to $25°$ in Figure 2.4 consist of a small hump at $2\theta = 21°$. This feature is described as being intermediate between a completely featureless XRD pattern, consistent with an amorphous material, and a series of sharp peaks, consistent with crystalline material. The feature observed is assigned to a loosely associated aggregation of the alkyl groups of the phosphonic acid arranged in primarily the same direction.[111] Mixtures with short-chain developers (Figure 2.4, g and h) show essentially featureless XRD patterns (note the change in intensity scale) indicative of amorphous materials. Binary amorphous mixtures tended to decolour slowly (if at all) upon heating because short-chain developers have less propensity to crystallize. In the same regard, they also tended to form coloured mixtures regardless of cooling rate. Dye-developer combinations of this type are typically mixed with a solvent that preferentially dissolves one of the components in the liquid state to produce a reversible thermochromic mixture described by Figure 1.9.[60,64,85,92,108,112,113,118]

Figure 2.5 shows the XRD pattern of one of the mixtures displaying aggregate formation, P18/FD1, at diffraction angles of $2\theta = 1$ to $10°$ and $18$ to $24°$ as it is heated from 27 to 90 °C.[85,92]
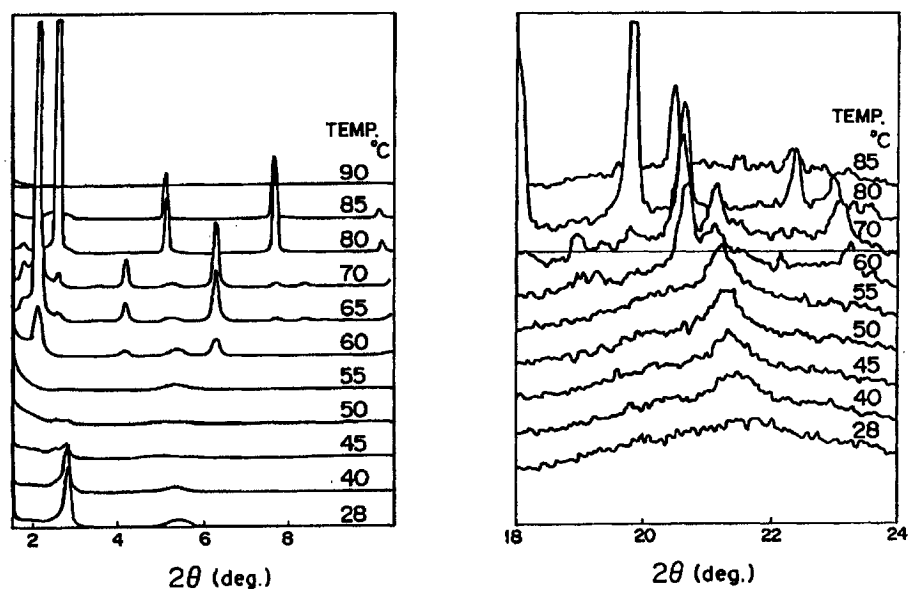
Figure 2.5. XRD patterns showing the heating of a rapidly cooled (1:5 dye-developer by mass) mixture of coloured 3-dibutylamino-7-(o-chloroanilino)aminofluoran (FD1) and octadecylphosphonic acid (P18) as it is heated from 27 to 90 °C. Figure adapted from references 85 and 92.

Peaks associated with long-range lamellar structure ($2\theta = 2.8$ and $5.5°$) disappear completely at about 45 to 50 °C. Between 28 to 55 °C the peak assigned to the aggregated alkyl-chains of developer ($2\theta = 21°$) appeared to sharpen. At 60 °C a series of crystalline peaks, corresponding to pure P18, appeared at diffraction angles of $2\theta = 2$ to 8° and $2\theta = 19$ to 23° as the mixture began to decolour.[85] At 80 °C a new set of crystalline peaks were observed. The identity of these peaks was not mentioned by the authors but they are presumably due to a solid-solid phase transition commonly observed in $n$-alkyl phosphonic acids.[124]

An added complication to the examination of metastable coloured states was that the structures observed varied with the ratio of dye and developer present in the mixtures. Figure 2.6 compares the XRD patterns of mixtures of FD1/P18 mixed in 5:1 (Figure 2.4) and 2:1 mole ratios.
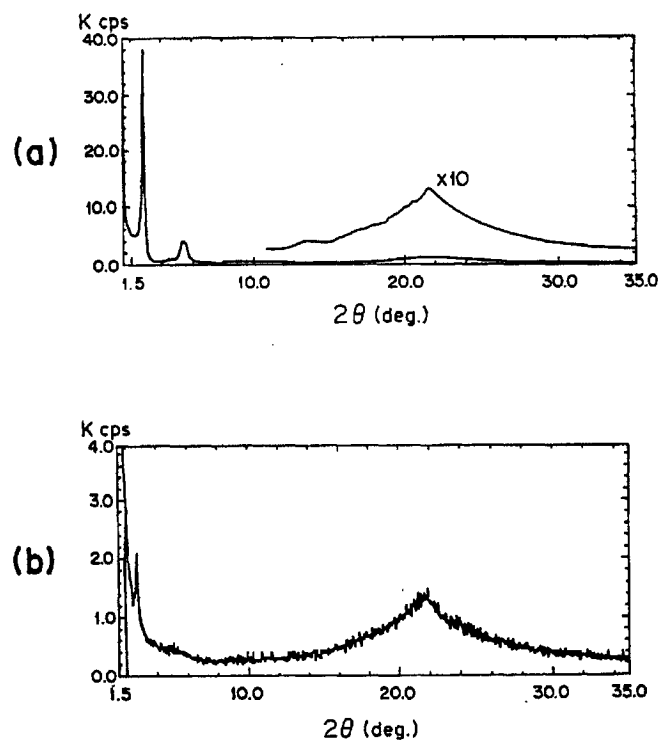
Figure 2.6. The dye-developer mixing ratio has an effect on the structural features of the metastable mixture observed by XRD. (a) FD1/P18 in a 5:1 mole ratio shows sharp peaks indicative of long-range lamellar order at diffraction angles of $2\theta = 0$ to $10°$ and a broad peak representing the aggregation of P18 alkyl groups at $2\theta = 20$ to $25°$. (b) FD1/P18 in a 2:1 mole ratio shows less long-range lamellar ordering of the mixture but still shows aggregation of the P18 alkyl groups.[111]

The 2:1 FD1/P18 mole ratio mixture displayed little evidence of long-range order in the $2\theta = 0$ to $10°$ region, but did show the same broad peak at $2\theta = 20$ to $25°$ consistent with the aggregation of alkyl-chains. The low intensity of the diffracted peaks shows that this structure is intermediate between the aggregate and amorphous metastable phases shown in Figure 2.4. Changes in metastable phase structure as a function of dye-developer ratios and developer alkyl-chain lengths make it difficult to predict the exact structure of the coloured state in a given dye-developer mixture.

In summary, examination of binary dye-developer interaction showed that metastable coloured structures formed on rapid cooling can either be aggregates or amorphous. Most authors indicated that aggregate metastable phases are better suited for rewritable thermal printing because they tend to convert to the equilibrium, non-coloured state more readily than the amorphous metastable coloured states.[60,64,85,92,108,111,112,113,118]

The detailed structures of aggregated phases are not known but two basic structural features were observed; (1) the formation of a long-range lamellar structure, and (2) aggregation of the alkyl-chains of the developers.[60,64,85,92,108,111,112,113,118]

While some authors note that the length of the alkyl-chain of the developer was the principal factor in determining whether an amorphous or aggregate structure forms,[85] the ratio of the two components was also a factor determining the structures observed. Given these difficulties it is not currently possible to predict with certainty what metastable structure will be formed in a given dye-developer mixture.

### 2.3.3. Role of the Solvent Component

Patent authors noted that the phase-separation of the developer from the metastable dye-developer structure does not occur efficiently and completely. This tends to be a problem regardless of the metastable phase structure. Practical applications require a solvent component to enhance rewritable thermochromic properties and produce a ternary system consistent with the schematic view shown in Figure 2.1.[60,64,85,92,108,112,113,118] Common solvents include alcohols, paraffins, esters, fatty acids, silicone oils, liquid crystalline materials, and surfactants.[60,64,85,92,108,112,113,118] The role of the solvent falls into one or more of three categories.

First, if the melting point of the solvent component is less than the melting point of the bulk mixture ($T_{m,solvent} < T_{m,mixture}$) the solvent provides a liquid medium to aid the phase-separation of the developer from the metastable structure in the mixture. Since $T_d = T_{m,solvent}$, the decolourisation temperature can be easily adjusted by changing the solvent composition. In this application, the solvent comprises a much smaller portion (0.5 to 10 mass%) of the mixture than in a standard thermochromic mixture (50 to 90 mass%).[60,64,88]

Second, when solvent is present in large amounts (50 to 90 mass%) the melting point of the bulk mixture is primarily determined by the melting point of the solvent ($T_{m,solvent} \sim T_{m,mixture}$)[60,64,88] and the entire mixture is a solid at the decolourisation temperature, $T_d$. If the solvent is highly crystalline, it can provide nucleation sites for the phase-separation of developer above $T_d$ and lower the activation energy for the phase-separation, resulting in an increased rate of decolourisation. The term "decolourisation accelerating agent" is used to describe the solvent when used in this manner.[64]

Third, if the solvent and developer are compatible and a metastable dye-developer aggregate is present, molecules of the solvent could incorporate themselves into an aggregate structure with the dye and developer. Addition of solvent molecules would then influence the cohesive properties and stability of the aggregate.[110] This property could be used to lower the decolourisation temperature of a molecular aggregate and/or aid in the phase-separation of the developer.

The third aspect was examined by Hideaki *et al.*, by combining two long-chain developer molecules and observing the structures formed.[85] A 5:1 (molar) mixture of docosylphosphonic acid (P20) and octadecyl gallate (3,4,5–trihydroxybenzoic acid octadecyl ester, ODG) was compared upon rapid and slow cooling. Figure 2.7 shows the

IR spectrum of the two mixtures. There are differences in the carbonyl region of the spectrum for the two mixtures.[85]
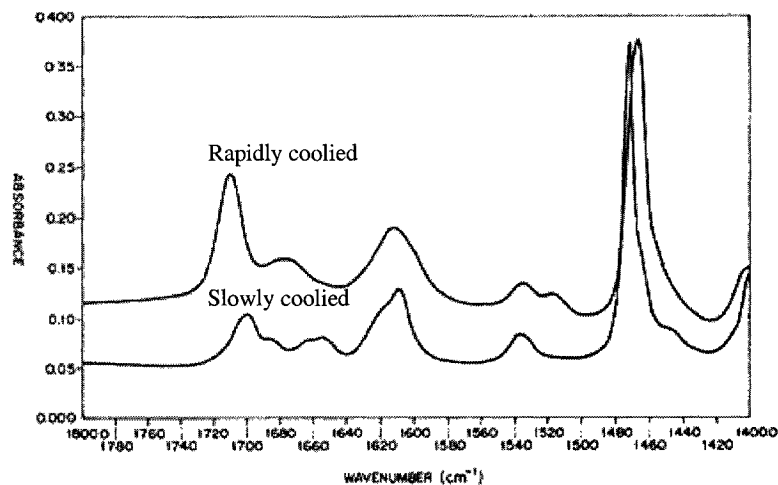


Figure 2.7. IR spectrum of a 5:1 (molar) mixture of docosylphosphonic acid (P20) and octadecyl gallate (ODG) that has been rapidly cooled and slowly cooled from the melt. The two mixtures show differences in the carbonyl region of ODG (1750 to 1600 cm$^{-1}$) indicating a difference in interaction between the two components as a function of thermal history. Adapted from reference 85.

The slowly cooled sample shows peaks at 1700, 1690, and 1660 cm$^{-1}$. The rapidly cooled sample has peaks at 1710 and 1680 cm$^{-1}$, indicating a difference in thermal history results in a change of the interaction between the two developers. Figure 2.8 shows the IR spectrum of the rapidly cooled sample as it is heated from 29 °C to 72 °C.
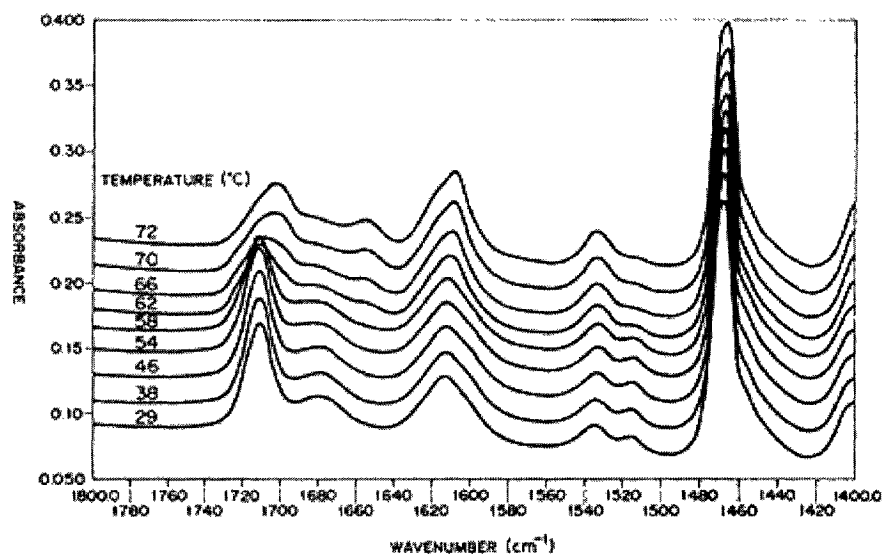
Figure 2.8. IR spectrum of a rapidly cooled 5:1 (molar) mixture of docosylphosphonic acid (P20) and octadecyl gallate (ODG) as it is heated. Shifts in the carbonyl region of ODG (1750 to 1600 cm$^{-1}$) begin to appear at about 60 °C. By 72 °C the spectrum is nearly converted to that of the slowly cooled sample in Figure 2.7. Adapted from reference 85.

Above 60 °C there was a slight shift of peak frequencies as the spectrum of the rapidly cooled sample transformed to that of the slowly cooled sample. Figure 2.9 and Figure 2.10 show XRD patterns for the different cooling rates. The rapidly cooled sample showed lamellar and aggregation structural features with peaks at diffraction angles of $2\theta$ = 1.6°, 3.2°, 4.8° and 21.1°. These peaks differed from peaks formed from either pure P20 or ODG and showed that a unique aggregate phase was formed. The slowly cooled sample displayed peaks at diffraction angles of $2\theta$ = 1.8°, 2.2°, 4.0°, 4.3°, 6.5, 8.7°, 10.9°, 22.3°, and 23.9° consistent with the presence of crystalline P20.[85]
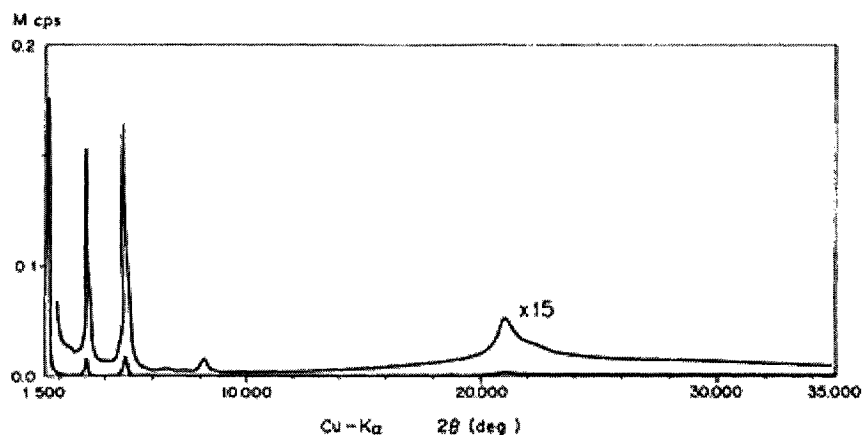
Figure 2.9. XRD pattern of a rapidly cooled mixture of (5:1) P20/ODG. Features consistent with lamellar order are observed at diffraction angles of $2\theta = 1$ to $10°$ and the broad peak at $2\theta = 20$ to $25°$ is consistent with aggregation of alkyl-chains. Adapted from reference 85.
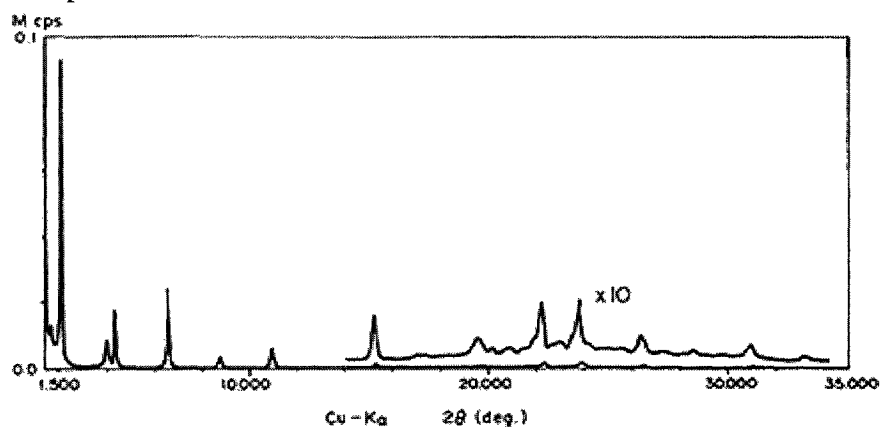


Figure 2.10. XRD pattern of a slowly cooled mixture of (5:1) P20/ODG. Diffraction peaks in this mixture are consistent with the phase-separation of pure P20. Adapted from reference 85.

The effect of the addition of a dye to this mixture was not reported, but the authors noted the significance two long-chain components forming metastable structures themselves. They noted that combinations of multiple developers and/or solvents could be used to influence the structure and stabilty of metastable phases. With this in mind, the authors vaguely referred to a "thermal control relationship" between the components of the mixture, but offered no further experimental evidence of its utility in rewritable thermochromic mixtures.[85]

To summarize, the role of the solvent is not actively pursued in the open literature or patents and is thought to be simply a means for accelerating phase-separation and/or setting the temperature of the thermochromic change. There is some discussion of the possibility of the interaction and metastable phase formation among multiple developers and/or solvents but beyond this, little consideration is given to the solvent's potential role in thermochromic properties.

## 2.4. Problems Within the Field

Beyond the characterization of the types of metastable phases formed there is little understanding of colouring (dye-developer) interactions, how they form, and what factors determine their stability. While there appears to be many experimental data outlining thermochromic formulations, it is not possible at present to predict thermochromic properties effectively.[60,64,85,92,108,112,113,118]

The previous sections show some examples of the research activities within this field. While many patents describe rewritable thermochromic mixtures, there are no data that systematically examine the mechanism of rewritable thermochromic mixtures.[79,89,125] Figure 2.11 shows a histogram of the numbers of patents issued in rewritable thermal printing since 1985.
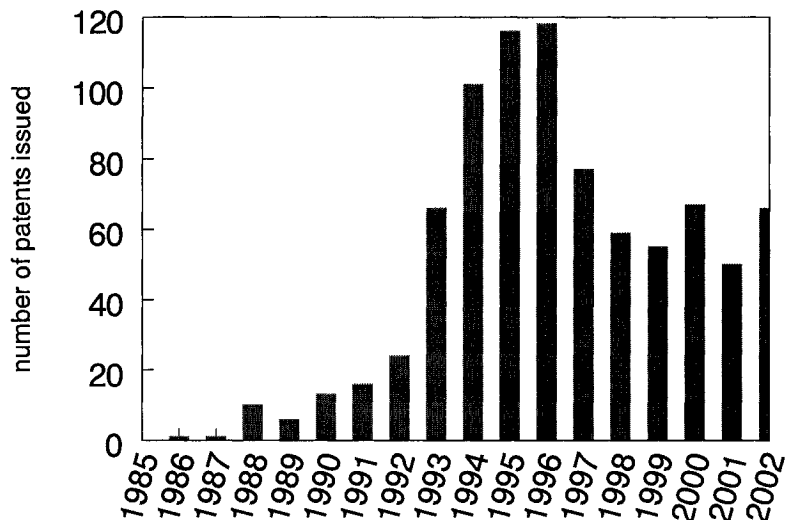
Figure 2.11. Histogram of the number of patents issued worldwide for reversible thermal printing/rewritable thermal printing since 1985. Data obtained from the CAS SciFinder Scholar.

Research in these materials increased sharply in the early 1990's and plateaued in the mid-to-late 1990's. While the correlation of patent activity with research interest is not a strictly scientific assessment, the drop in research activity might correspond with the inherent complexity of developing rewritable thermochromic mixtures. Considering that little is known about the binary dye-developer interaction, the examination of mixtures with three or more components presents a significant challenge.[110] It appears that many companies might have abandoned extensive research in these materials due to difficulties in the optimization of colour density, colour stability, and decolourisation rates. As recently as 2001 Maruyama and Sano commented, "(A)ccording to [the techniques outlined in Chapter 2.3] there have been no reversible, heat-sensitive

recording materials which give good image contrast, can form erase(d) images, and can maintain images having time stability under the daily environment."[113]

Other authors comment on a lack of detailed mechanistic information regarding the chemistry of the dye-developer interaction and the developer-solvent interaction. Mather[79], Burkinshaw *et al.*[89], and Luthern and Peredes[125] note that detailed examination of the thermal properties of these mixtures is necessary to better understand, optimize, and design thermochromic properties.

### 2.5. Research Aims

Review of the current literature in rewritable thermochromic materials has shown that a detailed examination of thermochromic properties is vital to their understanding and optimization. Nearly all of the existing literature in this field is directed at understanding the interaction between the dye and developer in the thermochromic mixture. The sheer variation in the observed structures of the metastable dye-developer mixtures as a function of developer functional group, developer chain length, and dye-developer mixing ratios could make its examination an entire thesis alone. However, it is unlikely that broad-reaching design rules will be developed to address this aspect of rewritable thermochromic mixtures.

While the dye-developer interaction is vital to thermochromic properties, in practical applications rewritable thermochromic mixtures contain large portions of solvent. The potential interaction between the developer and solvent in the ternary thermochromic mixture appears to have been overlooked in the literature.

Few authors speculate that interactions involving the solvent components are of significance. Hideaki *et al.* mentioned the importance of a "thermal control relationship" among the strengths of the interaction of components, including the solvent.[85] While they did not elaborate on how they measure or use these "relationships," they raised the important issue of the thermal properties of the mixture. Luthern and Peredes also speculate that ternary thermochromic properties might be a result of a balance of dye-developer and developer-solvent interactions but presented no systematic evidence of the relationship.[125]

The goals of the present research include systematic examination of the colouration and erasure mechanisms of reversible thermochromic mixtures. More specifically, the correlation of thermochromic properties to the interactions between the solvent and developer components will be examined. To this end, it is hoped that design rules might be developed to aid in the selection of solvent and developer components for rewritable thermochromic mixtures.

Since the field of rewritable thermochromic mixtures is complex and diverse, it is unlikely that design rules applying to all mixtures will ever be achieved. With this in mind, results for an archetypal ternary rewritable thermochromic mixture with significant composition dependent variation in thermochromic properties will be presented.

Emphasis will be placed on an examination of two primary interactions of the major components of the mixture: (1) the developer-dye interaction and (2) the developer-solvent interaction. Background data presented to this point show the importance of the formation of long lived metastable states, phase transitions, and

intermolecular interaction. All of these factors are examined in a quantitative and systematic fashion.

Thermal analysis and spectroscopy of the various binary and ternary interactions within the mixture enable the thermodynamic examination of equilibrium and metastability in the solid state. Comparison of factors defining these states aid in the understanding and development of design rules for the optimizing the colour contrast, colour stability, and decolourisation rates in rewritable thermochromic mixtures.

# Chapter 3. Experimental Methods

## 3.1. Components

All materials were obtained commercially and used without further purification. The melting point of each substance was characterized by differential scanning calorimetry (DSC). Crystal violet lactone 3,3-bis($p$-N,N-dimethylaminophenyl)-6-N,N-dimethylaminophthalide CVL, 97%, $T_{m,lit}$ = 180-182 °C,[126] $T_{m,DSC}$ = 181.3 ± 1 °C; lauryl gallate (dodecyl(3,4,5-trihydroxy)benzoate) LG, 97%, $T_{m,lit}$ = 96-97 °C,[127] $T_{m,DSC}$ = 97.2 ± 1 °C; and octyl gallate (octyl(3,4,5-trihydroxy)benzoate) OG, 97%, $T_{m,lit}$=100 ± 1 °C,[128] $T_{m,DSC}$ = 102 ±2 °C were obtained from Aldrich. 1-tetradecanol, TD ,96%, $T_{m,lit}$ = 38-40 °C[129-131], $T_{m,DSC}$ = 37.5 ±1 °C and 1-octadecanol, 99% , OD, $T_{m,lit}$ = 58-60 °C,[129-132] $T_{m,DSC}$ = 58.1 ± 1°C were obtained from Sigma. 1-hexadecanol, 96%, HD, $T_{m,lit}$ = 48-50 °C, [129-131] $T_{m,DSC}$ = 49.5 ± 1 °C, and propyl gallate (dodecyl(3,4,5-trihydroxy)benzoate) PG, 97%, $T_{m,lit}$ = 149-151 °C,[133] $T_{m,DSC}$ = 148.4 ± 1 °C were obtained from Eastman Kodak.

Ternary rewritable thermochromic mixtures were prepared by mixing the components at the desired composition in glass sample vials and heating to fusion. Cooling the molten mixtures generally produced homogeneous solid mixtures. Samples were digitally photographed in one of two ways: (1) from the bottom of the glass sample vial or (2) on paper treated with the thermochromic mixtures. For reflectance measurements, and some photography, molten mixtures were deposited on and allowed to saturate pieces of standard, white copy paper. After treatment, papers were covered

with clear plastic tape to minimize loss of the liquid system. In general, approximately 1.0 mL of molten mixture was applied to a 10 cm$^2$ area of paper. For the purposes of photography, rapid cooling was achieved by placing the paper in contact with an aluminum block immersed in liquid nitrogen.

### 3.2. Differential Scanning Calorimetry

DSC was introduced by Perkin-Elmer$^{TM}$ in 1964 and is currently the most widely used method of thermal analysis.[134,135,136] This technique consists of the measurement of differential calorimetric properties between a sample and reference material. Power-compensated DSC provides reliable thermodynamic information such as enthalpy and entropy changes and temperature of thermal events can also be determined with reasonable accuracy (~1-2% uncertainties).[134,136] It is a fast, commercially available technique designed for high throughput. Since small sample sizes are required (1 to 100 mg), reliable data are obtained from rapid scan rates, typically 5 to 10 K min$^{-1}$ but as high as 500 K min$^{-1}$, over a temperature range extending from 100 to 1500 K.[134-136]

### 3.2.1. DSC Apparatus

A basic power-compensated DSC apparatus is shown schematically in Figure 3.1 and it consists of two individual calorimeter chambers (sample and reference, S and R) made from Pt/Rh or Pt/Ir alloys.[136] An aluminum, gold, stainless steel, or platinum pan containing the sample material is placed in the sample chamber. The reference chamber contains an empty sample pan displaying no anomalous thermal effects throughout the temperature program.[134] Each chamber has its own resistance heater and Pt resistance

thermometer and is linked to the other chamber through a feedback circuit designed to minimize the temperature differential, $\Delta T_{SR}$, as both are heated (or cooled) through a temperature program.[134-136] S and R are both in contact with a heat sink cooled with ice for ambient temperature measurements ( > 288 K) and moderate cooling rates (0.01 to 50 K min$^{-1}$) or liquid nitrogen for low-temperature experiments (> 100 K) and/or rapid cooling rates (> 50 K min$^{-1}$).
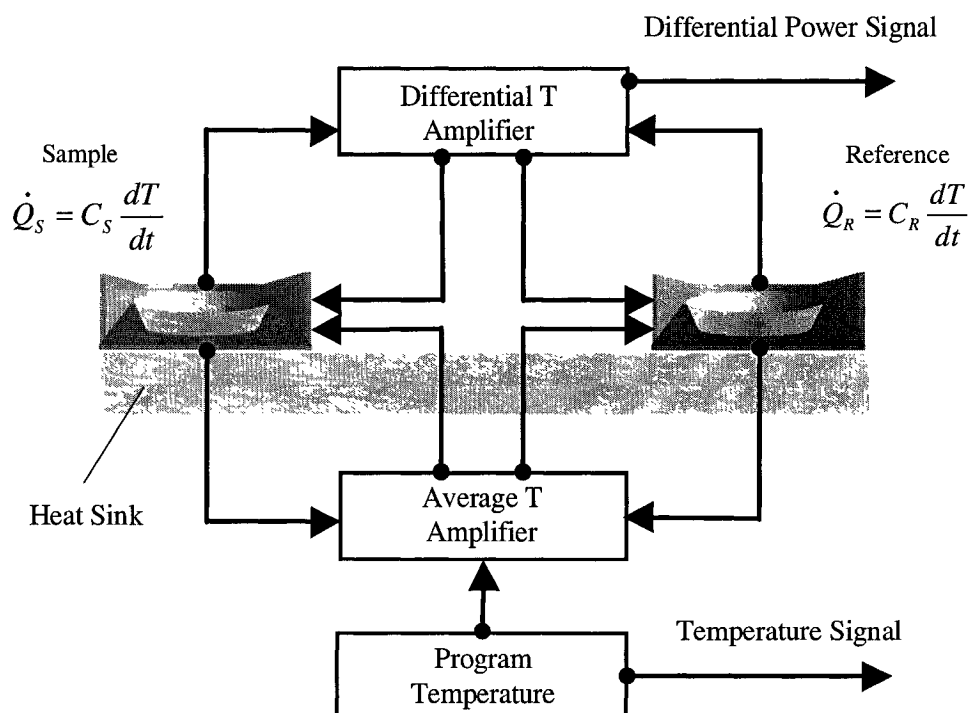


Figure 3.1. Schematic diagram of power-compensated DSC. Separate sample (S) and reference (R) chambers have their own thermometers and heaters linked through a feedback circuit that minimizes the differential temperature between S and R ($\Delta T_{SR}$). If $\Delta T_{SR}$ = 0, the average temperature amplifier heats S and R. If a thermal event occurs in S ($\Delta T_{SR} \neq 0$) the differential temperature amplifier and the average temperature amplifier heat S and R to keep $\Delta T_{SR}$ = 0. Adapted from references 134 and 136.

The temperature program is set by the average temperature amplifier, which heats S and R.[136] The amounts of power needed to heat S and R are expressed as:[134]

$$\dot{Q}_S = C_S \frac{dT}{dt} \qquad\qquad 3.1$$

$$\dot{Q}_R = C_R \frac{dT}{dt} \, , \qquad\qquad 3.2$$

where $\dot{Q}_S$ and $\dot{Q}_R$ are sample and reference power and $C_S$ and $C_R$ are sample and reference heat capacities. If the heat capacities of S and R are matched, $\Delta T_{SR} = 0$, and the average temperature amplifier heats the chambers exclusively while the differential temperature amplifier feedback loop remains open.[136]

In the case of a thermal event in the sample material (*e.g.* a first-order phase transition), $C_S$ changes significantly.[134-136] As $C_S$ increases, $T_S$ lags behind $T_R$ and, since only the average temperature is controlled, R heats faster. When $\Delta T_{SR}$ reaches a set threshold the differential temperature amplifier loop closes and adjusts power to the S and R to minimize $\Delta T_{SR}$.[136] In the case of an endothermic event ($C_S > C_R$) the differential temperature amplifier supplies power to S *in excess* of the power supplied by the average temperature amplifier. Conversely, during an exothermic sample event ($C_S < C_R$) excess power is supplied to R. Differential power supplied by the differential temperature amplifier is the power signal observed in the output data.[134-136] The observed power signal in DSC can be expressed as:[134]

$$Signal = \dot{Q}_S - \dot{Q}_R = C_S \frac{dT}{dt} - C_R \frac{dT}{dt} = (C_S - C_R)\frac{dT}{dt} . \qquad\qquad 3.3$$

It is impossible to match $C_S$ and $C_R$ perfectly throughout the temperature range of the experiment. Most DSC thermograms have a linear change in differential power called the baseline with a slope proportional to $(C_S - C_R)$. In the case of a thermal event, a peak appears on this baseline.[134] Thermograms are plotted as differential power versus time or

temperature. The enthalpy of a transition can be calculated by integrating the area under a power/time peak.

### 3.2.2. Calibration

The previous section describes an artificial system and does not consider the temperature lag between the actual temperature of the sample, $T_S$, and the temperature at the thermometer recording it, $T_{ST}$.[134] Temperature lag $(T_S - T_{ST})$ can be minimized by ensuring good contact between the sample and pan bottom and between the pan bottom and the surface of the sample chamber. Although these precautions can lower $(T_S - T_{ST})$, the scan rate of the experiment also plays an important role:[134]

$$\dot{Q}_S = \frac{1}{R_S}\left(T - T_{ST}\right),$$   3.4

where $\dot{Q}_S$ is the heat flow from S and $R_S$ is the resistance of the thermometer. Combining Eq. 3.4 with Eq. 3.1 gives:[134]

$$T_S - T_{ST} = R_S C_S \frac{dT}{dt}.$$   3.5

Since $(T_S - T_{ST})$ is directly proportional to scan rate $(dT/dt)$ it is important to calibrate the instrument using the scan rate used in the experiment.[134-136]

Calibration is performed by measuring the transition temperatures and enthalpy changes of highly pure materials.[134-136] Although many organics (e.g. benzoic acid) are available for calibration, as little as 0.1% impurity significantly lowers their melting temperatures. For this reason, metals such as In and Zn are favoured because they can be obtained in > 99.9 % purity.[134] In a calibration, the onset temperature, $T_{onset}$, and enthalpy of a transition, $\Delta_{tr}H$, are measured. $T_{onset}$ is defined as the intercept of the baseline with

the inflection point of the peak.[134-136] $T_{onset}$ is a more reliable measurement of transition temperature than the peak temperature because it is less sensitive to temperature scan rate.[134]

A Perkin-Elmer™ Pyris-1™ DSC was used for all experiments reported here. For ambient temperature operation, the instrument was calibrated using the melting point and enthalpy of indium (Aldrich 99.99%) under an atmosphere of ultra-dry nitrogen (20 mL min⁻¹). For low-temperature operation, the instrument temperature was controlled with a Perkin-Elmer™ CryoFill™ temperature control accessory. The instrument was calibrated by measuring the solid-solid phase transition temperature and enthalpy of dipentylammonium chloride[137] under an atmosphere of ultra-dry helium (20 mL min⁻¹). Scan rates of 5 to 10 K min⁻¹ were used for phase diagrams and annealing experiment and up to 300 K min⁻¹ for the preparation of metastable coloured mixtures.

### 3.3. Vibrational Spectroscopy

The energy of transition between vibrational energy levels is on the order of 8 to 40 kJ mol⁻¹ [138] and can be probed using vibrational spectroscopy.[139,140] Vibrational transition energy is expressed as:[139]

$$\Delta E = h\upsilon = hc\tilde{\upsilon} \ ,$$  3.6

where $\upsilon$ is the frequency of the energy and $\tilde{\upsilon}$ is defined as the wavenumber. The vibrational frequency of a mode is related to the force constant of the bond(s) involved:[138-140]

$$\upsilon = \frac{1}{2\pi} \sqrt{\frac{k}{\mu_m}} \ .$$  3.7

where $k$ is the Hooke's Law force constant and $\mu_m$ is the reduced mass of the system.

Changes in $\upsilon$ correspond to changes in the electronic density within bonds, providing

important chemical information.[138-140]

### 3.3.1. Infrared Spectroscopy

Infrared (IR) spectroscopy, shown in the schematic diagram in Figure 3.2, is a

transmission technique that measures the energy absorbed when light interacts with the

dipole moment of a vibrating bond. [138-140]
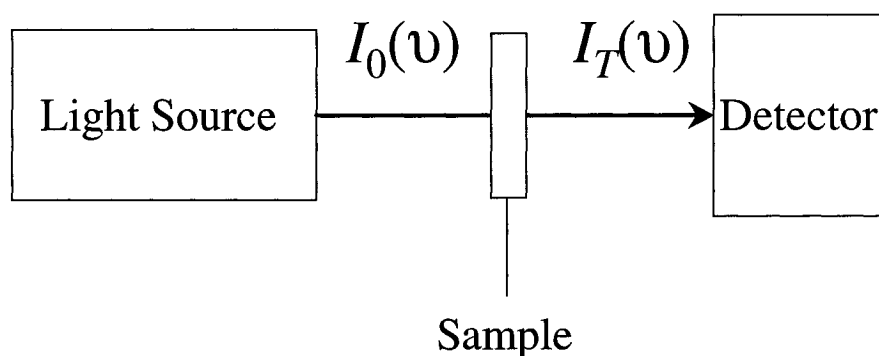


Figure 3.2. A schematic view of an IR spectrometer used in the present study. A light source penetrates the sample and transmitted light is collected at a detector. Light is absorbed by the sample according to the Beer-Lambert law. Adapted from reference 139.

In an IR experiment a broad spectrum of energy (4000 to 200 cm$^{-1}$) from a

tungsten or halogen light source penetrates the sample. Intensity of IR absorption is

expressed by the Beer-Lambert law:[138,139]

$$I_T = I_0 e^{-\varepsilon c d} \qquad\qquad 3.8$$

where $I_0$ is the initial intensity, $I_T$ is the transmitted intensity, $\varepsilon$ is the molar absorption

coefficient, $c$ is the molar concentration, and $d$ is the path length of the sample. IR

absorption is more commonly expressed in terms of absorbance, $A$:[138,139]

$$A = \log\frac{I}{I_0} = \varepsilon c d \ .$$  3.9

A typical IR spectrometer consists of a light source, sample holder, and detector (Figure 3.2).[138] Most IR spectrometers detect light of all frequencies transmitted and produce a time-domain (intensity *vs.* time) interferogram. This complex pattern is transformed into a frequency domain (intensity *vs.* frequency) spectrum through Fourier transformation (FT). FTIR eliminates the need to scan through all frequencies slowly using a monochrometer and allows for rapid spectral acquisition.[138]

IR data were obtained with a Bruker™ Vector 22™ IR spectrometer. Samples were evaporated from benzene on CsI plates. Typically, spectra consisted of 200 scans with a resolution of 2.0 cm$^{-1}$.

### 3.3.2. *Raman Spectroscopy*

Raman spectroscopy is a scattering technique shown schematically in Figure 3.3.

$$\upsilon_i$$

Sample

$$\upsilon_i \pm \upsilon_m \quad \text{Raman scattering}$$

$$\upsilon_i \quad \text{Rayleigh scattering}$$
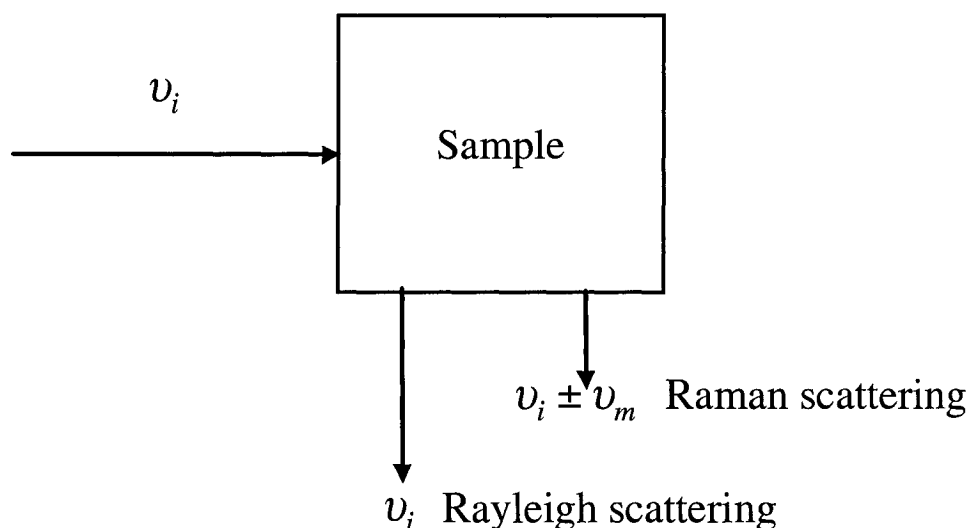
Figure 3.3. A schematic diagram of Raman scattering where incident radiation is scattered at $\upsilon_i$ and $(\upsilon_i \pm \upsilon_m)$. Adapted from reference 139.

High-energy laser light of frequency, $\upsilon_i$, enters the sample and is scattered. Some radiation is scattered elastically (at the same frequency, $\upsilon_i$) and other radiation is scattered inelastically (at frequencies $\upsilon_i \pm \upsilon_m$ ). The frequency $\upsilon_m$ is that of vibrational motion and is due to the interaction of light energy with the polarizability tensor of a molecule.[139]

An electromagnetic (EM) wave can be described as:

$$E = E_0 \cos 2\pi \upsilon_i t ,\qquad\qquad 3.10$$

where $E$ is the energy of the wave, $E_0$ is the wave amplitude, $\upsilon_i$ is the incident frequency, and $t$ is time. EM radiation can impose a dipole moment, $D$, on the molecule that can be expressed as:

$$D = \alpha_D E = \alpha_D E_0 \cos 2\pi \upsilon_i t,\qquad\qquad 3.11$$

where $\alpha_D$ is the polarizability of the static dipole. $\alpha_D$ can be thought of as the "flexibility" of the dipole to distortion by an EM field.[139,140] As a molecule vibrates, its atoms move and $\alpha$ can be expressed as a linear function of the atomic displacement:[139,140]

$$x = x_0 \cos 2\pi \upsilon_m t \qquad\qquad 3.12$$

where $x$ and $x_0$ represent the actual and initial atomic displacement, respectively, and

$$\alpha_D = \alpha_{D0} + \left(\frac{\partial \alpha_D}{\partial x}\right)_0 x_0 + \ldots \qquad . \qquad\qquad 3.13$$

where the subscript refers to the term in the expansion series. Combining Eq.s 3.11 to 3.13 gives new expressions for $D$:[139,140]

$$D = \alpha_D E_0 \cos 2\pi \upsilon_i t + \left(\frac{\partial \alpha_D}{\partial x}\right)_0 x_0 E_0 \cos 2\pi \upsilon_i t \cos 2\pi \upsilon_m t \qquad\qquad 3.14$$

and

$$D = \alpha_D E_0 \cos 2\pi \upsilon_i t + \frac{1}{2}\left(\frac{\partial \alpha_D}{\partial x}\right)_0 x_0 E_0 \left[\cos(2\pi t(\upsilon_i + \upsilon_m)) + \cos(2\pi t(\upsilon_i - \upsilon_m))\right] . \qquad 3.15$$

The first part of Eq. 3.16 is the same as Eq. 3.12 and represents the elastic scattering of energy at the incident frequency, $\upsilon_i$, known as Rayleigh scattering.[139,140] The second term in Eq. 3.16 is inelastic scattering at ($\upsilon_i$ - $\upsilon_m$) and ($\upsilon_i$ + $\upsilon_m$), called Stokes and anti-Stokes scattering, respectively.[139,140] A description of this process and its comparison with IR spectroscopy is shown in Figure 3.4.
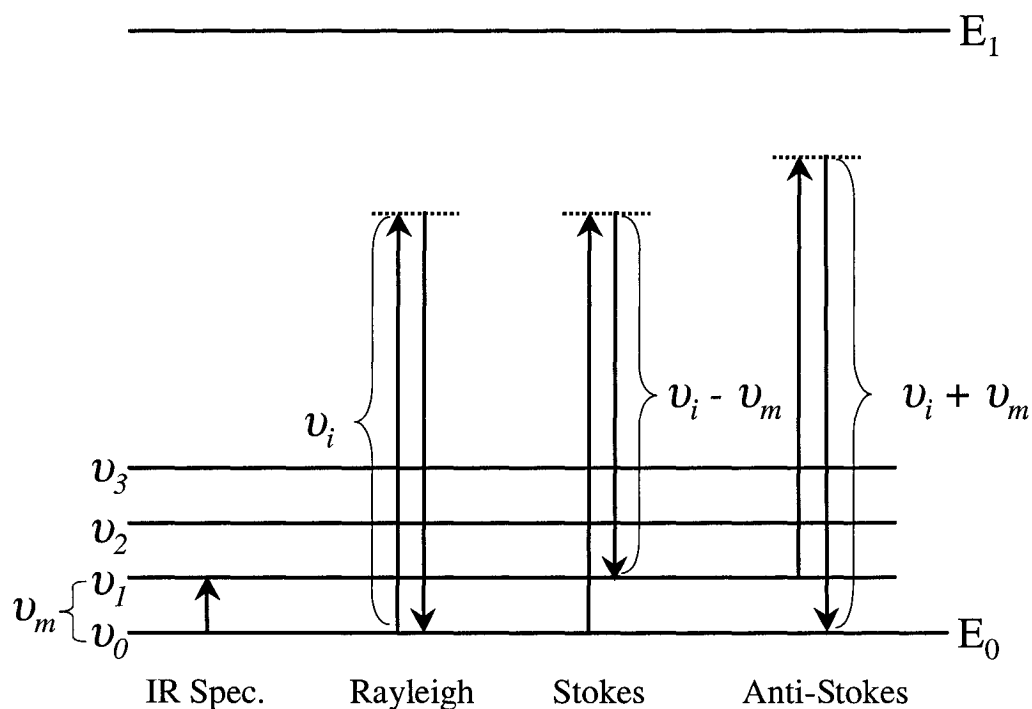
Figure 3.4. Comparison of the physics of elastic and inelastic Raman scattering with IR absorption. Adapted from references 139 and 140.

A molecule in an IR experiment absorbs incident radiation of $v_m$ corresponding to a $0{\rightarrow}1$ vibrational transition. In a Raman experiment, laser light of $v_i$, where $v_i$ is significantly beyond the vibrational transitions of the molecule, is incident on the molecule. Some light is scattered elastically at $v_i$ (Rayleigh) and other light is scattered at $(v_i \pm v_m)$.[139,140] Stokes scattering occurs when molecules in the ground state, $v_0$, absorb energy $v_i$ and then drop to the vibrationally excited state, $v_1$. Anti-Stokes reflection is a result of molecules in the $v_1$ vibrationally excited state absorbing energy of $v_i$ and relaxing back to their ground state, $v_0$. Since the number of molecules in the excited state (governed by the Boltzmann distribution) is not large at ambient temperature, anti-Stokes scattering is generally much weaker in intensity than Stokes scattering.[139,140]

A schematic Raman spectrometer is shown schematically in Figure 3.5. It consists of a laser light source, a sample holder, and a detection system. Since Raman scattering is measured in the UV region ($v_i - v_m$) and is quite weak, the photodiode detectors used are much more expensive than those used in IR spectroscopy. As in FT-IR, FT-Raman techniques allow for rapid sample acquisition. Since the measured light is perpendicular to the surface, a principal advantage of Raman over IR is that it can be used on solid and opaque samples.[139,140]
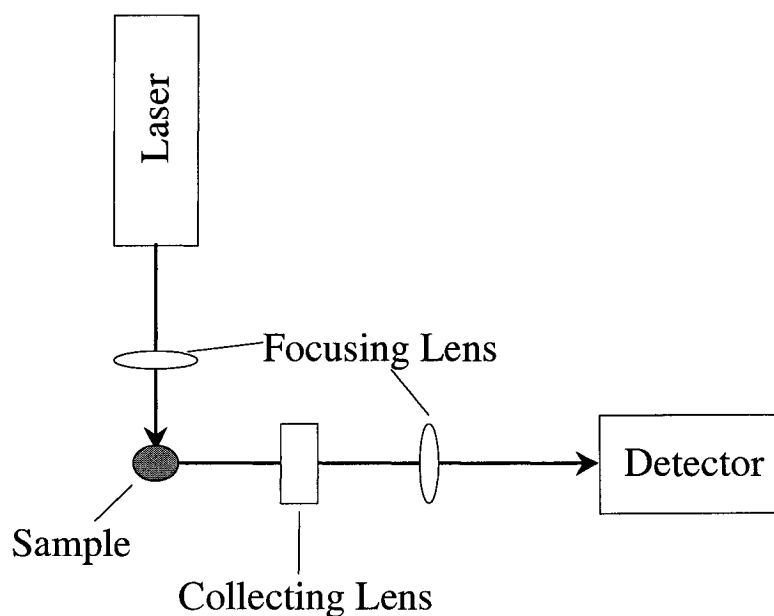


Figure 3.5. Schematic drawing of a Raman spectrometer. Laser light is focused into the sample and scattering is measured at 90° to the incident. Adapted from references 139 and 140.

Raman data were obtained with a Bruker™ RFS 100™ Raman spectrometer using the 1064.5 nm line of an Nd:YAG laser with an incident power of 447 mW. A Ge diode detector collected scattered light. For Raman measurements, sample material was

melted and depsoited in liquid form onto circular aluminium discs using a Pasteur pipette. Typical spectra consisted of 200 scans with a resolution of 2.0 cm$^{-1}$.

For time-dependent measurement experiments samples were melted onto circular aluminium discs, quenched in liquid nitrogen, placed into the Raman spectrometer, and allowed to equilibrate at 25 °C. For rapid measurement an average of 25 scans at 4.0 cm$^{-1}$ were obtained at approximately 30 s intervals. Acquisition intervals as low as 30 s were obtained at a spectral resolution of 4.0 cm$^{-1}$ resolution. For longer time acquisitions, spectra consisting of 200 scans at 2.0 cm$^{-1}$ resolution were obtained at intervals of 10 minutes.

### 3.4. Diffuse Reflectance Spectroscopy

Two types of reflection occur when light interacts with a surface, specular and diffuse. Specular reflection is associated with smooth surfaces and occurs at the same angle as light that was incident to the surface. Diffuse, or Lambertian, reflection occurs because real surfaces are not perfectly smooth and have small imperfections and facets that reflect light at all angles.[141-145] The intensity of diffuse reflected light is governed by Lambert's cosine law: [141,142]

$$I_d = s_d I_{in} \cos\theta, \qquad\qquad 3.16$$

where $I_d$ is the intensity of diffuse reflected light intensity, $I_{in}$ is the incident light intensity, $s_d$ is the diffuse reflection coefficient and $\theta$ is the angle from the normal of the surface. The intensity of diffuse reflected light is zero at $\theta = 0°$ and reaches a maximum of $s_d I_{in}$ at $\theta = 90°$.[141-145]

Specular reflection results in a reflection of light from the surface with little

interaction with the surface material (frequency of reflected light, $\upsilon_R \cong$ frequency of

incident light, $\upsilon_i$) at all wavelengths. In diffuse reflection, incident light photons are

absorbed by molecules in the surface material. If diffuse reflectance is measured at an

angle where specular reflectance is negligible, a spectrum similar to that of a transmission

spectrum (*e.g.* IR or UV-VIS) can be obtained. This technique is useful for obtaining the

spectra of solid, opaque materials such as and polymers,[143] pigments,[144] and minerals.[145]

### 3.4.1. Diffuse Reflectance Theory

Correlation of diffuse reflectance and transmission spectroscopy is obtained

through Kubelka-Munk theory, which describes diffuse reflection from an infinitely thick

layer of material, $R_\infty$:

$$R_\infty = \frac{\left(1 - \left(\frac{\varepsilon}{\varepsilon + 2\alpha_A}\right)^{\frac{1}{2}}\right)}{\left(1 + \left(\frac{\varepsilon}{\varepsilon + 2\alpha_A}\right)^{\frac{1}{2}}\right)}, \qquad 3.17$$

where $R$ is the diffuse reflectance, $\varepsilon$ is the absorption coefficient, and $\alpha_A$ is the scattering

coefficient.[141,142] Eq. 3.18 is rearranged to give the Kubelka-Munk function $F(R_\infty)$:[141,142]

$$F(R_\infty) = \frac{\left(1 - R_\infty{}^2\right)}{\left(2R_\infty\right)} \cong \frac{\varepsilon}{\alpha_A}. \qquad 3.18$$

In practice, absolute diffuse reflectance is rarely measured. Usually the

measurement, $r_\infty$, is made relative to a highly reflecting white standard with $R_{\infty,STD} = 1.00$

such that:[142]

$$\frac{R_\infty}{R_{\infty,STD}} = r_\infty .$$
<div align="right">3.19</div>

In this case, Eq. 3.19 can be rewritten as:[142]

$$F(r_\infty) = \frac{\left(1 - r_\infty^{\ 2}\right)}{\left(2r_\infty\right)} \cong \frac{\varepsilon}{\alpha_A} .$$
<div align="right">3.20</div>

A plot of log $F(r_\infty)$ versus wavelength produces a spectrum with the same form of that observed in transmission spectroscopy:[142]

$$\log F(r_\infty) = \log \varepsilon - \log \alpha_A$$
<div align="right">3.21</div>

with an offset in the intensity axis due to the scattering coefficient.

### 3.4.2. Apparatus

An Ocean Optics™ PC2000™ spectrometer with a hand-held reflectance probe is shown schematically in Figure 3.6.
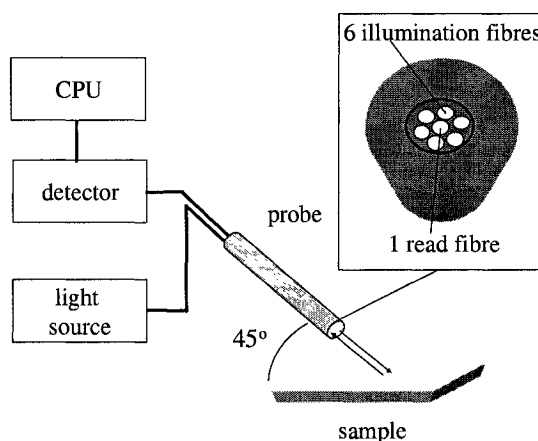


Figure 3.6. Schematic diagram of an Ocean Optics™ PC2000™ spectrometer with a hand-held reflectance probe. A tungsten halogen light source sends light to the probe through six 200 μm fibre optic cables. Reflectance is measured at 45° to the surface normal with a seventh 200 μm fibre optic cable. This is processed by a detector.

Light is sent to the probe through six 200 µm fibre-optic cables. A seventh 200

µm fibre-optic cable collects light reflected from the surface and sends it to a detector

where the signal is processed. The probe is held at an angle of 45° to the normal of the

sample surface. (45° is commonly used these measurements because it collects a

significant portion of diffuse reflected light, 0.707 $I_{in}$ by Eq. 3.17, and is free from the

effects of specular refection.) The instrument must be calibrated in "dark mode" (with the

light source off) where 0 % diffuse reflectance is detected and in "bright mode" where

100 % diffuse reflectance is detected such that $R_\infty = 1.00$. $R_\infty = 1.00$ from 200 to 800 nm

is obtained using a sintered polytetrafluoroethylene (Spectralon®) reference.[146] $R_\infty$ for the

Ocean Optics apparatus is given by:

$$\%R_\infty = \frac{R_{\infty,sample} - R_{\infty,dark}}{R_{\infty,reference} - R_{\infty,dark}} .$$
3.22

One of the most important features of reflectance spectrophotometry is to keep the

surface of the sample as consistent as possible—as the surface scattering of the light will

influence the intensity of the reflected light. This does not generally influence the

spectrum itself (*i.e.* the maximum wavelengths and the shape of the spectrum will be the

same, but the intensities will vary making it difficult to obtain quantitative results. A

preliminary study showed that using glass over the sample (microscope slide covers)

gave the best results compared with tape and raw samples.

The reflectance measurments were obtained at a single angle (45°) without the use

of an integrating sphere. While the measurements are reliable for relative comparison

within the thermochromic systems examined, the transmission intensity data cannot be

directly correlated to the concentration of CVL in its open form.

Measurements of ternary mixtures in the melt were performed on an electric hotplate and cooling was achieved by placing the glass slide in contact with an aluminum block cooled with liquid nitrogen.

## 3.5. Nuclear Magnetic Resonance Spectroscopy

Nuclear magnetic resonance (NMR) spectroscopy is a technique based on the behaviour of nuclei in a magnetic field. Some nuclei, such as $^1H$ and $^{13}C$, have nuclear magnetic moments that are sensitive to their electronic surroundings. In the presence of a magnetic field these nuclei split into high and low energy states ($\Delta E$) determined by the nuclear magnetic moment, $\mu$, and the chemical environment of the nucleus.[138,147,148]

### 3.5.1. Magnetic Resonance

In a magnetic field NMR active nuclei have orientations defined by the spin quantum number, $I$:[147,148]

$$I = 0, 1/2, 1, 3/2, 2, \dots \qquad 3.23$$

These orientations can be defined by, $I$, the spin angular momentum vector. Orientations of the nucleus are considered as projections along an axis, conventionally defined as $z$, such that $I_z$, the $z$ component of $I$, is quantized according to:[147,148]

$$I_z = m\hbar, \; m=I, I\text{-}1, I\text{-}2, \dots \text{-}I\text{+}1, \text{-}I, \qquad 3.24$$

where $m$, the magnetic quantum number, has $(2I + 1)$ values. The simplest example is for $I = 1/2$ (*e.g.* for $^1H$ and $^{13}C$) where only two orientations of spin angular momentum, $I_z = \pm 1/2\hbar$, are allowed.[138,147,148]

The magnetic moment of a nucleus, $\mu$, is a vector quantity related to $I$ by:[138,147,148]

$$\mu = \gamma I ,$$ 3.25

where $\gamma$ is the gyromagnetic ratio of the nucleus. As is the case with $I$, only the z-component of $\mu$ is considered:[138,147,148]

$$\mu_z = \gamma I_z .$$ 3.26

The direction of the $z$ projection of $I$ and $\mu$ vectors is arbitrary and the energies of nuclear orientations are degenerate except in the presence of a magnetic field, $B$. In the presence of $B$, the $z$ components of $I$ and $\mu$ are aligned parallel to the direction of the field.[138,147,148] The energy of a magnetic moment in a magnetic field is expressed as:

$$E = -\mu_z B.$$ 3.27

Combining Eqs. 3.26, 3.25, and 3.24 gives:[138,147,148]

$$E = -m\hbar\gamma B,$$ 3.28

which shows that the system is split into $(2I + 1)$ energy levels separated by $\hbar\gamma B$. Selection rules for NMR spectroscopy state that allowed transitions correspond to $\Delta m = \pm 1$, and therefore the resonance condition can be defined as:[138,147,148]

$$\Delta E = h\upsilon = \hbar\gamma B$$ 3.29

and

$$\upsilon = \gamma B / 2\pi ,$$ 3.30

where $\upsilon$ is the resonance frequency of the nucleus. This frequency will be absorbed by a nucleus if a magnetic field is applied.

### 3.5.2. Chemical Shift

When a molecule is placed in a magnetic field, electrons surrounding the nuclei impart their own magnetic fields. The magnetic field felt by the nucleus, $B$, might be

significantly different from the applied field, $B_0$. The shielding constant, $\sigma'$, is a tensor property that relates $B_0$ to $B$: [147,148]

$$B = B_0(1- \sigma').$$  3.31

The change in apparent field causes a change in the nuclear magnetic resonance frequency, $v$, and Eq. 3.25 becomes:[147,148]

$$v = \frac{\gamma B(1-\sigma')}{2\pi}.$$  3.32

Since shifts in resonance frequency are small compared to the resonance frequencies, the chemical shift, $\delta$, is defined by comparing the resonance frequency of the sample, $v$, with that of a reference molecule, $v_{ref}$:[138,147,148]

$$\delta = 10^6 \frac{(v - v_{ref})}{v_{ref}}.$$  3.33

$\delta$ is expressed in parts per million (ppm) and is measure of the de-shielding of a nucleus by its electronic environment.[138,147,148]

### 3.5.3. Apparatus

A simple diagram of an NMR instrument is shown in Figure 3.7.
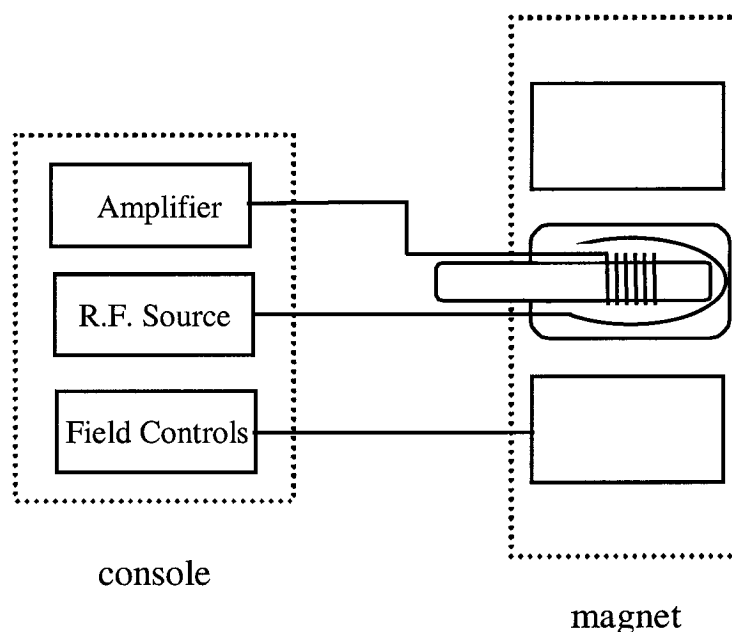
Figure 3.7. Diagram of an NMR spectrometer showing the console and magnet. A sample is placed within the magnet and subjected to RF pulses near the NMR frequency of the desired nuclei. The resulting signal is amplified, Fourier transformed, and processed. Adapted from references 147 and 148.

The apparatus consists of a console and a magnet. The sample is packed in a probe inserted within a super-conducting magnet. The sample is spun by a motor and is surrounded by a coil supplying a radiofrequency (RF) pulse with a range of frequencies near the NMR frequency, exciting all nuclei simultaneously. The resulting NMR resonance is detected by the signal coils, amplified, and Fourier transformed into a spectrum.[138,147,148]

Solid-state NMR spectra for this thesis were obtained on a Bruker AMX-400 spectrometer. For $^{13}$C NMR, $^{1}$H/$^{13}$C cross-polarization/magic-angle-spinning (CP/MAS) was used. The spinning rate was typically 7 to 9 kHz. A relaxation delay of 5 s, 5 ms contact time and over 1000 scan numbers were adopted.

# Chapter 4. Dye-Developer Interactions

## 4.1. Crystal Violet Lactone - CVL

3,3-bis(*p*-N,N-dimethylaminophenyl)-6-N,N-dimethylaminophthalide, also called crystal violet lactone (CVL) (Figure 1.6), is one of the most commonly used dyes in thermal printing and carbonless copy paper.[48] Figure 4.1 shows the crystal structure of CVL at 298 K. It is monoclinic, $P2_1/n$, with 4 molecules per unit cell.[126]
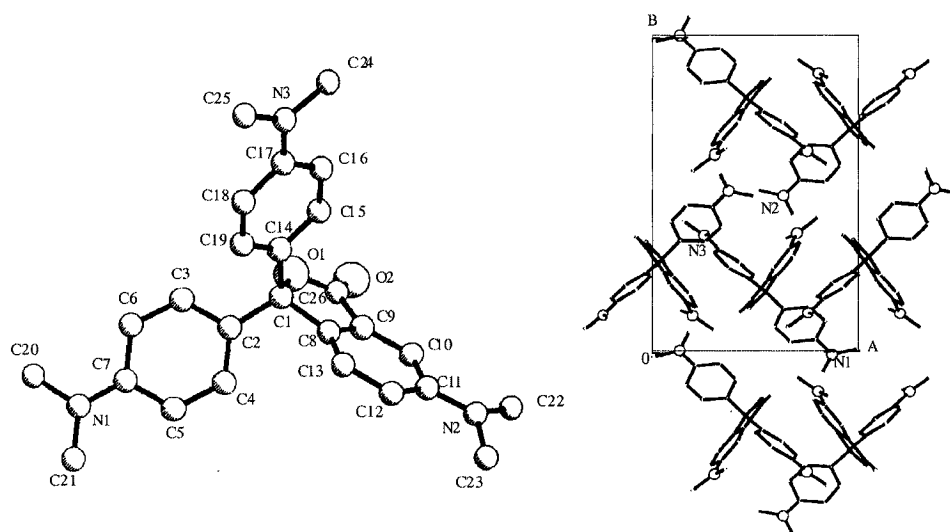


Figure 4.1. The crystal structure of crystal violet lactone (CVL) is monoclinic, $P2_1/n$, with 4 molecules per unit cell. Adapted from reference 126. The molecular structure of CVL is shown in Figure 1.6.

The lactone ring is coplanar with its attached phenyl ring to within 3°. Ring conjugation is limited because the lactone moiety lies nearly perpendicular to the dimethylaminophenyl rings with dihedral angles of 119.1° ($C_2$-$C_7$) and 92.6° to ($C_{14}$-$C_{19}$).[126] The dimethylaminophenyl rings take on a tilted "propeller" configuration where they tilt away from each other slightly due to the steric interactions of protons attached to carbons *ortho* the central carbon ($C_3$, $C_4$, $C_{15}$ and $C_{19}$).[126,149,150] The dihedral angle between ($C_2$-$C_7$) and ($C_{14}$-$C_{19}$) is 69.0°.[126] Lone electron pairs on the nitrogen atoms of the *N,N*-dimethylamino groups interact with the conjugated ring system in the lactone state; $C_7$-$N_1$ (1.382 Å) is shorter than $C_{20}$-$N_1$ (1.444 Å) and $C_{21}$-$N_1$ (1.436 Å).[101,126]

The IR spectrum of crystal violet lactone is shown in Figure 4.2 and is characterized by a prominent lactone carbonyl absorption, $\upsilon$(C=O) = 1755 cm$^{-1}$.[101,102] Carbonyl vibrations are of interest in vibrational spectroscopy because the frequencies are highly sensitive to changes in bonding and conjugation and are useful diagnostic tools in the assessment of structural changes in the system.[138-140]
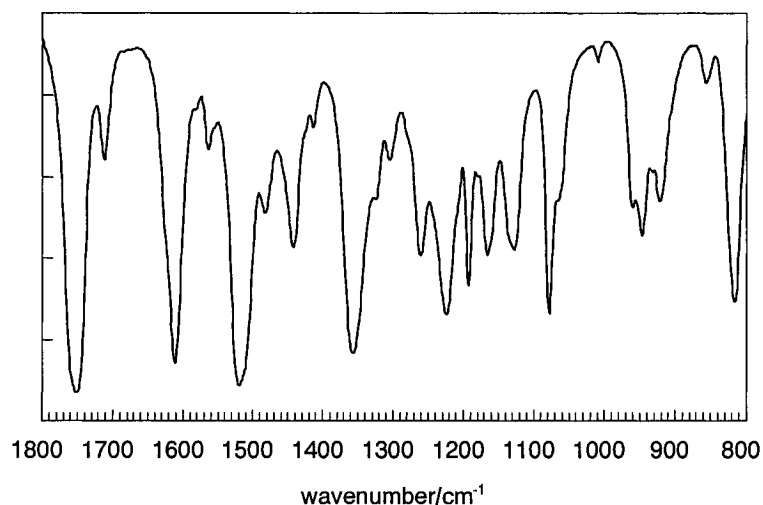


Figure 4.2. The IR spectrum of pure crystal violet lactone (CVL), obtained using techniques outlined in Section 3.3.1, is characterized by strong carbonyl absorption at 1755 cm$^{-1}$.

Figure 4.3 shows the colour-forming reaction where the CVL lactone ring undergoes ring-opening in the presence of an electron pair acceptor. The open structure is characterized by a three-coordinate spiro carbocation that allows the phenyl groups of the molecule to achieve a more planar configuration and extend its conjugation length. The coloured form of CVL is stabilized by quinoid resonance structures through the donation of free electrons from the N,N-dimethylamino groups.[7,65,66,151,152]
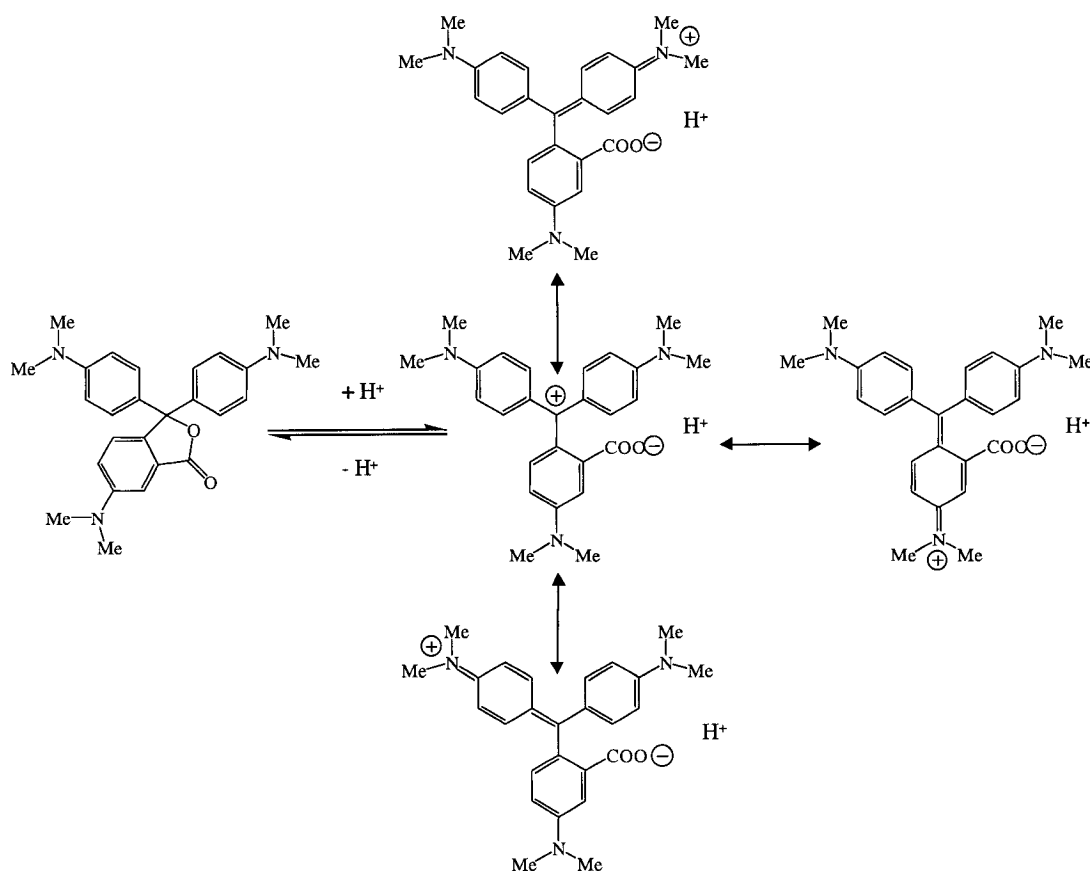


Figure 4.3. Crystal violet lactone (CVL) and its ring-opened resonance forms. The open form can display zwitterionic or quinoid stabilized resonance forms. The type of stabilization depends on the strength of the molecular interaction causing the ring-opening reaction.

The absorption maximum of CVL shifts from 280 nm in its leuco form to a broad absorption maximum of 620 nm with a shoulder at 570 nm when the ring is open.[70,122]

Figure 4.4 shows the UV-VIS absorption spectrum of CVL in acetonitrile acidified with acetic acid.
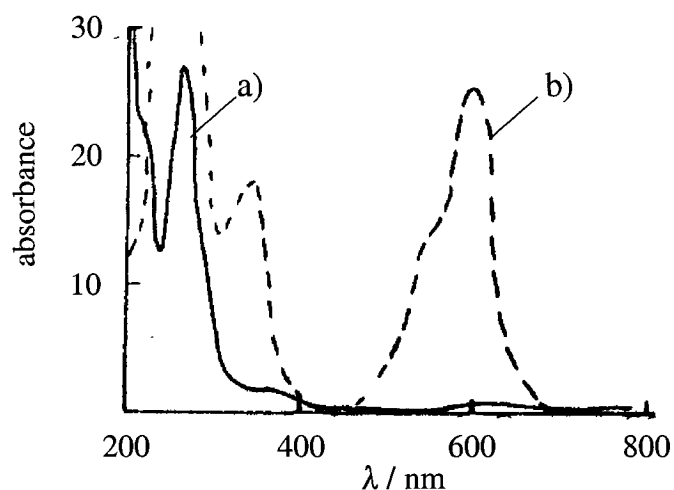


Figure 4.4. (a) The UV-VIS spectrum of crystal violet lactone in acetonitrile shows a single major band at 280 nm. (b) crystal violet lactone acidified with acetic acid shows a major band at 620 nm with a minor band at 570 nm. Adapted from reference 122.

The major band (620 nm) is due to the excitation of π-bonding electrons in the HOMO to the π*–antibonding LUMO. The minor absorption shoulder at 570 nm is due to π-electrons excited from the next lowest occupied molecular orbital, spread about what was the original phthalein moiety, to the LUMO.[70,122] The band at 380 nm in the coloured form is attributed to a CVL radical species.[122]

The colour displayed by CVL (along with most TPM dyes) is very intense. The molar extinction coefficient, $\varepsilon$, of ring-opened cationic crystal violet (CV, Figure 4.5), the parent form of CVL, is $1.09 \times 10^5 \text{ mol}^{-1} \text{ cm}^{-1}$ at 586 nm in acetonitrile acidified with acetic acid.[122]
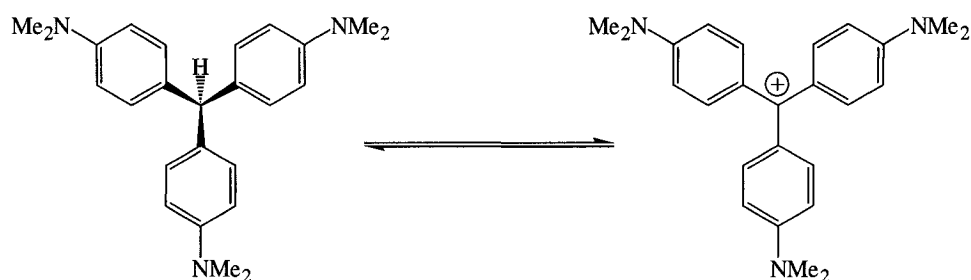
Figure 4.5. Crystal violet (CV) is the parent dye of crystal violet lactone. In its protonated state it is characterized by an $sp^3$ spiro carbon centre. Protonation of the dye results in a more planar cationic CV characterized by $D_3$ symmetry. Adapted from reference 122.

Examination of the molar extinction coefficient of CVL in acidified acetonitrile solutions showed a maximum $\varepsilon$ of 2.8 x $10^4$ mol$^{-1}$ cm$^{-1}$ in a solution of 90% acetic acid.[122] This result is important because, even in highly acidic media, ~75% of the CVL is in its leuco form.[122] The pH is important in establishing the ring-opening reaction, but there is an optimum range in which it can occur effectively. Above an acid concentration of 90% acetic acid, $\varepsilon$ dropped significantly to ~ 1.4 x $10^4$ mol$^{-1}$ cm$^{-1}$ at 95% acetic acid and ~ 8 x $10^3$ mol$^{-1}$ cm$^{-1}$ in 99% acetic acid.[122] The same phenomenon was observed by Lingjie *et al.* in the examination of a colourless solution of CVL in *d*-DMSO.[153] Through continual addition of HCl, colour first appeared and then disappeared as the pH was lowered. Colour loss was due to the protonation of the *N,N*-dimethylamino groups and the formation of an HCl salt at very low pH.[122,153]

Much of the literature on CVL and other TPM systems presents the behaviour of molecules in solution. Equilibrium between the colourless form and the coloured form has been examined for various fluoran and spirolactone dyes.[65-67,69,122,151,152] Protic solvents with moderate to high dielectric constants are most effective at promoting the charge-separated zwitterionic form.[65,66] Hydrogen bonding plays an important role in the stabilization of the negatively charged carboxylate moiety on the open lactone.[65,66,151]

Literature examining the solid-state properties of TPM dyes and their colour-forming interactions is somewhat limited. Rihs and Weis examined the crystal structures of CVL complexed with metal halides (Figure 4.6).[101,102] Metal halides are strongly polarizing and open the lactone ring to form a CVL complex with the resulting carboxylate oxygens. In [2CVL•3CdI₃•acetone], CdI₃ forms a polymeric matrix to which open CVL is complexed as a substituent. [2CVL•3ZnI₂•acetone] forms a molecular complex consisting of two open CVL molecules joined by a zinc iodate bridge.[101]



(a)                                                  (b)
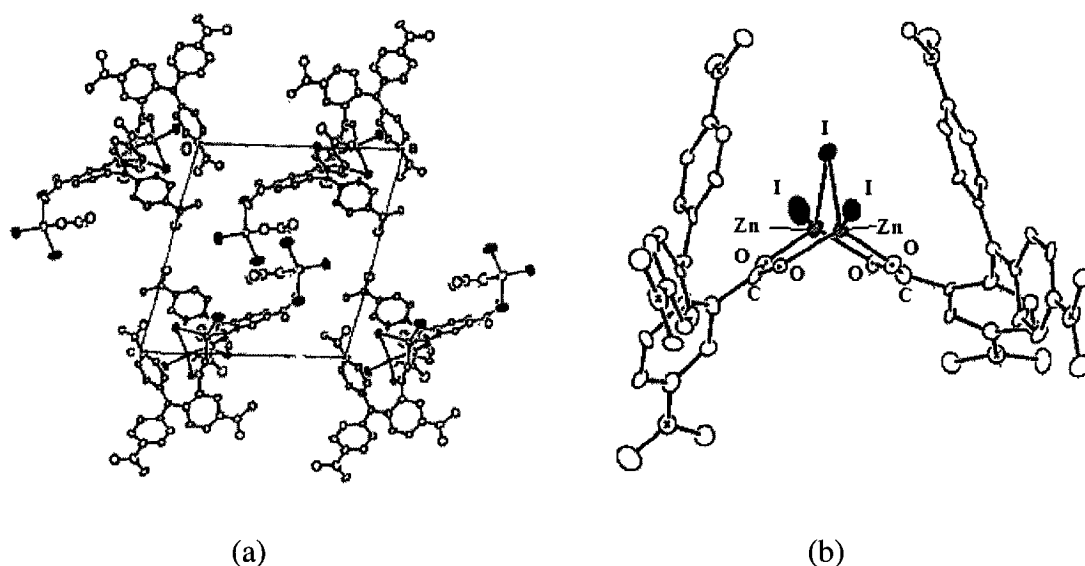
Figure 4.6. Structures of metal halide-crystal violet lactone complexes. (a) [2CVL•3CdI₃•acetone] is characterized by polymeric matrix formed by CdI₃ to which open crystal violet lactone is complexed as a substituent. (b) [2CVL•3ZnI₂•acetone] forms a molecular complex consisting of two open crystal violet lactone molecules joined by a zinc iodate bridge. Adapted from reference 101.

Although the structures of the complexes are quite different, the structure of CVL within them is almost identical. The CVL lactone carbonyl absorption at 1755 cm⁻¹ disappears in the IR spectra of both complexes and is replaced by a band at 1579 cm⁻¹ corresponding to an asymmetric carboxylate (C-O)⁻ vibration.[101] The remainder of the IR spectrum is identical to that of the CV cation.[154,155] Resonance stabilization of the three-

coordinate spiro carbocation centre from the dimethylamino groups occurs in both complexes; the $C_\phi$-N bonds of the dimethylaminophenyl moiety are slightly smaller (1.28 to 1.39 Å) than the average $C_\phi$-N bond length (1.47 Å). It is also of interest to note that the open form of CVL is not perfectly planar, but maintains a propeller configuration similar to that observed in open CV (Figure 4.5) with dihedral angles of 24° to 33° for the dimethylaminophenyl rings and 51° for the carboxyaminophenyl ring.[101] These structures show not only a large decrease in the dihedral angle of the lactoid moiety but also a significant decrease in the dihedral angles of the dimethylaminophenyl rings from 69° (Figure 4.1) to ~30°. Both factors contribute to an increase in conjugation and resonance stabilization in the molecule.

NMR can be used to probe the electronic environment of CVL in its coloured state and provide information on the stability of the coloured molecule. Table 4.1 compares $^{13}C\{^1H\}$NMR data from the examination of (1) leuco CVL in $CDCl_3$, (2) ring-opened CVL, in acidified $CDCl_3$,[153] and (3) the solid crystalline complex [2CVL•3ZnI$_2$•acetone] in $CD_2Cl_2$[101]

Table 4.1. $^{13}C\{^1H\}$NMR data for various forms of crystal violet lactone

| C # | CVL – Leuco Form (1) (CDCl₃) /ppm [153] | CVL – Open Form (2) (acetic acid) /ppm [153] | CVL – Open Form (3) [2CVL•3ZnI₂•acetone] (CD₂Cl₂/ppm [101] |
|---|---|---|---|
| 1 | 149.9 | 148.4 | 156.7 |
| 2 | 111.6 | 117.4 | 113.5 |
| 3 | 128.0 | 128.5 | 140.5 |
| 4 | 129.3 | 135.4 | 128.5 |
| 5 | 92.2 | 95.8 | 179.3 |
| 6 | 141.1 | 140.4 | 127.3 |
| 7 | 124.0 | 125.8 | 138.6 |
| 8 | 118.6 | 120.3 | 112.4 |
| 9 | 150.8 | 152.4 | 153.8 |
| 10 | 106.6 | 108.4 | 115.0 |
| 11 | 125.5 | 127.6 | 143.8 |
| 12 | 171.1 | 172.1 | 175.1 |
| 13a | 40.5 | 40.8 | 41.05 |
| 13b | 40.3 | 43.4 | 40.8 |
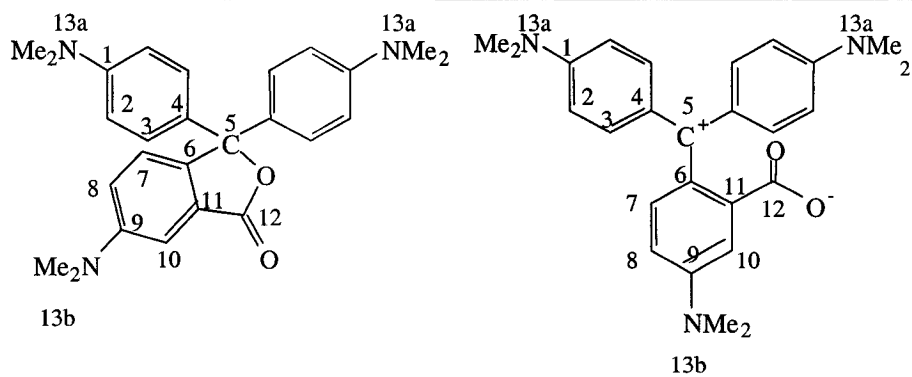


Closed leuco form (1)          Open coloured form (2) & (3)

The most prominent features of the NMR spectra of the two coloured systems are the $\Delta\delta$ of the spiro carbon centre ($C_5$) relative to the closed leuco form (1); $\Delta\delta_{C5}$ for the ring-opened form (2) relative to (1) is +3.6 ppm and $\Delta\delta_{C5}$ for the complex (3) relative to (1) is +87 ppm. Complex (3) displays significant $sp^2$ character with $\delta_{C5} = 179.3$ ppm.[101]

In (2), positive charge is delocalized throughout the system's quinoid resonance structures (cf. Figure 4.3) relative to the lactoid form of CVL. This is shown by an average $\Delta\delta_{(2)-(1)}$ of +5 to 6 ppm for carbons $C_1$-$C_4$ of the dimethylaminophenyl rings and +3 ppm for of the methyl groups in the $N,N$-dimethylamino substituent ($C_{13a}$). The remaining ring system, $C_6$-$C_{11}$, shows less significant NMR changes between the open and closed forms.[153]

Ring-opened CVL complex (3) shows significantly lowered contribution of quinoid resonance compared to (2). While there is some increase in the shift of the carbons $C_1$-$C_4$, $\Delta\delta_{(3)-(1)}$ is much smaller relative to the $\Delta\delta_{(3)-(1)}$ of $C_5$. There is little change in peaks $C_{13a}$ and $C_{13b}$ for the dimethylamino groups. The lack of quinoid resonance contribution in (3) is confirmed by the N-C bond lengths of the solid coloured structure; the average N-C distances of complex (3) (1.42-1.45 Å)[153] are comparable to those seen in the crystal structure of pure leuco CVL (1.38-1.45 Å).[126]

Complexes (2) and (3) demonstrate the two types of stabilization possible for open CVL. (2) shows significant changes in the C-N bonds of the $N,N$-dimethylamino substituents, but only small changes in the electronic density of carbons in the open-lactone moiety. (3) is stabilized through bonding with the carboxylate moiety and shows little change in the C-N bonds.

These results are consistent with the examination of solid CVL in a binary rewritable thermochromic system by Ibata *et al.*[156] CVL was complexed with a weak acid developer, 2,2-bis(hydroxyphenyl)propane or bisphenol A (BPA), and the IR carbonyl absorption of the lactone ring as a function of BPA was examined. At a CVL mole fraction, $x_{CVL}$, of 0.65, or approximately 2CVL:BPA, a decrease in the lactone carbonyl absorption at 1755 cm$^{-1}$ and an increase in absorption at 1730 cm$^{-1}$ was observed. At $x_{CVL}$ = 0.50 the peak at 1730 cm$^{-1}$ decreased and a peak at 1584 cm$^{-1}$ appeared. At $x_{CVL}$ = 0.166 the only major carbonyl absorption present was that at 1584 cm$^{-1}$, corresponding to the asymmetric carboxylate stretch of the open lactone. This study shows that at least three possible structures of CVL can be observed: (1) the lactoid CVL with a lactone $\upsilon$(C=O) of 1755 cm$^{-1}$, (2) an open form of CVL with the lactone moiety opened and characterized by an acidic carboxyl (-COOH) moiety with $\upsilon$(C=O) = 1730 cm$^{-1}$, and (3) an open form of CVL with a charged carboxylate (-COO$^-$) moiety with $\upsilon$(C=O) = 1584 cm$^{-1}$.[156]

The change in $\upsilon$(C=O) as a function of developer concentration was attributed to increasing electron-pair-accepting strength for the developer as more developer molecules become available to complex with CVL.[155] At low BPA concentrations the phenolic developer protons are able to support a weak CVL:BPA complex characterized by a conversion of the lactone carbonyl to -COOH. As more phenolic groups become available, the strength of the interaction increases and the developer molecules support CVL with a charged carboxylate structure comparable to that observed in the CVL-metal halide complexes.[156]

### 4.2. Alkyl Gallates

Alkyl gallates were chosen for study here because of their prevalence in the patent literature, relatively low pK$_a$ values, plurality of phenolic protons, and their availability in various alkyl-chain lengths.[157-159] The general structure of an alkyl gallate is shown in Figure 4.7.
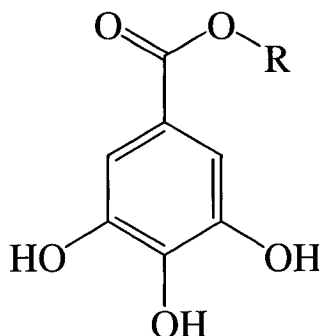


Figure 4.7. Structure of a gallic acid ester. An alkyl gallate is a benzoic acid ester with phenolic hydroxy groups in the 3,4, and 5 positions of the phenyl ring.

Dodecyl(3,4,5-trihydroxy)benzoate, also known as either dodecyl gallate, or lauryl gallate (LG), was the most extensively examined developer here. Other developers examined include propyl(3,4,5-trihydroxy)benzoate, also known as propyl gallate (PG) and octyl(3,4,5-trihydroxy)benzoate, also known as octyl gallate (OG).

The pK$_a$ for the first dissociation of PG (hydroxy group in the 4-position) is 7.22.[160] Calculated literature pK$_a$ values for OG and LG are 7.82 ± 0.20, and 7.81 ± 0.20 respectively.[161] The low pK$_a$ relative to other phenols is due to the *para* electron-accepting ester substituent.[157,158] Searches of the Cambridge Crystallographic Database did not provide crystal structural data for pure PG, OG, or LG and subsequent attempts at crystallization using techniques described in the patent litereature[162] proved unsuccessful here. However, crystal structures of propyl gallate monohydrate and octyl gallate

dihydrate are reported in the literature and are shown in Figure 4.8 and Figure 4.9, respectively.[128,163]
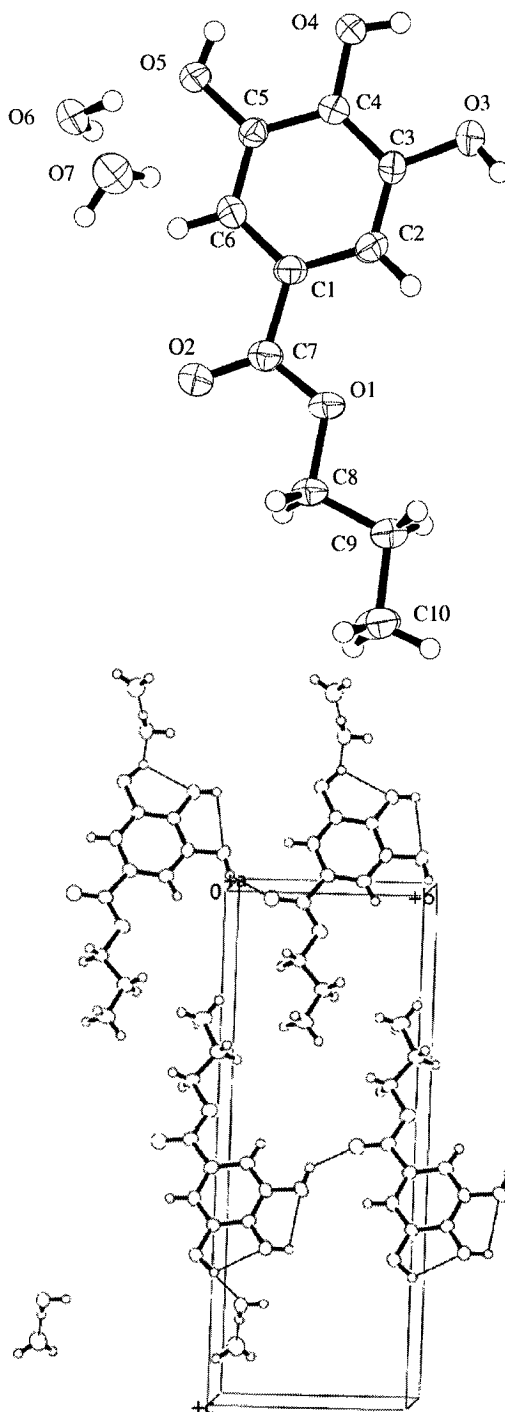


Figure 4.8. The crystal structure of propyl gallate monohydrate is monoclinic, $P2_1/c$, Z = 4, with $a$ = 7.872 Å, $b$ = 7.560 Å, $c$ = 19.836 Å and with $\beta_l$ = 101.03°.[163]
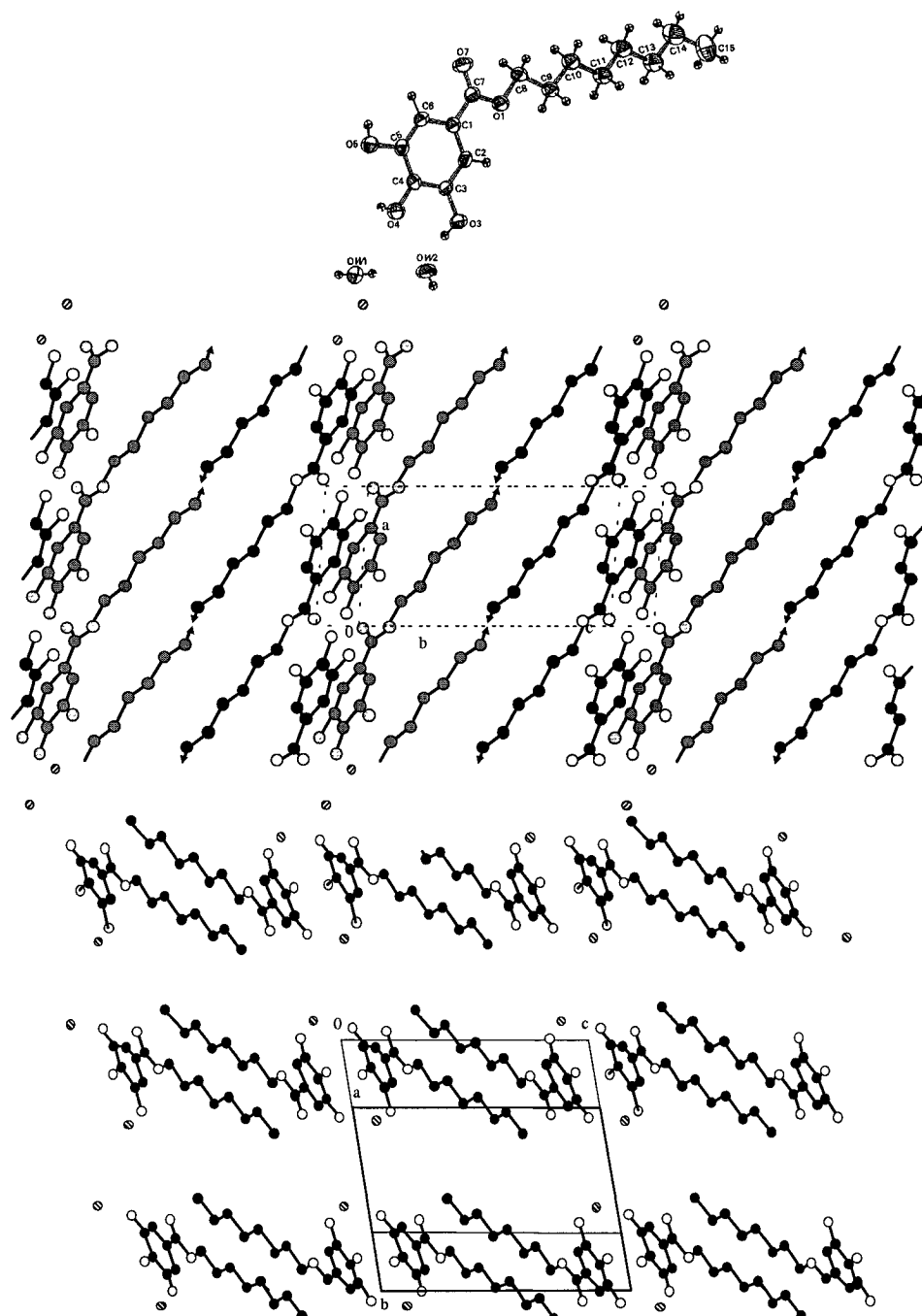
Figure 4.9. The crystal structure of octyl gallate dihydrate is triclinic, $P1$, $Z = 2$, with $a = 6.617$ Å, $b = 9.956$ Å, $c = 14.088$ Å and with $\alpha_l = 79.08°$, $\beta_l = 85.58°$, and $\gamma_l = 70.80°$. Adapted from reference 128.

PG monohydrate is monoclinic, $P2_1/c$, Z = 4, with $a$ = 7.872 Å, $b$ = 7.560 Å, $c$ =

19.836 Å and with $\beta_l$ = 101.03° [163] ($\beta_l$ is the ac angle and Z is the number of molecules

per unit cell). The molecule is planar to within 2° with the alkyl group extended in a *trans*

zig-zag pattern. Terminal methyl groups interact with each other and no phenyl stacking

was observed. Hydroxy groups are oriented in the same direction with hydrogen bonding

occurring between the 3,4 and 4,5 positions.[163]

OG dihydrate is triclinic, $P1$, Z = 2, with $a$ = 6.617 Å, $b$ = 9.956 Å, $c$ = 14.088 Å;

with $\alpha_l$ = 79.08°, $\beta_l$ = 85.58°, and $\gamma_l$ = 70.80°[128] ($\alpha_l$ is the bc angle and $\gamma_l$ is the ab angle).

The phenyl group is planar to within 3° of the alkyl-chain with the alkyl-chains oriented

in a *trans* zig-zag pattern. The alkyl-chains form an interdigitizing structure and support

the formation of a head-to-head bilayer structure with significant phenyl stacking.[128]

Hydrogen bonding between the 3,4 and 4,5 hydroxy groups is similar to that observed in

PG monohydrate.[128,163]

While there are structural differences between PG and OG, enough similarity

exists to postulate the structure of LG: (1) both systems are planar with extended alkyl

groups, (2) both systems are oriented with the alkyl groups interacting, and (3) both

systems show similar hydrogen bonding in the 3,4 and 4,5 hydroxy positions.[128,163]

LG, with a 12 carbon alkyl-chain, probably possesses a structure similar to OG. It

is assumed to have alkyl groups planar with respect to the phenyl ring and have a head-

to-head bilayer structure in which the chains interdigitate. Figure 4.10 compares the

Raman spectra of PG, OG, and LG in the < 2000 cm$^{-1}$ region. Spectral features of PG

differ slightly from those of OG while those of OG and LG are nearly identical, a good

indication that the two molecules share a similar structure.
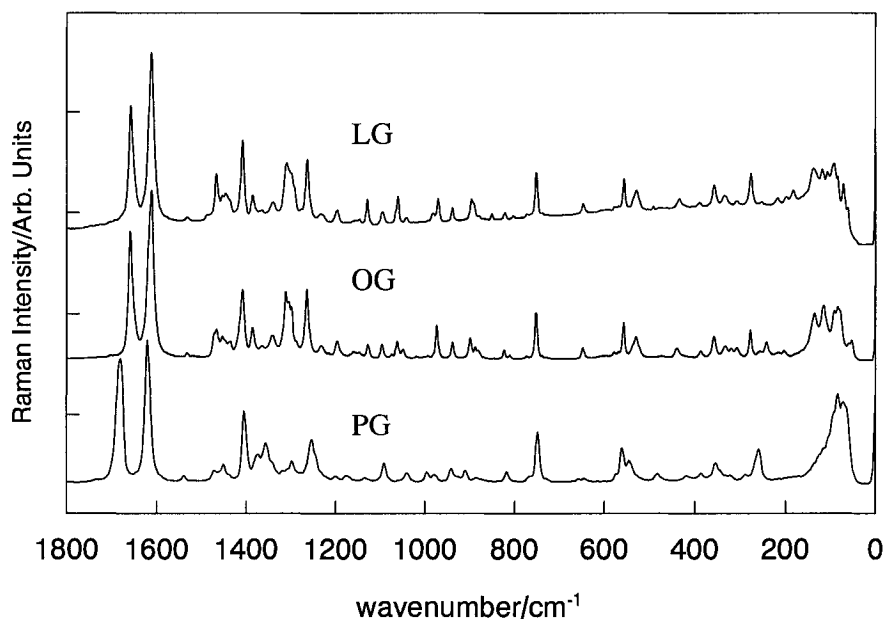
Figure 4.10. Raman spectra of propyl gallate (PG), octyl gallate (OG), and lauryl gallate (LG), obtained here. Spectral features differ slightly between propyl gallate and octyl gallate consistent with the differences in crystal structure. Spectral features of octyl gallate and lauryl gallate are nearly identical throughout the entire region shown indicating that they are structurally similar.

## 4.3. Lauryl Gallate/Crystal Violet Lactone Binary Mixtures

Much of the present work on the heat treatment and spectroscopy of lauryl gallate/crystal violet lactone (LG/CVL) mixtures has recently been published.[164] In the melt, LG/CVL binary systems are thick liquids where the viscosity increases with increasing $x_{CVL}$. Liquid mixtures are deep blue, and this colour is maintained upon solidification.

### *4.3.1. Annealing of Lauryl Gallate/Crystal Violet Lactone Mixtures*

When cooled from the melt, all the LG/CVL mixtures examined form coloured glasses. Crystallization within the mixture is observed in some samples after aging at room temperature for periods ranging from one hour to several days. Microscopy of the glass shows it to be opaque and featureless, but annealing at 65 to 75 °C produced crystalline material morphologically consistent with pure LG. Colour images of glassy and annealed samples are shown in Figure 4.11.
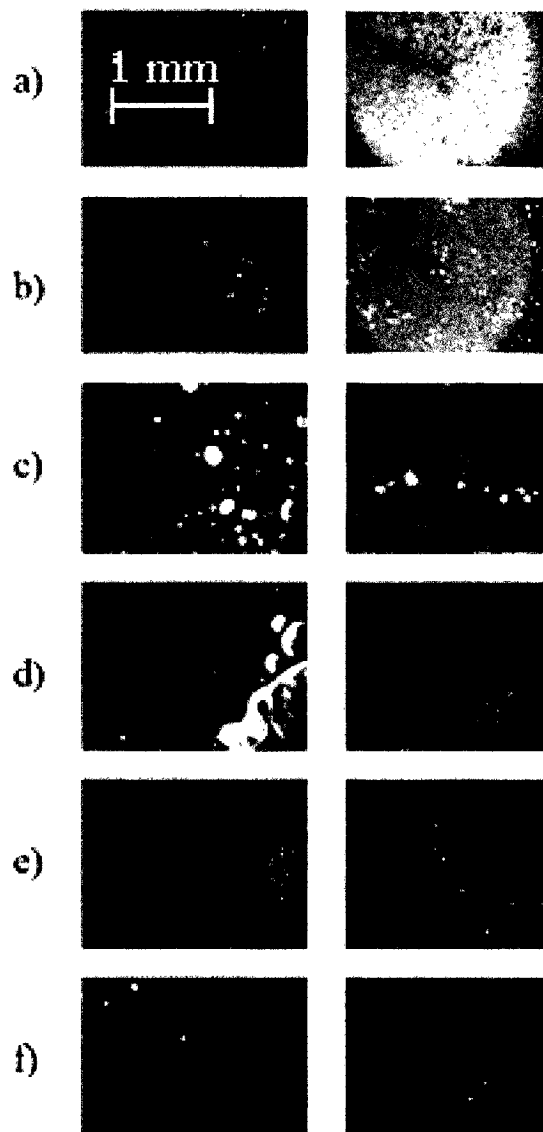
Figure 4.11. The left column shows images of the glassy forms of lauryl gallate/crystal violet lactone mixtures and the right column shows annealed forms where $x_{CVL}=$ (a) 0.13 b) 0.14 (c) 0.17 (d) 0.20 (e) 0.25 and (f) 0.33. Mixtures a) and (b) were annealed at 45 °C for 30 min and show significant crystallization of fine white material. Mixtures (c) and (d) were annealed at 65 °C for 30 min and display larger crystals with morphology consistent with that of pure lauryl gallate. Mixtures (e) and (f) were annealed at 75 °C for 60 minutes showing very little (e) to no formation (f) of lauryl gallate crystals.

The left column of Figure 4.11 shows images of glassy LG/CVL mixtures and the right column shows annealed mixtures where $x_{CVL}$ ranges from 0.13 to 0.33. Mixtures a) and b) were annealed at 45 °C for 30 min and show significant crystallization of fine

white material. Mixtures c) and d) were annealed at 65 °C for 30 min and display larger

crystals morphologically consistent pure LG. Mixtures e) and f) were annealed at 75 °C

for 60 minutes showing very little (e) or no formation (f) of LG crystals.

Figure 4.12 compares images of mixture c) and pure LG. LG crystals grow as

clusters of needles growing in a radial pattern. This LG morphology is also observed in

the crystals formed in annealed LG/CVL.
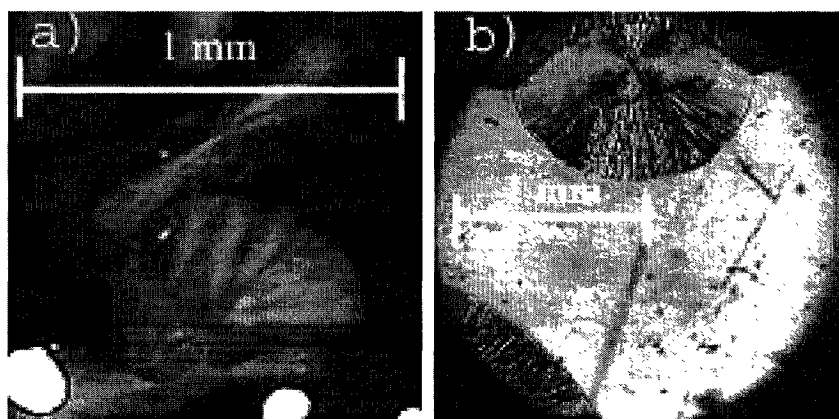


Figure 4.12. Comparison of annealed LG/CVL sample with pure lauryl gallate. (a)
A photographic enlargement of the annealed sample of lauryl gallate/crystal violet
lactone $x_{CVL}=$ 0.17 (Figure 4.11c) shows crystalline features consistent with the
morphology of pure lauryl gallate crystals, as shown in (b).

Since it is of interest to determine the equilibrium LG/CVL ratio in the coloured

complex for thermal and spectroscopic investigations, an appropriate annealing procedure

was determined using DSC. LG/CVL mixtures were heated to fusion and cooled at 10 K

min$^{-1}$. Most samples display no significant exothermic event on cooling to 298 K,

confirming glass formation. The samples were then heated at 10 K min$^{-1}$ to just below

their fusion temperatures and large exothermic events, corresponding to crystallization,

were observed. Figure 4.13 shows DSC thermograms for the heating of the glassy

mixtures shown in Figure 4.11. All mixtures were heated at rates of 10 K min$^{-1}$. Large exotherms are observed between 30 to 70 °C upon heating followed by a large endothermic peak at 85 to 95 °C ($T_{m,LG}$ = 99 °C). The enthalpy changes of the exothermic and endothermic events decrease with increasing $x_{CVL}$ to 0.33, indicating that no free LG exists at that composition. These thermal events are consistent with the images observed in Figure 4.11.
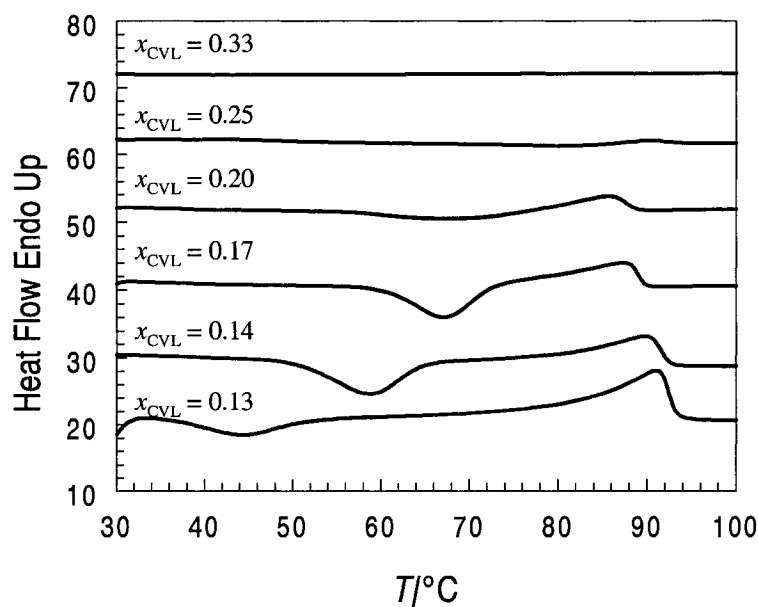


Figure 4.13. DSC thermograms on heating of glassy lauryl gallate/crystal violet lactone (LG/CVL) mixtures. All mixtures were heated at rates of 10 K min$^{-1}$. Large exotherms were observed between 30 to 70 °C upon heating followed by a large endothermic peak at 85 to 95 °C ($T_{m,LG}$ = 99 °C). The enthalpy changes of the exothermic and endothermic events decrease as $x_{CVL}$ increases to $x_{CVL}$ = 0.333, indicating that no free lauryl gallate exists at that composition.

### 4.3.2. Vibrational Spectroscopy of Lauryl Gallate/Crystal Violet Lactone Mixtures

Raman and IR spectra were obtained for annealed LG/CVL mixtures. Most important to the examination are changes in the carbonyl and amino vibrations associated with CVL structure. IR and Raman spectroscopy are complementary techniques in this examination because C=O vibrations tend to be strong in the IR and weak in the Raman, while the reverse is true for C-N/C=N stretches.[140] Peaks of interest in the present study are presented in Table 4.1.[165]

Table 4.1. Selected IR and Raman vibrational frequencies.[140,165] The abbreviations correspond to the average peak intensities; (s) strong, (m) medium, and (w) weak.

| Vibration | IR/cm$^{-1}$ | Raman/cm$^{-1}$ |
|---|---|---|
| $\upsilon$(C=O)$_{sym.}$ carboxylic acid on aromatic ring | 1710-1660 (s) | not Raman active |
| $\upsilon$(C=O)$_{asym.}$ carboxylic acid on aromatic ring | not IR active | 1686-1625 (w) |
| $\upsilon$(C=O) carboxylic acid H-bonded at –OH | 1760-1735 (m-s) | 1760-1735 (w) |
| $\upsilon$(C=O) carboxylic acid H-bonded at C=O | 1730-1705 (m-s) | 1730-1705 (w) |
| $\upsilon$(C=O)$_{sym.}$ carboxylate | 1450-1360 (m-w) | 1450-1360 (s) |
| $\upsilon$(C=O)$_{asym.}$ carboxylate | 1650-1540 (s) | 1650-1540 (w) |
| $\upsilon$(C-N) R-NR$_2$ | not IR active | 1250-1000 (s) 833-740 (s) |
| $\upsilon$(C=N) | 1650-1600 (m) | 1650-1600 (s) |

Raman and IR spectra of various LG/CVL mixtures are shown in Figure 4.14 and Figure 4.15. All LG/CVL samples prepared for Raman spectroscopy were annealed at 60 to 70 °C for 30 to 60 minutes prior to measurement to ensure crystallization of excess LG from the mixtures. Thin film IR samples only required 5 to 10 minute annealing periods

to ensure equilibration. As $x_{CVL}$ decreases ($x_{LG}$ increases), the opening of the CVL ring (and concomitant formation of a coloured complex) was observed.

As $x_{CVL}$ decreases, Raman and IR peaks at 1745 cm$^{-1}$, corresponding to the closed lactone carbonyl vibration, decrease in intensity and are not observed below $x_{CVL} = 0.75$. In the region $0.70 < x_{CVL} < 1.00$, a feature was observed at 1710 cm$^{-1}$ (weak peak in Raman, shoulder in IR). This likely is correlated with an acidic carbonyl (-COOH) vibration from the ring-open form of CVL[156] where the carbonyl oxygen is involved in hydrogen bonding.[140,165] Peaks at 1710 and 637 cm$^{-1}$ decrease in intensity below $x_{CVL} < 0.70$.

Between $0.25 < x_{CVL} < 0.70$ a strong peak in both the Raman and IR at about 1584 cm$^{-1}$ increases in intensity as $x_{CVL}$ decreases. At $x_{CVL} = 0.25$ this is the most prominent IR feature in the carbonyl region and is assigned as the asymmetric carboxylate vibration of the CVL carboxylate structure. Below $x_{CVL} = 0.25$ the peak at 1584 cm$^{-1}$ decreases in intensity.

These IR data are consistent with the observations of Ibata $et$ $al.$[156] of the formation of a complex of CVL with an acidic developer. A second strong Raman peak at 1360 cm$^{-1}$ has an intensity that behaves the same as the 1584 cm$^{-1}$ peak as $x_{CVL}$ is varied. (These peaks are the two strongest Raman peaks at $x_{CVL} = 0.25$.) The symmetric carboxylate vibration has a strong Raman intensity and weak IR intensity, therefore the peak at 1360 cm$^{-1}$ is assigned as the symmetric carboxylate vibration.[165] The wag deformation, $\gamma_{sym}(COO^-)$, for the carboxylate form is observed at 726 cm$^{-1}$,[165] supporting the assignment.
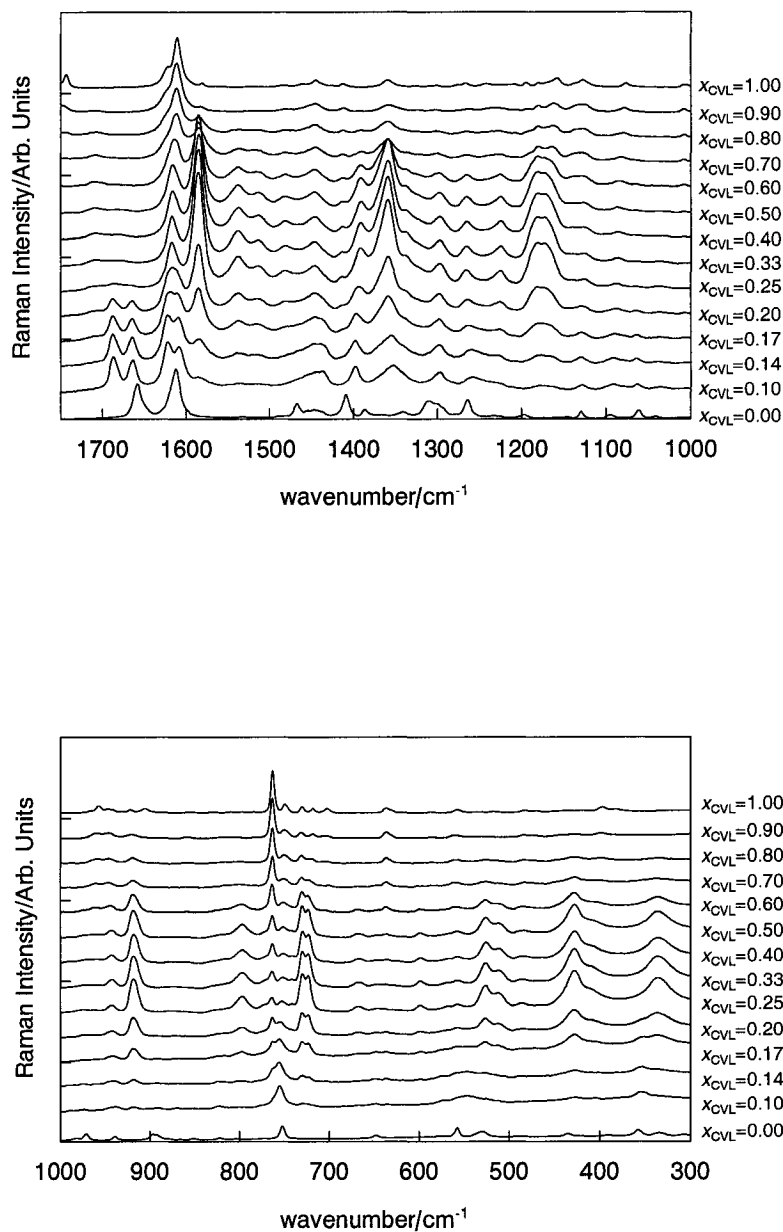
Figure 4.14. The Raman spectra of lauryl gallate/crystal violet lactone (LG/CVL) mixtures show the formation of a coloured complex at $\sim x_{CVL}$=0.25. This coloured complex is characterized by carboxylate carbonyl modes at 1359 cm$^{-1}$ and 720 cm$^{-1}$, C=NR$_2$ modes at 1584 cm$^{-1}$ and 918 cm$^{-1}$, and a broad peak at 1180 to 1160 cm$^{-1}$ corresponding to phenolic OH bending vibrations.
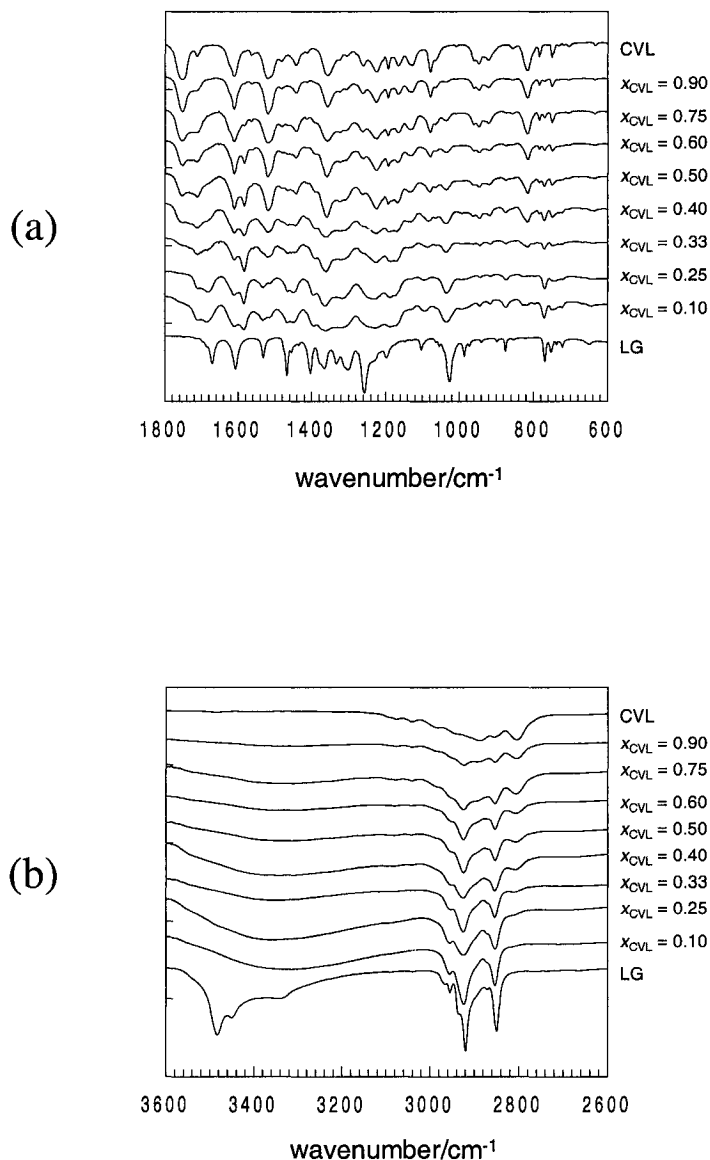
Figure 4.15. IR spectra of selected lauryl gallate/crystal violet lactone (LG/CVL) mixtures showing (a) 1800 to 600 cm$^{-1}$ and (b) 3600 to 2600 cm$^{-1}$ regions. The prominent peak at 1745 cm$^{-1}$ corresponding to closed crystal violet lactone develops a large shoulder at 1715 cm$^{-1}$ as $x_{CVL}$ drops to 0.75. At $x_{CVL}$ = 0.25 the most significant peak is 1580 cm$^{-1}$, corresponding to the asymmetric carboxylate vibration. Peaks corresponding to H-bonding in pure lauryl gallate broaden and lower in frequency as the coloured complex is formed.

The Raman peak at 1584 cm$^{-1}$ is assigned to the asymmetric C=N vibration formed in the open carboxylate form of the dye. Opening the lactone ring of CVL results in the formation of a positive charge on the central carbon. Electron density is donated through the phenyl rings to stabilize the spiro center, resulting in an increase in double bond character of the C-N bond. The observed peak at 1584 cm$^{-1}$ lies between the average vibrational frequencies for $\upsilon$(C=NR$_2$) (1600 to 1650 cm$^{-1}$)[140,165] and $\upsilon$(C-NR$_2$) (1000 to 1255 cm$^{-1}$)[140,165] and is attributed to a C-N vibration with significant double bond character. Neutral C-NR$_2$ displays strong Raman active low frequency bending modes, $\beta$(C-NR$_2$), in the range 740-833 cm$^{-1}$.[140] A peak at 763 cm$^{-1}$, corresponding to the C-NR$_2$ bend in pure CVL,[154] decreases in intensity as $x_{CVL}$ decreases and is accompanied by the formation of a new peak at 918 cm$^{-1}$. The new peak could be consistent with the formation of a much stronger C-N bond as the coloured complex is formed. Two other CN peaks associated with open CVL are observed at 940 cm$^{-1}$ and 790 cm$^{-1}$ and are consistent with the symmetric and asymmetric bending mode, $\beta$(N$^+$C$_4$) in the Ar=N$^+$(CH$_3$)$_2$ moiety.[140]

A broad peak at 1160-1180 cm$^{-1}$ is also prominent in the $0.20 < x_{CVL} < 0.70$ samples. The frequency is consistent with symmetric scissoring, $\beta_s$(OH), of phenolic hydroxy groups but the peak intensity is greater than predicted for this type of vibration.[140,165] The increase in intensity might be due to a change in the polarization of phenolic groups on LG which presumably contribute to the stability of the coloured complex through H-bonds.

The $\upsilon$(OH) region of the IR spectrum shows three peaks for pure LG at 3490, 3460 and 3340 cm$^{-1}$ (Figure 4.15). These peaks are assigned to intermolecular and

intramolecular H-bonding; as LG interacts with CVL, H-bonding changes significantly. Distinct peaks associated with LG become one large broad peak ($\Delta\upsilon \sim 500$ cm$^{-1}$) centred at about 3350 cm$^{-1}$ when CVL is added to the mixture. The width of the peak and the general lowering of the frequency distribution show that the average strength of H-bonding increases in the system as the LG/CVL complex is formed. As the basicity of the acceptor site increases, the H-bond strength increases and the $\upsilon$(OH) decreases. The broad $\upsilon$(OH) is prominent in the region $0.17 < x_{CVL} < 0.55$, and above $x_{CVL} = 0.70$ it is not observed at all.

## 4.4. Propyl Gallate/Crystal Violet Lactone

Like the lauryl gallate/crystal violet lactone (LG/CVL) mixtures discussed in the previous section, propyl gallate/crystal violet lactone (PG/CVL) mixtures formed glassy solids coloured solids upon cooling from the melt.

### 4.4.1. Annealing of Propyl Gallate/Crystal Violet Lactone Mixtures

DSC was used to examine the crystallization behaviour of PG from the mixture in an effort to determine complex stoichiometry and annealing conditions. Figure 4.16 shows DSC thermograms of glassy PG/CVL mixtures. Samples were cooled to 25 °C from the melt at 10 K min$^{-1}$ and heated at 10 K min$^{-1}$ until fusion. Exothermic events corresponding to the crystallization of PG were observed between 80 to 120 °C in mixtures with $x_{CVL} \leq 0.25$. These were followed by endothermic events consistent with the fusion of pure PG ($T_{m, PG} = 130$ °C). No thermal events were observed in mixtures with $x_{CVL} > 0.25$.
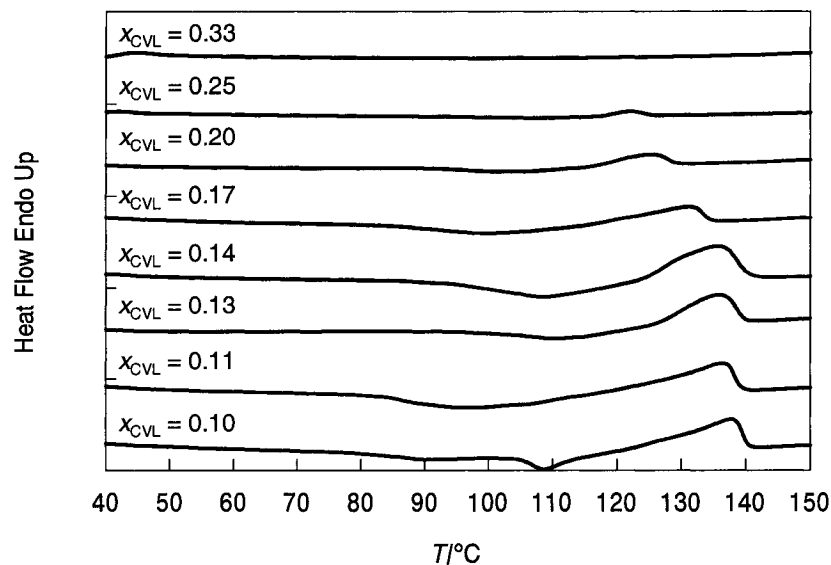
Figure 4.16. DSC thermograms of propyl gallate/crystal violet lactone (PG/CVL) mixtures show an exothermic event analogous to that observed in lauryl gallate/crystal violet lactone mixtures due to the crystallization of excess propyl gallate from the mixture. Exotherms were observed in between 80 to 120 °C for mixtures with $x_{CVL} < 0.33$. No thermal events were observed in mixtures with $x_{CVL} > 0.25$.

### 4.4.2. Vibrational Spectroscopy of Propyl Gallate/Crystal Violet Lactone Mixtures

Raman spectra obtained for PG/CVL mixtures are shown in Figure 4.17. All PG/CVL samples prepared for Raman spectroscopy were annealed at 100 °C for 60 minutes prior to measurement to ensure crystallization of excess PG from the mixtures. Spectral features consistent with the formation of an open lactone structure with carboxylate moiety stabilized by increased electron density in the dimethylaminophenyl substituents were observed.
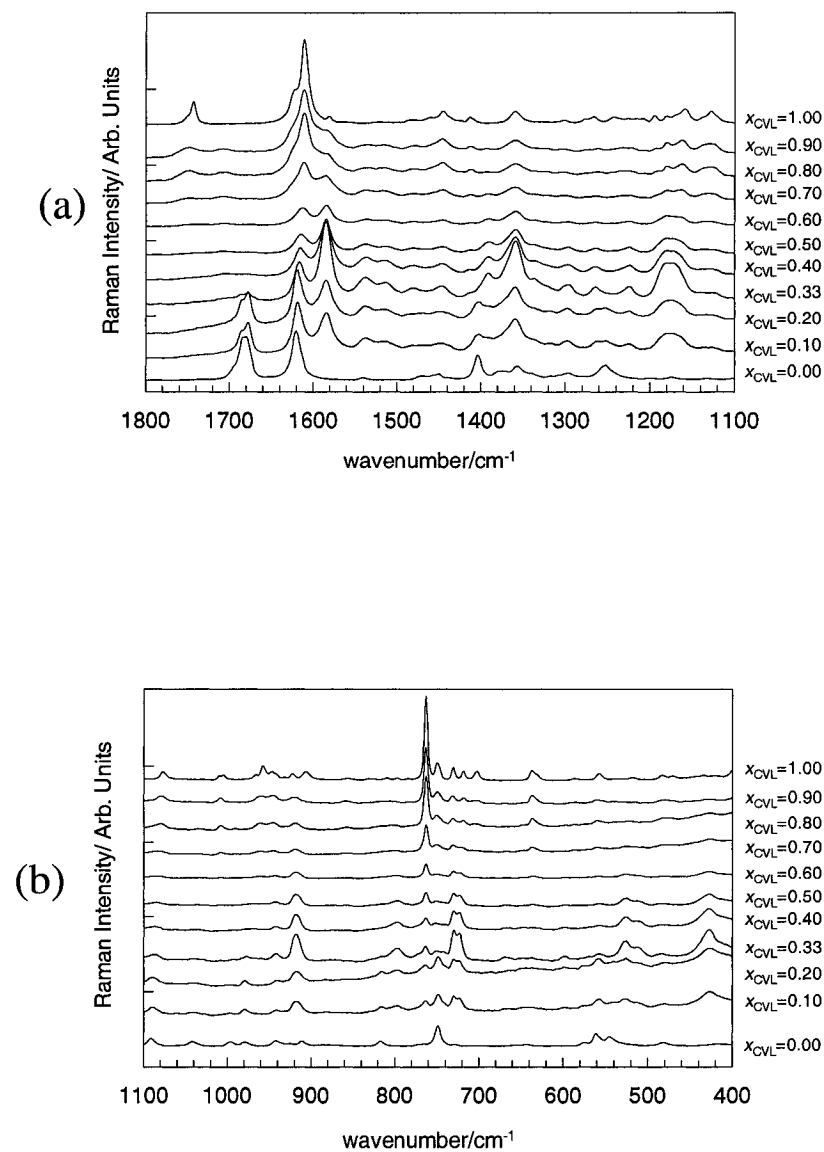
Figure 4.17. Raman spectra of propyl gallate/crystal violet lactone (PG/CVL) mixtures in (a) the 1800 to 1100 cm$^{-1}$ and (b) 1100 to 400 cm$^{-1}$ regions. Spectral features consistent with the formation of an open lactone structure with carboxylate moiety stabilized by increased electron density in the dimethylaminophenyl substituents were observed.

Spectral features observed in the formation of coloured complex were essentially the same as those observed in the LG/CVL binary system. Peaks at 1584 and 918 cm$^{-1}$, corresponding to the formation of strong C=N bonds, grow in intensity between $0 < x_{CVL} < 0.33$ and then gradually weaken in intensity as $x_{CVL} \rightarrow 1$.

The symmetric carboxylate vibration at 1360 cm$^{-1}$ and carboxylate wag at 726 cm$^{-1}$ grow and diminish in intensity in the same manner as the C=N peaks. A broad peak between 1180 to 1160 cm$^{-1}$ is consistent with the symmetric scissoring $\beta_S(OH)$ of phenolic hydroxy groups discussed in section 4.3.1.

Peaks corresponding to pure CVL, $\beta(C-NR_2)$ at 763 cm$^{-1}$ and $\upsilon_{asym.}(C=O)$ at 1749 cm$^{-1}$, decrease in intensity as $x_{CVL}$ decreases from 1 to 0.33. A peak at 918 cm$^{-1}$, corresponding to a significant strengthening of $\beta(C-NR_2)$ in the coloured complex, increases in intensity below $x_{CVL} = 0.33$ and then gradually weakens in intensity as $x_{CVL} \rightarrow 1$. As for the LG/CVL mixtures, a second carbonyl peak, corresponding to the acid form (-COOH) of the open lactone, is observed in the range $0.70 < x_{CVL} < 1$.

### 4.5. Octyl Gallate/Crystal Violet Lactone

Octyl gallate/crystal violet lactone (OG/CVL) formed coloured glassy solids upon cooling from the melt in the same manner as lauryl gallate/crystal violet lactone (LG/CVL) and propyl gallate/crystal violet lactone (PG/CVL).

### 4.5.1. Annealing of Octyl Gallate/Crystal Violet Lactone Mixtures

Octyl gallate/crystal violet lactone (OG/CVL) forms glassy solids upon cooling in the same manner as lauryl gallate/crystal violet lactone (LG/CVL) and propyl

gallate/crystal violet lactone (PG/CVL). DSC was used to examine the crystallization behaviour of OG from the mixtures in an effort to determine complex stoichiometry and annealing conditions. Figure 4.18 shows DSC thermograms of glassy OG/CVL mixtures. Samples were cooled to 25 °C from the melt at 10 K min$^{-1}$ and heated at 10 K min$^{-1}$ until fusion. Exothermic events corresponding to the crystallization of OG were observed between 50 to 80 °C in mixtures with $x_{CVL} < 0.20$. These were followed by endothermic events consistent with the fusion of pure OG ($T_{m, OG} = 100$ °C). No thermal events were observed in mixtures with $x_{CVL} > 0.17$.
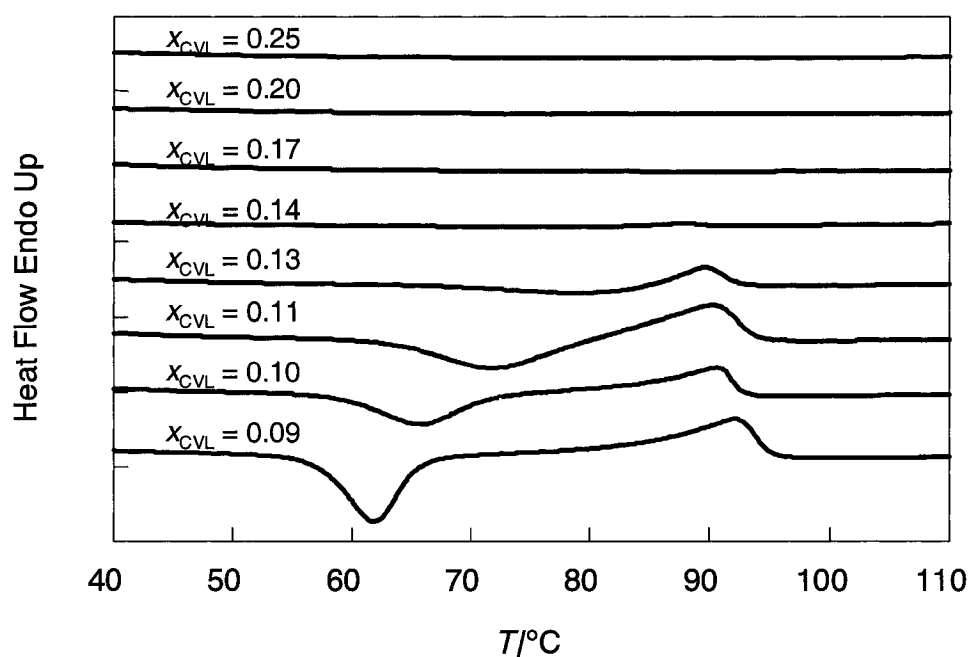


Figure 4.18. DSC thermograms of octyl gallate/crystal violet lactone (OG/CVL) mixtures shows an exothermic event analogous to that observed in lauryl gallate/crystal violet lactone mixtures due to the crystallization of excess OG from the mixture. Exotherms are observed in between 60 to 80 °C for mixtures with $x_{CVL} < 0.20$. No thermal events were observed in mixtures with $x_{CVL} > 0.17$.

### 4.5.2. Vibrational Spectroscopy of Octyl Gallate/Crystal Violet Lactone Mixtures

Raman spectra obtained for OG/CVL mixtures are shown in Figure 4.19. All OG/CVL samples prepared for Raman spectroscopy were annealed at 80 °C for 60

minutes prior to measurement to ensure crystallization of excess OG from the mixtures. Peaks consistent with an open lactone with a carboxylate moiety (1359 cm$^{-1}$ and 720 cm$^{-1}$) and significant double bond character in the dialkylaminophenyl substituents (1584 cm$^{-1}$ and 918 cm$^{-1}$) are analogous to those observed in LG/CVL and PG/CVL mixtures. The only significant difference between OG/CVL and the other mixtures is the range of $x_{CVL}$ over which the coloured complex is formed. Unlike LG/CVL and PG/CVL mixtures, which show peak intensity for coloured complex formation is at a maximum at about $x_{CVL}$ = 0.25 to 0.40, the peaks for coloured complex in OG/CVL appear to increase sharply in intensity at $x_{CVL}$ = 0.17 and then lower in the same manner as the other developer/dye mixtures.



(a)
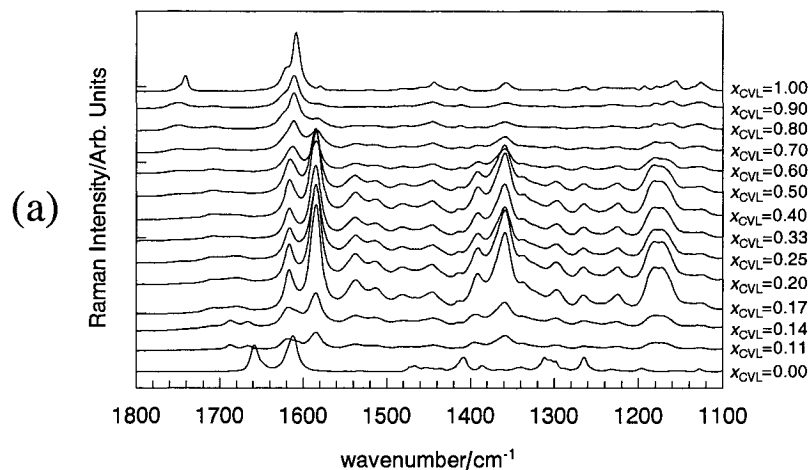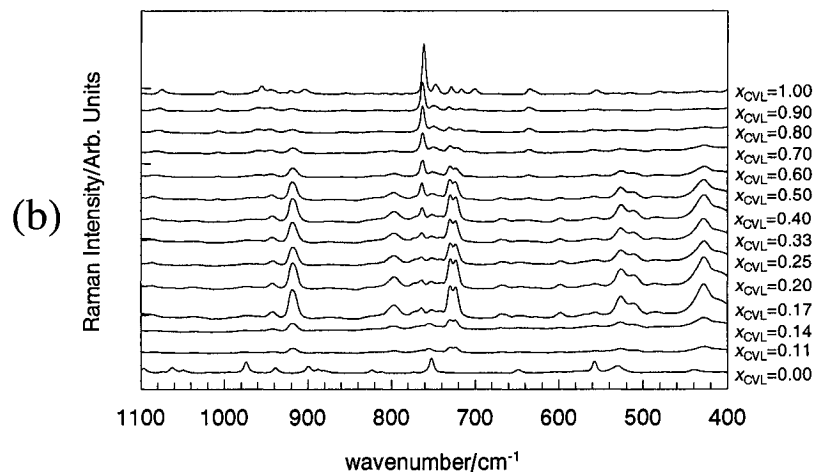
Figure 4.19. Raman spectra of octyl gallate/crystal violet lactone (OG/CVL) mixtures in (a) the 1800 to 1100 cm$^{-1}$ and (b) 1100 to 400 cm$^{-1}$ regions. Spectral features consistent with the formation of an open lactone structure with carboxylate moiety stabilized by increased electron density in the alkylaminophenyl substituents were observed.

## 4.6. Alkyl Gallate/Crystal Violet Lactone Complex Stoichiometry

In general, more than one developer molecule per dye molecule is necessary for optimal colour development. The concept of supramolecular complexes of weak acids and thermochromic dyes was proposed by Tsutsui et al.[60] They note that observed colour density could be optimized by preparing dye-developer mixtures at the exact dye-developer ratio of the coloured complex. To determine stoichiometry they used an adaptation of Job's method of continuous variation.[125,166] IR spectra of mixtures of 3-dibutylamino-7-(o-chloroanilino)aminofluoran (FD1) and octadecylphosphonic acid (P18) were examined and the intensity of the lactone carbonyl band in coloured and non-

coloured forms was examined. The change in infrared intensity, $\Delta I$, reached a maximum at a dye:developer ratio of 7:1 indicating that approximately 7 molecules of P18 act to hold the FD1 in its open form.[60]

### 4.6.1. Stoichiometry Determination via Job's Method

The stoichiometry of a coloured complex can be determined using a variation of Job's method, or the method of continuous variation. The formation of complex can be written as follows:[125,166]

$$a \text{ CVL} + b \text{ LG} = c \text{ Complex} \qquad\qquad 4.1$$

If the coefficients are divided through by $a$ the expression becomes:[125,166]

$$\text{CVL} + x \text{ LG} = y \text{ Complex} , \qquad\qquad 4.2$$
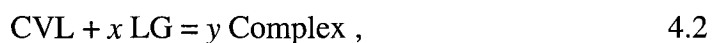
where $x=b/a$ and $y=c/a$ .

Job's method states that if two components (A and B) are mixed with continuously varying mole ratios such that $x_A + x_B = 1$ the maximum amount of product will exist in the mixture where $r$, the mole ratio of A and B, is equal to $y$. If the amount of complex, $y$, is plotted against $r$ the maximum is correlated with the stoichiometric mole ratio.[125,166]

In this study the intensities of the peaks corresponding to the coloured state (alkyl gallate$_x$•CVL) were used to represent the amount of complex present. Present results for the stoichiometry of LG/CVL complexes have been published.[164] The results for PG/CVL, OG/CVL and LG/CVL mixtures are shown in Figures 4.20, 4.21, and 4.22, respectively. The intensities of peaks corresponding to the coloured complex (1584 cm$^{-1}$, 1359 cm$^{-1}$, 918 cm$^{-1}$, and 720 cm$^{-1}$) were plotted against the molar ratio of alkyl gallate

to CVL. Since the developer-dye binary mixtures are known to be highly sensitive to a third component (hence the basis of rewritable thermochromism), an internal standard was not used. To compensate for this, uniformity of the sample preparation and experimental conditions was maintained. Binary mixture samples were prepared as a batch with approximately uniform mass and measured immediately using identical Raman laser power and sample position. While some variation in the absolute intensities occurs from batch to batch, the resulting trends are significant.
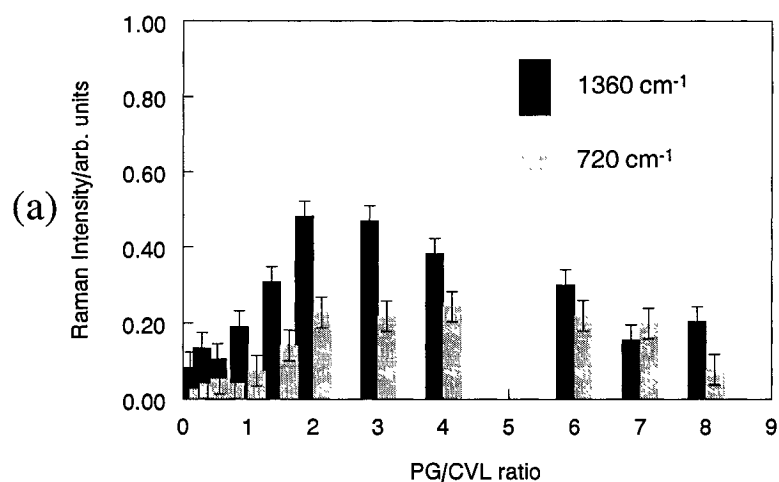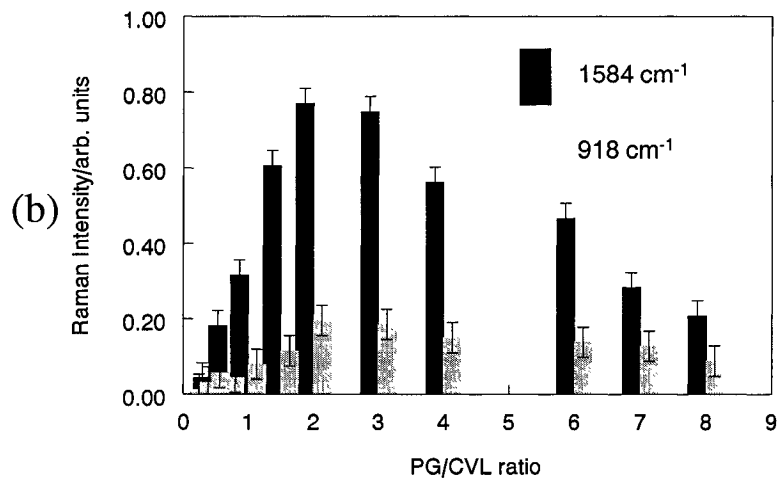
Figure 4.20. Job plots of the intensity of selected peaks corresponding to the coloured complex PG$_x$•CVL in the Raman spectra of propyl gallate/crystal violet lactone (PG/CVL) mixtures: (a) peaks corresponding to carboxylate functionality (-COO); (b) peaks corresponding to aminophenyl functionality (Ar-NR$_2$). Error bars represent the uncertainty of three measurements.
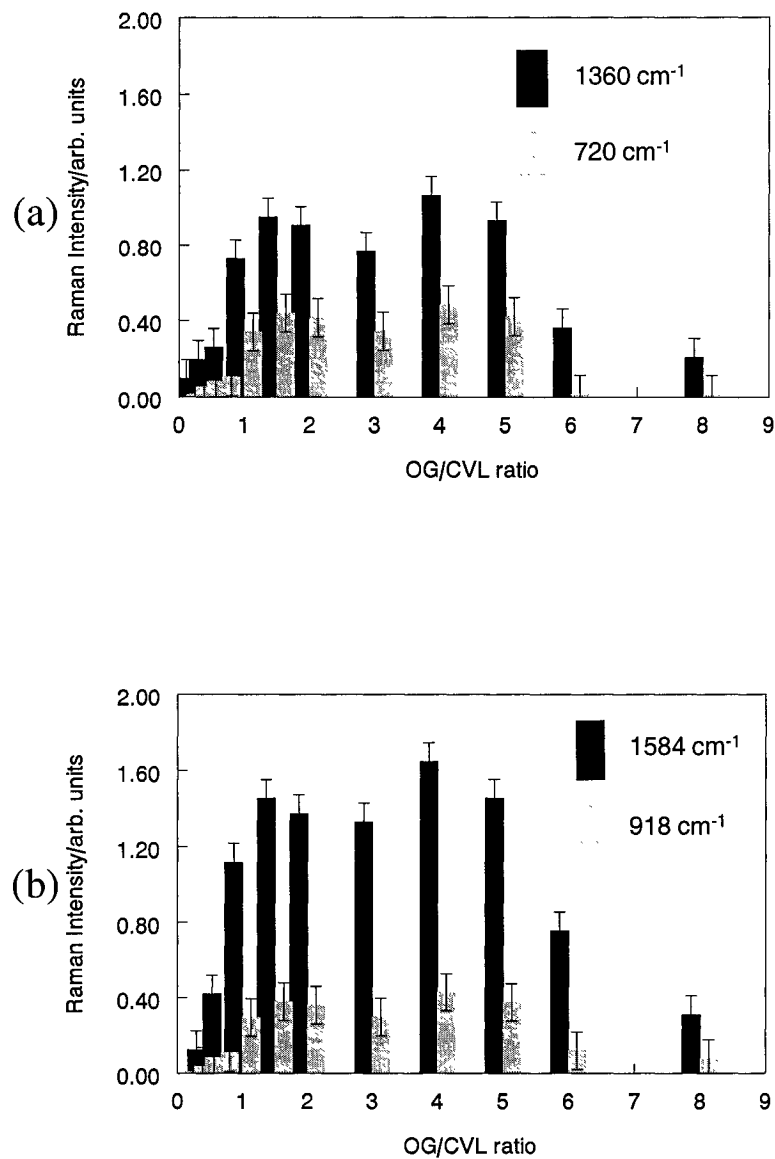
Figure 4.21. Job plots of the intensity of selected peaks corresponding to the coloured complex $OG_x \cdot CVL$ in the Raman spectra of octyl gallate/crystal violet lactone (OG/CVL) mixtures: (a) peaks corresponding to carboxylate functionality (-COO); (b) peaks corresponding to aminophenyl functionality ($Ar-NR_2$). Error bars represent the uncertainty of three measurements.
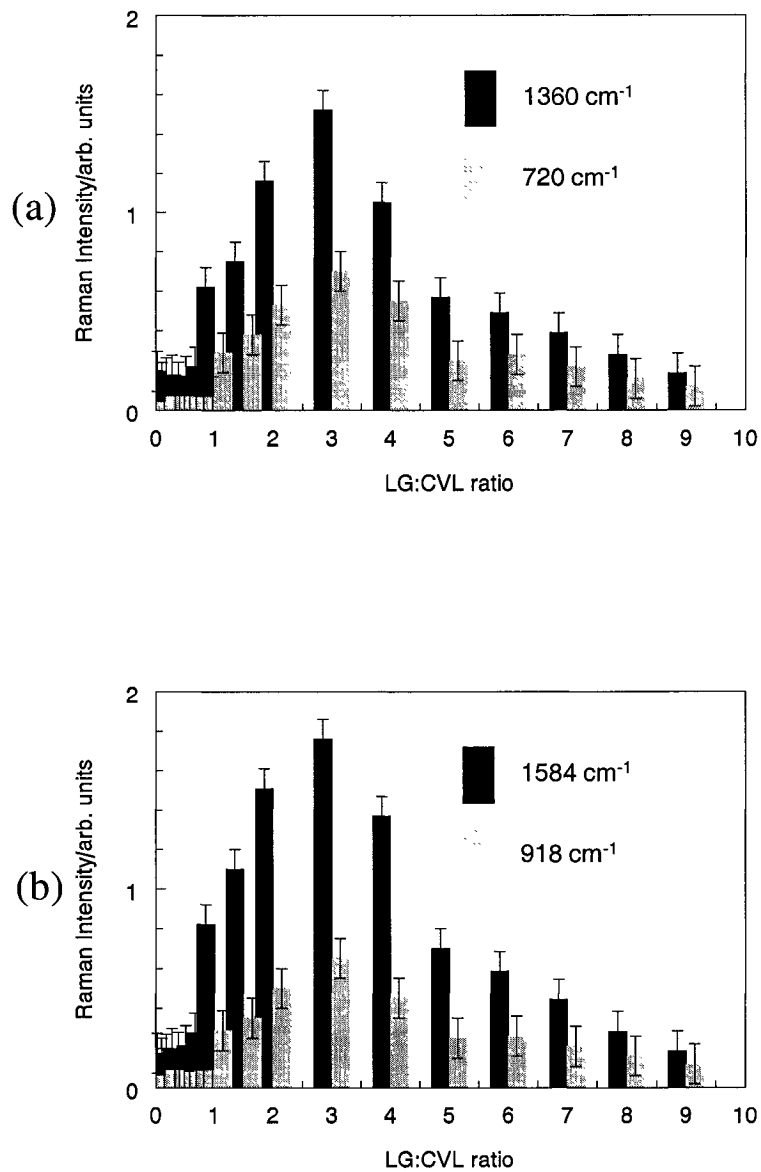
Figure 4.22. Job plots of the intensity of selected peaks corresponding to the coloured complex $LG_x \bullet CVL$ in the Raman spectra of lauryl gallate/crystal violet lactone (LG/CVL) mixtures: (a) peaks corresponding to carboxylate functionality (-COO); (b) peaks corresponding to aminophenyl functionality ($Ar\text{-}NR_2$). Error bars represent the uncertainty of three measurements.

Peak intensities for coloured complex observed for PG/CVL mixtures (Figure 4.20) show an increase of all peaks to a maximum PG/CVL ratio of 2 to 3, indicating a stoichiometry of $(PG)_2 \bullet CVL$ or $(PG)_3 \bullet CVL$. In these systems the Job's method analysis alone does not always provide a conclusive result. Examination of the DSC thermograms of these mixtures (Figure 4.16) obtained in the annealing analysis aids in the assignment of stoichiometry. The thermogram for $x_{CVL} = 0.25$ (PG:CVL = 3) shows a small endotherm near the melting point of PG, indicating that a small amount of free PG is present in this composition. On the other hand, the thermogram for $x_{CVL} = 0.33$ (PG:CVL = 2) shows no detectable thermal events. A combination of DSC analysis and a Job plot obtained from Raman intensity data allow an assignment of $(PG)_2 \bullet CVL$ as the equilibrium coloured complex stoichiometry in the PG/CVL binary system.

The same method described above is used for the OG/CVL and LG/CVL mixtures. A Job plot of selected Raman intensities of OG/CVL (Figure 4.21) shows high intensities for coloured complex at an OG/CVL ratio of 4 to 5. DSC thermograms of OG/CVL (Figure 4.18) show no thermal events in mixtures with $x_{CVL} > 0.17$ (OG:CVL = 4). A very small endotherm is observed at ~ 90°C in the mixture corresponding to $x_{CVL} = 0.17$. According to the DSC analysis the assignment of stoichiometry for this complex is $(OG)_4 \bullet CVL$.

The "double hump" in the Job plot in Figure 4.21 might seem to indicate the formation of two distinct complexes of $(OG)_x \bullet CVL$. However, there is no evidence in the Raman spectra of these mixtures to support the formation of a second complex; (the spectra are essentially the same as PG/CVL and LG/CVL).

The assignment of equilibrium (LG)$_x$•CVL stoichiometry is of primary importance to the present study. The Job plot for selected Raman intensities of LG/CVL is shown in Figure 4.22. Maximum intensities occur at (LG:CVL = 3) with the intensities of (LG:CVL = 2) appearing slightly smaller. DSC thermograms (Figure 4.13) of LG/CVL mixtures show thermal events consistent with the crystallization and melting of pure LG at $x_{CVL} < 0.25$. This is consistent with a stoichiometry of (LG:CVL = 3), i.e. an equilibrium coloured complex with the formula (LG)$_3$•CVL.

### 4.7. Comparison of Alkyl Gallate/CVL Mixtures

The mixtures form highly coloured amorphous mixtures that display small amounts of colour loss (in regions where pure alkyl gallate crystallizes) when annealed. The bulk colour density of annealed samples remains high and these mixtures do not display optimal rewritable thermochromic properties.

The spectroscopic features of the coloured complexes formed in the three mixtures are identical; equilibrium coloured complexes are characterized by a ring-opened CVL molecule with a carboxylate moiety with C-O bond distances consistent with a charged (-COO) group. The positive charge on the spiro carbon centre is presumably stabilized by a significant increase in bond strength in the Ph-N bonds of the dialkylamino ring substituents consistent with the resonance structures shown in Figure 4.3. All systems show a broad, intense peak consistent with phenolic hydroxy groups. The phenolic hydroxy groups of the alkyl gallates act to stabilize the carboxylate moiety in CVL, likely through H-bonding.

All three binary systems form glassy mixtures and are capable of forming equilibrium and metastable complexes; more alkyl gallate can be incorporated into the coloured complex than the equilibrium stoichiometries. This is shown by the crystallization of alkyl gallate during the annealing of the glassy mixtures at high temperatures. Raman spectra of non-annealed samples reveal metastable stoichiometries of up to $(PG)_9 \cdot CVL$, $(OG)_9 \cdot CVL$, and $(LG)_9 \cdot CVL$ in PG/CVL, OG/CVL and LG/CVL mixtures. Figures 4.23, 4.24 and 4.25 show the comparison of annealed and non-annealed samples of 9:1 mixtures of PG/CVL, OG/CVL, and LG/CVL.

In PG/CVL, $x_{PG} = 0.11$, the shape and position of the asymmetric carbonyl peaks of PG at 1678 $cm^{-1}$ do not change after annealing (Figure 4.23), however the ratio of the intensity of the C=N vibration of ring-opened CVL at 1584 $cm^{-1}$ to the PG carbonyl peak at 1678 $cm^{-1}$ ($I_{1584}/I_{1678}$) changes from 3.6 in the non-treated sample to 0.8 in the heat-treated sample. This shows a combination of growth of the 1678 $cm^{-1}$ peak and decrease of the 1584 $cm^{-1}$ peak, consistent with the crystallization of pure PG and destruction of some coloured CVL complex in the mixture.
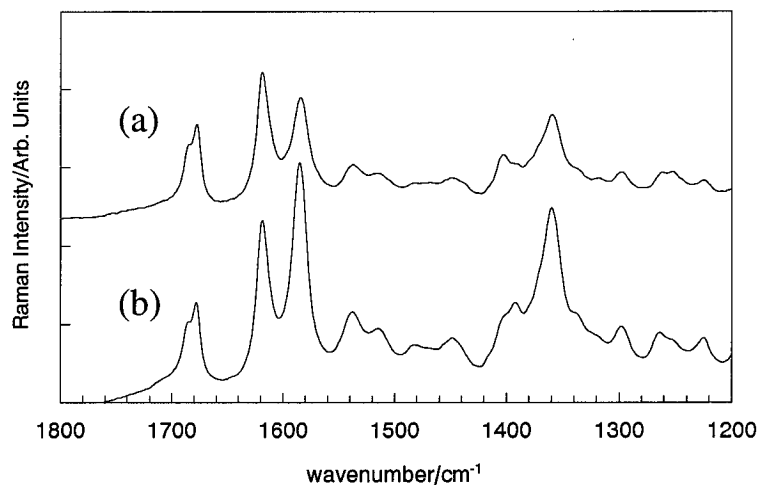
Figure 4.23. Comparison of mixtures of propyl gallate/crystal violet lactone (PG/CVL), $x_{CVL}$ = 0.11 that have been (a) annealed at 100 °C for 60 minutes and (b) not annealed. Changes in the peak ratios of 1584 cm$^{-1}$ to 1678 cm$^{-1}$ indicate a decrease of coloured complex and increase of pure propyl gallate in the mixture.
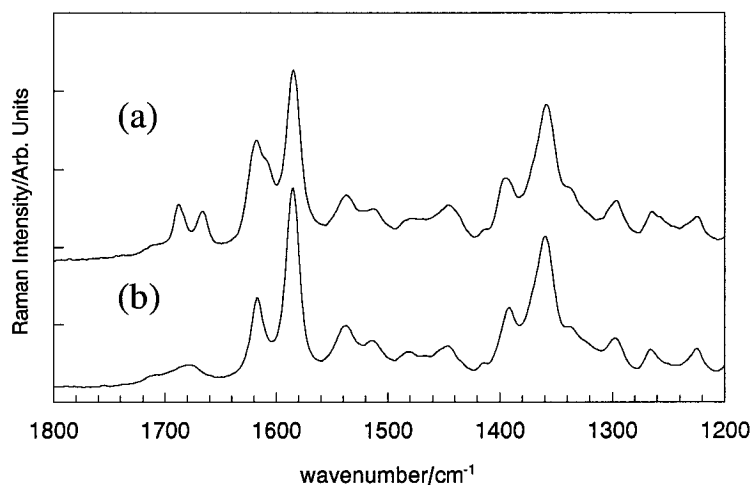


Figure 4.24. Comparison of mixtures of octyl gallate/crystal violet lactone (OG/CVL), $x_{CVL}$ = 0.11 that have been (a) annealed at 80 °C for 60 minutes and (b) not annealed. Upon annealing peaks at 1688 and 1667 cm$^{-1}$, corresponding to free octyl gallate, appear in the mixture.
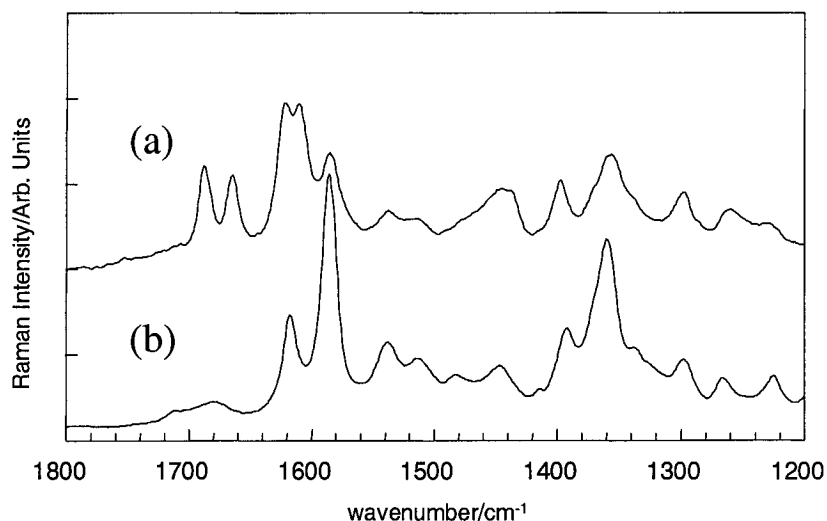
Figure 4.25. Comparison of mixtures of lauryl gallate/crystal violet lactone (LG/CVL), $x_{CVL} = 0.11$ that have been (a) annealed at 70 °C for 60 minutes and (b) not annealed. Upon annealing peaks at 1684 and 1687 cm$^{-1}$, corresponding to free lauryl gallate, appear in the mixture.

OG/CVL and LG/CVL show similar behaviour upon annealing. Peaks corresponding to the asymmetric carbonyl vibration of the alkyl gallate carbonyl become more prominent in the 1700 to 1650 cm$^{-1}$ region while the peaks corresponding to coloured complex (1584 and 1360 cm$^{-1}$) decrease in intensity. This is consistent with the loss of coloured CVL and the crystallization of OG and LG.

Pure OG displays an asymmetric carbonyl vibration at 1656 cm$^{-1}$ that splits at concentrations slightly below $x_{CVL} = 0.20$ to 1688 and 1667 cm$^{-1}$. Pure LG has an analogous peak at 1658 cm$^{-1}$ that shows splitting to 1664 and 1687 cm$^{-1}$ below $x_{CVL} = 0.20$. This implies that there might be two forms of free alkyl gallate interacting with the alkyl gallate/CVL complex, one form with an asymmetric carbonyl vibration shifted +6 to 10 cm$^{-1}$, the other with its asymmetric carbonyl vibration shifted +30 cm$^{-1}$. Figure 4.26 shows how the carbonyl vibrations of alkyl gallates are at lower frequencies than average

ester C=O vibrations (1750-1715 cm$^{-1}$)[140] because ester group accepts electron density from the aromatic ring, effectively lowering the C=O bond strength.
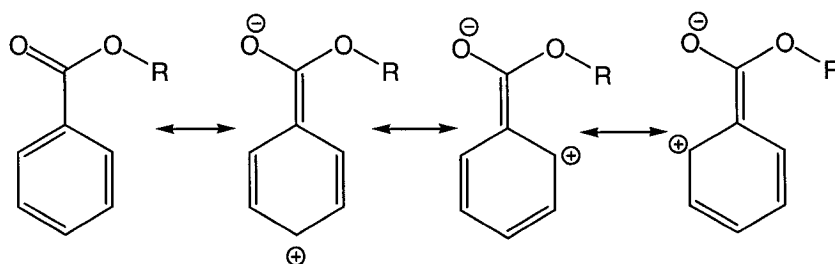


Figure 4.26. The carbonyl vibrations of an ester on an aromatic ring are at lower frequencies than average C=O bonds because the ester group accepts electron density to the aromatic ring, effectively lowering the C=O bond strength.

A large increase in carbonyl vibrational frequency indicates that the planar configuration of the ester and aromatic ring necessary for effective conjugation is disrupted. This implies that the angle between the ester and the aromatic ring deviates from planarity as it interacts with the alkyl gallate/CVL complex. It is possible that multiple layers of OG or LG interact within the coloured complex. Possibly, the layer closest to the coloured complex has a significantly tilted ring, whereas the outer layers of interaction behave more like pure LG or OG.

Pure PG in annealed PG/CVL mixtures does not show the shifting and splitting in asymmetric carbonyl frequency in the low $x_{CVL}$ compositions. This might be due to the different packing requirements observed in PG relative to OG (Figure 4.8 and Figure 4.9). OG, and presumably LG, crystallize in a head-to-head bilayer structure that shows more pronounced phenyl stacking than PG.[163] This, combined with the larger steric bulk of OG and LG, might result in disruption of the packing manifested in enhanced ring tilt of the phenyl group relative to the alkyl-chain.

Although the structures of the complexes produced are not known specifically, the following information has been presented in this study. The coloured complex is a glassy solid with the CVL in the open-carboxylate form stabilized by the formation of C=N bonds at the aminophenyl substituents. This implies a strong interaction with the weakly acidic colour developer, most likely an interaction between the phenolic hydroxy groups of alkyl gallate and the carboxylate of CVL.

The equilibrated coloured complex has a stoichiometry of $(Alkyl\ Gallate)_{2-4} \bullet CVL$, so the ring-open CVL is stabilized by the phenol groups of two to four alkyl gallate molecules. Alkyl gallates present in the mixture in excess of the equilibrium coloured complex stoichiometry interact strongly with the coloured complex. In the longer chain species this interaction appears to involve a ring tilt causing an increase in the $\upsilon(C=O)$ frequency.

# Chapter 5. Developer-Solvent Interactions

## 5.1. Polymorphism in 1-Alcohols

In the previous chapter the interactions between a thermochromic dye, CVL, and a series of alkyl gallate colour developers were examined. Equilibrium and metastable complex stoichiometries were assigned and characterized using Raman spectroscopy and DSC. While the dye/developer interaction is crucial for the development of colour, the solvent component of a rewritable thermochromic mixture plays an important role in many secondary characteristics such as decolourisation rates and colour contrast. The role of the solvent component of these ternary mixtures has not been examined in detail in the open literature. This chapter will present the information concerning the role of a series of 1-alcohol solvents by examining its interaction with alkyl gallate colour developers.

### 5.1.1. Introduction

The $n$-higher alcohols ($C_nH_{(2n+1)}OH$, $n > 12$) display polymorphism similar to paraffins and other long-chain alkyl species.[167-169] Most importantly, they posses solid rotator phases at temperatures near their melting point.[131,132,167,170-,178] The 1-alcohol rotator phase is characterized by enhanced values of the molar heat capacity,[131,132] proton conductivity,[173,179] and dielectric constant[180-183] relative to the low-temperature solid and high-temperature liquid phases.

Three phases are observed in 1-alcohols with alkyl-chains greater than 12 carbons. All show a head-to-head bilayer structure with extensive hydrogen

110

bonding.[131,167,171,177,178,183] First, a monoclinic phase, β, is formed at low temperatures where the long axis of molecule is nearly perpendicular to a continuous hydrogen bonded plane formed by the hydroxy end groups.[131,167,168,173-177] Second, a monoclinic phase, γ, can be formed at low temperature where the long axis of the molecule is tilted about 60° to the normal of the hydroxy plane.[131,167,173-177,183] Third, a disordered rotator phase, α, where the long axis of the molecule is tilted slightly from the normal to the hydroxy plane (7°) and rotation occurs about the long axis of the molecule,[184] exists immediately below the melting point.[130] The α-phase is also known as a rotator,[167,176,184] high-entropy,[130] or disordered intermediate solid[168] phase and is analogous to rotator phases observed in paraffins.[131,167,173,174,175,177] The entropy of the various alcohol phases increases as follows: $S_\gamma < S_\beta < S_\alpha < S_{liquid}$.[173,174]

Literature regarding the polymorphism of 1-alcohols is not entirely clear,[168,177] but the following rules explain the general consensus of most authors. The β-phase is the thermodynamically stable, low-temperature phase for 1-dodecanol, 1-tetradecanol (TD) and odd ($C_nH_{2n+1}OH$, $n$ = odd) 1-alcohols with $n > 12$.[130,132,168,171] Odd $n$-alcohols do not display tilted low-temperature γ-phases due to energy considerations.[130,132,168,171] This odd-even γ-β phase behaviour is also observed in paraffins and can be explained by examining the packing of the end groups of the molecule (Figure 5.1).[185]
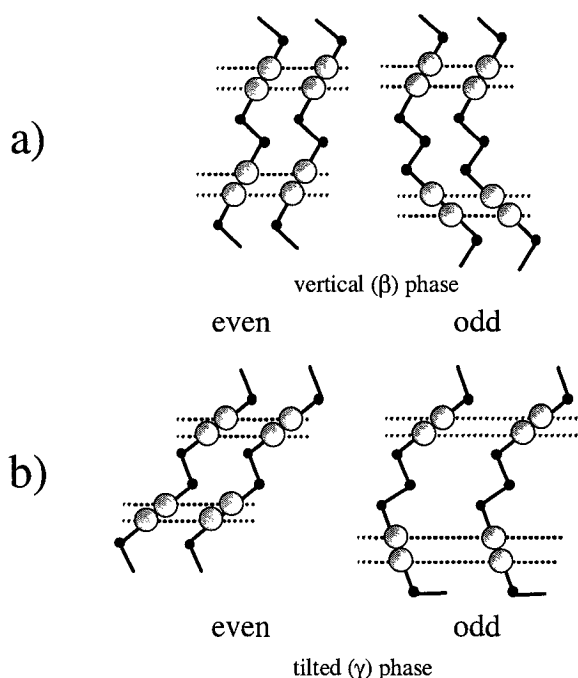
Figure 5.1. The image shows the packing of even and odd 1-alcohols in (a) vertical (α- and β- ) and (b) tilted (γ-) phases. Unfavourable packing of the end groups in tilted phases precludes the presence of γ- phases in odd 1-alcohols with $n > 14$. Grey spheres represent the end groups (in the case of alcohols these are hydroxy groups) and the black spheres represent truncated carbon chains. In vertical (β-) phases there is no significant difference between the packing distances of the end groups of odd or even alcohols. Adapted from reference 185.

In $n$ = even alcohols, the packing distances for the end groups are slightly closer in the tilted phase than in the vertical phase. In $n$ = odd alcohols, the extra carbon in the chain forces the end group into a higher energy conformation with its neighbor than in the case of the even alcohol.[185]

For even 1-higher alcohols with $n > 14$, the γ-phase is the thermodynamically stable low-temperature phase, although metastable β-phases can be observed in 1-hexadecanol (HD) and 1-octadecanol (OD).[130,168,173,174]

While end-group packing is similar for β- and γ-phases in even alcohols, the side-chain packing of the alkyl groups in the γ-phase is closer than in the vertical β-

phase.[131,172,173] As the alkyl-chain length increases, side-chain packing interactions become dominant and make the γ-phase more thermodynamically stable.[172,173] The α-phase is observed in alcohols with carbon chain lengths > 13 and gives the solid a translucent, waxy appearance compared to the opaque appearance of low-temperature solid phases.[131,167,173,174,175,177] Transition of the α-phase to a low-temperature ordered phase upon cooling requires nucleation and displays sub-cooling.[131] This sub-cooling can be enhanced by the presence of impurities and/or mixtures of other alcohols or aliphatic hydrocarbons, resulting in a dramatic increase in the apparent stability of the α-phase.[131,168186,187]

Literature concerning the structure of the α-phase is somewhat varied. Seto *et al.* proposed a monoclinic unit cell with space group *C2/m*.[188] Ventolá *et al.* also proposed a monoclinic unit cell with a structure similar to the $R_{IV}$-phase of *n*-paraffins.[171] On the other hand, Tanaka *et al.* described the structure to be hexagonal and analogous to the $R_{II}$-phase of *n*-paraffins,[173,174] while Ishikawa and Ando described its internal alkyl-chain behaviour as analogous to orthorhombic *n*-alkanes.[176]

### 5.1.2. Structures of 1-Alcohols

The structures of the β- and γ-phases of 1-higher alcohols with chain lengths between 1-tetradecanol and 1-eicosanol can be described by the crystal structures of 1-heptadecanol (Figure 5.2) and 1-octadecanol (Figure 5.3).[131,171]
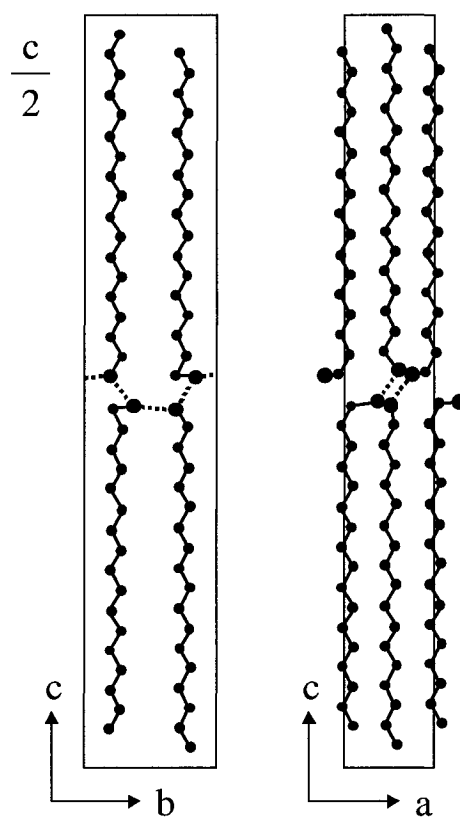
Figure 5.2. The crystal structure of the β-phase of 1-heptadecanol is representative of the β-phase of 1-alcohols between 1-dodecanol and 1-eicosanol. This phase is characterized by a head-to-head bilayer stacking arrangement with the alkyl-chains oriented nearly perpendicular to the hydroxy plane. Large and small spheres represent O and C respectively. Adapted from reference 131.
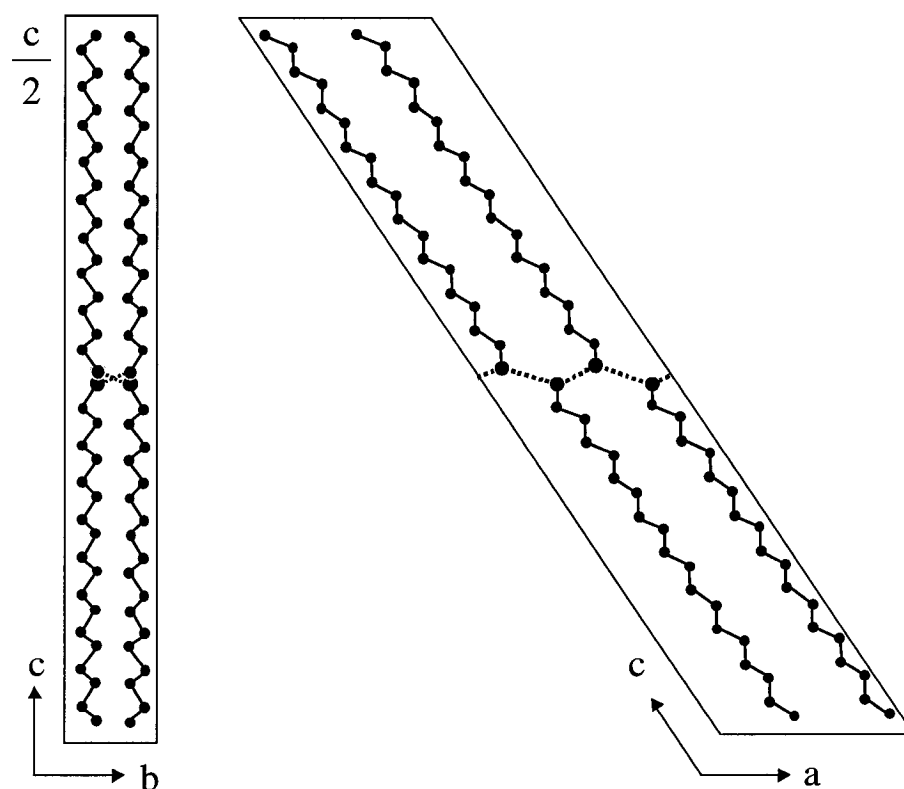
Figure 5.3. The crystal structure of the γ-phase of 1-octadecanol is representative of the γ-phase of 1-alcohols between 1-dodecanol and 1-eicosanol. This phase is characterized by a head-to-head bilayer stacking arrangement with the alkyl-chains oriented at an angle of approximately 60° to the hydroxy plane. Large and small spheres represent O and C respectively. Adapted from reference 131.

The β-phases of 1-tetradecanol, 1-hexadecanol, and 1-octadecanol are monoclinic

($P2_1/c$) with 8 molecules per unit cell and 2 molecules in an asymmetric unit cell. The

two conformers include one molecule in an all-*trans* configuration (analogous to the γ-

phase) and one molecule with an all-*trans* skeletal carbon configuration with the C-C-C-

O(H) torsion angle in a *gauche* configuration.[131,171,176] Lattice constants for the β-phases

of 1-tetradecanol, 1-hexadecanol, and 1-octadecanol are given in Table 5.1.

Table 5.1 Lattice constants for 1-alcohol β-phases adapted from references 131 and 173.

| Alcohol | $\beta_l$ | $a/Å$ | $b/Å$ | $c/Å$ |
|---|---|---|---|---|
| 1-tetradecanol | 91°23' | 5.05 | 7.37 | 39.64 |
| 1-hexadecanol | 91°21' | 5.04 | 7.38 | 44.92 |
| 1-octadecanol | 91°19' | 5.04 | 7.39 | 50.30 |

The γ-phases of 1-hexadecanol and 1-octadecanol are monoclinic ($C2/c$) with 8 molecules per unit cell.[131,171] The γ-phases are characterised by an all-*trans* configuration of the skeletal carbons of the alkyl-chain. Lattice constants for the γ-phases of 1-hexadecanol and 1-octadecanol are given in Table 5.2.

Table 5.2. Lattice constants for 1-alcohol γ-phases adapted from references 131 and 173.

| Alcohol | $\beta_l$ | $a/Å$ | $b/Å$ | $c/Å$ |
|---|---|---|---|---|
| 1-hexadecanol | 52°31' | 9.11 | 4.94 | 46.95 |
| 1-octadecanol | 52°48' | 9.10 | 4.94 | 51.85 |

Although no crystal structural data exist on the rotational phases of 1-alcohols, authors have used XRD to compare the spacing of the molecules. Table 5.3 shows that the α-phase has long spacing similar to the β-phase.

Table 5.3. Long spacing of 1-alcohol polymorphs in Å. [131,173,174]

| Alcohol | α-phase | β-phase | γ-phase |
|---|---|---|---|
| 1-tetradecanol | 38.9 | 39.6 | 33.05 |
| 1-hexadecanol | 43.83 | 44.9 | 37.27 |
| 1-octadecanol | 48.93 | 50.28 | 41.6 |

### 5.1.3. Thermodynamic Parameters of 1-Alcohols

1-tetradecanol transforms from the low-temperature $\beta$-phase to the $\alpha$-phase at 311.2 K with a transition enthalpy of 23.8 kJ mol$^{-1}$ and it can be annealed to produce $\gamma$-phase if heated at very slow rates.[130] Mosselman *et al.* produced a heating curve for 1-tetradecanol showing two arrests. At heating rates of less than 0.03 K min$^{-1}$ a $\beta$-$\gamma$ transition was observed. The enthalpy of the transition was very small (1.8 kJ mol$^{-1}$) and was overrun by the more substantial $\beta$-$\alpha$ transition at 311.2 K when heated at faster rates.[130]

Table 5.4. Thermodynamic data for the phase transitions observed in 1-tetradecanol.[130]

| $\Delta_{trs}H/(kJ\ mol^{-1})$ | T/K | Initial Phase | Final Phase |
|---|---|---|---|
| 1.8 | 306 | Crystalline, $\beta$ | Crystalline, $\gamma$ (metastable) |
| 23.8 | 311.2 | Crystalline, $\beta$ | Crystalline, $\alpha$ |
| 25.1 | 310.8 | Crystalline, $\alpha$ | Liquid |
| 47.0 | 311.2 | Crystalline, $\gamma$ (metastable) | Liquid |

The transition of the stable low-temperature phase, $\gamma$-HD, to metastable $\beta$-HD is very slow and is not observed by most authors. Similarly, only $\gamma$-$\alpha$ and $\alpha$-liquid transitions are observed in 1-octadecanol. Tables 5.5 and 5.6 show the thermodynamic parameters for the phase transitions of pure 1-hexadecanol and 1-octadecanol.

Table 5.5. Thermodynamic data for the phase transitions observed in 1-hexadecanol.[130]

| $\Delta_{trs}H/(kJ\ mol^{-1})$ | T/K | Initial Phase | Final Phase |
|---|---|---|---|
| 33.06 | 321.81 | Crystalline, $\alpha$ | Liquid |
| 21.7 | 315.8 | Crystalline, $\gamma$ | Crystalline, $\alpha$ |

Table 5.6. Thermodynamic data for the phase transitions observed in 1-octadecanol.[132]

| $\Delta_{trs}H/(kJ\ mol^{-1})$ | T/K | Initial Phase | Final Phase |
|---|---|---|---|
| 25.60 | 324.55 | Crystalline, $\gamma$ | Crystalline, $\alpha$ |
| 41.07 | 334.2 | Crystalline, $\alpha$ | Liquid |

## 5.2. Lauryl Gallate/Alcohol Interactions

The developer/solvent interactions of lauryl gallate/1-tetradecanol (abbreviated LG/TD hereafter), lauryl gallate/1-hexadecanol (abbreviated LG/HD hereafter), and lauryl gallate/1-octadecanol (abbreviated LG/OD hereafter) were examained using DSC and Raman spectroscopy. Binary phase diagrams of the three systems were determined and the phase compositions confirmed using Raman spectroscopy.

### 5.2.1. Lauryl Gallate/Alcohol Phase Diagrams

The binary phase diagrams of LG//TD are shown in Figures 5.4, 5.5, and 5.6, respectively. Scan rates of 5 K min$^{-1}$ were used and the onset temperatures of thermal events are reported. Phase diagrams were determined both on heating and cooling, and both are shown.
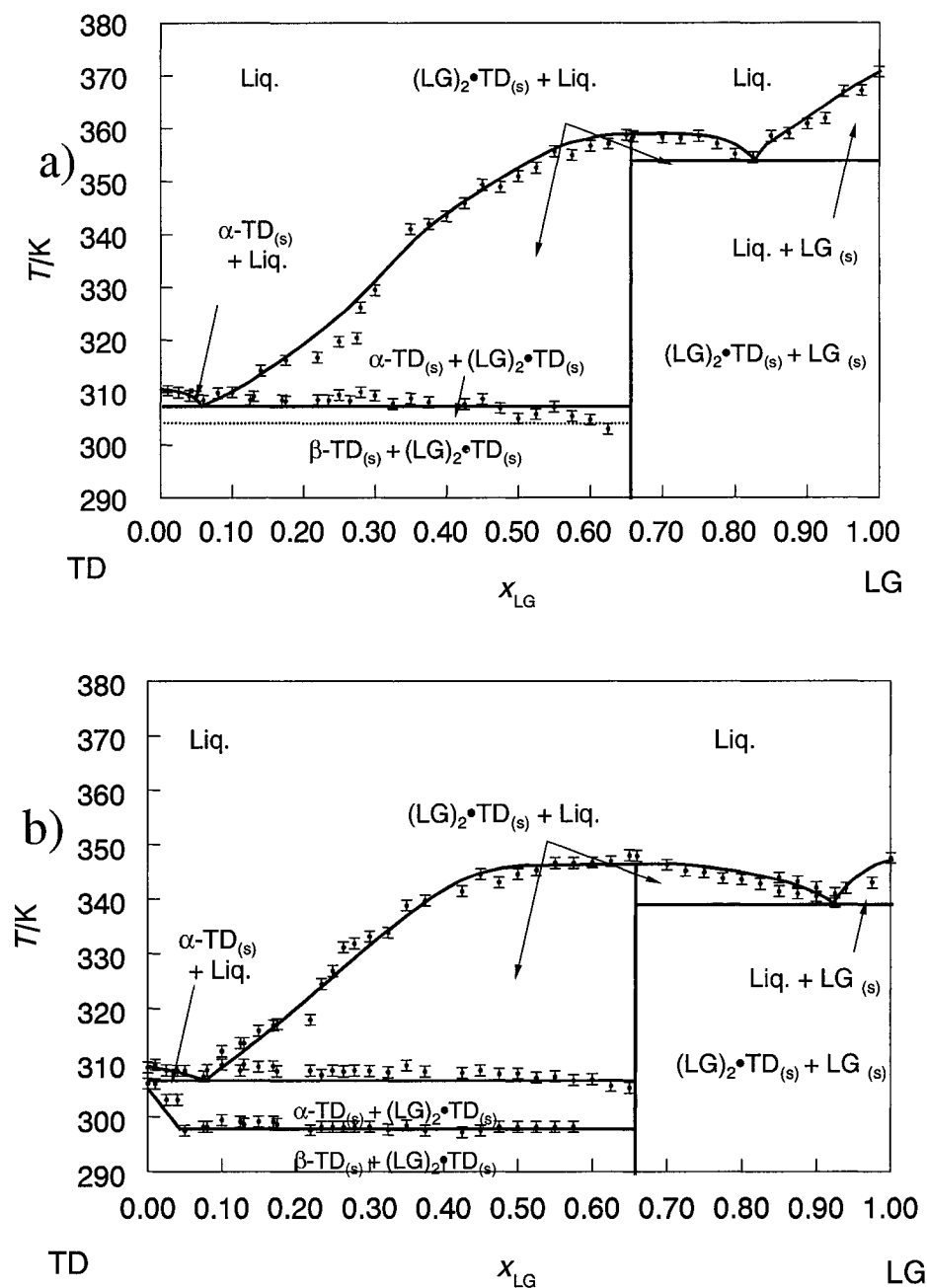
Figure 5.4. The binary lauryl gallate/1-tetradecanol (LG/TD) phase diagram measured on (a) heating and (b) cooling. The points with error bars represent measured DSC transition (onset) temperatures and uncertainties. The phase boundaries are added to aid the eye. The most prominent feature of this diagram is the formation of a complex, $(LG)_2 \bullet TD$, at $x_{LG} = 0.67$.
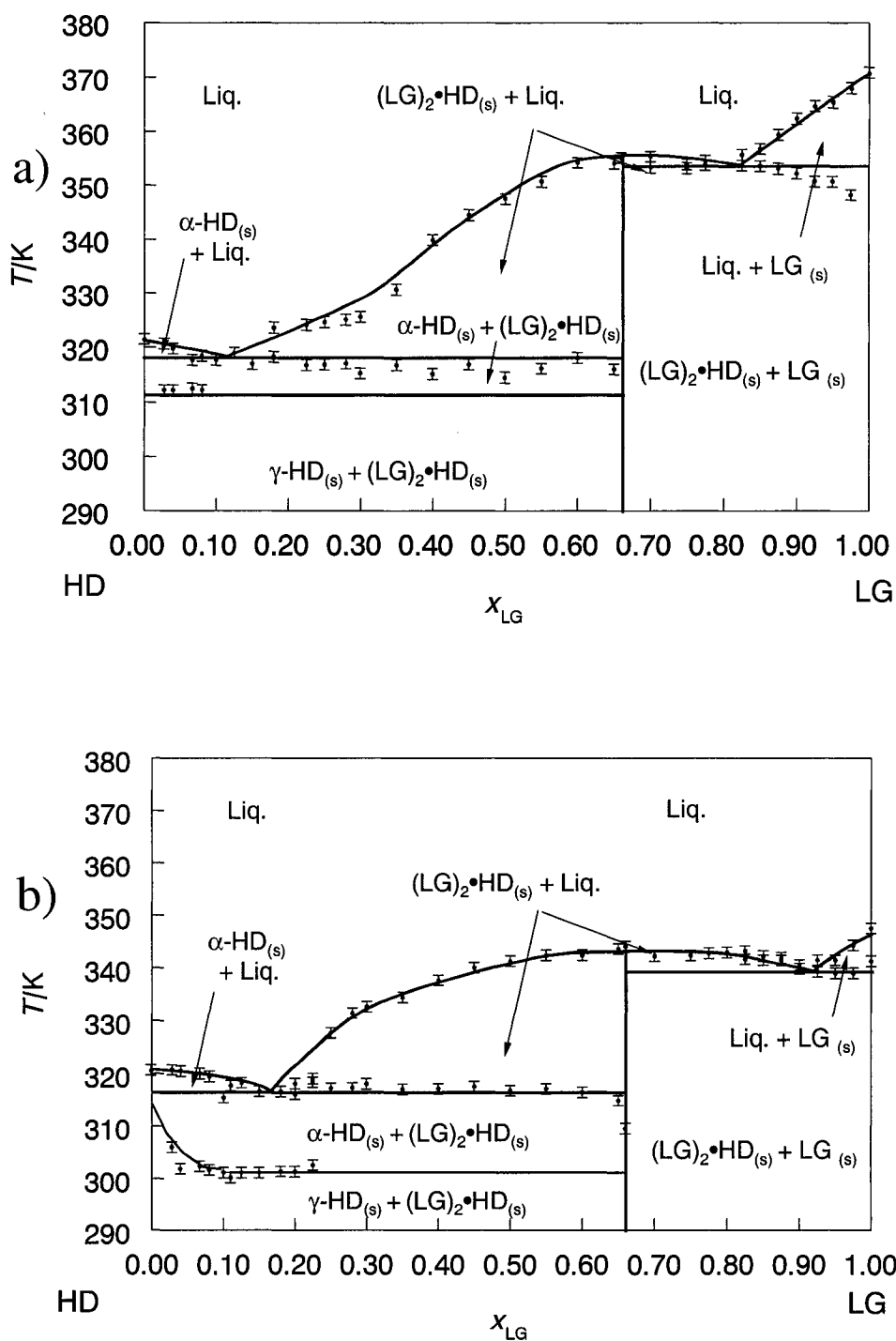
Figure 5.5. The binary lauryl gallate/1-hexadecanol (LG/HD) phase diagram measured on (a) heating and (b) cooling. The points with error bars represent measured DSC transition (onset) temperatures and uncertainties. The phase boundaries are added to aid the eye. The most prominent feature of this diagram is the formation of a complex, $(LG)_2 \cdot HD$ , at $x_{LG} = 0.67$.
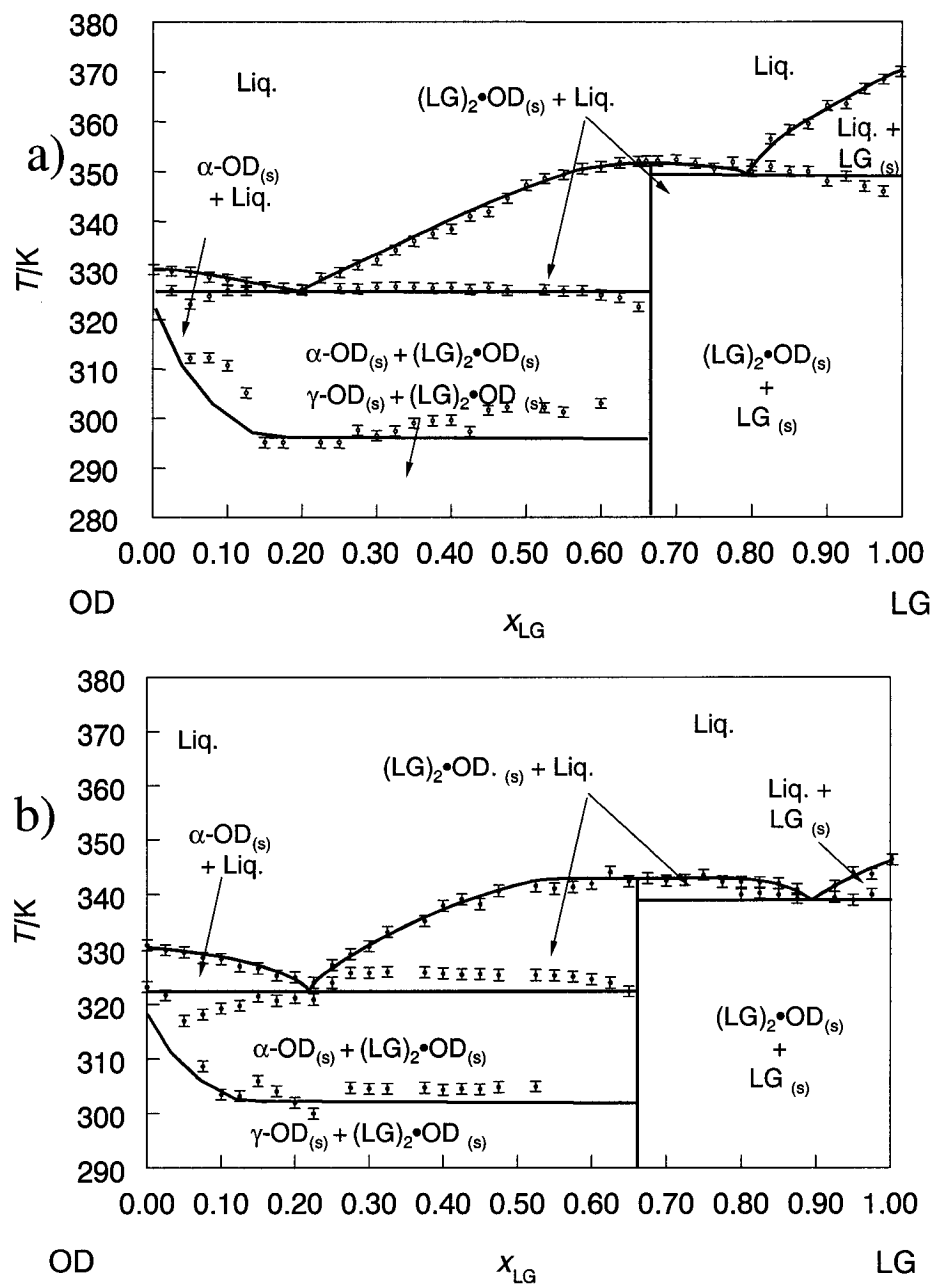
Figure 5.6. The binary lauryl gallate/1-octadecanol (LG/OD) phase diagram measured on (a) heating and (b) cooling. The points with error bars represent measured DSC transition (onset) temperatures and uncertainties. The phase boundaries are added to aid the eye. The most prominent feature of this diagram is the formation of a complex, $(LG)_2 \cdot OD$, at $x_{LG} = 0.67$.

These phase diagrams represent the solid-liquid equilibrium of immiscible solids and consist of a series of liquidus and solidus curves.[1,189-191] The liquidus curves represent the boundaries between a fully liquid composition and a (solid + liquid) composition. The solidus curves represent the boundaries between fully solid compositions and (solid + liquid) compositions. The liquidus for a pure component begins at its melting temperature and curves toward a eutectic point.[1,189-191] The eutectic point is the intersection of two liquidus curves and the solidus and represents a composition that melts completely at the eutectic temperature.[1,189-191] The eutectic point of a simple binary phase diagram is governed by the curvature of the liquidus curves that intersect. The basic curvature of a liquidus curve is governed by the ideal freezing point depression of component A by the addition of component B:[189-191]

$$\ln x_A = \frac{\Delta_{fus} H_A^o}{R} \left( \frac{1}{T_{fus,A}^o} - \frac{1}{T_{fus}^{obs}} \right), \qquad 5.1$$

where $x_A$ is the mole fraction of component A, $\Delta_{fus}H^o{}_A$ is the fusion enthalpy of pure A, $R$ is the gas constant, $T^o{}_{fus,A}$ is the fusion temperature of pure A and $T^{obs}{}_{fus}$ is the observed fusion temperature. Deviation from the ideal freezing point depression arise from either attractive or repulsive interactions between components.[189-191] The details of this will be discussed later in this thesis, but to a simple approximation, a steeper downward curvature represents an increase in attractive interaction and *vice versa*.

All three LG/alcohol phase diagrams display congruently melting compounds of the form (LG)$_2$•alcohol at $x_{LG} = 0.67$. This effectively splits the phase diagrams into two sections, an alcohol/(LG)$_2$•alcohol portion and a (LG)$_2$•alcohol /LG portion, each with its own eutectic composition. (It is important to note that this simplification is not strictly

true. The slope of the liquidus at the $(LG)_2$•alcohol composition ($x_{LG} = 0.67$) will be zero whereas the liquidus slope at the pure alcohol and LG compositions will be non-zero.)[1,192] The zero slope of the phase diagram liquidus at the compound composition shows that the congruently melting compound, $(LG)_2$•alcohol, completely dissociates into a solution of $2(LG) + 1$(alcohol) on melting.[192]

### 5.2.1.1. Presence of Rotational Phases

The distinction between the α-phases and low-temperature phases near the alcohol composition of LG/TD and LG/HD was not clear in the DSC thermograms obtained upon heating. In the case of LG/TD this is not surprising as there was only ~1 to 2 K separating the pure TD α- and β- phases upon heating (*cf.* Table 5.4). Enthalpy changes measured at $0 < x_{LG} < 0.67$ were generally consistent with the sum of the β-α and β-liquid phase transitions (~ 49 kJ mol$^{-1}$). In LG/HD the γ-α and α-liquid phase transitions were resolved between $0 < x_{LG} < 0.10$. As $x_{LG}$ increased further ($0.15 < x_{LG} < 0.67$), only one transition was observed (~315 K) with an enthalpy change consistent with the sum of the γ-α and α-liquid phase transition enthalpy changes. The two solid HD phases (α and γ) were observed in the phase diagrams obtained upon cooling from the liquid state, where significant sub-cooling of the α-γ phase transition occured. The α-γ phase transition of OD was observed in both the heating and cooling of the binary mixtures.

All three binary mixtures showed enhanced α-alcohol phase stability in the $0.15 < x_{LG} < 0.67$ range. In all systems the α-β/α-γ alcohol phase transition occurred at about 300-305 K. An interesting feature of 1-alcohols is that the presence of impurities tends to

stabilize the rotator phases in the system.[167,168,193] This behaviour is also observed in paraffins, and is particularly dramatic when alcohols of different chain lengths are mixed.[167,193] In a binary mixture of mismatched chain lengths the effective interlayer coupling of the molecules decreases and suppresses the formation of the more stable low-temperature phase.[167,168] Sirota *et al.*[167] and Al-Mamun[193] examined several binary alcohol mixtures and report significant variation in the stability range of the α-phase.

Table 5.7. The α-phase stability temperature ranges, $\Delta T_\alpha$, for selected 1-alcohols and 1-alcohol mixtures. [167,168,193]

| Sample | $\Delta T_\alpha / K$ |
|---|---|
| 1-hexadecanol | 6.06 |
| 1-heptadecanol | 11.70 |
| 1-octadecanol | 5.39 |
| 1-nonadecanol | 9.65 |
| 1:1 1-hexadecanol / 1-octadecanol | 35.0 |
| 1:1 1-hexadecanol / 1-heptadecanol | 17.0 |
| 1:1 1-octadecanol / 1-nonadecanol | 16.1 |

While onset temperatures indicated enhanced α-alcohol phase stability for the three LG/alcohol mixtures, the measured enthalpy changes showed that a significant degree of metastability exists for the α-phase in the binary mixtures below the onset temperatures observed.

Measured enthalpy changes for the α- to low-temperature phase transitions for LG/TD, LG/HD, and LG/OD are given in Tables 5.8, 5.9, and 5.10.

Table 5.8. Measured enthalpy changes of the $\alpha$-$\beta$ transition of free 1-tetradecanol observed by DSC in lauryl gallate/1-tetradecanol (LG/TD) mixtures ($\Delta_{trs}H$ = -23.8 kJ mol$^{-1}$ for pure 1-tetradecanol[130]). $\Delta_{trs}H$ is reported based on the amount of 1-tetradecanol$_{(solid)}$ present in the solid phase of composition (TD$_{(solid)}$ + (LG)$_2$•TD$_{(solid)}$).

| $x_{LG}$ | $\Delta_{trs}H/(kJ\ mol^{-1})$ |
|---|---|
| 0.01 | -13.5 ± 0.5 |
| 0.03 | -12.5 ± 0.5 |
| 0.08 | -9.9 ± 0.5 |
| 0.10 | -10.6 ± 0.5 |
| 0.15 | -14.0 ± 0.5 |

Table 5.9. Measured enthalpy changes of the $\alpha$-$\gamma$ transition of free 1-hexadecanol observed in lauryl gallate/1-hexadecanol (LG/HD) mixtures ($\Delta_{trs}H$ = -21.7 kJ mol$^{-1}$ for pure 1-hexadecanol[130]). $\Delta_{trs}H$ is reported based on the amount of 1-hexadecanol$_{(solid)}$ present in the solid phase of composition (HD$_{(solid)}$ + (LG)$_2$•HD$_{(solid)}$).

| $x_{LG}$ | $\Delta_{trs}H/(kJ\ mol^{-1})$ |
|---|---|
| 0.04 | -2.4 ± 0.5 |
| 0.08 | -0.6 ± 0.1 |
| 0.10 | -0.5 ± 0.1 |
| 0.125 | -0.4 ± 0.1 |
| 0.175 | -0.2 ± 0.1 |
| 0.20 | -0.1 ± 0.1 |

Table 5.10. Measured enthalpy changes of the α-γ transition of free 1-octadecanol observed in lauryl gallate/1-octadecanol (LG/OD) mixtures ($\Delta_{trs}H$ = -25.6 kJ mol$^{-}$ $^1$ for pure 1-octadecanol[132]). $\Delta_{trs}H$ is reported based on the amount of 1-octadecanol$_{(solid)}$ present in the solid phase of composition (OD$_{(solid)}$ + (LG)$_2$•OD$_{(solid)}$).

| $x_{LG}$ | $\Delta_{trs}H/(kJ \; mol^{-1})$ |
|---|---|
| 0.075 | -1.8 ± 0.5 |
| 0.10 | -0.8 ± 0.1 |
| 0.15 | -0.6 ± 0.1 |
| 0.175 | -0.4 ± 0.1 |
| 0.20 | -0.2 ± 0.1 |
| 0.225 | -0.1 ± 0.1 |

In all cases the observed enthalpy changes are much smaller than ideal. This is because the α-β (or α-γ) alcohol phase transitions are solid-solid transitions and take place at slower rates compared with liquid-solid and liquid-liquid transitions.[123] While the onset temperatures observed provide information on the thermodynamic stability of the α-alcohol phases, the small enthalpy changes show that the α-alcohol phase has significant kinetic stability, or metastability, at temperatures below the equilibrium α-β (or α-γ) transition temperature.

The large enthalpy changes observed in LG/TD mixtures indicate that much of the free TD in the mixture converts to the low-temperature form on the time scale of the DSC measurement (5 K min$^{-1}$) . Enthalpy changes observed in LG/HD and LG/OD mixtures are very small (0 to 2 kJ mol$^{-1}$) and indicate that very little α-γ alcohol conversion occurs

on the time scale of the DSC measurement. This indicates that while the $\alpha$-phases of HD and OD are thermodynamically unstable below 300 to 305 K they show a high degree of kinetic stability at room temperature.

### 5.2.2. Raman Spectroscopy of Lauryl Gallate/Alcohol Mixtures

Raman spectra of binary LG/alcohol mixtures in the 1800 to 800 cm$^{-1}$ region were obtained at room temperature and are shown in Figures 5.7, 5.8, and 5.9. The major feature of interest observed in all three systems is the carbonyl region, where the asymmetric $\upsilon$(C=O) frequency for pure LG is 1658 cm$^{-1}$.[140] The frequency of this mode rises to 1683 cm$^{-1}$ in all three (LG)$_2\bullet$alcohol compounds, indicating that the C=O bond strength of LG increases significantly. The planar configuration of the ester and aromatic ring necessary for effective conjugation is disrupted, *i.e.* the ester and the aromatic ring are no longer coplanar when LG interacts with the alcohol in (LG)$_2\bullet$alcohol (*cf.* Figure 4.26). Hideaki *et al.* reported that the carbonyl peak of octadecylgallate (ODG) showed a similar change in frequency ($\upsilon$(C=O) for ODG moves from 1660 to 1680 cm$^{-1}$ in the quenched mixtures shown in Figures 2.7 and 2.8) when mixed with docosylphosphonic acid (P20) in a 5:1 (P20:ODG) mole ratio.[85] The authors reported the formation of a "unique aggregate" in the ODG/P20 mixture reported, but it was metastable with respect to phase separated P20 and ODG. [85]
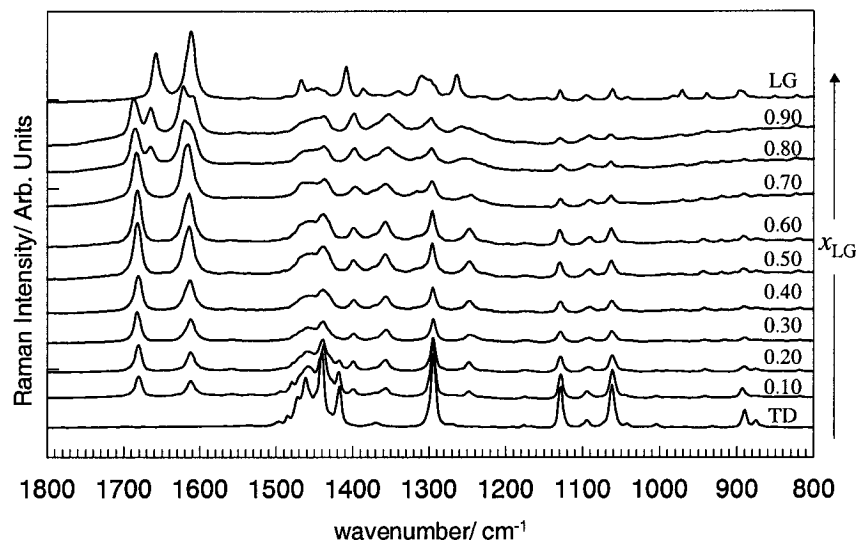
Figure 5.7. Raman spectra of lauryl gallate/1-tetradecanol (LG/TD) mixtures showing the phase distribution of the binary mixture. The most prominent feature is the presence of two asymmetric carbonyl peaks between 1700 to 1650 cm$^{-1}$ at compositions of $x_{LG}$ > 0.70. The carbonyl peak for the ester moiety moves from 1658 cm$^{-1}$ in lauryl gallate to 1683. cm$^{-1}$ in the complex. Spectral features are consistent with phase compositions of TD$_{solid}$ + (LG)$_2$•TD$_{solid}$ $x_{LG}$ < 0.67 and (LG)$_2$•TD$_{solid}$ + LG$_{solid}$ at 0.67 < $x_{LG}$ < 1.
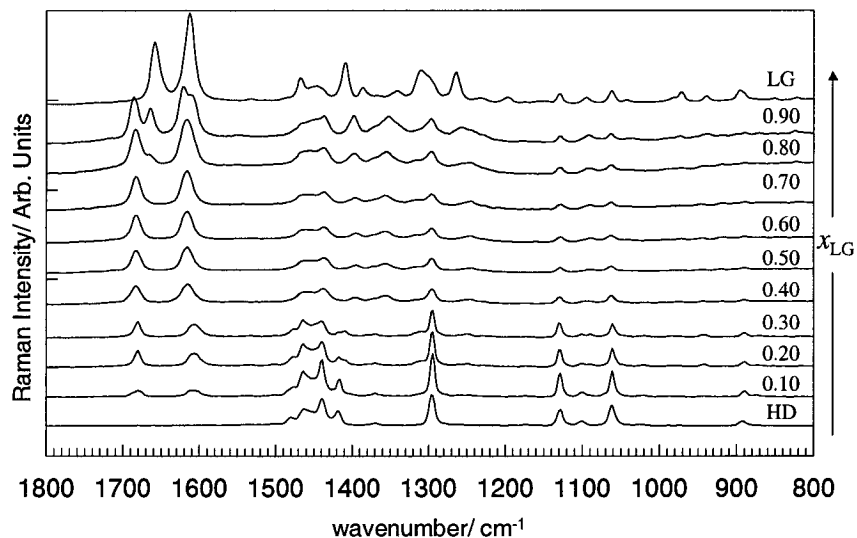
.Figure 5.8. Raman spectra of lauryl gallate/1-hexadecanol (LG/HD) mixtures showing the phase distribution of the binary mixture. The most prominent feature is the presence of two asymmetric carbonyl peaks between 1700 to 1650 cm$^{-1}$ at compositions of $x_{LG} > 0.70$. While not as prominent as in the lauryl gallate/1-tetradecanol system, the carbonyl peak for the ester moiety moves from 1658 cm$^{-1}$ in LG to 1683 cm$^{-1}$ in the complex. Spectral features are consistent with phase compositions of $HD_{solid} + (LG)_2 \cdot HD_{solid}$ for $x_{LG} < 0.67$ and $(LG)_2 \cdot HD_{solid} + LG_{solid}$ at $0.67 < x_{LG} < 1$.
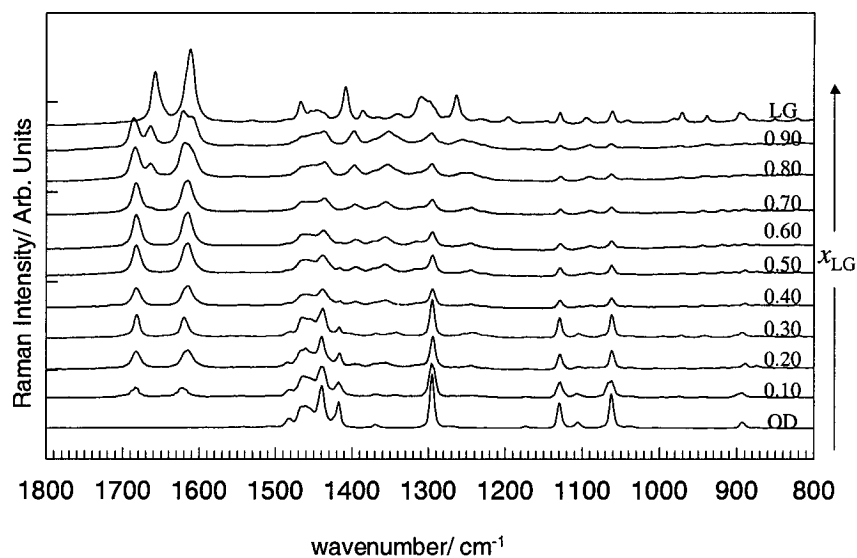
Figure 5.9. Raman spectra of lauryl gallate/1-octadecanol (LG/OD) mixtures showing the phase distribution of the binary mixture. The most prominent feature is the presence of two asymmetric carbonyl peaks between 1700 to 1650 cm$^{-1}$ at compositions of $x_{LG} > 0.70$. The carbonyl peak for the ester moiety moves from 1658 cm$^{-1}$ in lauryl gallate to 1683 cm$^{-1}$ in the complex. Spectral features are consistent with phase compositions of OD$_{solid}$ + (LG)$_2$•OD$_{solid}$ for $x_{LG} < 0.67$ and (LG)$_2$•OD$_{solid}$ + LG$_{solid}$ at $0.67 < x_{LG} < 1$.

Figure 5.10 shows Raman spectra obtained for pure LG compared to the spectra of the three (LG)$_2$•alcohol compounds and shows their structural similarity. (LG)$_2$•TD, (LG)$_2$•HD, and (LG)$_2$•OD all display asymmetric carbonyl peaks at 1683 cm$^{-1}$ that are distinct from the carbonyl peak for pure LG at 1658 cm$^{-1}$.
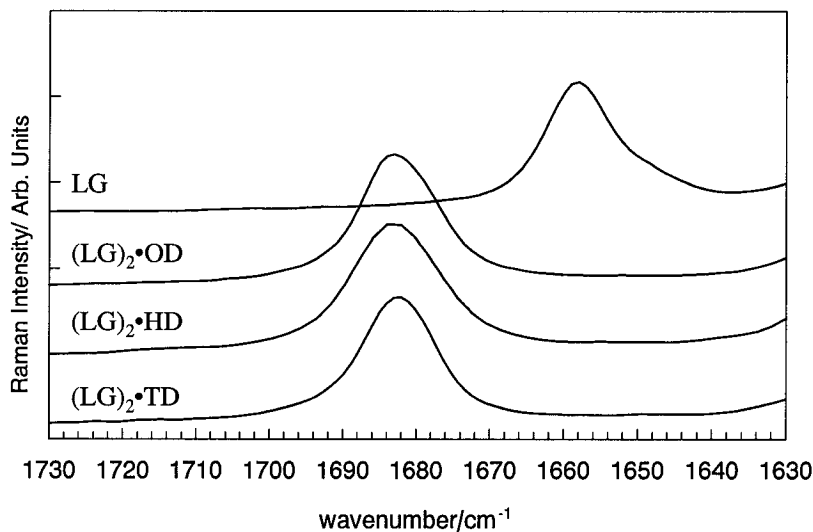
Figure 5.10. Comparison of the asymmetric carbonyl vibrations of the (LG)$_2$•alcohol compounds formed with the asymmetric carbonyl vibration of pure lauryl gallate.

Another interesting aspect of the binary LG/alcohol mixtures is a feature observed in the Raman spectrum of LG/HD and LG/OD mixtures of low $x_{LG}$ ($x_{LG} < 0.30$) when samples were measured within several minutes after cooling from the melt. Figure 5.11 and Figure 5.12 show the Raman spectra of LG/HD and LG/OD at $x_{LG} = 0.10$ obtained after 15 minutes and 24 hours after slow cooling from the melt. A peak appearing at 1710 cm$^{-1}$ is present for a long period of time following the cooling of the mixtures. LG/TD mixtures do not display the peak at 1710 cm$^{-1}$ upon slow cooling.
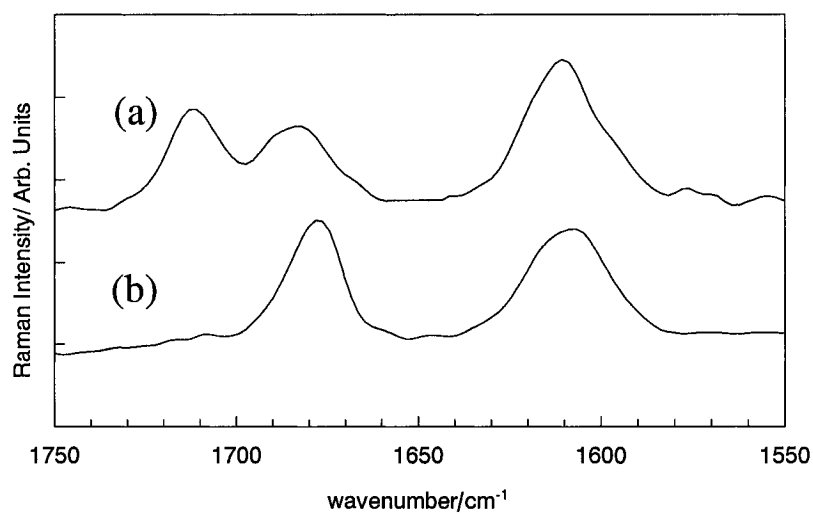
Figure 5.11. Raman spectra in the 1750 to 1550 cm$^{-1}$ region of lauryl gallate/1-hexadecanol (LG/HD, $x_{LG}$ = 0.10): (a) 15 minutes and (b) 24 hours after slow cooling from the melt.
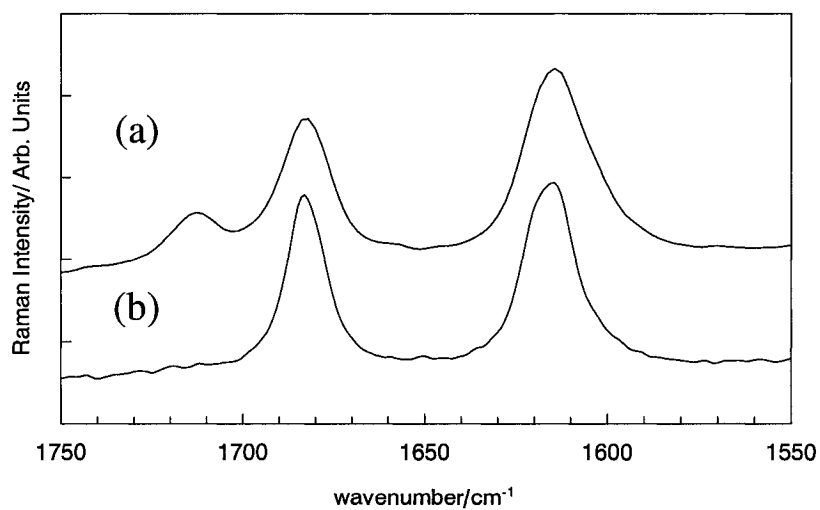


Figure 5.12. Raman spectra in the 1750 to 1550 cm$^{-1}$ region of lauryl gallate/1-octadecanol (LG/OD, $x_{LG}$ = 0.10): (a) 15 minutes and (b) 24 hours after slow cooling from the melt.

The peak at 1710 cm$^{-1}$ is in the carbonyl region and must be attributed to LG. Whether or not it is due to free LG or LG within (LG)$_2$•alcohol is not known. A reasonable explanation for this peak is the presence of $\alpha$-alcohol rotational phase within the mixtures. Binary mixtures of LG/HD and LG/OD with $x_{LG} < 0.30$ appeared waxy and translucent immediately upon cooling and gradually became white and opaque at equilibrium. This is consistent with the appearance of the pure alcohols as they transformed from their $\alpha$-phase to their low-temperature phase.

A frequency of 1710 cm$^{-1}$ represents an even greater increase in C=O bond strength than that observed for LG in (LG)$_2$•alcohol. This frequency is very close to the standard carbonyl frequency reported for a carbonyl with no aromatic interactions (1750-1715 cm$^{-1}$).[140] This peak could represent a LG structure with even greater deviation from planarity than observed in (LG)$_2$•alcohol. In principle, if the carbonyl ester group rotated until it was perpendicular to the ring plane, the effective conjugation with the phenyl ring would be nearly negligible due to the inability for the molecular orbitals to overlap.[6]

Raman spectra presented in Figure 5.11 and Figure 5.12 display convincing evidence for $\alpha$-phase metastability for LG/HD and LG/OD mixtures. Recall, the $\alpha$-$\gamma$-alcohol phase transitions in the low $x_{LG}$ regions of the LG/HD and LG/OD phase diagrams (Figures 5.5 and 5.6) occur at about 300 to 305 K and the low transition enthalpy changes observed indicate that conversion occurs slowly. These Raman data also show that the $\alpha$-$\beta$ phase transition in LG/TD mixtures occurs quickly relative to the $\alpha$-$\gamma$ phase transition of LG/HD and LG/OD mixtures at low $x_{LG}$. The significance of the

1710 cm$^{-1}$ Raman peak and its relationship to the presence of α-alcohol phases in ternary

CVL/LG/alcohol mixtures will be examined in greater detail in Chapter 6.

### 5.2.3. NMR of (LG)₂•Alcohol Compound

Attempts at understanding the structure of the (LG)₂•alcohol compounds were

thwarted by an inability to produce a crystal structure of the material. However, a

combination of spectroscopic techniques provided valuable information. Raman

spectroscopic analysis of LG/alcohol mixtures in the previous section showed virtually

identical spectra for LG/TD, LG/HD, and LG/OD mixtures. Since the phase diagrams of

all three binary mixtures show the same form, it is assumed that the interactions between

LG and alcohol that lead to (LG)₂•alcohol are essentially the same.

The CPMAS $^{13}$C NMR spectrum of LG is shown in Figure 5.13. Aromatic peak

assignments were determined through the calculation of expected peaks based on

spectroscopic tables for aromatic $^{13}$C chemical shifts[138] and confirmed by comparison to

$^{13}$C NMR spectra of octyl gallate (OG), and octadecylgallate (ODG) obtained from the

Integrated Spectral Database for Organic Compounds (SDBS).[194,195]
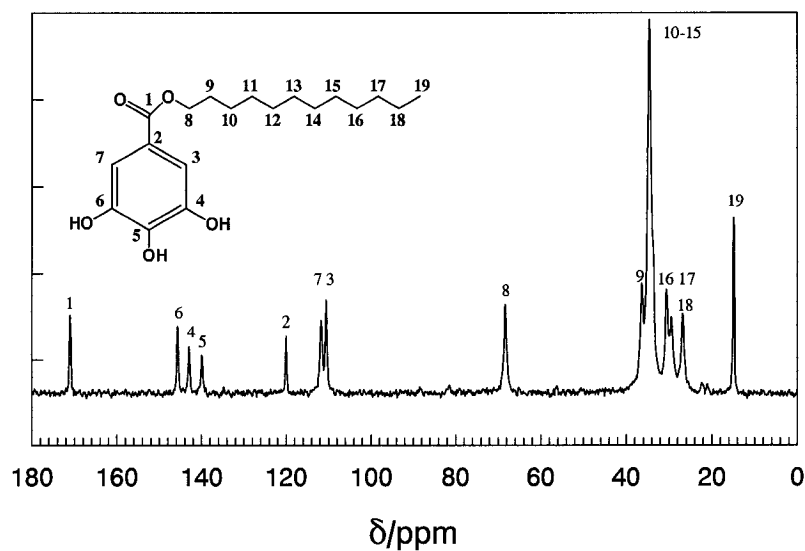
Figure 5.13. $^{13}$C CPMAS NMR spectrum of lauryl gallate (LG), obtained here.

The CPMAS $^{13}$C NMR spectrum of OD is shown in Figure 5.14. Peak assignments are based on those of Ishikawa and Ando.[176] The most prominent feature in the spectrum is the pair of peaks at 62 to 63 ppm due to the $\alpha$-carbon of the OD alkyl-chain. This feature is assigned to an alternating *gauche/trans* configuration of the hydroxy groups as they hydrogen bond in pure γ-OD (Figure 5.15).[176] Since OD has no NMR peaks above 65 ppm, the 180 to 70 ppm region was free to examine changes in the aromatic and carbonyl chemical shifts of LG in (LG)$_2$•OD.
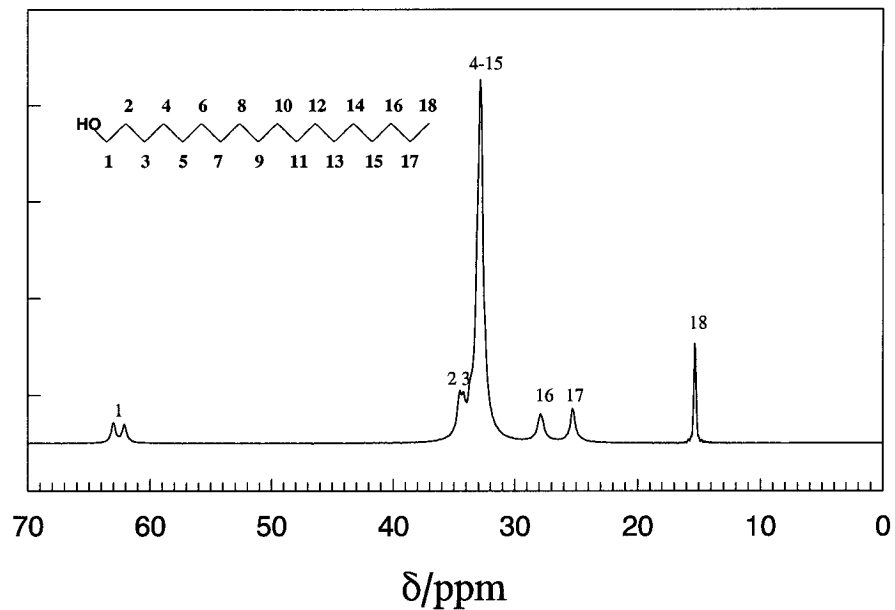
Figure 5.14. $^{13}$C CPMAS NMR spectrum of 1-octadecanol (OD), obtained here. The $\alpha$-carbon (C$_1$) is characterized by a pair of peaks (62-63 ppm) that represent H-atom environments for hydroxy groups in arrangements *gauche* and *trans* to the alkyl-chain.
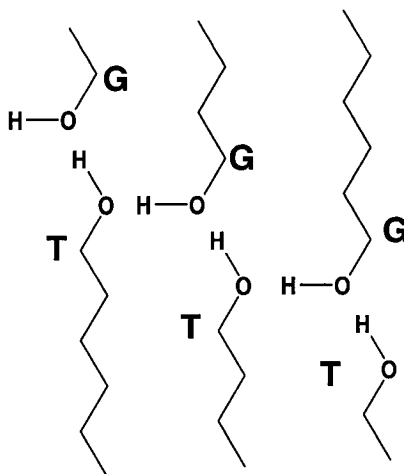


Figure 5.15. The $\alpha$-carbons of octadecanol are configured in *gauche* (G) and *trans* (T) configurations in the alternating layers of the structure. This alternation is necessary to achieve optimal configuration of the hydroxy groups for H-bonding. Adapted from reference 176.
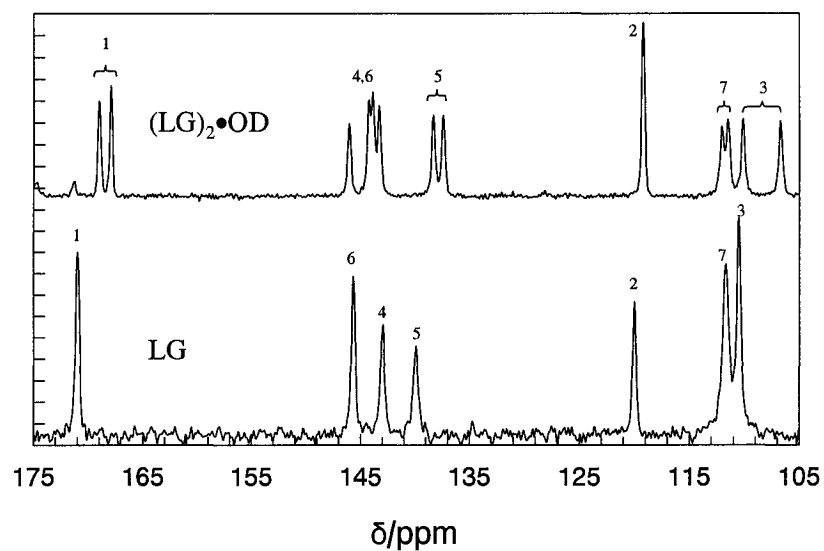
Figure 5.16. $^{13}$C CPMAS NMR spectra of lauryl gallate and (LG)$_2$•OD showing the aromatic region. (LG)$_2$•OD peaks appear to split and are consistent with the presence of two chemical environments. See Figure 5.13 for carbon atom assignments.

$^{13}$C NMR data for LG and (LG)$_2$•OD in the 180 to 100 ppm region are listed in Table 5.11.

Table 5.11. $^{13}$C CPMAS NMR data for the aromatic and carbonyl peaks of lauryl gallate and (LG)$_2$•OD in the 180 to 100 ppm region. See Figure 5.13 for carbon atom assignments. Assignments for (LG)$_2$•OD are tentative.

| C# | δ LG/ppm | δ(LG)$_2$•OD /ppm | Δδ/ppm |
|----|----------|-------------------|--------|
| 1 | 171.0 | 168.9, 167.8 | -2.1, -3.2 |
| 2 | 120.0 | 119.0 | -1.0 |
| 3 | 110.5 | 110.0, 106.5 | -0.5, -4.0 |
| 5 | 139.9 | 138.2, 137.3 | -1.7, -2.6 |
| 7 | 111.7 | 111.9, 111.3 | +0.2, -0.4 |

The carbonyl carbon (1) shifts upfield and splits to 168.9 and 167.8 ppm. The *ipso*

(to the ester) carbon (2) shows a slight upfield shift to 119.0 ppm and is the only aromatic

peak that does not split. The *para* carbon (5) appears to split and move upfield to 138.2

and 137.3 ppm. *Ortho* carbons (3,7) also show splitting and upfield shifts; 110.0 and

106.5 ppm for (3) and 111.9 and 111.3 ppm for (7). The *meta* carbons (4,6) form a

complicated group of peaks in the 146 to 143 ppm region. The presence of four peaks is

consistent with each *meta* carbon splitting into two pairs. The six possible assignments

for carbons 4 and 6 for the four peaks are shown in Table 5.12.

Table 5.12. Summary of the six possible assignments of the *meta* lauryl gallate carbons (4,6) in $(LG)_2 \cdot OD$.

| $C_4$ /ppm | $C_4$ /ppm | Shift (Relative to pure LG) | Splitting /ppm | $C_6$ /ppm | $C_6$ /ppm | Shift (Relative to pure LG) | Splitting /ppm |
|---|---|---|---|---|---|---|---|
| 143.7 | 143.1 | (↑,↑) | 0.6 | 145.9 | 144.0 | (↑,↓) | 1.8 |
| 144.0 | 143.1 | (↑,↑) | 0.9 | 145.9 | 143.7 | (↑,↓) | 2.2 |
| 144.0 | 143.7 | (↑,↑) | 0.4 | 145.9 | 143.1 | (↑,↓) | 2.8 |
| 145.9 | 143.1 | (↑,↑) | 2.8 | 144.0 | 143.7 | (↓,↓) | 0.3 |
| 145.9 | 143.7 | (↑,↑) | 2.2 | 144.0 | 143.1 | (↓,↓) | 0.9 |
| 145.9 | 144.0 | (↑,↑) | 1.8 | 143.1 | 143.7 | (↓,↓) | 0.6 |

These tentative assignments show possible peak splitting of 0.4 to 2.8 ppm for

carbons (4) and (6). In all six assignments one *meta* carbon has a splitting at least 2 times

(and as great as 7.5 times) the other. Carbon (4) experiences a downfield shift, consistent

with a decrease in electronic density in all assignments while, in general, the assignments

for carbon (6) show upfield shifts consistent with an increase in electron density.

Raman spectroscopy of (LG)$_2$•alcohol compounds shows an increase in carbonyl bond strength due to a decrease in conjugation between the ester and aromatic ring. The resonance structures of the phenolic esters (Figure 4.26) show that a decrease in conjugation results in strengthening of the C=O bond and a decrease in the double bond character of the ester carbon (1) and *ipso* carbon (2). Conjugation loss also results in a decrease in net positive charge (*i.e.* increase in negative charge) on carbons in positions *ortho* and *para* to the ester (3, 5, 7).

Although the exact interaction between OD and LG in (LG)$_2$•OD is not known, it is reasonable to assume that the complex involves hydrogen bonding between the phenolic hydroxy groups of LG and the comparatively basic OD hydroxy group. The effect of a weak base interacting with a phenol was examined by Nakashima and Maciel.[196] As the pH of a phenolic mixture was increased the chemical shifts of carbons *ipso* and *ortho* the phenol group moved upfield, *meta* carbons remained unchanged and the *para* carbon shift moved downfield.[196] If a phenolic group in LG acts as an H-bond donor, these shift changes could be observed. This phenomenon might explain some of the possible upfield shifts of the *meta* carbons. However, the combination of H-bonding and ester conjugation loss due to ring tilting make the *meta* carbons difficult to assign conclusively.

The 80 to 50 ppm regions of the $^{13}$C NMR spectra of LG, OD, and (LG)$_2$•OD are compared in Figure 5.17, where two peaks are observed corresponding to $\alpha$-carbon shifts of OD in (LG)$_2$•OD. The peak with the largest intensity is assigned as that of the $\alpha$-carbon of LG and the smaller peak is assigned to the $\alpha$-carbon of OD in the (LG)$_2$•OD compound. The change in the $\alpha$-carbon NMR signals on complexation is of particular

interest. First, in (LG)$_2$•OD the alcohol $\alpha$-carbon is no longer split (Figure 5.15), indicating that the even distribution of *gauche/trans* conformers observed in pure OD no longer exists. The $\alpha$-carbon of OD in (LG)$_2$•OD is in only one environment and is consistent with the alcohol interacting with a species other than itself in a unique manner. Second, values of $\Delta\delta$ for the OD and LG $\alpha$-carbons in (LG)$_2$•OD are substantial.
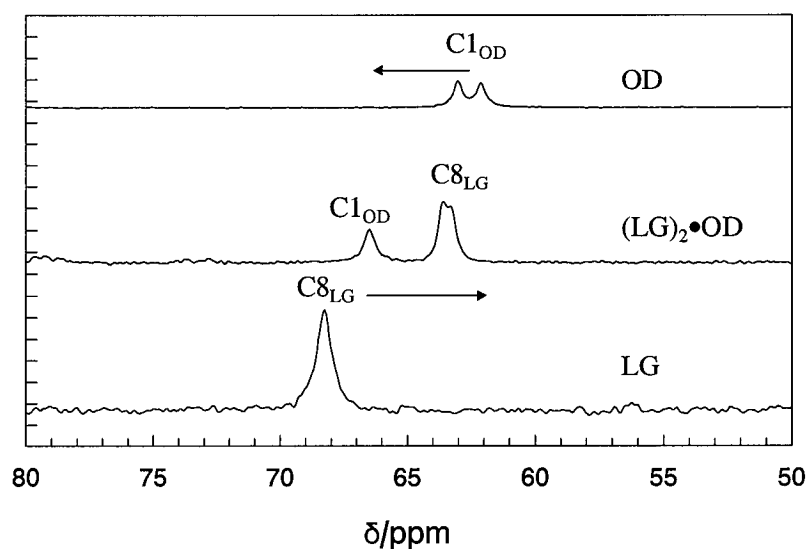


Figure 5.17. $^{13}$C CPMAS NMR spectra of lauryl gallate, 1-octadecanol, and (LG)$_2$•OD showing the $\alpha$-carbon region. 1-octadecanol in (LG)$_2$•OD appears as a single peak at 66.35 ppm indicating that the gauche/trans hydroxy configuration (Figure 5.15) has been disrupted. The peak of lauryl gallate in (LG)$_2$•OD appears to split slightly and is consistent with the presence of two chemical environments. The larger change in chemical shift, $\Delta\delta$, of lauryl gallate relative to 1-octadecanol in (LG)$_2$•OD is consistent with hydrogen bonding between the 1-octadecanol hydroxy and the lauryl gallate ester oxygen. See Figures 5.13 and 5.14 for carbon atom assignments.

Table 5.13. $^{13}C$ CPMAS NMR data of the $\alpha$-carbon peaks of LG, 1-octadecanol and $(LG)_2 \bullet OD$. See Figures 5.13 and 5.14 for carbon atom assignments.

| *Peak* | *δ/ppm* |
|---|---|
| $C1_{OD}$ | 62.6 |
| $C1_{OD}$ in $(LG)_2 \bullet OD$ | 66.4 |
| $\Delta\delta$ ( $C1_{OD}$ ) | +3.8 |
| $C8_{LG}$ | 68.3 |
| $C8_{LG}$ in $(LG)_2 \bullet OD$ | 63.4 |
| $\Delta\delta$ ( $C8_{LG}$ ) | -4.9 |

When LG and OD combine to form $(LG)_2 \bullet OD$, the OD $\alpha$-carbon shift moves downfield 3.8 ppm and the LG $\alpha$-carbon chemical shift moves upfield by almost 5 ppm. This is correlated with a significant increase in the electron density about the LG $\alpha$-carbon and a corresponding decrease in the electron density of the OD $\alpha$-carbon. This could be due to the formation of hydrogen bond between the OD hydroxy group and the ester oxygen adjacent the $\alpha$-carbon of LG. The ester oxygen, as the H-bond acceptor, has a partial negative charge. This increase in electron density would account for the dramatic (-4.9 ppm) change in the LG $\alpha$-carbon shift. The OD oxygen loses electron density to the H-bond resulting in a deshielding of its $\alpha$-carbon (+3.8 ppm). The LG $\alpha$-carbon shift shows some very slight splitting, indicating that the electronic environment of the LG $\alpha$-carbon, and consequently the H-bonding of the ester oxygen, is similar for the two LG molecules interacting with OD in $(LG)_2 \bullet OD$.

If it is assumed that LG packs in a manner similar to OG (Figure 4.8), a head-to-head stacking of the phenyl rings occurs in the LG crystal. Between each successive

head-to-head stacking unit (*cf.* the origin in the unit cell of OG in Figure 4.8) there are ten oxygen atoms present (six phenolic groups, two carbonyl oxygens, and two ester oxygens) where two LG molecules could form a complex network of H-bonds with an alcohol molecule. The two environments observed in the NMR data are probably due to slightly different H-bond environments for the two rings.

To summarize, the present NMR data show that two environments for the LG aromatic ring are observed in $(LG)_2 \cdot OD$ and the ring tilt predicted by the Raman data is confirmed. The alcohol hydroxy groups, phenolic hydroxy groups, and the ester oxygen contribute to extensive H-bonding in the compound. Finally, only one environment is observed for OD hydroxy orientation in $(LG)_2 \cdot OD$, compared to the two observed in pure OD.

### 5.3. Propyl Gallate/Alcohol Interactions

The developer/solvent interactions of propyl gallate/1-tetradecanol (abbreviated PG/TD hereafter), propyl gallate/1-hexadecanol (abbreviated PG/HD hereafter), and propyl gallate/1-octadecanol (abbreviated PG/OD hereafter) were examained using DSC and Raman spectroscopy. Binary phase diagrams of the three systems were determined and the phase compositions confirmed using Raman spectroscopy.

### 5.3.1. Propyl Gallate/Alcohol Phase Diagrams

The binary phase diagrams obtained upon heating of PG/TD, PG/HD, and PG/OD mixtures are shown in Figures 5.18, 5.19, and 5.20, respectively.
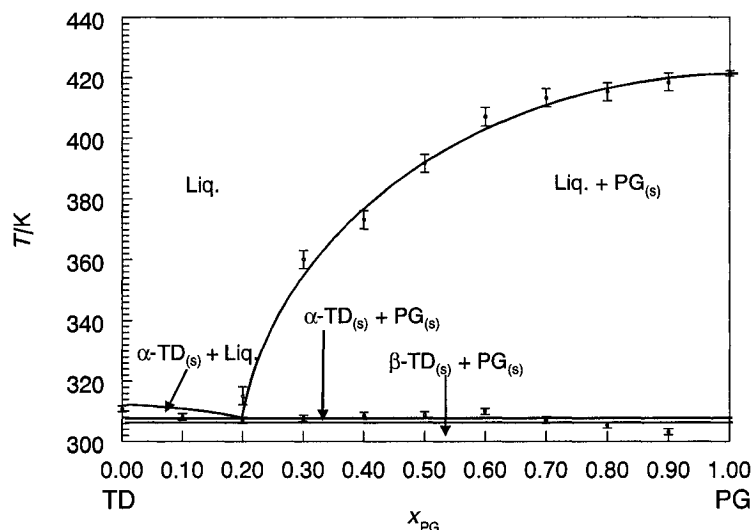
Figure 5.18. The binary propyl gallate/1-tetradecanol (PG/TD) phase diagram. The points with error bars represent measured DSC transition (onset) temperatures and uncertainties. The phase boundaries are added to aid the eye. This system is characterized by a single eutectic at $x_{PG} = 0.20 \pm 0.05$, $308 \pm 1$ K.
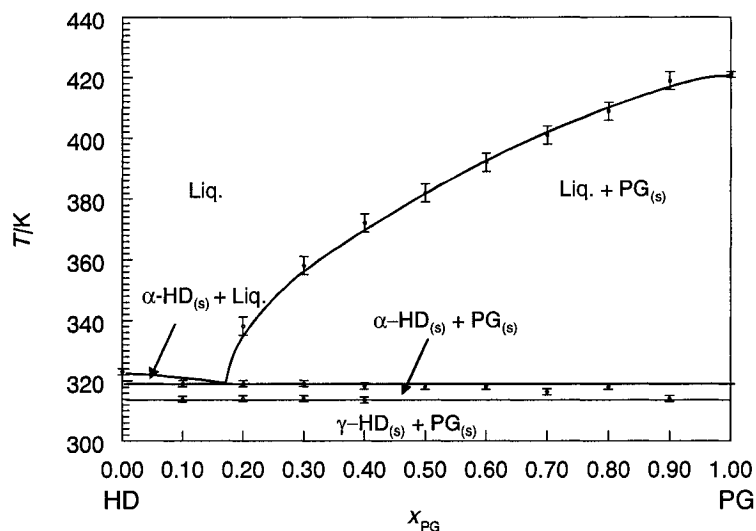


Figure 5.19. The binary propyl gallate/1-hexadecanol (PG/HD) phase diagram. The points with error bars represent measured DSC transition (onset) temperatures and uncertainties. The phase boundaries are added to aid the eye. This system is characterized by a single eutectic at $x_{PG} = 0.15 \pm 0.05$, $318 \pm 1$ K.
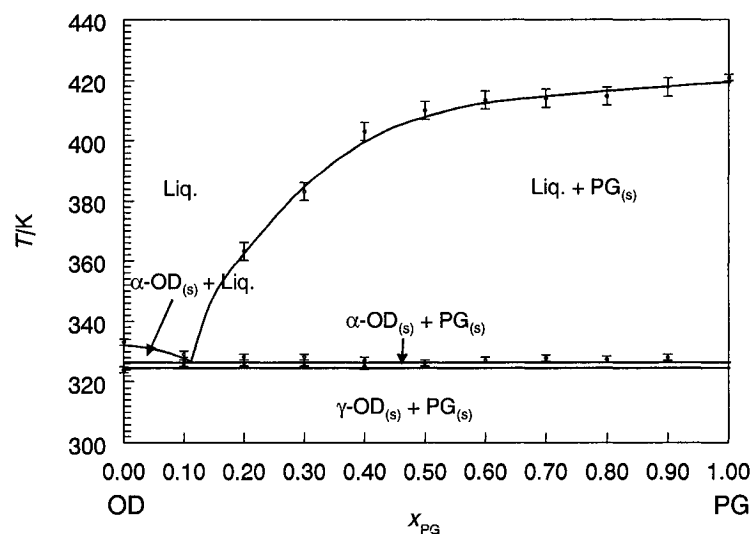
Figure 5.20. The binary propyl gallate/1-octadecanol (PG/OD) phase diagram. The points with error bars represent measured DSC transition (onset) temperatures and uncertainties. The phase boundaries are added to aid the eye. This system is characterized by a single eutectic at $x_{PG} = 0.10 \pm 0.05$, $328 \pm 1$ K.

In contrast with the LG/alcohol mixtures, PG/alcohol mixtures are simple eutectics with no compound formation between the components. Eutectic data are presented in Table 5.14.

Table 5.14. Eutectic compositions for propyl gallate/alcohol mixtures.

| Mixture | Eutectic Composition/$x_{PG}$ | Eutectic Temperature/K |
|---------|------------------------------|------------------------|
| PG/TD | $0.20 \pm 0.05$ | $308 \pm 1$ |
| PG/HD | $0.15 \pm 0.05$ | $318 \pm 1$ |
| PG/OD | $0.10 \pm 0.05$ | $328 \pm 1$ |

Eutectic compositions fall in the $0.10 < x_{PG} < 0.20$ region of the phase diagrams and become richer in alcohol as the alkyl-chain length of the alcohol increases. The eutectic temperatures range from 308 to 328 K and are consistent with the melting temperatures of the pure alcohol components.

PG/alcohol mixtures do not show the increased alcohol $\alpha$-phase stability as observed in LG/alcohol mixtures. The $\beta$-$\alpha$ and $\gamma$-$\alpha$ phase transitions for PG/alcohol were observed in temperature ranges comparable with those observed in the pure alcohol phases.[130,132]

### 5.3.2. Raman Spectroscopy of Propyl Gallate/Alcohol Mixtures

Raman spectra of PG/alcohol mixtures in the 1800 to 800 cm$^{-1}$ region were obtained at room temperature and are shown in Figures 5.21, 5.22, and 5.23. As $x_{PG}$ increases, the pure alcohol peaks decrease and pure PG peaks increase in intensity without the formation of any secondary compounds. This is most apparent in the 1800 to 1600 cm$^{-1}$ region where the asymmetric carbonyl vibration for pure PG at 1685 cm$^{-1}$ remains unchanged at all compositions.
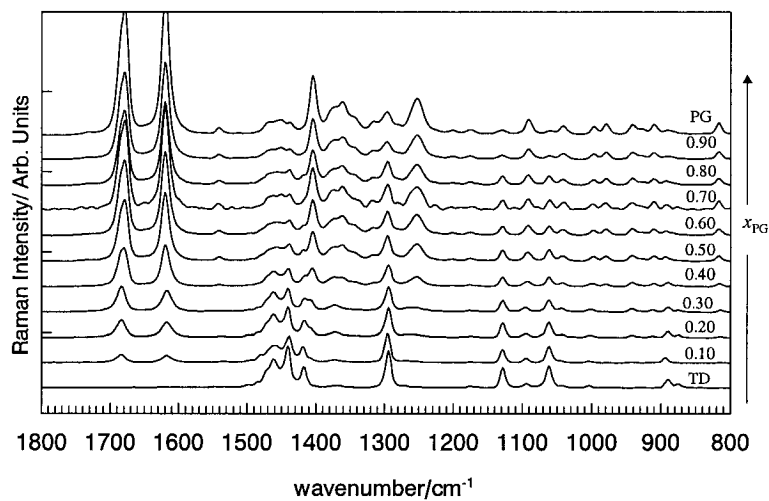
Figure 5.21. Raman spectra of propyl gallate/1-tetradecanol (PG/TD) mixtures showing phase composition. Spectral features are consistent with an assignment of a heterogeneous mixture of $TD_{solid} + PG_{solid}$ for all compositions.
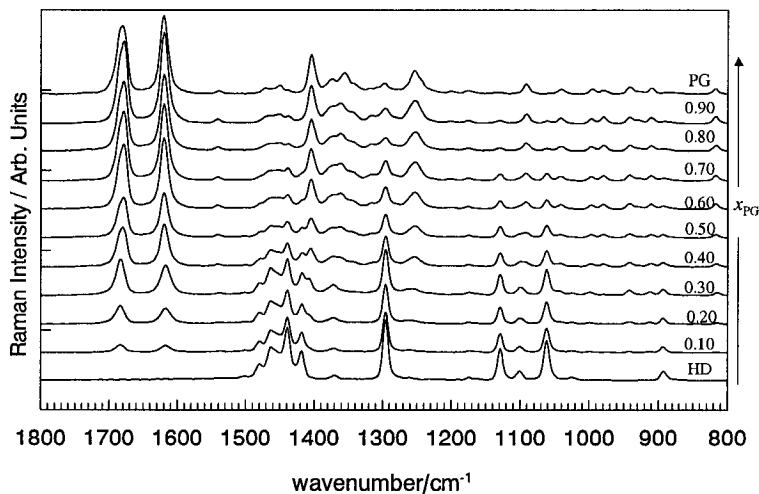


Figure 5.22. Raman spectra of propyl gallate/1-hexadecanol (PG/HD) mixtures showing phase composition. Spectral features are consistent with an assignment of a heterogeneous mixture of $HD_{solid} + PG_{solid}$ for all compositions.
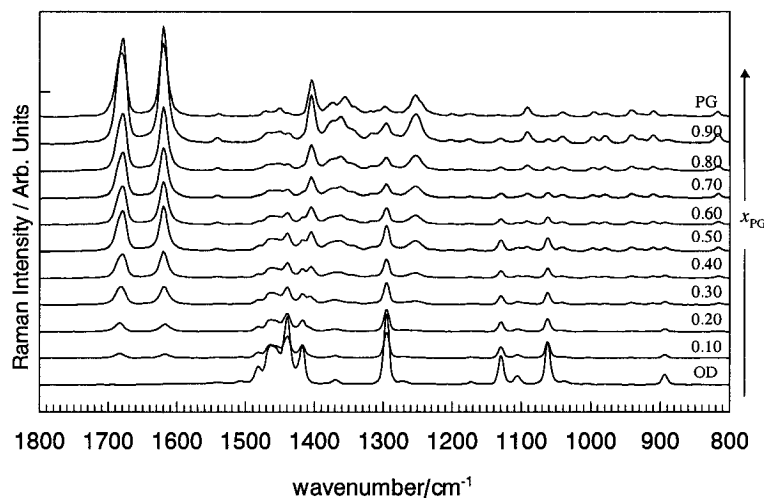
Figure 5.23. Raman spectra of propyl gallate/1-octadecanol (PG/OD) mixtures showing phase composition. Spectral features are consistent with an assignment of a heterogeneous mixture of $OD_{solid} + PG_{solid}$ for all compositions.

## 5.4. Octyl Gallate/Alcohol Interactions

The developer/solvent interactions of octyl gallate/1-tetradecanol (abbreviated OG/TD hereafter), octyl gallate/1-hexadecanol (abbreviated OG/HD hereafter), and octyl gallate/1-octadecanol (abbreviated OG/OD hereafter) were examained using DSC and Raman spectroscopy. Binary phase diagrams of the three systems were determined and the phase compositions confirmed using Raman spectroscopy.

### 5.4.1. Octyl Gallate/Alcohol Phase Diagrams

The phase diagrams obtained upon heating of OG/TD, OG/HD, and OG/OD mixtures are shown in Figures 5.24, 5.25, and 5.26, respectively.
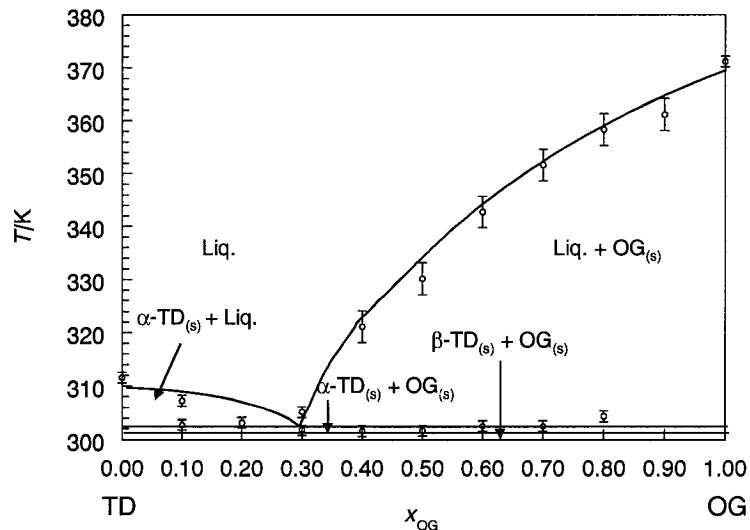
Figure 5.24. The binary octyl gallate/1-tetradecanol (OG/TD) phase diagram. The points with error bars represent measured DSC transition (onset) temperatures on heating and uncertainties. Phase boundaries are added to aid the eye. This system is characterized on heating by a single eutectic at $x_{OG} = 0.20 \pm 0.05$, $302 \pm 1$ K.
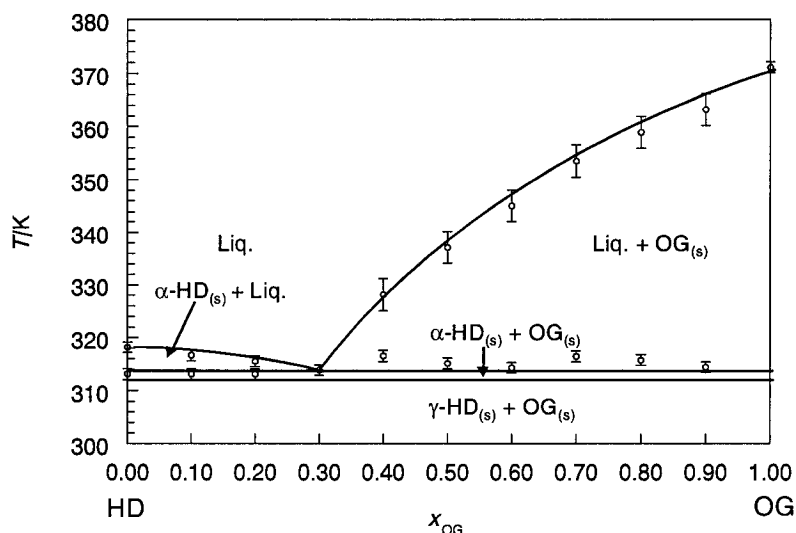


Figure 5.25. The binary octyl gallate/1-hexadecanol (OG/HD) phase diagram. The points with error bars represent measured DSC transition (onset) temperatures on heating and uncertainties. Phase boundaries are added to aid the eye. This system is characterized on heating by a single eutectic at $x_{OG} = 0.25 \pm 0.05$, $315 \pm 1$ K.
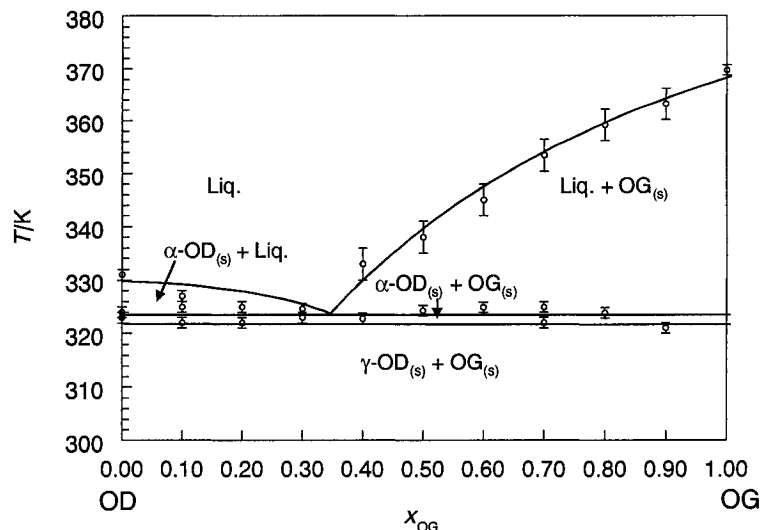
Figure 5.26. The binary octyl gallate/1-octadecanol (OG/OD) phase diagram. The points with error bars represent measured DSC transition (onset) temperatures on heating and uncertainties. Phase boundaries are added to aid the eye. This system is characterized on heating by a single eutectic at $x_{OG} = 0.30 \pm 0.05$, $324 \pm 1$ K.

OG/alcohol mixtures form simple eutectic mixtures with no compound formation between the components. Eutectic data are given in Table 5.15. The eutectic compositions fall in the $0.20 < x_{PG} < 0.30$ region of the phase diagrams and do not correlate with the alcohol component in the same way as observed in PG/alcohol mixtures.

Table 5.15. Eutectic compositions for octyl gallate/alcohol mixtures.

| Mixture | Eutectic Composition/$x_{PG}$ | Eutectic Temperature/K |
|---------|-------------------------------|------------------------|
| OG/TD   | $0.20 \pm 0.05$               | $302 \pm 1$            |
| OG/HD   | $0.25 \pm 0.05$               | $315 \pm 1$            |
| OG/OD   | $0.30 \pm 0.05$               | $324 \pm 1$            |

OG/alcohol mixtures do not show the increased $\alpha$-phase stability observed in LG/alcohol mixtures. The $\beta$-$\alpha$ and $\gamma$-$\alpha$ phase transitions occur close to the temperatures observed in the pure alcohol phases.[130,132]

### 5.4.2. Raman Spectroscopy of Octyl Gallate/Alcohol Mixtures

Raman spectra of OG/alcohol mixtures in the 1800 to 800 $cm^{-1}$ region were obtained at room temperature are shown in Figure 5.27, Figure 5.28, and Figure 5.29.
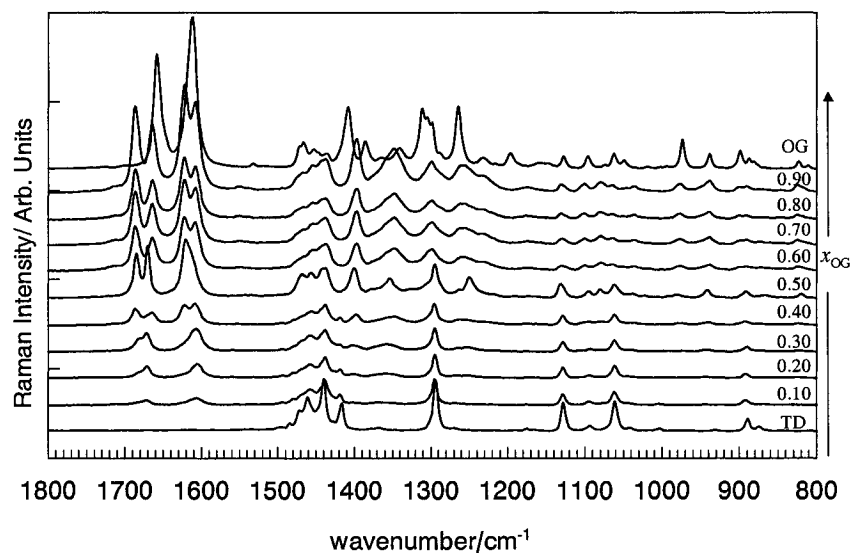


Figure 5.27. Raman spectra of octyl gallate/1-tetradecanol (OG/TD) mixtures showing phase composition. Two sets of asymmetric carbonyl peaks are observed at all compositions indicating that, although compound formation does not occur, a stronger interaction (relative to PG/TD mixtures) appears to take place between 1-tetradecanol and octyl gallate. Spectral features are consistent with an assignment of heterogeneous mixtures of $TD_{solid}$ + $OG_{solid}$ for all compositions.
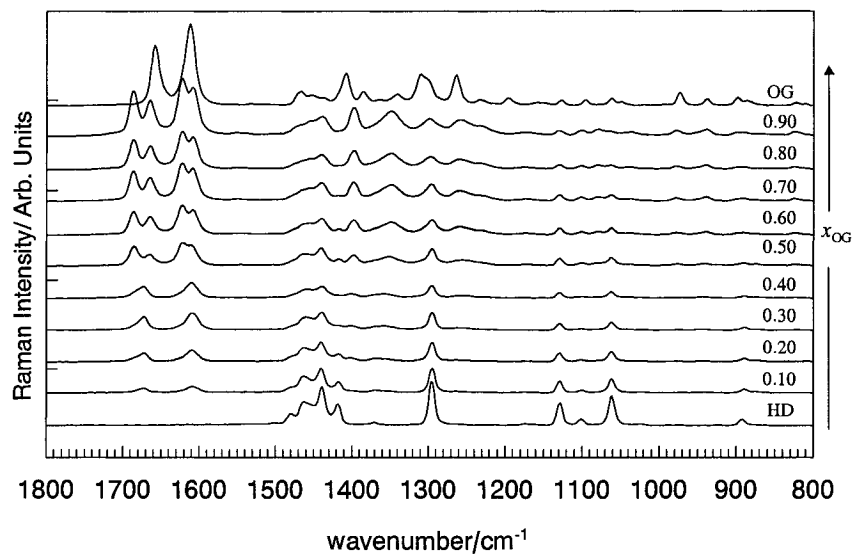
Figure 5.28. Raman spectra of octyl gallate/1-hexadecanol (OG/HD) mixtures showing phase composition. Two sets of asymmetric carbonyl peaks are observed at all compositions indicating that, although compound formation does not occur, a stronger interaction (relative to PG/HD mixtures) appears to take place between 1-hexadecanol and octyl gallate. Spectral features are consistent with an assignment of heterogeneous mixtures of $HD_{solid} + OG_{solid}$ for all compositions.
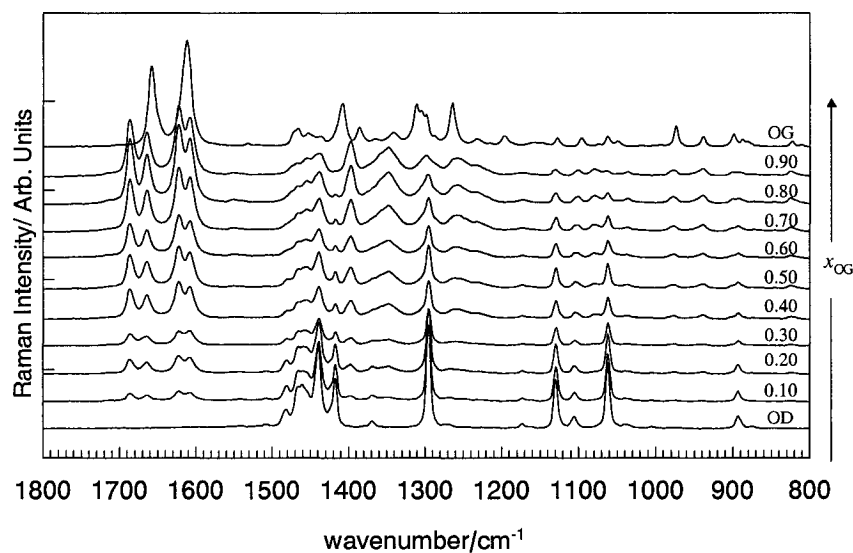
Figure 5.29. Raman spectra of octyl gallate/1-octadecanol (OG/OD) mixtures showing phase composition. Two sets of asymmetric carbonyl peaks are observed at all compositions indicating that, although compound formation does not occur, a stronger interaction (relative to PG/OD mixtures) appears to take place between 1-octadecanol and octyl gallate. Spectral features are consistent with an assignment of heterogeneous mixtures of $OD_{solid}$ + $OG_{solid}$ for all compositions.

These spectra are different from those shown in Figure 5.21 to Figure 5.23 for the PG/alcohol mixtures. In all three binary mixtures a splitting of the asymmetric carbonyl peaks and aromatic C=C peaks at 1700 to 1680 $cm^{-1}$ and 1630 to 1600 $cm^{-1}$ is observed. The formation of OG/alcohol compound is ruled out from the determination of the binary phase diagrams, however it appears that there is an enhanced degree of attractive interaction between the components of the OG/alcohol mixtures relative to the PG/alcohol mixtures. The splitting in the frequencies of $\upsilon_{asym}(C=O)$ are likely a result of enhanced aromatic ring tilt in OG, similar to that observed in the LG/alcohol mixtures. It

is possible that a layering of OG molecules around the alcohol molecules present in the mixture might occur. This would be similar to the splitting observed in free LG interacting with $(LG)_3 \cdot CVL$ complexes (Chapter 4) and might account for the two forms of OG interacting with the alcohols in these mixtures.

It is of interest to note that neither PG/alcohol nor OG/alcohol mixtures display peaks at 1710 $cm^{-1}$ regardless of equilibration time. This could be because the alcohol components of all of these mixtures are in their thermodynamically stable low-temperature phases at room temperature.

## 5.5. Discussion

Alkyl gallates with three carbon (propyl gallate) and eight carbon (octyl gallate) chains display simple eutectic mixtures with no secondary compound formation when combined with TD, HD, and OD. Raman spectra of PG/alcohol mixtures confirm the formation a simple mixture with no significant interaction between the two components. Raman spectra of OG/alcohol mixtures show some interaction between the two components but no evidence of compound formation, as confirmed by the binary phase diagrams.

The situation is different with an alkyl gallate with 12 carbons in the alkyl chain, lauryl gallate (LG). LG/alcohol mixtures interact strongly and form a compound of the form $(LG)_2 \cdot$alcohol This is observed in the binary phase diagram and is confirmed in Raman spectra of the mixtures. CPMAS $^{13}C$ NMR spectra of $(LG)_2 \cdot OD$ indicate that the aromatic and carbonyl carbons of LG are in two distinct environments in the compound.

Ring tilt of LG and extensive H-bonding are shown to be characteristic of the (LG)$_2 \bullet$alcohol compounds.

The length of the alkyl-chain of the gallate is apparently important in controlling the interaction between the alkyl gallates and alcohols. The shortest chain alkyl gallate examined (PG) produces little interaction with TD, HD, or OD. The long chain alkyl gallate examined (LG) forms a compound, (LG)$_2 \bullet$alcohol. The examined alkyl gallate of intermediate chain length (OG) shows behaviour intermediate between PG and LG when mixed with TD, HD, and OD. Raman spectra of OG/alcohol show enhanced interaction relative to PG/alcohol mixtures but no compound formation is observed.

(LG)$_2 \bullet$alcohol is probably stabilized by significant van der Waals interactions between the LG and alcohol alkyl-chains of the alcohol. The other alkyl gallates have the same functional groups, and, in principle, the same ability to H-bond with the alcohol. It appears that an alkyl gallate of chain length greater than about 8 carbons is necessary to produce a stable compound with TD, HD, or OD.

A more detailed thermodynamic examination of the role of the combination of differing alkyl-chain lengths in (LG)$_2 \bullet$alcohol compounds and in the other alkyl gallate/alcohol mixtures will be presented in Chapter 7 and Chapter 8. The role of the developer-solvent interaction in a ternary rewritable thermochromic mixture will be addressed in the next chapter.

# Chapter 6. Ternary Rewritable Thermochromic Mixtures

## 6.1. Ternary Phase Diagrams

In previous chapters, dye-developer and developer-solvent interactions have been examined and characterized. Prior to the examination of the thermochromic properties of crystal violet lactone/lauryl gallate/alcohol mixtures, it is of use to briefly examine its ternary phase diagram.

Phase diagrams for ternary mixtures are commonly represented by a triangular diagram at constant temperature, as shown in Figure 6.1 for CVL, LG, and a long-chain alcohol.
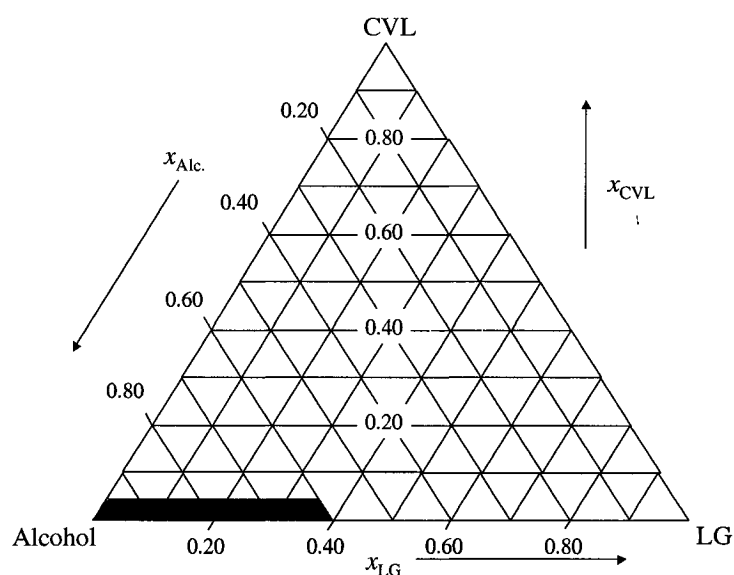
Figure 6.1. A schematic view of the crystal violet lactone/lauryl gallate/alcohol phase diagram. The shaded region represents the composition range examined in rewritable thermochromic mixtures in the present study. It is bounded by $x_{CVL} <$ 0.05, $x_{LG} < 0.40$, and $x_{alcohol} > 0.60$.

Mixtures considered in the present study have compositions similar to those outlined in the patent literature; they are rich in solvent ($x_{alcohol} > 0.60$) with only a small amount of CVL dye ($x_{CVL} < 0.05$).[64,86,87,89,116] With this in mind, only the shaded part of the phase diagram shown in Figure 6.1 is of interest in the examination of the equilibrium properties of ternary rewritable thermochromic mixtures.

A series of ternary CVL/LG/alcohol mixtures was prepared in standard DSC pans. Mixtures were heated to fusion and cooled slowly (5 K min$^{-1}$) to achieve equilibrium solid compositions. The onset temperature of the liquidus on cooling for each mixture was recorded onto a three-dimensional array of points corresponding to the phase composition. The liquidus surface was optimized and contour maps were prepared. Eutectic temperatures remained constant within experimental error and are represented by straight lines. The transition temperatures of $\alpha$-alcohol to $\beta$- or $\gamma$-alcohol phases also showed little variation in temperature as $x_{CVL}$ was varied compared with the transition temperatures observed in LG/alcohol binary mixtures. In crystal violet lactone/lauryl gallate/1-hexadecanol (CVL/LG/HD) and crystal violet lactone/lauryl gallate/1-octadecanol (CVL/LG/HD) mixtures the enthalpy changes observed for $\alpha$-$\gamma$ alcohol transitions were small, reflecting their $\alpha$-phase metastability, as discussed in Chapter 5.

To aid in the discussion of the ternary liquidus, slices of the ternary phase diagram data are presented in Figures 6.2, 6.3, and 6.4 such that $x_{CVL}$ is kept constant. These are effectively horizontal slices through Figure 6.1 and show the behaviour of the LG/alcohol mixtures as CVL is added.

Figure 6.2 shows the crystal violet lactone/lauryl gallate/1-tetradecanol (CVL/LG/TD) phase diagram at $x_{CVL} = 0$ (the binary LG/TD mixture), $x_{CVL} = 0.025$, $x_{CVL} = 0.050$, and a contour map of the liquidus surface.
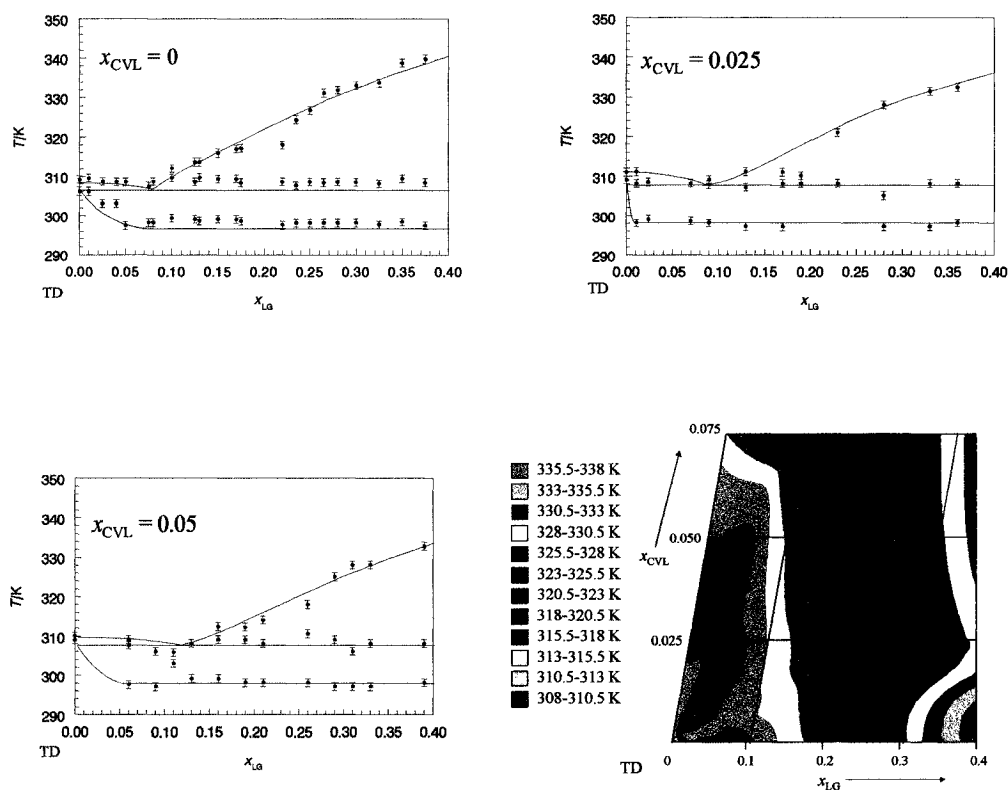


Figure 6.2. The effect of adding CVL to a binary lauryl gallate/1-tetradecanol mixture is shown by the phase diagrams of crystal violet lactone/lauryl gallate/1-tetradecanol (CVL/LG/TD) where $x_{CVL}$ is kept constant. An approximation of the crystal violet lactone/lauryl gallate/1-tetradecanol ternary liquidus surface in the region of interest to the present study is shown in the contour map.

The eutectic temperature and α-β phase TD transitions are invariant with the amount of CVL present and appear at 308 ± 1 K and 300 ± 2 K, respectively. There was little change in the eutectic composition, within experimental error, upon addition of

CVL to the LG/TD mixture. The contour of the liquidus surface shows a surface consistent with a LG/TD eutectic composition of $\sim x_{LG} = 0.05$-$0.075$ below $x_{CVL} = 0.075$.

Figure 6.3 shows the CVL/LG/HD liquidus at $x_{CVL} = 0$, $x_{CVL} = 0.025$, $x_{CVL} = 0.050$, and a contour map of the liquidus surface. The liquid to $\alpha$-HD transition is invariant with the amount of CVL present and appears at $318 \pm 1$ K. The enthalpy change of the $\alpha$-$\gamma$ HD transition was very small, if observed at all, due to its kinetic stability and appeared at $300 \pm 2$ K in some compositions. The presence of CVL did not affect the temperature of the $\alpha$-$\gamma$ HD phase transition.
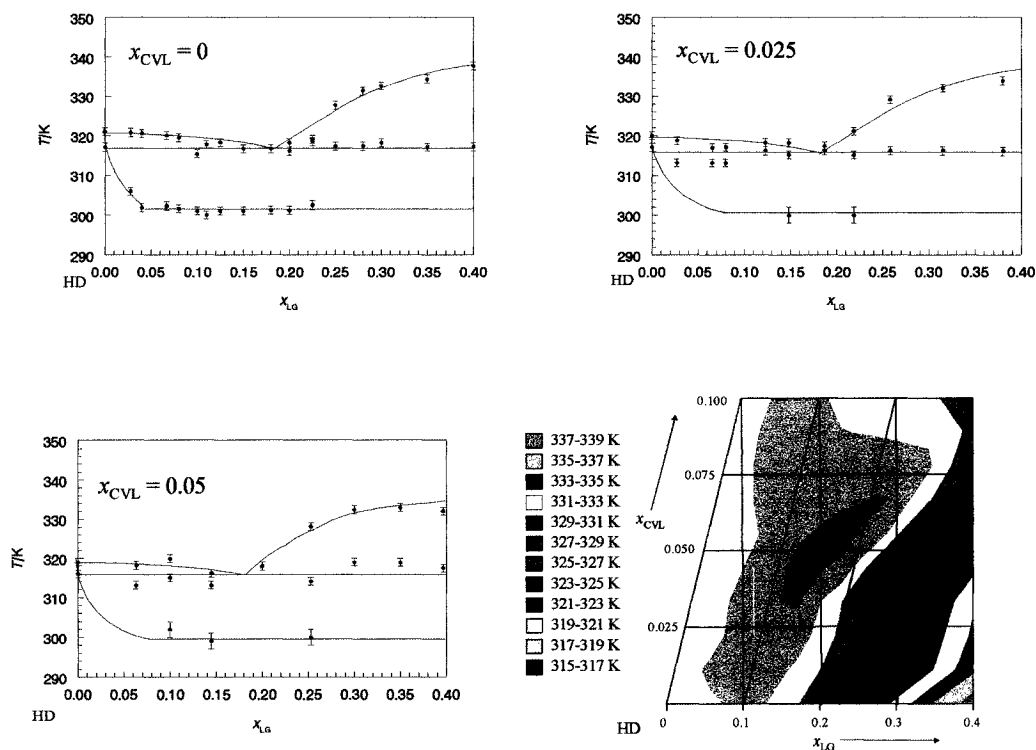


Figure 6.3. The effect of adding CVL to a binary lauryl gallate/1-hexadecanol mixture is shown by the phase diagrams of crystal violet lactone/lauryl gallate/1-hexadecanol (CVL/LG/HD) where $x_{CVL}$ is kept constant. An approximation of the crystal violet lactone/lauryl gallate/1-hexadecanol ternary liquidus surface in the region of interest to the present study is shown in the contour map.

Within experimental error, there is no significant change in the eutectic composition of LG/HD upon addition of CVL. The CVL/LG/HD ternary liquidus contour, estimated in Figure 6.3, shows a eutectic composition of $x_{LG}$ = 0.10 to 0.15 below $x_{CVL}$ = 0.10.

Figure 6.4 shows the CVL/LG/OD liquidus at $x_{CVL}$ = 0, $x_{CVL}$ = 0.025 , $x_{CVL}$ = 0.050, and a contour map of the liquidus surface.
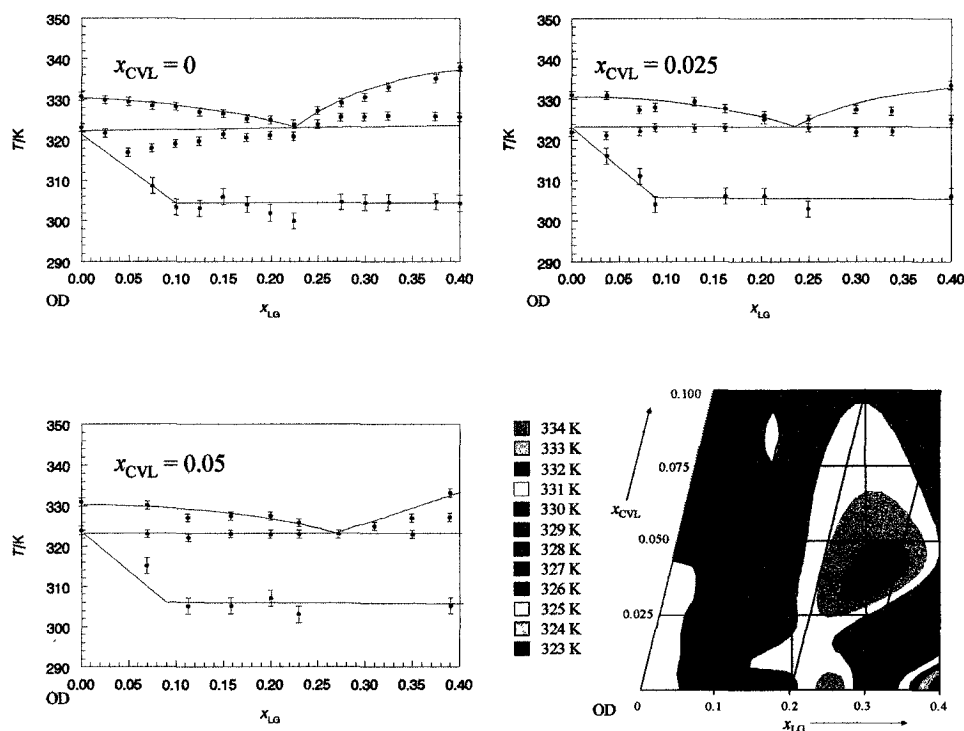


Figure 6.4. The effect of adding CVL to a binary lauryl gallate/1-octadecanol mixture is shown by the phase diagrams of crystal violet lactone/lauryl gallate/1-octadecanol (CVL/LG/OD) where $x_{CVL}$ is kept constant. An approximation of the crystal violet lactone/lauryl gallate/1-octadecanol ternary liquidus surface in the region of interest to the present study is shown in the contour map.

The eutectic is observed at $x_{LG}$ = 0.23 to 0.25 in the LG/OD mixture at $x_{CVL}$ = 0. The eutectic temperature is invariant with the amount of CVL present and appears at 324 ± 1 K. The enthalpy change of the α-γ OD transition was very small, if observed at all, due to its kinetic stability and appeared at 303 ± 2 K in some compositions. As in the

other ternary mixtures, the effect of CVL on the LG/OD eutectic composition is minimal. The contour of the ternary CVL/LG/OD liquidus shows a eutectic composition of ~ $x_{LG}$ = 0.25 below $x_{CVL}$ = 0.10.

Ternary compositions presented in this chapter have $x_{CVL}$ values of less than 0.025, therefore the effect on the overall liquidus properties of the binary LG/alcohol matrix is assumed to be minimal within the ternary mixtures presented in the following sections.

## 6.2. Images and Bulk Properties of Thermochromic Mixtures

The major portion of the present study was concerned with three-component rewritable thermochromic mixtures consisting of CVL dye, LG developer, and one of three long-chain 1-alcohol solvents: TD, HD, or OD. The CVL/LG/alcohol system was examined in detail because it displays interesting variation in thermochromic properties as a function of solvent composition. This purpose of this section is to graphically introduce the thermochromic mixtures studied, to give the reader an understanding of the thermochromic properties of the mixtures, and to provide insight into the motivation of the research that follows.

### 6.2.1. Crystal Violet Lactone/Lauryl Gallate/1-Tetradecanol

A schematic view of the general thermochromic properties of crystal violet lactone/lauryl gallate/1-tetradecanol (CVL/LG/TD) mixtures is shown in Figure 6.5. At room temperature the solid mixture has very low colour density. Melting the mixture results in the development of colour that can be maintained in a metastable, but long lived, state if the mixture is rapidly cooled ($dT/dt$ > 300 K min$^{-1}$). Mixtures maintain high

colour density in the solid state below 10 °C. This temperature is therefore termed the decolourisation temperature, $T_d$. Above 10 °C, the mixture rapidly loses colour and is at its original colour density in less than 30 s.
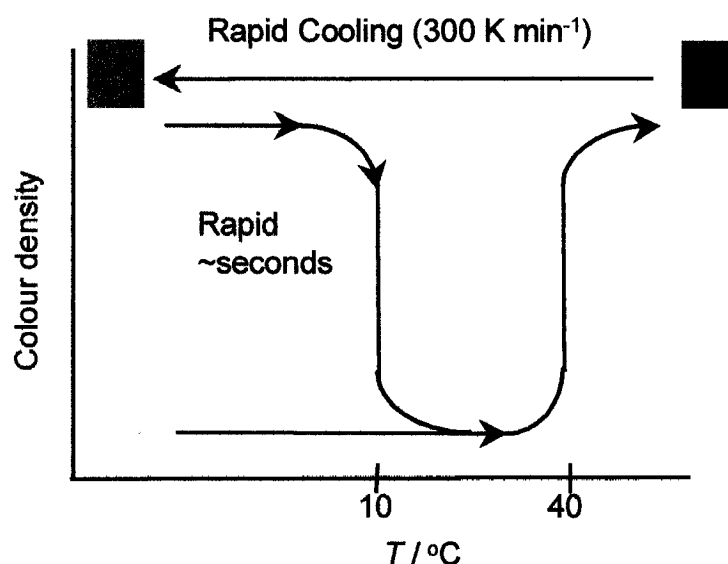


Figure 6.5. Schematic view of the thermochromic behaviour of a representative crystal violet lactone/lauryl gallate/1-tetradecanol mixture (CVL/LG/TD, 1:6:49 mole ratio). Coloured plates are digital images of paper treated with the ternary mixture. The mixture has low colour density at room temperature and undergoes colour development above its melting point (~ 40 °C). Rapid cooling of the molten mixture results in metastable colour development that is long-lived below 10 °C. Heating above 10 °C results in rapid (< 30 s) and complete loss of colour density.

Mixtures of this type display good rewritable thermochromic properties. They display reasonable contrast between coloured and non-coloured states, are quite stable below $T_d$, and rapidly decolour when heated above $T_d$.

Figure 6.6 shows a series of CVL/LG/TD mixtures with varying LG and TD compositions at equilibrium. Images were obtained for sample vials that had been stored for 24 hr at 25 °C. In general, they show low colour density at equilibrium. Increasing the

LG/CVL and/or LG/TD ratios increases the colour density of the equilibrium solid and influences the contrast ratio in the ternary thermochromic mixture.



| 1:1:96 | 1:1:50 | 1:1:40 | 1:1:30 |

| 1:3:96 | 1:3:50 | 1:3:40 | 1:3:30 |

| 1:6:96 | 1:6:50 | 1:6:40 | 1:6:30 |

| 1:12:96 | 1:12:50 | 1:12:40 | 1:12:30 |
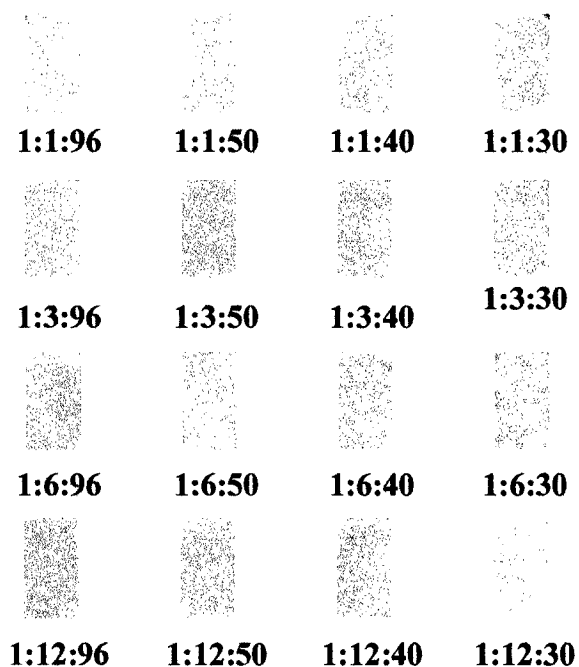
Figure 6.6. Crystal violet lactone/lauryl gallate/1-tetradecanol (CVL/LG/TD) mixtures with varying lauryl gallate and 1-tetradecanol compositions at equilibrium. Colour digital images were obtained of the bottoms of sample vials that had been stored at 25 °C for 24 hr following slow cooling from the melt. Ratios given are CVL/LG/TD mole ratios.

### 6.2.2. Crystal Violet Lactone/Lauryl Gallate/1-Hexadecanol

Rewritable thermochromic properties of crystal violet lactone/lauryl gallate/1-hexadecanol (CVL/LG/HD) mixtures are represented schematically in Figure 6.7. These mixtures differ from CVL/LG/TD mixtures in that the equilibrium colour density in the solid state is higher. The colour density increases markedly in the liquid state (above ~ 50 °C) and enhanced colour density is maintained if the mixture is rapidly cooled. These mixtures have a relatively low $T_d$ of about 10 to 15 °C, above which colour density is lost and a solid with low colour density is produced. Not only do these mixtures display poor

colour contrast, but they also display slow rates of decolourisation. It takes 30 to 60 min for the observation of significant loss of metastable colour density.
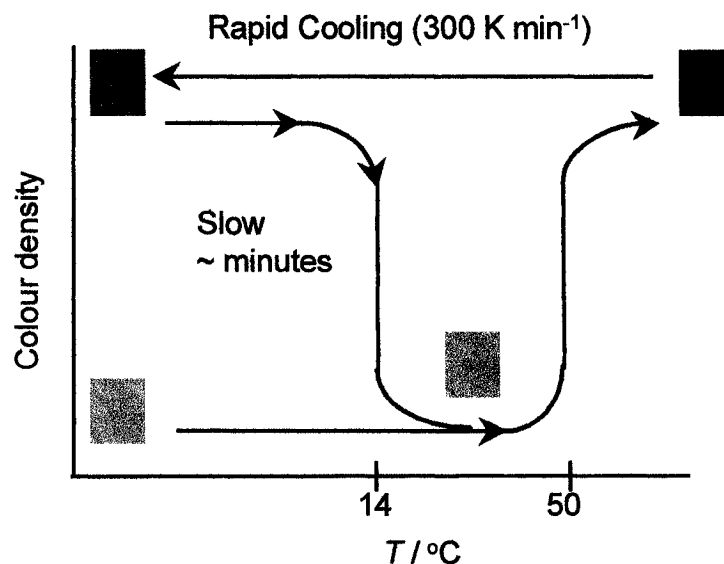


Figure 6.7. Schematic view of the thermochromic behaviour of a representative crystal violet lactone/lauryl gallate/1-hexadecanol mixture (CVL/LG/HD, 1:6:43 mole ratio). Coloured plates are digital images of paper treated with the ternary mixture. The mixture has moderate colour density at room temperature but achieves enhanced colour development above its melting point (~ 50 °C). Rapid cooling of the molten mixture results in maintenance of enhanced colour density that is long lived below 10 to 15 °C. Heating above this temperature results in slow (minutes) loss of colour density.

These CVL/LG/HD mixtures display rewritable thermochromic properties, as in CVL/LG/TD. Colour contrast is comparable, but only because the metastable colour is more intense. The equilibrium mixture does not provide effective erasure and suffers from poor colour contrast and slow decolourisation rates.

In general, CVL/LG/HD mixtures display moderate colour density at equilibrium at 25 °C. Figure 6.8 shows a series of CVL/LG/HD mixtures photographed 24 hr after slow cooling from the melt. Like CVL/LG/TD mixtures, increasing the LG/HD and/or LG/CVL ratios results in an increase in equilibrium colour density. In the case of CVL/LG/HD, this effect is more pronounced.

1:1:86     1:1:43     1:1:35     1:1:25

1:3:86     1:3:43     1:3:35     1:3:25

1:6:86     1:6:43     1:6:35     1:6:25

1:12:86    1:12:43    1:12:35    1:12:25
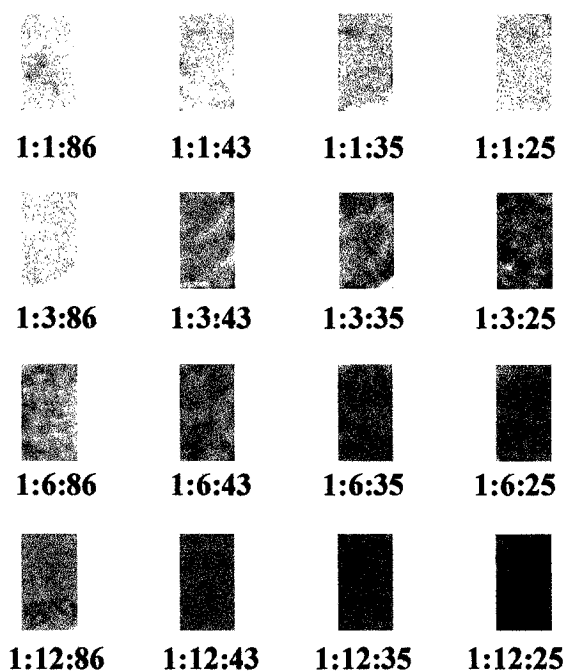
Figure 6.8. Crystal violet lactone/lauryl gallate/1-hexadecanol (CVL/LG/HD) compositions at equilibrium. Colour digital images were obtained of the bottoms of sample vials that had been stored at 25 °C for 24 hr following slow cooling from the melt. Ratios given are CVL/LG/HD mole ratios.

### 6.2.3. Crystal Violet Lactone/Lauryl Gallate/1-Octadecanol

Crystal violet lactone/lauryl gallate/1-octadecanol (CVL/LG/OD) mixtures are thermochromic, but have properties quite inferior to CVL/LG/TD, and even CVL/LG/HD. Figure 6.9 shows a schematic view of the thermochromic properties of a representative CVL/LG/OD mixture.
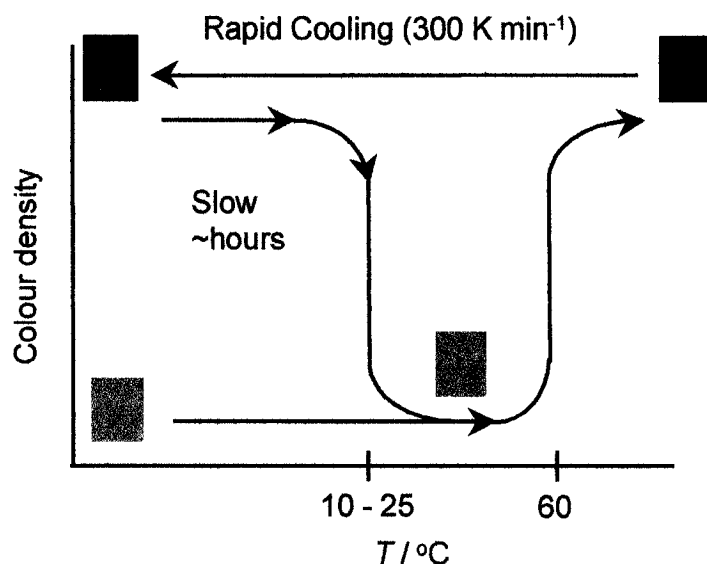
Figure 6.9. Schematic view of the thermochromic behaviour of a representative crystal violet lactone/lauryl gallate/1-octadecanol mixture (CVL/LG/OD, 1:6:40 mole ratio). Coloured plates are digital images of paper treated with the ternary mixture. The mixture has moderate colour density at room temperature but achieves enhanced colour development above its melting point (~ 60 °C). Rapid cooling of the molten mixture results in maintenance of enhanced colour density that is long lived below 10 to 25 °C. Heating above this temperature results in very slow (hours) loss of colour density.

These mixtures are characterized by high equilibrium colour density in the solid state. However, melting of the mixture results in the development of higher colour density. Like the other two systems examined in this section, this enhanced colour density can be maintained by quenching to the solid state. Enhanced colour density is remarkably stable and remains in the system for several hours at room temperature.

CVL/LG/OD mixtures display rewritable thermochromic properties as for CVL/LG/TD and CVL/LG/HD; they can form metastable coloured solids with enhanced colour density. These mixtures display colour contrast, but like CVL/LG/HD mixtures the increased colour density in the metastable solid is offset by higher colour density at equilibrium. A more serious problem is the very slow rate of decolourisation of

CVL/LG/OD mixtures. At room temperature it takes several hours for the mixtures to convert from metastable to equilibrium colour densities.

Figure 6.10 shows a series of CVL/LG/OD mixtures photographed 24 hr after slow cooling from the melt. At all compositions the equilibrium colour density is high, but increasing LG/CVL and/or LG/OD ratios results in moderate increases in colour density.



| 1:1:76 | 1:1:40 | 1:1:30 | 1:1:25 |

| 1:3:76 | 1:3:40 | 1:3:30 | 1:3:25 |

| 1:6:76 | 1:6:40 | 1:6:30 | 1:6:25 |

| 1:12:76 | 1:12:40 | 1:12:30 | 1:12:25 |
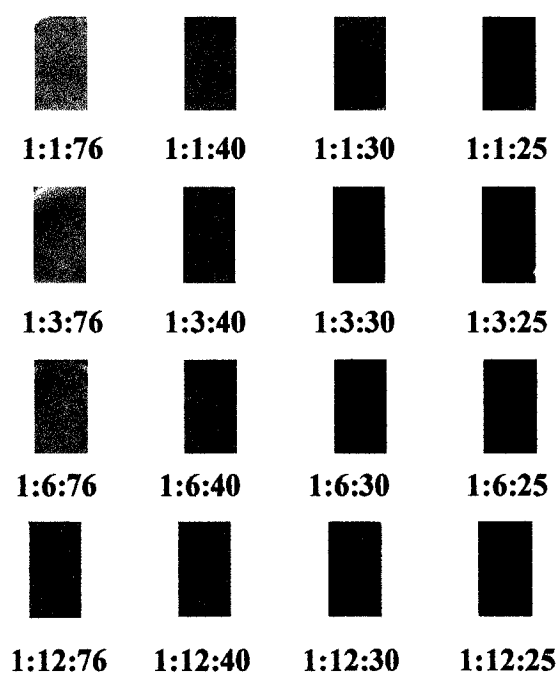
Figure 6.10. Crystal violet lactone/lauryl gallate/1-octadecanol (CVL/LG/OD) compositions at equilibrium. Colour digital images were obtained of the bottoms of sample vials that had been stored at 25 °C for 24 hr following slow cooling from the melt. Ratios given are CVL/LG/OD mole ratios.

### 6.2.4. Decolourisation Temperatures

The decolourisation of metastable coloured mixtures is generally associated with the phase separation and crystallization of components within the mixture.[60,89,125] Since the decolourisation event is exothermic, the $T_d$ of rewritable thermochromic mixtures can

be estimated using DSC.[110] When ternary mixtures were quenched and slowly heated exothermic events corresponding to the initiation of decolourisation were observed. Figure 6.11 compares DSC thermograms of the slow heating (5 K min⁻¹) of selected quenched (300 K min⁻¹) and slowly cooled (5 K min⁻¹) ternary mixtures. Quenched CVL/LG/TD (1:9:40 mole ratio) shows a broad exothermic event with an onset temperature of approximately 10 to 12 °C. In general, quenched CVL/LG/TD mixtures with various LG concentrations display exothermic events with onset temperatures of approximately 10 to 15 °C. This event is not observed in the heating of slowly cooled mixtures.
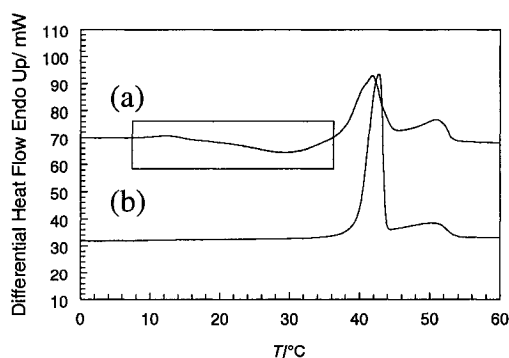


Figure 6.11. DSC thermograms of the heating (5 K min⁻¹) of (a) rapidly cooled (300 K min⁻¹) and (b) slowly cooled (5 K min⁻¹) mixtures of crystal violet lactone/lauryl gallate/1-tetradecanol (CVL/LG/TD, 1:9:40 mole ratio). A large exothermic event ($\Delta H$ = -40 J (g sample)⁻¹) with an onset temperature of 10 °C is consistent with the decolourisation of the mixture.

Quenched CVL/LG/HD of 1:9:40 mole ratio (see Figure 6.12) has a much smaller exothermic event with an onset temperature of approximately 15 °C. Other quenched CVL/LG/HD mixtures show small exothermic events at various LG concentrations with onset temperatures of approximately 10 to 15 °C. The small enthalpy changes observed

relative to the CVL/LG/TD mixture are consistent with the much lower rate of decolourisation (*i.e.*, crystallization) in the CVL/LG/HD mixture.
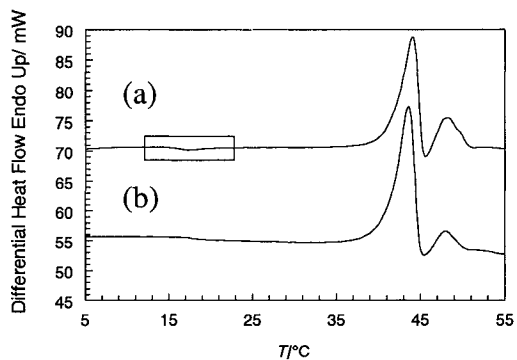


Figure 6.12. DSC thermograms of the heating (5 K min$^{-1}$) of (a) rapidly cooled (300 K min$^{-1}$) and (b) slowly cooled (5 K min$^{-1}$) mixtures of crystal violet lactone/lauryl gallate/1-hexadecanol (CVL/LG/HD, 1:9:40 mole ratio). A small exothermic event ($\Delta H = -3$ J (g sample)$^{-1}$) with an onset temperature of 10 to 15 °C is consistent with the decolourisation of the mixture.

The $T_d$ of CVL/LG/OD (1:9:40 mole ratio) cannot be obtained through a DSC measurement because the rate of decolourisation is too slow to be detected on the time scale of the scan. On heating from 0 °C no significant thermal event was observed that distinguished the quenched from the slowly cooled sample (see Figure 6.13).
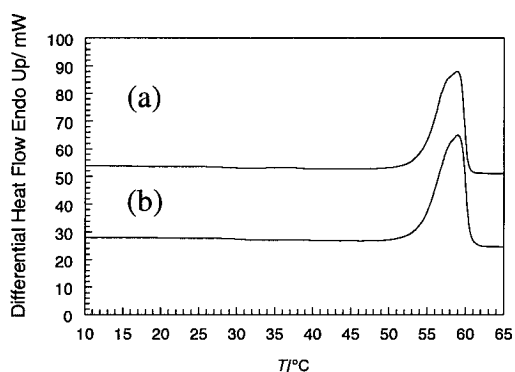
Figure 6.13. DSC thermograms of the heating (5 K min$^{-1}$) of (a) rapidly cooled (300 K min$^{-1}$) and (b) slowly cooled (5 K min$^{-1}$) mixtures of crystal violet lactone/lauryl gallate/1-octadecanol (CVL/LG/OD, 1:9:40 mole ratio) showed no distinct thermal events consistent with decolourisation of the mixture.

CVL/LG/TD, CVL/LG/HD, and CVL/LG/OD mixtures maintained stable colour density when stored at ~5 °C for long periods of time and all display decolourisation at 25 °C. With this in mind the vaules of $T_d$ of CVL/LG/OD mixtures are assumed to be somewhere between the $T_d$ of CVL/LG/TD and CVL/LG/HD mixtures and room temperature, or approximately 10 to 25 °C.

### 6.3. Diffuse Reflectance Measurements

A typical diffuse reflectance spectrum is shown in

Figure 6.14 for CVL/LG/OD, (mole ratio 1:6:40) taken 24 hr after rapid quenching. Prominent features are the absorption peak at 620 nm with a shoulder at 550 to 570 nm. This is consistent with the observations of Allen et al. for ring-opened CVL.[122]
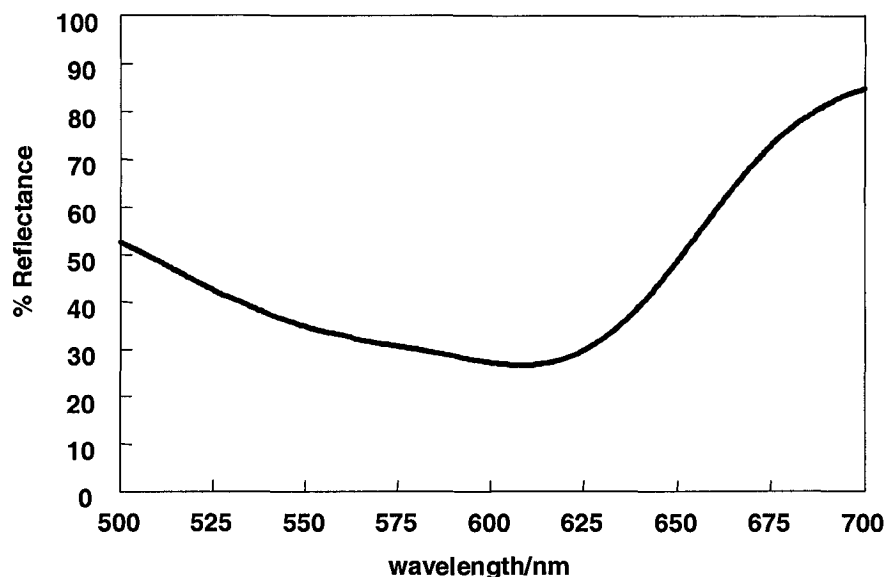
Figure 6.14. The reflectance spectrum obtained using the PC2100 reflectance spectrophotometer of crystal violet lactone/lauryl gallate/1-octadecanol (CVL/LG/OD, 1:6:40 mole ratio) taken 24 hr after quenching from the melt, showing an absorption maximum at 620 nm.

The following diffuse reflectance results, shown in Figures 6.15, 6.16, and 6.17, examine the reflectance intensity at $\lambda_{max}$ for ring-opened CVL (620 nm). Overall behaviours of the three system types (CVL/LG/TD, CVL/LG/HD, and CVL/LG/OD) are similar; colour intensity increases in the melt, is maintained or enhanced upon quenching, and is lost at equilibrium. Colour density is moderate to high in the melt and increases with increasing $x_{LG}$. The increase in colour density in the melt could be attributed to the solubility of LG in the molten alcohol solvent. Increasing the amount of developer beyond its equilibrium solubility in the solvent has been shown to produce greater interaction with the dye in the melt.[89] Metastable colour densities achieved after rapid cooling in a particular CVL/LG/alcohol system are similar, within experimental error, regardless of LG composition. Metastable colour density for CVL/LG/TD mixtures is

lower than that observed in CVL/LG/HD and CVL/LG/OD. However, this could be due

to the loss of colour density of CVL/LG/TD mixtures during measurement.
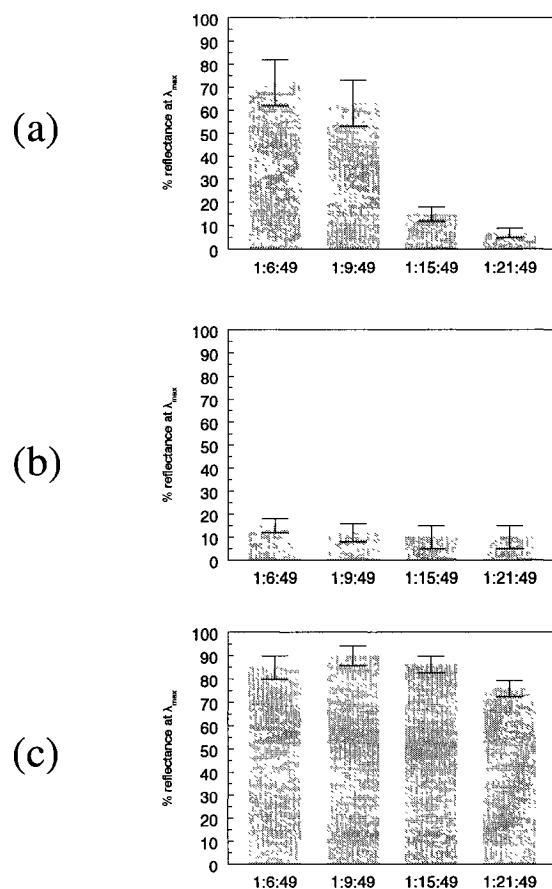


Figure 6.15. Diffuse reflectance intensity at 620 nm for selected crystal violet lactone/lauryl gallate/1-tetradecanol (CVL/LG/TD) mixtures given by mole ratios (a) in the melt (b) after rapid quenching and (c) at equilibrium.
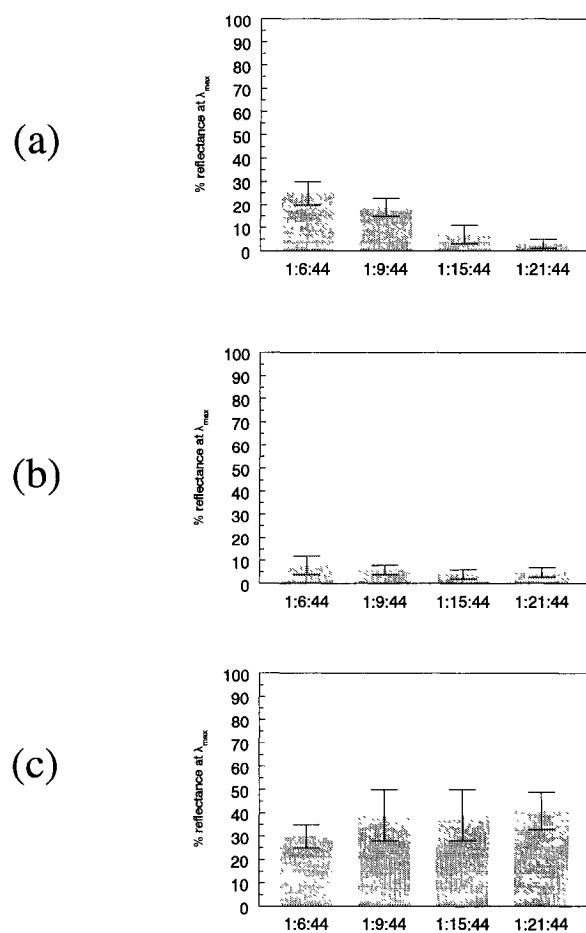
Figure 6.16. Diffuse reflectance intensity at 620 nm for selected crystal violet lactone/lauryl gallate/1-hexadecanol (CVL/LG/HD) mixtures given by mole ratios (a) in the melt (b) after rapid quenching and (c) at equilibrium.
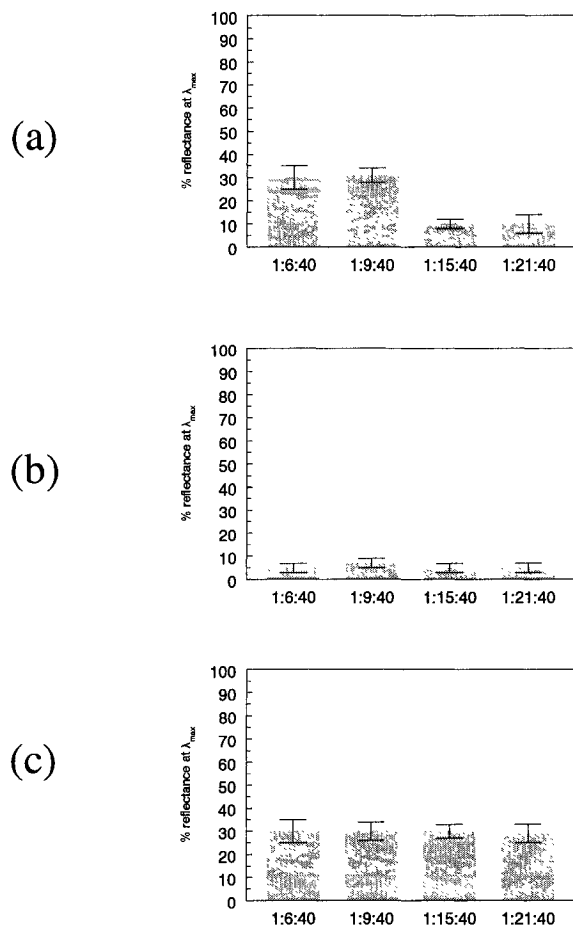
Figure 6.17. Diffuse reflectance intensity at 620 nm for selected crystal violet lactone/lauryl gallate/1-octadecanol (CVL/LG/OD) mixtures given by mole ratios (a) in the melt (b) after rapid quenching and (c) at equilibrium.

Equilibrium colour density of all systems is significantly lower than the metastable colour density. The contrast of CVL/LG/TD mixtures is good; the average intensity difference is 72 % for mixtures in Figure 6.15. The colour contrast between metastable and equilibrium mixtures decreases as the solvent is changed to HD and OD; average intensity differences for CVL/LG/HD and CVL/LG/OD mixtures are 31 % and 25 %, respectively.

Figure 6.18 compares the diffuse reflectance intensity at 620 nm for CVL/LG/TD, CVL/LG/HD, and CVL/LG/OD mixtures of comparable dye-developer-solvent ratios (1:6:40).
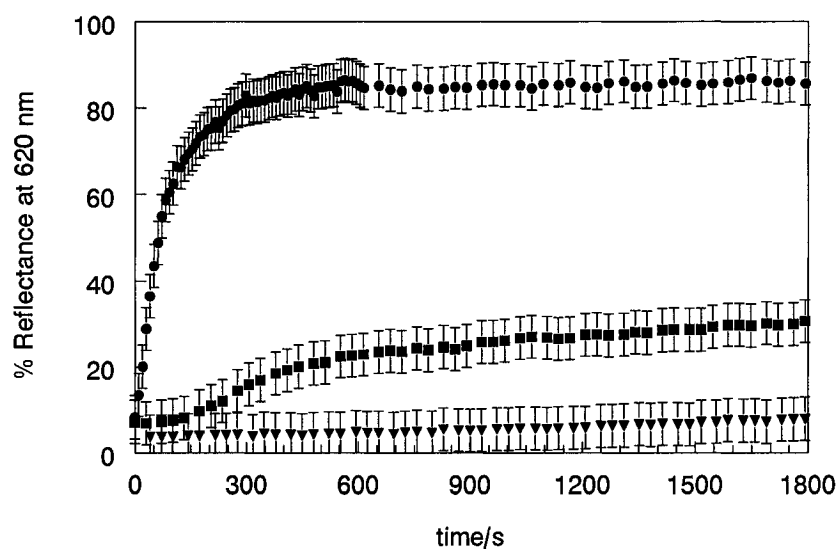


Figure 6.18. Comparison of the diffuse reflectance intensity at 620 nm at mole ratios of 1:6:40 for (●) crystal violet lactone/lauryl gallate/1-tetradecanol (CVL/LG/TD), (■) crystal violet lactone/lauryl gallate/1-hexadecanol (CVL/LG/HD), and (▼) crystal violet lactone/lauryl gallate/1-octadecanol (CVL/LG/OD). A dramatic decrease in decolourisation rate and subsequent increase in equilibrium colour density is observed as the alkyl-chain length of the solvent is increased.

A dramatic change in decolourisation rate was observed as the solvent is changed from TD through OD. The CVL/LG/TD mixture reaches its equilibrium colour density in about 300 to 600 s while the CVL/LG/HD mixture takes well over 1800 s. During the

1800 s of the measurement the CVL/LG/OD mixture shows very little change in colour density, but after 24 hr a reflectance intensity of 30 ± 5% was noted.

These diffuse reflectance measurements provide quantitative data that confirm the observed differences in rewritable thermochromic behaviour between CVL/LG/TD, CVL/LG/HD, and CVL/LG/OD mixtures. While these experiments provide useful information on the behaviour of these mixtures they are only an indicator of the colour of the system and the LG/CVL interaction. To correlate the chemistry of all the components of these mixtures to the observed colour density requires a technique that probes the bonding within these mixtures in their various states.

### 6.4. Time-Resolved Raman Data

Rewritable thermochromic mixtures produce high colour density in metastable phases obtained upon rapid quenching of the system. In this section, selected ternary CVL/LG/alcohol mixtures are examined using time-resolved Raman spectroscopy. Results for CVL/LG/OD mixtures have recently been published.[197] Figure 6.19 and Figure 6.20 show the Raman spectra of selected CVL/LG/TD, CVL/LG/HD, and CVL/LG/OD mixtures in their metastable (high colour density) and equilibrium (low colour density) states obtained 60 s and 24 hr after rapid quenching.
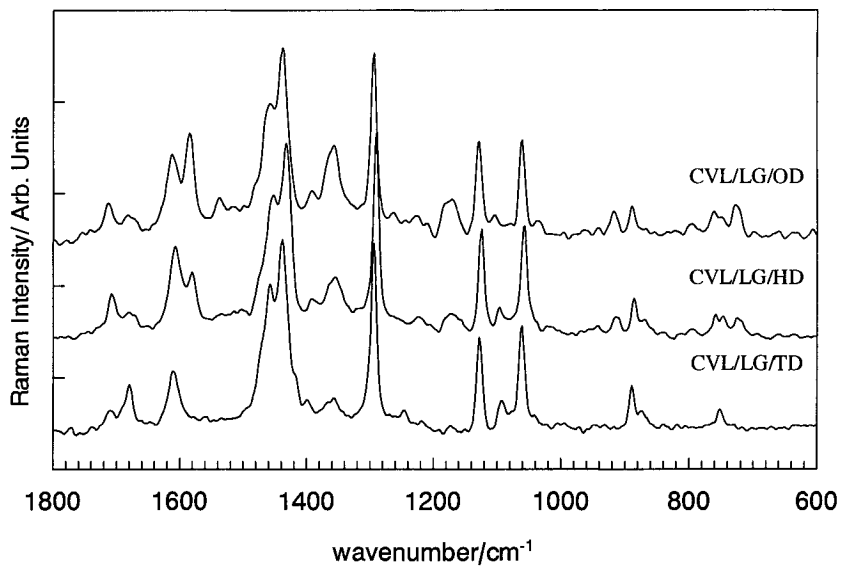
Figure 6.19. Raman spectra of selected crystal violet lactone/lauryl gallate/alcohol (1:6:40 mole ratio) mixtures obtained 60 s after rapid quenching from the melt.
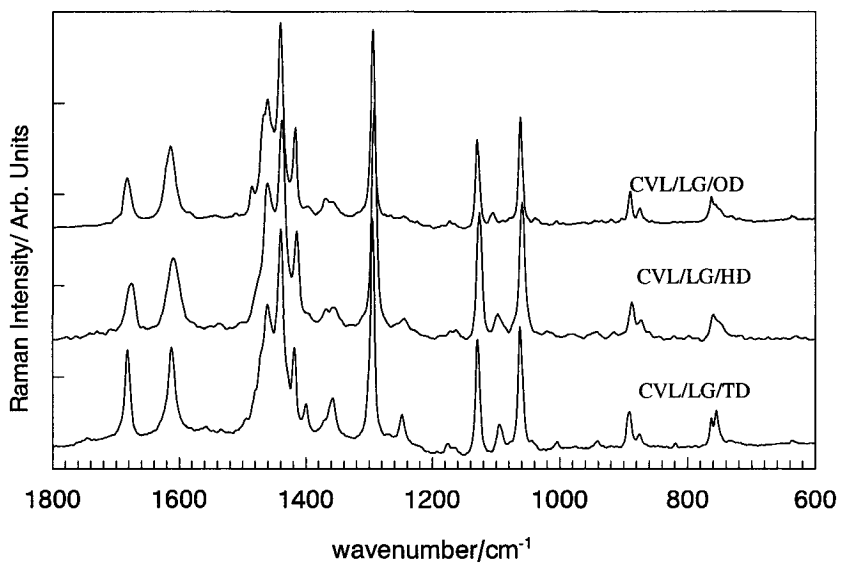


Figure 6.20. Raman spectra of selected crystal violet lactone/lauryl gallate/alcohol (1:6:40 mole ratio) mixtures obtained 24 hr after rapid quenching from the melt.

CVL/LG/TD (1:6:40) loses its colour density so quickly after quenching that little evidence for the presence of ring-opened CVL is observed after 60 s. CVL/LG/HD (1:6:40) and CVL/LG/OD (1:6:40) both show features consistent with strong $(LG)_x \cdot CVL$ bonding, as discussed in Chapter 4. Peaks with carbon-nitrogen bond character characteristic of ring-opened CVL are observed at 1584 cm$^{-1}$ ($\upsilon$(C=N)) and 920 cm$^{-1}$ (($\beta$(C=NR$_2$) with the asymmetric and symmetric bending modes of $\beta$(N$^+$C$_4$) appearing as weak peaks at 940 and 790 cm$^{-1}$. Peaks assigned to the carboxylate moiety of ring-opened CVL are observed at 1359 cm$^{-1}$ ($\upsilon$(CO-)$_{sym.}$) and 730 cm$^{-1}$ ($\gamma_{sym}$(CO-)).

Changes in the Raman spectra as the mixtures equilibrate are not limited to peaks associated with $(LG)_x \cdot CVL$ complexes. The $\upsilon$(C=O)$_{asym.}$ and aromatic $\upsilon$(C=C) of LG in the $(LG)_2 \cdot$alcohol compound at 1683 cm$^{-1}$ and 1616 cm$^{-1}$ are broad and lower in intensity in the quenched mixtures than at equilibrium. This implies that not all LG and alcohol present in the quenched mixtures have combined to produce equilibrium amounts of $(LG)_2 \cdot$alcohol.

Another prominent feature of the quenched mixtures is a peak at 1710 cm$^{-1}$. In Chapter 5 this peak was shown for LG/HD and LG/OD mixtures with low $x_{LG}$. It has been assigned to a carbonyl vibration of LG (or $(LG)_2 \cdot$alcohol) in contact with the $\alpha$-rotational phase of free alcohol in the mixture. This shows that the metastable $\alpha$-alcohol phases are present in the quenched ternary mixtures.

CVL/LG/TD (mole ratio 1:6:40) is the only mixture that displays no significant colour density at equilibrium. Weak peaks assigned to $\upsilon$(C=O)$_{asym.}$ and (C-NR$_2$) bend of ring-closed CVL were observed at 1745 cm$^{-1}$ and 763 cm$^{-1}$, respectively. Equilibrium mixtures of CVL/LG/HD and CVL/LG/OD displayed moderate to high colour density, but showed none of the peaks assigned to strong LG/CVL bonding discussed above. A

small shoulder on the aromatic $\upsilon$(C=C) of (LG)$_2\bullet$alcohol could be due to the peak at 1584 cm$^{-1}$ and represent a very small amount of coloured complex within the mixtures. (The molar extinction coefficient for the ring-opened CVL is quite high[122] therefore not much is required to produce intense blue colour.)

Comparison of metastable and equilibrium Raman spectra of these ternary mixtures shows that three processes occur. These processes can be examined by following the time evolution of selected Raman peak intensities.

First, the destruction of the highly coloured (LG)$_x\bullet$CVL complex is correlated with the disappearance of $\upsilon$(C=N) of ring-opened CVL at 1584 cm$^{-1}$, hereafter designated as *Peak I*. Second, the apparent formation of (LG)$_2\bullet$alcohol in the ternary mixture is followed by examining the intensity of the $\upsilon$(C=O)$_{asym.}$ at 1683 cm$^{-1}$, hereafter designated as *Peak II*. Third, the presence of metastable $\alpha$-alcohol phases will be probed by examining the intensity of the peak at 1710 cm$^{-1}$, hereafter designated as *Peak III*.

### 6.4.1. Crystal Violet Lactone/Lauryl Gallate/1-Tetradecanol

Figure 6.21 shows the Raman spectrum of CVL/LG/TD (1:6:40 mole ratio) as a function of time. Decolourisation of this mixture was so rapid that peaks corresponding to the coloured complex, (LG)$_3\bullet$CVL, were not observed at 30-60 s. No distinct peak at 1584 cm$^{-1}$ (Peak I) was observed 60 s after quenching, but a low frequency shoulder was observed on the aromatic $\upsilon$(C=C) peak at 1616 cm$^{-1}$.
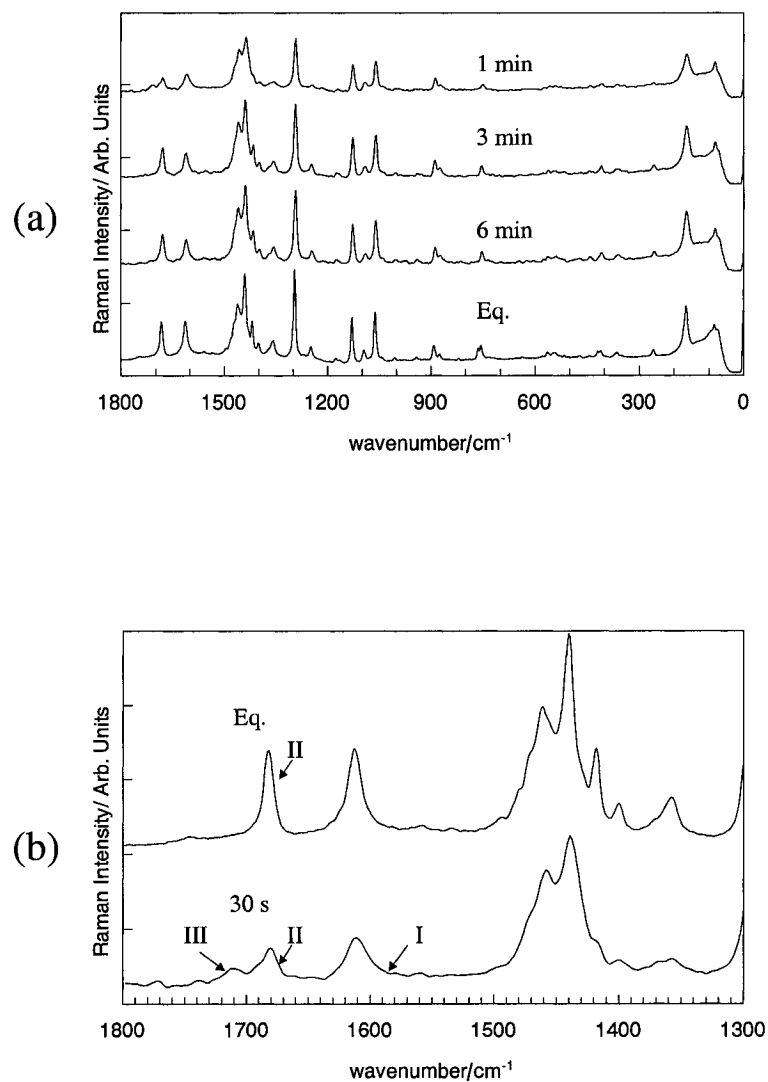
Figure 6.21. Raman spectrum of crystal violet lactone/lauryl gallate/1-tetradecanol (CVL/LG/TD, 1:6:40 mole ratio) that is rapidly quenched in liquid nitrogen and allowed to equilibrate at 25 °C. (a) The Raman spectrum taken at selected time intervals shows the decrease of a C=N vibration at 1584 cm$^{-1}$ (Peak I), the growth of a carbonyl vibration at 1683 cm$^{-1}$ (Peak II), and the decrease of a C=O vibration at 1710 cm$^{-1}$ (Peak III). (b) Comparison of the Raman spectrum of crystal violet lactone/lauryl gallate/1-tetradecanol, (1:6:40 mole ratio) immediately upon quenching (30 s) and at equilibrium (Eq.).

Figure 6.22 shows the 1800 to 1600 cm$^{-1}$ region of CVL/LG/TD (1:6:40 mole ratio) obtained in intervals of 45 s. Peak II quickly grows in intensity as the sample

equilibrates. Peak III is also observed for only 2 to 3 min following quenching of the mixture.
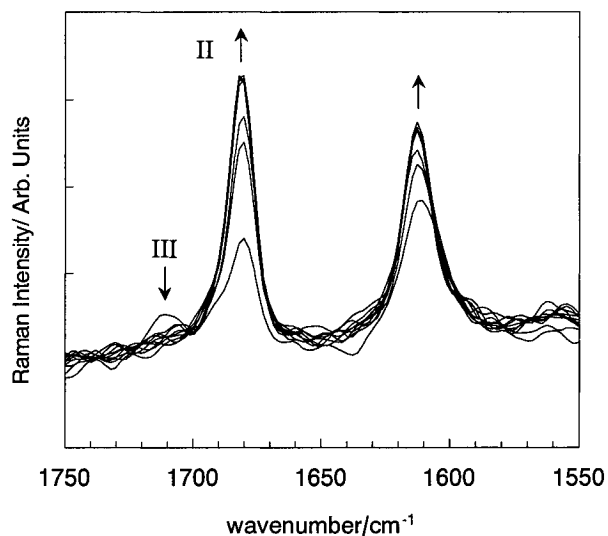


Figure 6.22. Raman spectrum of crystal violet lactone/lauryl gallate/1-tetradecanol (CVL/LG/TD), 1:6:40 mole ratio) obtained at 45 s intervals at 25 °C following rapid quenching in liquid nitrogen. Significant growth of the $(LG)_2\cdot TD$ carbonyl vibration at 1683 $cm^{-1}$ (Peak II) is observed in the first few minutes. A weak peak at 1710 $cm^{-1}$ (Peak III) is observed for approximately 2-3 min following quenching of the mixture.

At equilibrium (24 hrs after quenching; see Figure 6.23), the spectra of equilibrated CVL/LG/TD and LG/TD (both with 6:40 LG:TD mole ratios) are nearly identical with the exception of the peaks assigned to ring-closed CVL discussed earlier.
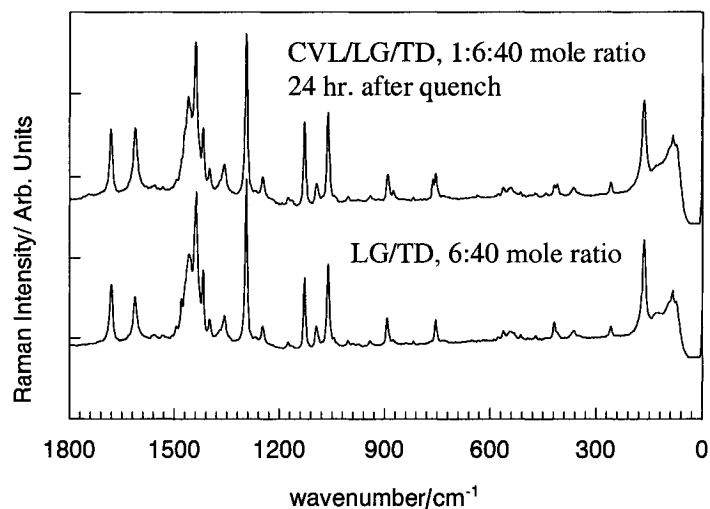
Figure 6.23. Comparison of the Raman spectra of equilibrated crystal violet lactone/lauryl gallate/1-tetradecanol (CVL/LG/TD, 1:6:40 mole ratio) and LG/1-tetradecanol (LG/TD, 6:40 mole ratio) shows that the spectral features are nearly identical.

The rapid disappearance of Peak III at 1710 cm$^{-1}$ is shown as a function of time in Figure 6.24, where the intensity decreases to zero approximately 3 min following quenching. DSC analysis of LG/TD mixtures (Chapter 5) showed that the conversion of α- to β-TD was nearly complete on the time scale of the measurement. The rapid disappearance of Peak III (1710 cm$^{-1}$) correlates with the instability of α-TD within the ternary mixture, which rapidly converts to β-TD at room temperature.
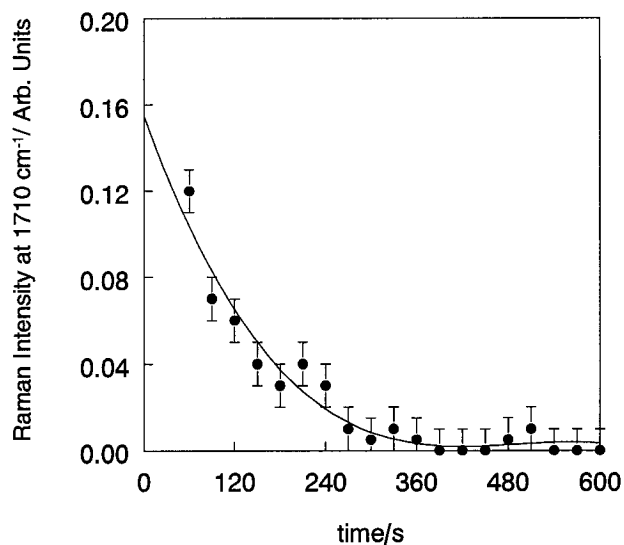
Figure 6.24. Raman Intensity of Peak III at 1710 cm⁻¹ in crystal violet lactone/lauryl gallate/1-tetradecanol (CVL/LG/TD, 1:6:40 mole ratio). Peak III is observed as a low intensity peak which decays into the baseline within about 3 minutes. LG/1-tetradecanol mixtures do not display Peak III intensity within the time limit of the time-resolved Raman experiment (~45 s). Error bars represent the averages over three experiments.

Since the composition of CVL within the ternary mixture is quite small (~2 mol %), the behaviour of the corresponding binary LG/TD mixture (6:40) also was examined using time-resolved Raman spectroscopy to determine the effect of CVL on the LG/TD developer/solvent matrix. Figure 6.25 shows that the intensity of Peak II (1683 cm⁻¹) in the spectrum of LG/TD appears nearly constant in the time following quenching.
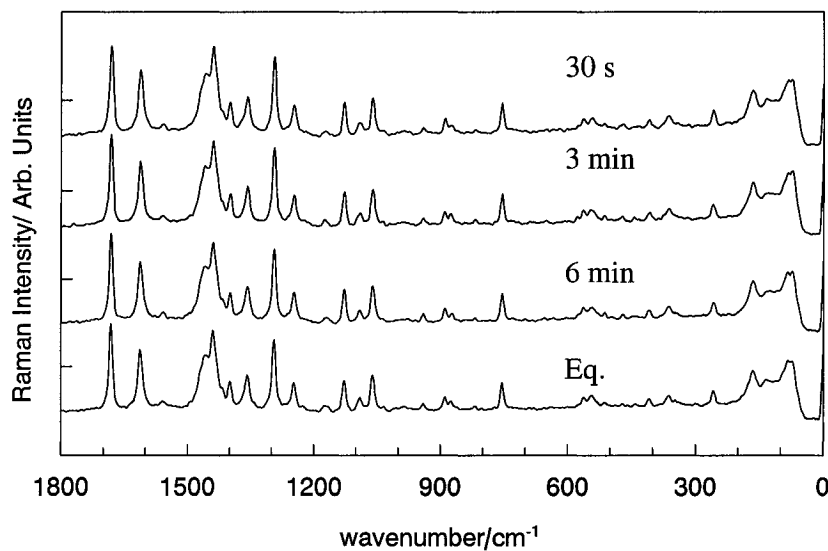
Figure 6.25. The Raman spectrum of lauryl gallate/1-tetradecanol (LG/TD, 6:40 mole ratio) as a function of time after quenching in liquid nitrogen. Peak II, the carbonyl peak of lauryl gallate in (LG)$_2$•TD at 1683 cm$^{-1}$, has high intensity after quenching and undergoes little change with time.

Figure 6.26 compares the time evolution of Peak II (1683 cm$^{-1}$) in CVL/LG/TD and LG/TD. There is a slight increase in the intensity of Peak II upon quenching in the LG/TD mixture, but equilibrium intensity is achieved within approximately 2 to 3 min. The equilibration of Peak II is slightly slower in the CVL/LG/TD mixture, taking about 4 to 6 min to equilibrate. In both cases, the formation of (LG)$_2$•TD occurs very quickly after quenching. The addition of ~ 2 mol % CVL to the binary LG/TD (6:40) results in a decrease in the rate of (LG)$_2$•TD formation in the quenched system. No peak intensity for Peak III (1710 cm$^{-1}$) was observed in LG/TD 6:40 at times greater than 1 minute following quenching.
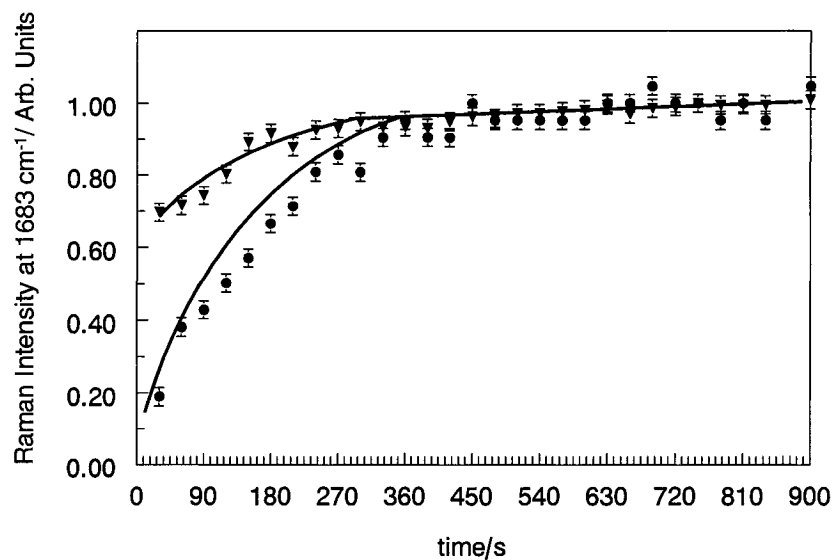
Figure 6.26. Time evolution of the intensity of Peak II, the carbonyl peak at 1683 cm$^{-1}$ of lauryl gallate in (LG)$_2$•TD for: (▼) a mixture of lauryl gallate/1-tetradecanol (LG/TD, 6:40 mole ratio), and (●) a mixture of crystal violet lactone/lauryl gallate/1-tetradecanol (CVL/LG/TD, 1:6:40 mole ratio), both quenched from the melt in liquid nitrogen and equilibrated at 25 °C. Intensities are normalized to their equilibrium values. Lines are added to guide the eye. Error bars represent averages over three experiments.

### 6.4.2. Crystal Violet Lactone/Lauryl Gallate/1-Hexadecanol

Figure 6.27 shows the Raman spectrum of CVL/LG/HD (1:6:40 mole ratio) as a function of time.
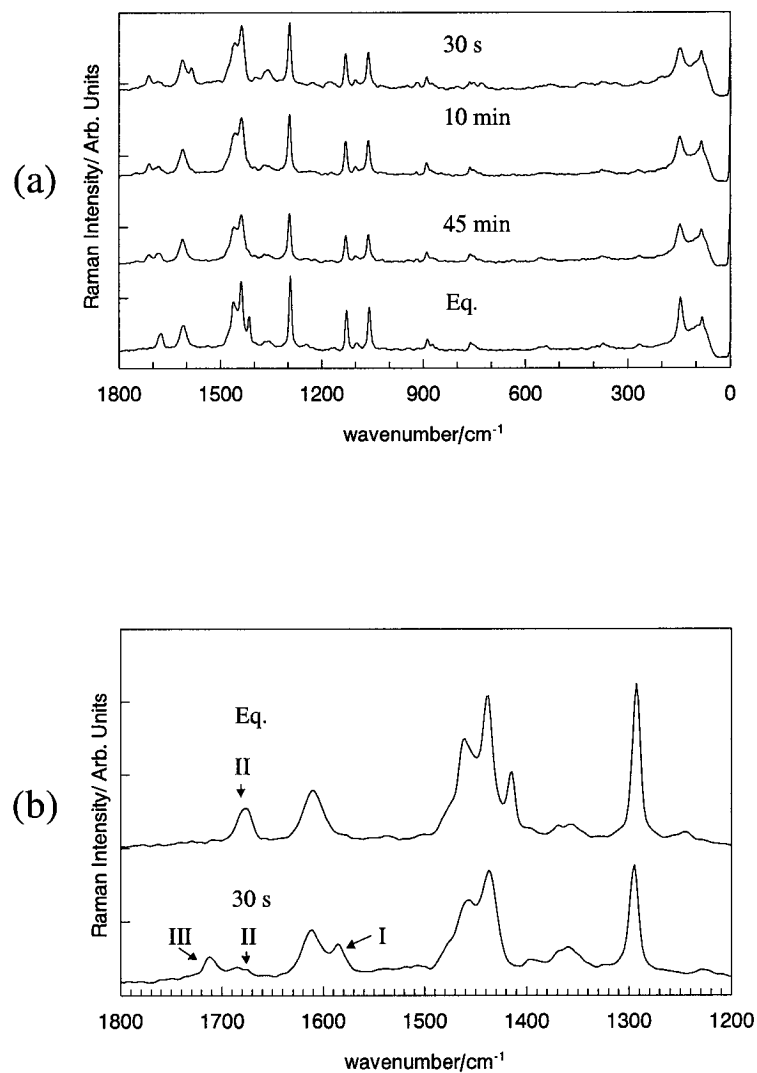
Figure 6.27. Crystal violet lactone/lauryl gallate/1-hexadecanol (CVL/LG/HD, 1:6:40 mole ratio) was rapidly quenched in liquid nitrogen and allowed to equilibrate at 25 °C. (a) The Raman spectrum taken at selected time intervals shows the decrease of a C=N vibration at 1584 cm$^{-1}$ (Peak I), the growth of a carbonyl vibration at 1683 cm$^{-1}$ (Peak II), and the decrease of a C=O vibration at 1710 cm$^{-1}$ (Peak III). (b) Comparison of the Raman spectrum of crystal violet lactone/lauryl gallate/1-hexadecanol (1:6:40 mole ratio) immediately upon quenching (30 s) and at equilibrium (Eq.).

Figure 6.28 shows the 1750 to 1550 cm$^{-1}$ region of CVL/LG/HD (1:6:40 mole ratio) obtained in time intervals of 45 s and 10 min. Peak I (1584 cm$^{-1}$) decreases rapidly

with time and becomes a weak shoulder within 5 to 6 min. Peak II (1683 cm$^{-1}$) grows in

intensity as the sample equilibrates while, at the same time, Peak III (1710 cm$^{-1}$)

decreases slowly in intensity.
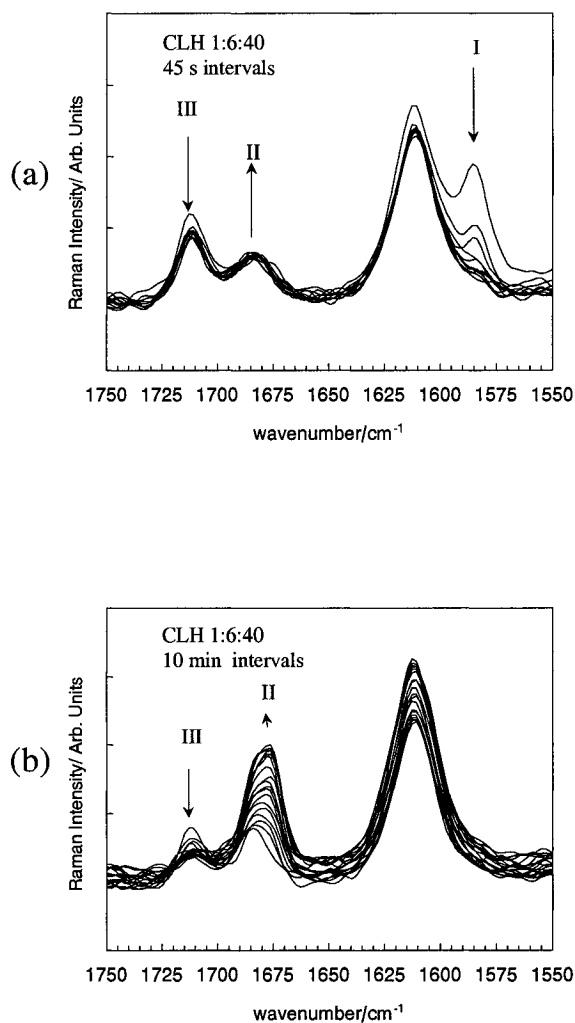


Figure 6.28. Raman spectrum of crystal violet lactone/lauryl gallate/1-hexadecanol (CVL/LG/HD, 1:6:40 mole ratio) obtained at (a) 45 s intervals and (b) 10 minute intervals at 25 °C following rapid quenching in liquid nitrogen. A rapid decrease in Peak I (1584 cm$^{-1}$) intensity and slow growth of Peak II (1683 cm$^{-1}$) intensity is observed. Peak III (1710 cm$^{-1}$) intensity decreases slowly with time following quenching.

The Raman spectra of equilibrated CVL/LG/HD (1:6:40 mol ratio) and its corresponding binary developer/solvent mixture, LG/HD (6:40 mole ratio, see Figure 6.29) are virtually identical. A LG/HD mixture (6:40 mole ratio) was quenched in liquid nitrogen and its Raman spectrum was measured as a function of time (see Figure 6.30)
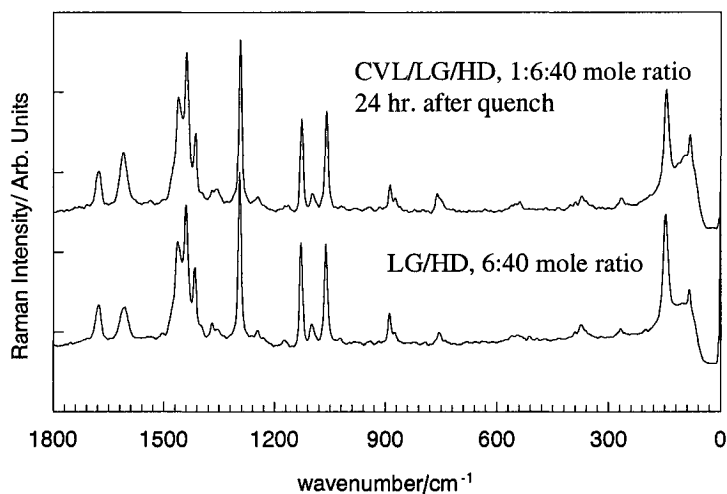


Figure 6.29. Comparison of the Raman spectra of equilibrated crystal violet lactone/lauryl gallate/1-hexadecanol (CVL/LG/HD, 1:6:40 mole ratio) and lauryl gallate/1-hexadecanol (LG/HD, 6:40 mole ratio) shows that the spectral features are nearly identical.
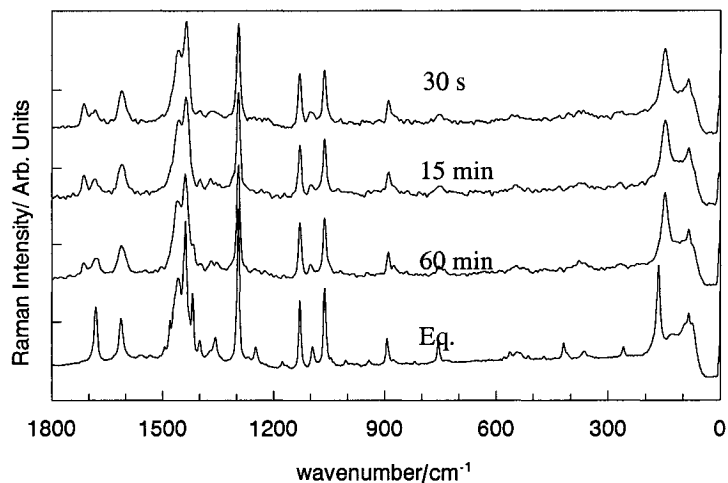
Figure 6.30. The Raman spectrum of lauryl gallate/1-hexadecanol (LG/HD, 6:40 mole ratio) as a function of time after quenching in liquid nitrogen. Initially, the intensity of Peak II (1683 cm$^{-1}$), the carbonyl peak of lauryl gallate in (LG)$_2\bullet$HD, is relatively weak. As time passes, the intensity of Peak II increases, corresponding to the formation of more (LG)$_2\bullet$HD in the mixture.

Figure 6.31 compares the Peak II (1683 cm$^{-1}$) intensity for LG/HD and CVL/LG/HD. The formation of Peak II occurs more quickly in the binary LG/HD mixture. As is the case in the CVL/LG/TD mixture, the presence of CVL appears to inhibit the formation of (LG)$_2\bullet$alcohol compound.
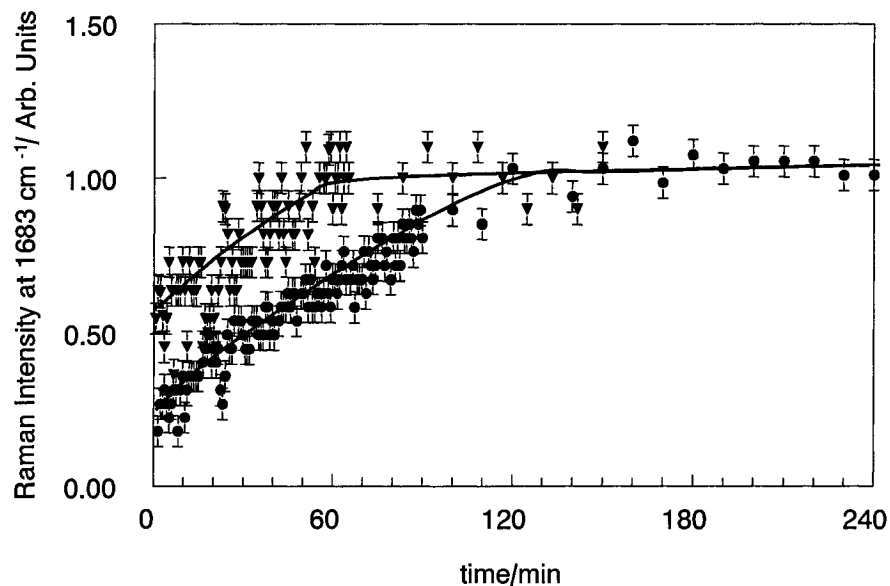
Figure 6.31. Time evolution of the intensity of Peak II, the 1683 cm$^{-1}$ carbonyl peak of lauryl gallate in $(LG)_2$•HD, plotted as a function of time for: (▼) a mixture of lauryl gallate/1-hexadecanol (LG/HD) of mole ratio 6:40, and (•) a mixture of crystal violet lactone/lauryl gallate/1-hexadecanol (CVL/LG/HD) of mole ratio 1:6:40, both quenched from the melt in liquid nitrogen and equilibrated at 25 °C. Intensities are normalized to their equilibrium values. Lines are added to guide the eye. Error bars represent the uncertainty over three experiments.

Peak III (1710 cm$^{-1}$) is observed upon quenching in both the CVL/LG/HD and

LG/HD mixtures. Figure 6.32 shows the Raman intensity of Peak III for CVL/LG/HD

1:6:40 mole ratio and LG/HD 6:40 mole ratio as a function of time following quenching.
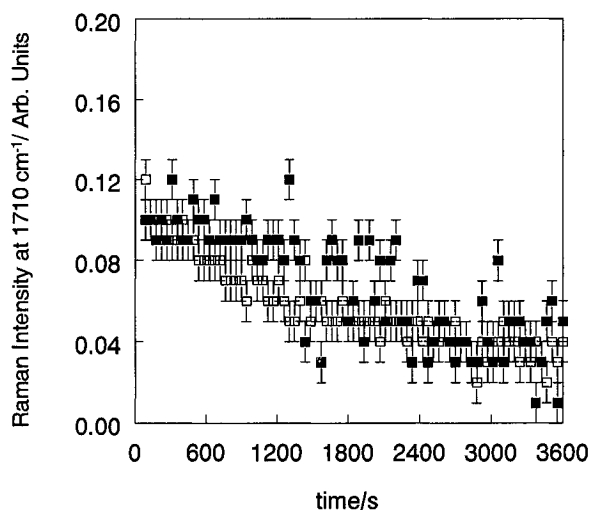
Figure 6.32. Peak III (1710 cm$^{-1}$) intensity for (■) crystal violet lactone/lauryl gallate/1-hexadecanol (CVL/LG/HD, 1:6:40 mole ratio) and (□) lauryl gallate/1-hexadecanol (LG/HD, 6:40 mole ratio) as a function of time following quenching in liquid nitrogen and equilibrating at 25 °C. Within experimental error the rate of Peak III decay is the same for the ternary and binary mixture. Error bars represent the uncertainty over three experiments.

Within experimental error, the rate of Peak III decay is the same in the ternary and binary mixtures. Unlike the growth of Peak II, the presence of CVL does not appear to influence the rate of the transition represented by Peak III. The slow decay of Peak III is also consistent with the slow conversion of α- to γ-HD, as discussed in Chapter 5.

### 6.4.3. Crystal Violet Lactone/Lauryl Gallate/1-Octadecanol

Figure 6.33 shows the Raman spectrum of CVL/LG/OD (1:6:40 mole ratio) as a function of time. Figure 6.34 shows the 1800 to 1300 cm$^{-1}$ region of CVL/LG/OD (1:6:40 mole ratio) obtained in intervals of 45 s and 10 min. On a short time scale, the decrease of

the Peak I (1584 cm$^{-1}$) was most prominent, while over longer time periods the growth of

Peak II (1683 cm$^{-1}$) and decrease of Peak III (1710 cm$^{-1}$) were observed.
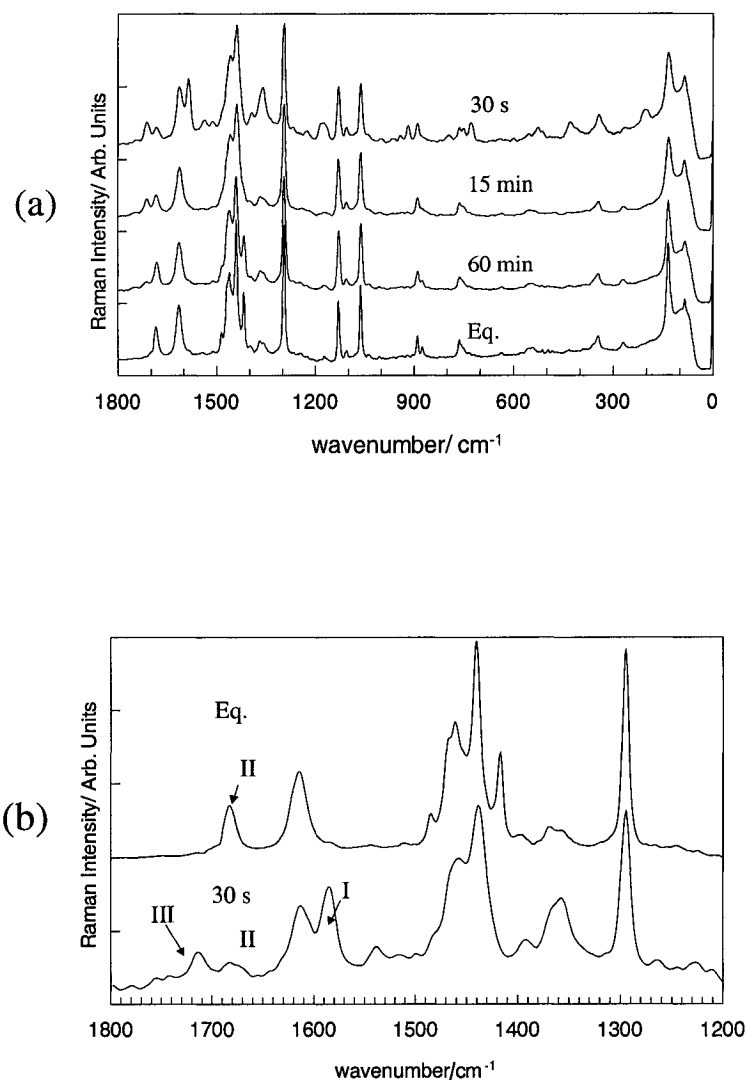
Figure 6.33. Crystal violet lactone/lauryl gallate/1-octadecanol (CVL/LG/OD, 1:6:40 mole ratio) was rapidly quenched in liquid nitrogen and allowed to equilibrate at 25 °C. (a) The Raman spectrum taken at selected time intervals shows the decrease of a C=N vibration at 1584 cm$^{-1}$ (Peak I), the growth of a carbonyl vibration at 1683 cm$^{-1}$ (Peak II), and the decrease of a C=O vibration at 1710 cm$^{-1}$ (Peak III). (b) Comparison of the Raman spectrum of crystal violet lactone/lauryl gallate/1-octadecanol (CVL/LG/OD, 1:6:40 mole ratio) immediately upon quenching (30 s) and at equilibrium (Eq.).
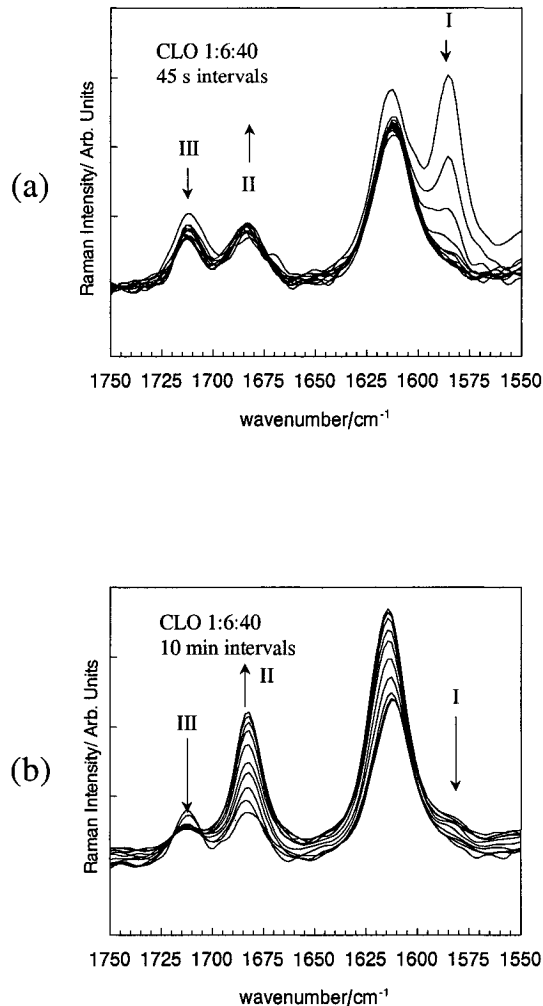
Figure 6.34. Raman spectrum of crystal violet lactone/lauryl gallate/1-octadecanol (CVL/LG/OD, 1:6:40 mole ratio) obtained at (a) 45 s intervals and (b) 10 minute intervals at 25 °C following rapid quenching in liquid nitrogen. A rapid decrease in the $(LG)_x \bullet CVL$ 1584 cm$^{-1}$ (Peak I) peak intensity and slow growth of the $(LG)_2 \bullet OD$ carbonyl vibration at 1683 cm$^{-1}$ (Peak II) is observed. Peak III (1710 cm$^{-1}$) decreases slowly following quenching.

At equilibrium the spectra of CVL/LG/OD (1:6:40 mole ratio) and LG/OD (6:40 mole ratio) were nearly identical (see Figure 6.36). LG/OD (6:40 mole ratio) was quenched in liquid nitrogen and its Raman spectrum measured as a function of time. Figure 6.36 shows the intensity of Peak II (1683 cm$^{-1}$) at selected time intervals.
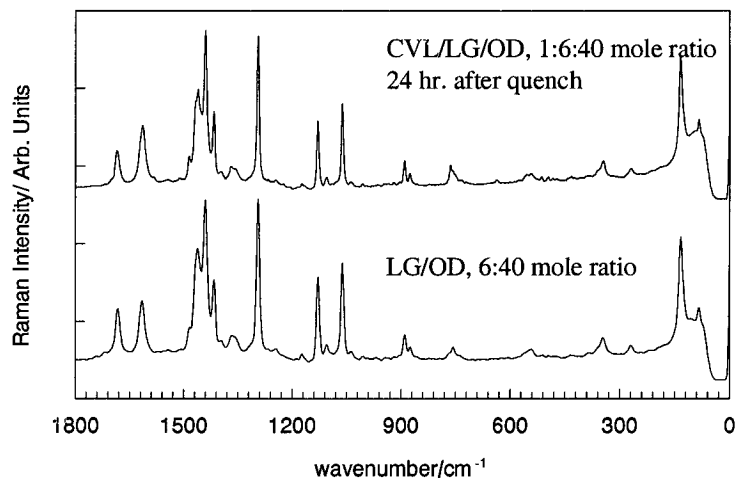
Figure 6.35. Comparison of the Raman spectra of equilibrated crystal violet lactone/lauryl gallate/1-hexadecanol (CVL/LG/OD, 1:6:40 mole ratio) and lauryl gallate/1-octadecanol (LG/OD, 6:40 mole ratio) shows that the spectral features are nearly identical.
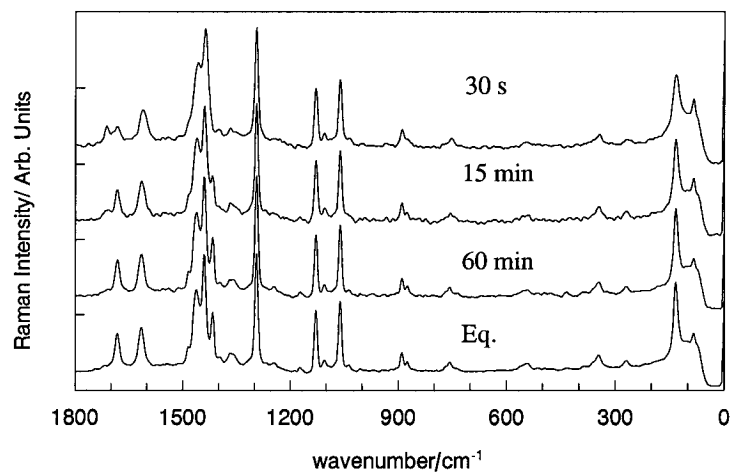


Figure 6.36. The Raman spectrum of lauryl gallate/1-octadecanol (LG/OD, 6:40 mole ratio) as a function of time after quenching in liquid nitrogen. Initially, the intensity of Peak II (1683 cm$^{-1}$), the carbonyl peak of lauryl gallate in (LG)$_2$•OD, is relatively weak. As time passes, the intensity of Peak II increases, corresponding to the formation of more (LG)$_2$•OD in the mixture.

Figure 6.37 compares the Peak II intensity for LG/OD and CVL/LG/OD. The formation of Peak II occurs more quickly in the binary LG/OD mixture. As is the case in the CVL/LG/OD mixture, the presence of CVL inhibits the formation of $(LG)_2$•alcohol compound.
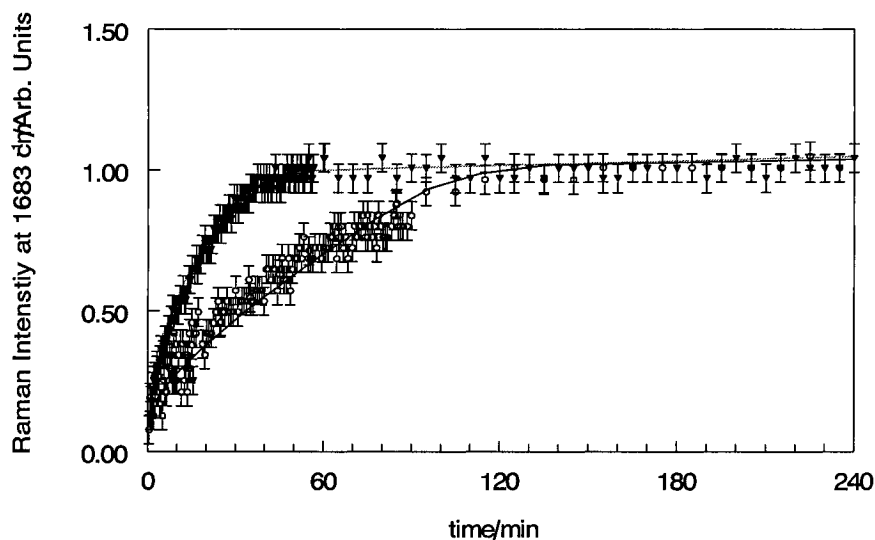


Figure 6.37. The intensity of Peak II, the carbonyl peak of lauryl gallate in $(LG)_2$•OD, plotted as a function of time for: (▼) a mixture of lauryl gallate/1-octadecanol (LG/OD, 6:40 mole ratio), and (○) a mixture of crystal violet lactone/lauryl gallate/1-octadecanol (CVL/LG/OD, 1:6:40 mole ratio), both quenched from the melt in liquid nitrogen and equilibrated at 25 °C. Intensities are normalized to their equilibrium values. Lines are added to guide the eye. Error bars represent the uncertainty over three experiments.

Peak III ($1710 \ cm^{-1}$) is observed upon quenching in both CVL/LG/OD 1:6:40 mole ratio and LG/OD 6:40 mole ratio and remains in the mixtures for long periods of time. Figure 6.38 shows the Raman intensity of the Peak III for CVL/LG/OD 1:6:40 and LG/OD 6:40 as a function of time following quenching in liquid nitrogen.
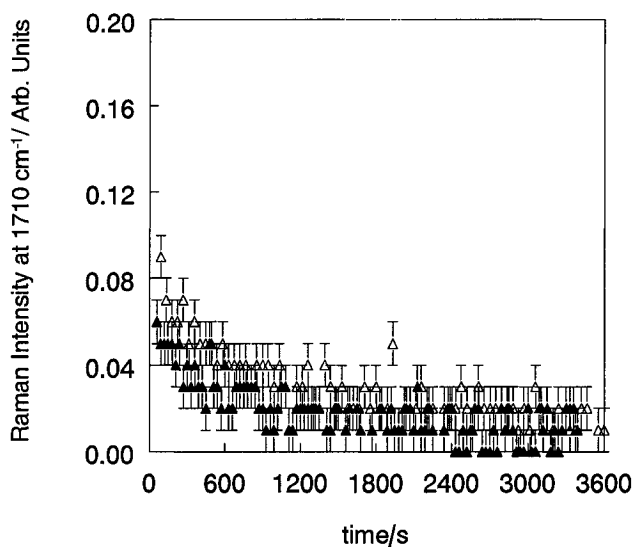
Figure 6.38. Peak III (1710 cm$^{-1}$) intensity for (▲) crystal violet lactone/lauryl gallate/1-octadecanol (CVL/LG/OD) 1:6:40 and (△) lauryl gallate/1-octadecanol (LG/OD) 6:40 as a function of time following quenching in liquid nitrogen and equilibration at 25 °C. Within experimental error the rate of Peak III decay is the same for the ternary and binary mixture. Error bars represent the uncertainty over three experiments.

Within experimental error, the rate of Peak III decay is the same in the ternary and binary mixtures. As is the case in the CVL/LG/HD system, the presence of CVL does not appear to influence the rate of the Peak III decay.

## 6.5. Discussion of Time-Resolved Raman Results

Time-resolved Raman spectroscopy is an excellent probe for examining the behaviour of thermochromic mixtures as the solvent component is changed. While the three thermochromic systems examined here show distinctively different thermochromic properties, all show the same three major features in the time-resolved Raman experiment. The only marked difference is in the rate at which they occur.

### 6.5.1. Peak I Summary

The rate of disappearance of Peak I (1584 cm$^{-1}$, shown in Figure 6.39) decreases as the solvent is changed from TD (where the peak is barely observable at 60 s) to HD and OD (where the peak remains present for approximately 5 min). The initial intensity of Peak I ($I^I$) also increases as the alkyl-chain length of the solvent is increased such that: $I^I_{CVL/LG/TD} \ll I^I_{CVL/LG/HD} < I^I_{CVL/LG/OD}$. This shows that increasing the solvent chain length results in the formation of more (LG)$_x$•CVL coloured complex in the metastable phase.

The decrease in Peak I (1584 cm$^{-1}$) intensity only indicates destruction of a strongly bonded (LG)$_x$•CVL complex, but colour still remains in CVL/LG/HD and CVL/LG/OD mixtures over long periods of time. No detectable ring-open CVL structure was observed in the Raman spectra of the mixtures at equilibrium. The composition of CVL is only about 2 mol% within the mixture, so it could be difficult to observe significant structural features using Raman spectroscopy. The predicted molar extinction coefficients for ring-open CVL are very high[122] and allow for significant colour density to exist with relatively small amounts of CVL.
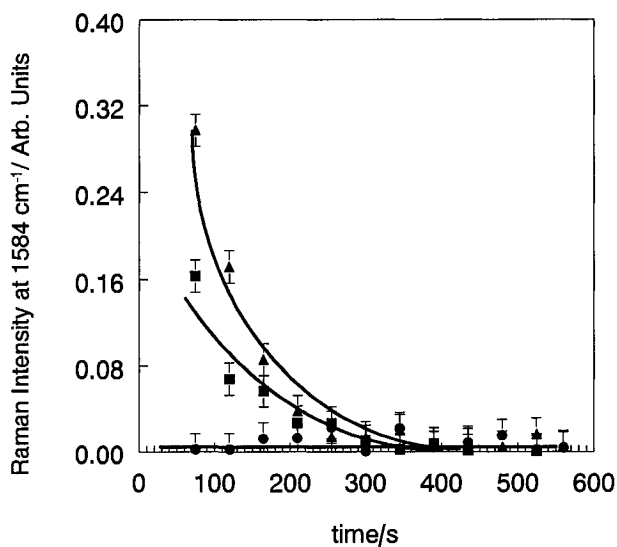
Figure 6.39. Comparison of the Raman intensity of Peak I, the C=N vibration at 1584 cm$^{-1}$ attributed to strongly bound ring-opened crystal violet lactone in (●) crystal violet lactone/lauryl gallate/1-tetradecanol (CVL/LG/TD, 1:6:40 mole ratio), (■) crystal violet lactone/lauryl gallate/1-hexadecanol (CVL/LG/HD, 1:6:40 mole ratio), and (▲) crystal violet lactone/lauryl gallate/1-octadecanol (CVL/LG/OD, 1:6:40 mole ratio). Error bars represent the uncertainty over three measurements.

Presumably, only small amounts of residual LG are required to produce visible colour at equilibrium. That most CVL/LG/TD mixtures display little detectable colour at equilibrium shows that there is very little, if any, interaction between LG and CVL in the mixture after equilibration following quenching from the melt.

### 6.5.2. Peak II Summary

Figure 6.22 and Figure 6.26 show that the Peak II (1683 cm$^{-1}$) intensity of CVL/LG/TD (1:6:40 mole ratio) equilibrates in about 3 to 6 min. This is much faster than the Peak II growth in corresponding CVL/LG/HD and CVL/LG/OD in 1:6:40 mole

ratios, which appear to equilibrate at about the same rate, or 1.5 to 2 hr. Therefore, the rate of Peak II formation is as follows: Rate Peak $II_{CVL/LG/TD}$ >> Rate Peak $II_{CVL/LG/HD}$ ~ Rate Peak $II_{CVL/LG/OD}$.

The rate of Peak II formation is slower in ternary mixtures than in their corresponding binary developer/solvent mixtures. The rate of Peak II formation in the binary mixtures shows a similar trend with the alcohol chain length such that: Rate Peak $II_{LG/TD}$ > Rate Peak $II_{LG/HD}$ ~ Peak Rate $II_{LG/OD}$.

In all ternary mixtures examined the intensity of Peak II observed 60 s after quenching is approximately 25% of the equilibrium intensity. In the corresponding binary mixtures, the initial Peak II intensity relative to equilibrium values varies from 70% in LG/TD, 50% in LG/HD, and 30% in LG/OD. This shows that the presence of CVL influences not only the rate of $(LG)_2\bullet$alcohol formation, but also the initial amounts present.

### 6.5.3. Peak III Summary

Figure 6.40 compares Peak III (1710 $cm^{-1}$) intensity of CVL/LG/TD, CVL/LG/HD, and CVL/LG/OD mixtures. It is interesting to note that the rate of Peak III loss is slowest in CVL/LG/HD. This indicates that the kinetic stability of $\alpha$-HD in CVL/LG/HD might be greater than that of $\alpha$-OD in CVL/LG/OD. In all CVL/LG/HD and CVL/LG/OD mixtures, the rate of Peak III loss is the same within experimental error. The rate of Peak III decay does not have an apparent effect on the observed thermochromic properties of the mixture; its slow conversion in HD systems does not

appear to effect the trends observed in equilibrium colour density and decolourisation rates. The role of the α-alcohol phase will be examined in more detail in Chapter 7.
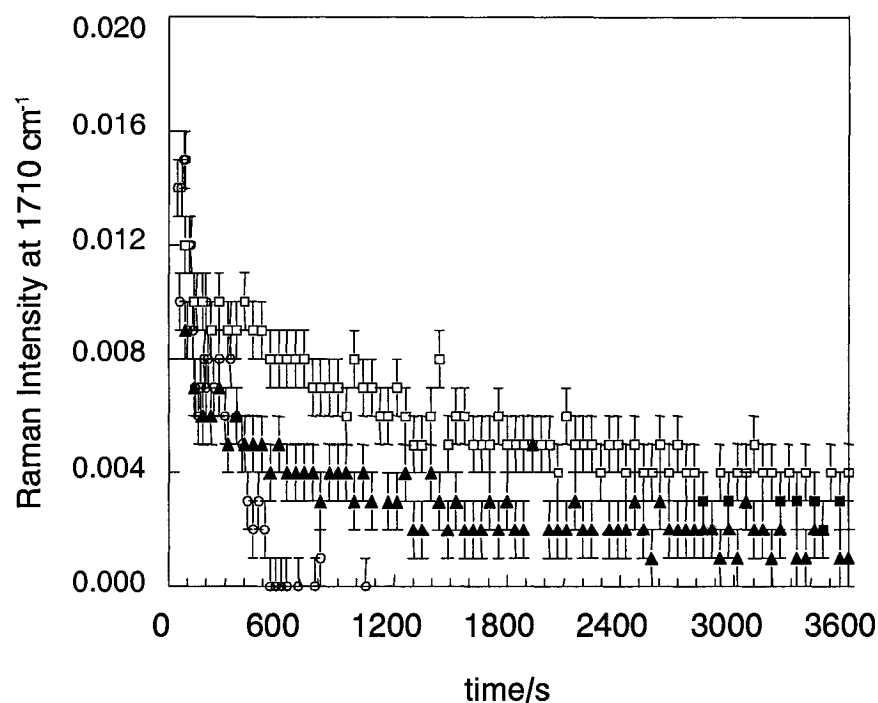


Figure 6.40. Comparison of the Raman intensity of the C=O vibration at 1710 cm$^{-1}$ attributed to weakly bound ring-opened in (○) crystal violet lactone/lauryl gallate/1-tetradecanol (CVL/LG/TD) 1:6:40, (□) crystal violet lactone/lauryl gallate1-hexadecanol (CVL/LG/HD) 1:6:40, and (▲) crystal violet lactone/lauryl gallate/1-octadecanol (CVL/LG/OD) 1:6:40. Error bars represent the uncertainty over three experiments.

### 6.5.4. Role of Competition in Thermochromic Properties

That $(LG)_2$•alcohol does not form equilibrium concentrations upon quenching in the binary system implies that some free LG and alcohol solvent exist in the metastable mixture that must combine to form $(LG)_2$•alcohol as the system equilibrates. The lower intensities of Peak II (1683 cm$^{-1}$) in the ternary mixtures relative to the binary mixtures after quenching implies that lower amounts of $(LG)_2$•alcohol are present due to the

interaction of LG with CVL. This is consistent with LG interacting initially (and strongly) with CVL. In order for LG to interact with the alcohol, it must first overcome its interaction with CVL. This interaction is a barrier to the transition that the binary LG/alcohol system does not encounter.

These observations, also presented in a recent publication,[197] imply that a competition exists between the dye and solvent for interaction with the developer. Interaction between LG and alcohol is weak in the melt, and the stronger interaction is between LG and CVL, producing a coloured complex, $(LG)_x$•CVL. Upon quenching the melt, the coloured complex is metastable with respect to the formation of $(LG)_2$•alcohol. If the temperature of the system is kept below its decolourisation temperature, the metastable coloured complex is long lived. Raising the temperature of the system allows the movement of LG from coloured complex $(LG)_x$•CVL and releases CVL to its colourless state, leading to decolourisation of the mixture.[197]

This role of the solvent is different than those proposed in Chapter 2.3.3. Some authors did mention the role of a developer-solvent aggregate, but it was metastable with respect to phase separated developer and solvent and acted to open the leuco dye and stabilize metastable colour density.[85]

Variation of thermochromic properties with the alkyl-chain length of the solvent implies that the interaction between LG and the alcohol solvent changes as the alkyl-chain length of the solvent is changed. The high concentration of $(LG)_2$•TD in the metastable state, combined with its rapid rate of formation, implies a strong attractive interaction between LG and TD. Decreased Raman peak intensities and rates of formation of $(LG)_2$•HD and $(LG)_2$•OD imply that the LG/HD and LG/OD attractive interactions are weaker than LG/TD. The degree of attractive interaction between the

solvent and developer components has a significant effect on the observed thermochromic properties and will be examined in detail in the next chapter.

# Chapter 7. Thermodynamic Analysis of Crystal Violet Lactone/Lauryl Gallate/Alcohol Mixtures

## 7.1. Lauryl Gallate/1-Alcohol Interactions

Important rewritable thermochromic properties such as colour contrast, colour stability, and decolourisation rates undergo dramatic changes in an archetypal thermochromic mixture as the solvent component is changed. The present spectroscopic studies lead to the conclusion that there is a competition between the thermochromic dye and the solvent for the colour developer. Changes in decolourisation rates, contrast, and colour stability of ternary thermochromic mixtures are related to the degree of attractive interaction between the solvent and colour developer.[197]

CVL is not soluble in the pure alcohols used in the present study; the presence of LG is necessary to ensure the formation of a homogeneous solution. With this in mind the interaction between CVL and the pure alcohols will not be considered.

The change in attractive interaction between lauryl gallate (LG) and three alcohols (1-tetradecanol (TD), 1-hexadecanol (HD), and 1-octadecanol (OD)) will be examined here through a thermodynamic analysis of the LG/alcohol solid-liquid phase diagrams and fusion enthalpy data. This body of work represents the first detailed assessment of the thermal properties of ternary thermochromic mixtures and provides valuable insight into the role of competition, as proposed in Chapter 6.

### 7.1.1. Lauryl Gallate/1-Alcohol Eutectic and (LG)$_2$•Alcohol Thermodynamic Behaviour

Phase diagrams are powerful analytical tools because they provide information on the stable distribution of phases and compositions at equilibrium.[1,189-191] Since the initial thermochromic mixtures are prepared through quenching to metastable states, phase diagrams indicate the preferred composition of the system at equilbrium and give insight into processes occurring as equilibrium is established. Eutectic and compound data provide preliminary information on the degree of interaction between LG and 1-alcohols. Eutectic data for the heating and cooling of LG/alcohol mixtures are shown in Table 7.1. The alcohol/(LG)$_2$•alcohol eutectic (eutectic 1) moves from $x_{LG}$ of about 0.07 in LG/TD through $x_{LG}$ of 0.22 in LG/OD while the eutectic 1 temperature increases consistently with the increase of the melting point of the pure alcohols (Tables 5.4-5.6). Eutectic 1 temperatures observed upon cooling the mixtures from the melt are lower than on heating due to sub-cooling of the mixture but also show an ascending trend as the alkyl-chain length of the alcohol increases. The position of the (LG)$_2$•alcohol/LG eutectic (eutectic 2) is more difficult to ascertain because the temperature difference between it and the (LG)$_2$•alcohol melting temperature is very small. Eutectic 2 falls in the range ~ 0.80 < $x_{LG}$ < 0.90 for all three mixtures when heated and tends toward the higher end of this range upon cooling. LG shows significant sub-cooling with a difference of 20 to 25 K in its melting temperature upon heating (371 to 373 K) and cooling (345 to 347 K).

Table 7.1. Eutectic data for the binary phase diagram of lauryl gallate/1-tetradecanol (*cf.* Figures 5.4-5.6). Eutectics are estimated from DSC thermograms of samples prepared near the eutectic composition. In general, three replicate measurements were obtained for each sample.

| *Heating* | $T_{eutectic\ 1}/K$ | $x_{LG,eutectic\ 1}$ | $T_{eutectic\ 2}/K$ | $x_{LG,eutectic\ 2}$ |
|---|---|---|---|---|
| LG/TD | $308 \pm 1$ | $0.07 \pm .01$ | $355 \pm 1$ | $0.80 \pm .05$ |
| LG/HD | $316 \pm 1$ | $0.16 \pm .02$ | $353 \pm 1$ | $0.80 \pm .05$ |
| LG/OD | $326 \pm 1$ | $0.22 \pm .02$ | $351 \pm 1$ | $0.80 \pm .05$ |

| *Cooling* | $T_{eutectic\ 1}/K$ | $x_{LG,eutectic\ 1}$ | $T_{eutectic\ 2}/K$ | $x_{LG,eutectic\ 2}$ |
|---|---|---|---|---|
| LG/TD | $307 \pm 1$ | $0.07 \pm .01$ | $342 \pm 1$ | $0.90 \pm .05$ |
| LG/HD | $316 \pm 1$ | $0.18 \pm .02$ | $341 \pm 1$ | $0.90 \pm .05$ |
| LG/OD | $324 \pm 1$ | $0.22 \pm .02$ | $340 \pm 1$ | $0.90 \pm .05$ |

The change in eutectic 1 as the chain length of the alcohol is increased indicates that there could be a chain length dependent change in interaction between the components of the mixture. Since the position of eutectic 1 is defined by the curvature of the alcohol liquidus and the $(LG)_2$•alcohol liquidus, such changes in interaction could occur in one component or both. It is not possible to make more quantitative conclusions without calculating the liquidus curves for each component.

Thermodynamic data for the $(LG)_2$•alcohol compound are shown in Table 7.2. $(LG)_2$•alcohol melting and fusion temperatures show a 2 to 3 K decrease for every two carbon increase in the alcohol alkyl-chain, *i.e.* $T_{fus,(LG)_2•OD} < T_{fus,(LG)_2•HD} < T_{fus,(LG)_2•TD}$. This is in contrast to the melting and fusion temperatures for the pure alcohols, which are in the opposite alkyl-chain length order, *i.e.* $T_{fus,OD} > T_{fus,HD} > T_{fus,TD}$ (Tables 5.4-5.6). The change in transition temperatures indicates that the stability of $(LG)_2$•alcohol increases as the alkyl-chain length of the alcohol decreases.

Table 7.2. Thermodynamic data for (LG)$_2$•alcohol formed in 1-tetradecanol/lauryl gallate, 1-hexadecanol/lauryl gallate, and 1-octadecanol/lauryl gallate mixtures. Temperature, enthalpy, and entropy data for (LG)$_2$•alcohol and lauryl gallate are based on the results of six replicate measurements. $T_m$ is the melting temperature, $\Delta_m H$ is the melting enthalpy change, $\Delta_m S$ is the melting entropy change, and $\Delta_{mix}S^{ideal}$ is the ideal mixing entropy change.

| | $T_m/K$ | $\Delta_m H/$ ($kJ$ $mol^{-1}$) | $\Delta_m S/$ ($J$ $K^{-1} mol^{-1}$) | $2\Delta_m S_{LG} + \Delta_m S_{alcohol} +$ $\Delta_{mix}S^{ideal}$ /($J$ $K^{-1} mol^{-1}$)[130,132] |
|---|---|---|---|---|
| (LG)$_2$•TD | 358.5 ± 0.5 | 94.9 ± 5 | 265 ± 15 | 246 ± 15 |
| (LG)$_2$•HD | 355.1 ± 0.5 | 95.1 ± 5 | 268 ± 15 | 272 ± 15 |
| (LG)$_2$•OD | 352.1 ± 0.5 | 91.5 ± 5 | 260 ± 15 | 298 ± 15 |

Enthalpy changes on melting for the three (LG)$_2$•alcohol compounds observed are the same within experimental error. However, as the alcohol chain length is increased, the melting temperature of the compound decreases slightly. Assuming an ideal LG/alcohol interaction in the melt, this implies that the strength of the bonding within the compound decreases slightly as the alcohol chain length increases. A possible explanation for this phenomenon is changes in the van der Waals interactions between the long chains of the two components. Although the structures of the compounds are not known, it is possible that inter-chain overlap plays a role in stabilization of (LG)$_2$•alcohol, *i.e.* the alkyl chain of the alcohol interdigitates with the alkyl-chains of LG. As the chain length of the alcohol becomes successively longer than 12 carbons (the chain length of LG) the degree of interchain interaction, and hence the net van der Waals stabilization, seems to decrease. Alcohols that are more weakly bound seem to break away from the complex at lower temperatures due to their enhanced mobility, resulting in lower melting temperatures of (LG)$_2$•alcohol relative to the pure constituent components.

Within experimental uncertainty, the melting entropy change ($\Delta_m S$) of all

(LG)$_2 \cdot$alcohol compounds examined are equal and comparable to the sum of $\Delta_m S$ for the

melting of 2 LG molecules and 1 alcohol molecule plus the ideal entropy of mixing,

$\Delta_{mix} S^{ideal}$ :

$$\Delta_{mix} S^{ideal} = -R \sum_i x_i \ln x_i \,.$$  7.1

Since the melting point of (LG)$_2 \cdot$alcohol is 20 to 40 K higher than the low-$T$ to $\alpha$-phase

transition of the three pure alcohol components, $\Delta_m S$ for the alcohol was represented by

$\Delta_m S$ for the melting of the $\alpha$-alcohol phase. That is, the lower-temperature phase

transitions were ignored although the disordering of the alcohol in the $\alpha$-phase phase

gives a much lower $\Delta_m S$ relative to ordered organic molecular compounds.[198,199]

### 7.1.2. Thermodynamic Analysis of Phase Diagram Data

Overall examination of a phase diagram provides only limited information

concerning the interaction between components. In order to develop detailed

understanding of component interaction, determination, and comparison of any deviation

from ideal interaction is required.

Determination of the interactions between the components of LG/alcohol

mixtures can be performed using regular solution theory.[189-191] An ideal solution is

assumed to have no interaction between components. Regular solutions account for non-

uniform intermolecular forces between the components by assuming that the change in

Gibbs energy of mixing ($\Delta_{mix} G$) and change in enthalpy of mixing ($\Delta_{mix} H$) are non-zero,

but the entropy change of the mixing ($\Delta_{mix} S$) is ideal (Eq. 7.1).[189]

When examining the interaction between two components in a mixture it is convenient to determine the Gibbs energy of mixing, $\Delta_{mix}G$, and enthalpy of mixing, $\Delta_{mix}H$. $\Delta_{mix}G$ and $\Delta_{mix}H$ represent the energies required to overcome repulsive interactions when mixing components, or the energies liberated when two components with attractive interactions are mixed.[189-191] When two components interact they deviate from ideal behaviour: this deviation can be described by an excess thermodynamic function. The excess thermodynamic function, $Z^{EX}$, can be defined for a general thermodynamic function, $Z$, as:[189]

$$Z^{EX} = Z^{real} - Z^{ideal}. \qquad\qquad 7.2$$

For an AB mixture, $\Delta_{mix}G^{EX}$, the excess Gibbs energy of mixing, is expressed as:[189]

$$\Delta_{mix}G^{EX} = RT\sum_i x_i \ln \gamma_i = RTx_A \ln \gamma_A + RTx_B \ln \gamma_B, \qquad 7.3$$

where $\gamma_i$ is the activity coefficient for component, $i$.

A full expression of the excess Gibbs energy of mixing requires knowledge of the activity coefficients ($\gamma_i$) for all the components present in the solution. Since the activity coefficients are dependent on $T$, $P$, and composition, they would need to be determined for all compositions, temperatures, and pressures under consideration for a full description of the mixture.[189] For practical application of regular solution theory it is convenient to use an approximation for the activity coefficients.[189] The simplest approximation is to represent the excess Gibbs energy as a parabolic function of the form:[189-191]

$$\Delta G^{EX} = W^G x_A x_B, \qquad\qquad 7.4$$

where $W^G$ is defined as an interaction parameter. $W^G$ is expressed in energy units and is the energy required to replace a mole of component A with a mole of component B in a binary AB mixture.[189-191] A negative value of $W^G$ is correlated with an attractive interaction between A and B in the system and a negative deviation from ideal behaviour. A positive value of $W^G$ indicates a repulsive interaction between A and B and a positive deviation from ideal behaviour. $W^G$ replaces the activity coefficients in Eq. 7.3 as follows:[189-191]

$$\ln \gamma_A = \frac{W^G}{RT}\left(1 - x_A\right)^2 \qquad 7.5$$

$$\ln \gamma_B = \frac{W^G}{RT}x_A^2, \qquad 7.6$$

allowing Eq. 7.3 to be expressed as:

$$\Delta_{mix}G^{EX} = x_A W^G x_B^2 + x_B W^G x_A^2. \qquad 7.7$$

Since $x_B = 1-x_A$, Eq. 7.7 can be rewritten as:

$$\Delta_{mix}G^{EX} = W^G x_A x_B. \qquad 7.8$$

The Gibbs energy of mixing for an AB mixture $(\Delta_{mix}G)$ therefore can be expressed as:

$$\Delta_{mix}G = \Delta_{mix}G^{ideal} + \Delta_{mix}G^{EX} = RTx_A \ln x_A + RTx_B \ln x_B + W^G x_A x_B. \qquad 7.9$$

The first two terms in Eq. 7.9 are the ideal entropy of mixing (Eq. 7.1) multiplied by $T$, therefore the excess enthalpy of mixing can be expressed as:

$$\Delta_{mix}H^{EX} = \Delta_{mix}G^{EX} - T\Delta_{mix}S^{EX} = W^G x_A x_B = W^H x_A x_B, \qquad 7.10$$

where $\Delta_{mix}H^{EX} = \Delta_{mix}G^{EX}$ and $W^H = W^G$.[189-191]

In the present study, interaction parameters were determined for binary mixtures using two methods. The first method involved an examination of the experimental

liquidus of the binary phase diagram of a mixture. This method is based upon that of Farnia *et al.*[200] and Prigogine and Defay.[190]

Deviation of the liquidus temperature from values predicted by the ideal freezing point depression (Eq. 5.1) is caused by interaction between components. The liquidus of each component, $i$, in an AB system is expressed as:[190,200]

$$T_m^{obs,i} = \left[ \frac{\dfrac{\Delta_m H_i^o}{R} + \dfrac{W^H{}_i x_i^2}{R}}{\dfrac{\Delta_m H_i^o}{RT_{m,i}} - \ln(1 - x_i)} \right].$$
7.11

Eq. 7.11 can be fit to experimental liquidus data using $W^H{}_i$ as a fitting parameter.

A second method of determining interaction parameters is by examining the enthalpy changes of phase transitions observed in binary mixtures using the Margules equation. The simplest form is the one-parameter Margules equation, defined as: [189]

$$\Delta H^{EX} = W^H x_A x_B$$
7.12

such that for the melting of a component within the mixture:[189]

$$\Delta_m H_i^{obs} = \Delta_m H_i^{ideal} + \Delta H_i^{EX} = x_i \Delta_m H_i^o + W^H x_i (1 - x_i).$$
7.13

Observed enthalpy changes can be plotted as a function of mole fraction and Eq. 7.13 fit to the experimental enthalpy data with $W^H$ as a fitting parameter.

### 7.1.3. Examination of 1-Alcohol Liquidus and Transition Enthalpy Changes

The alcohol liquidus for each LG/alcohol phase diagram was calculated by fitting Eq. 7.11 to the experimental liquidus data. Experimental and calculated liquidus data are shown in Figures 7.1, 7.2, and 7.3.
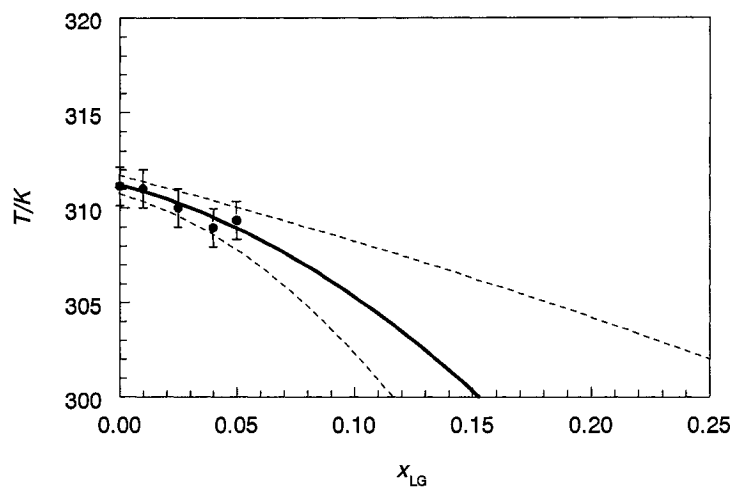
Figure 7.1. Calculated and experimental data for the 1-tetradecanol liquidus of the lauryl gallate/1-tetradecanol (LG/TD) binary phase diagram. An interaction parameter $W^H{}_{TD}$ of $-20 \pm 10$ kJ mol$^{-1}$ produces a liquidus in reasonable agreement with experimental data. Dashed lines represent the range of uncertainties associated with $T_m$ and $\Delta_m H$ for 1-tetradecanol in Eq. 7.11.
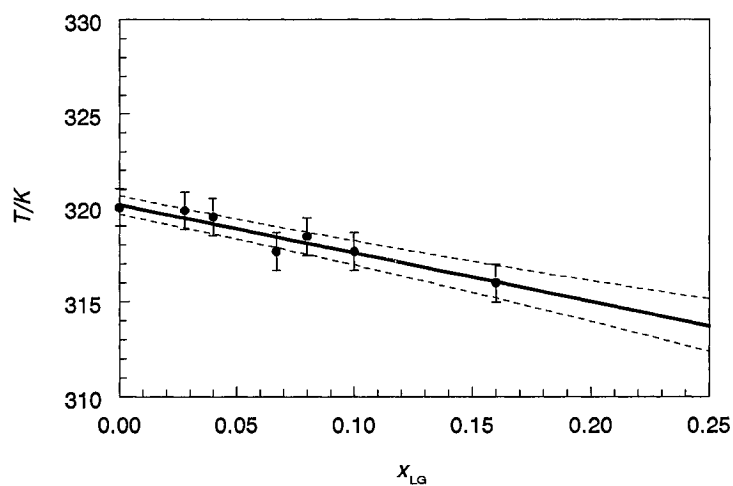


Figure 7.2. Calculated and experimental data for the 1-hexadecanol liquidus of the lauryl gallate/1-hexadecanol (LG/HD) binary phase diagram. An interaction parameter $W^H{}_{HD}$ of $+1.4 \pm 4$ kJ mol$^{-1}$ produces a liquidus in reasonable agreement with experimental data. Dashed lines represent the range of uncertainties associated with $T_m$ and $\Delta_m H$ for 1-hexadecanol in Eq. 7.11.
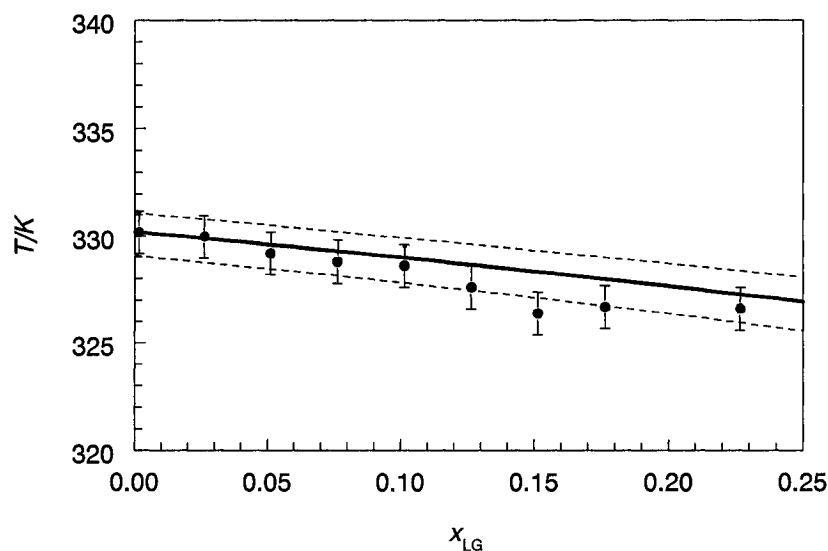
Figure 7.3. Calculated and experimental data for the 1-octadecanol liquidus of the lauryl gallate/1-octadecanol (LG/OD) binary phase diagram. An interaction parameter $W^H_{OD}$ of -2.2 ± 2 kJ mol$^{-1}$ produces a liquidus in reasonable agreement with experimental data. Dashed lines represent the range of uncertainties associated with $T_m$ and $\Delta_m H$ for 1-octadecanol in Eq. 7.11.

Calculated $W^H_{alcohol}$ values (Table 7.3) show an attractive interaction when the alcohol chain length is 14 carbons, and nearly no non-ideal interaction at longer chain lengths.

Table 7.3. $W^H_{alcohol}$ values determined through alcohol liquidus calculation for 1-tetradecanol, 1-hexadecanol, and 1-octadecanol in lauryl gallate/alcohol mixtures. $r^2$ is the statistical goodness-of-fit.

| System | $W^H_{alcohol}$ / (kJ mol$^{-1}$) | $r^2$ |
|--------|--------|--------|
| LG/TD | -20 ± 10 | 0.864 |
| LG/HD | +1.4 ± 4 | 0.803 |
| LG/OD | -2.2 ± 2 | 0.852 |

Eq. 7.13 was used to analyze the fusion enthalpies of the binary mixtures determined by DSC. Since significant kinetic stabilization of the $\alpha$-alcohol phase occurs, examination of the heating of the mixtures was problematic. First, the $\beta/\gamma$-$\alpha$ and $\alpha$-liquid transitions of alcohols within LG/alcohol mixtures were not easily resolved in the DSC thermogram. Second, the LG/alcohol mixtures were generally heated soon after preparation or following a cooling step within the DSC program. This made the relative amount of $\alpha$ and $\beta/\gamma$ phase unknown as the mixture was heated. The two transitions (liquid-$\alpha$ and $\alpha$-$\beta$ or $\gamma$) were more resolved in the cooling DSC thermograms, where it was assumed that all liquid alcohol present in the mixture first transformed to the $\alpha$-phase prior to conversion to the lower temperature phase. Therefore, transition enthalpies of the liquid to $\alpha$-alcohol transition were used to calculate the excess properties for the three binary mixtures.

Using Eq. 7.13 to examine the alcohol fusion enthalpy required an adjustment of the mole fractions used relative to those used in the phase diagram liquidus calculation. According to the phase diagrams in Chapter 5, the ideal fusion enthalpy of the pure alcohol phase goes to zero at $x_{LG} = 0.67$ (*i.e.* $x_{(LG)_2\bullet alcohol} = 1$). The enthalpy changes analyzed at present are those of the solidus transitions on the $(LG)_2\bullet$alcohol rich side of the alcohol/$(LG)_2\bullet$alcohol eutectic (eutectic 1). Since solid $(LG)_2\bullet$alcohol is formed at the liquidus transition, the amount of alcohol transforming at the solidus is less than that given by $x_{LG}$, and must determined by $x_{(LG)_2\bullet alcohol}$.

In the conventional determination of enthalpy of mixing discussed in Section 7.1.2, heating, melting, and mixing of components is generally examined. In this case, an

attractive interaction (negative deviation) is represented by a decrease in the magnitude of the endothermic melting enthalpy because mixing is exothermic. In this analysis of the cooling of LG/alcohol mixtures, the fusion and subsequent *demixing* of a mixture was examined. In this case, a negative deviation from ideality was represented by a positive *demixing* enthalpy that decreased the magnitude of the exothermic fusion event. Thus, positive interaction parameters represent negative deviation and *vice versa*. (For example, $W^{H}$= -8 kJ mol$^{-1}$ for the mixing of components A+B upon melting to a liquid phase is equivalent to $W^{H}$= +8 kJ mol$^{-1}$ for the demixing of the liquid back to the solid phase.) Figures 7.4, 7.5, and 7.6 show the observed and calculated fusion enthalpies of the liquid-$\alpha$ alcohol transition of LG/TD, LG/HD, and LG/OD mixtures.
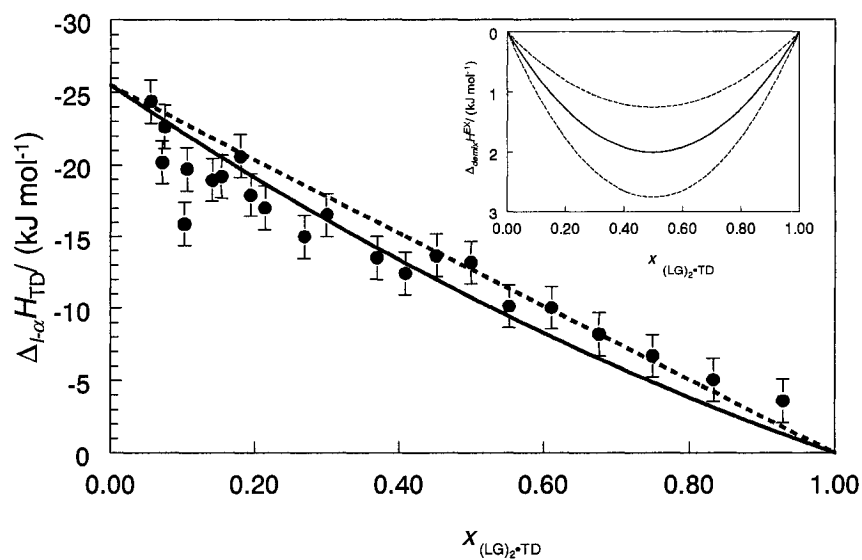
Figure 7.4. Experimental (points) and calculated (solid line) enthalpy changes for the liquid-α transition of 1-tetradecanol within the lauryl gallate/1-tetradecanol (LG/TD) binary mixture at 307 ± 1 K. $W^H{}_{TD}$ = +8 ± 3 kJ mol$^{-1}$ was found in agreement with experimental data. The ideal fusion enthalpy is shown by the dashed line. Data are plotted so that negative deviations from ideality fall below the ideal enthalpy line. The excess enthalpy for the fusion event and its uncertainty are shown in the inset.
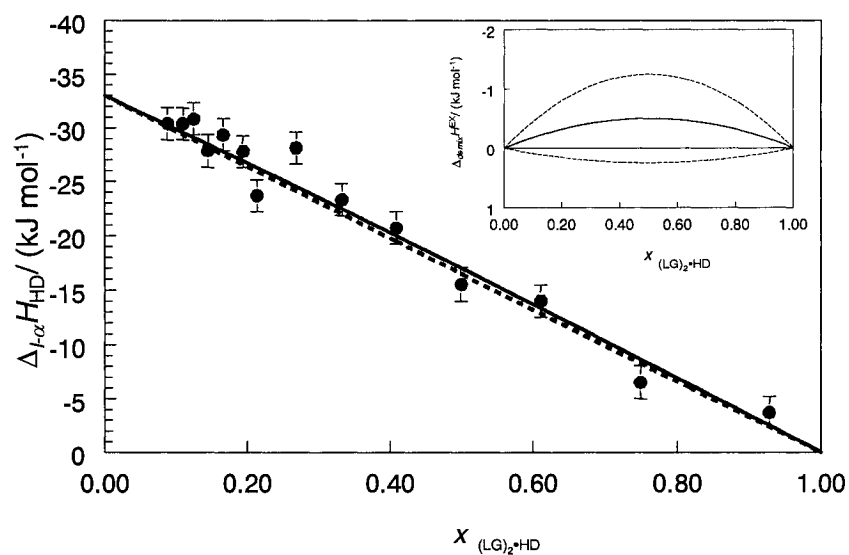
Figure 7.5. Experimental (points) and calculated enthalpy changes for the liquid-$\alpha$ transition of 1-hexadecanol within the lauryl gallate/1-hexadecanol (LG/HD) binary mixture at 316 ± 1 K. $W^H{}_{HD}$ = -2 ± 3 kJ mol$^{-1}$ was found in agreement with experimental data. The ideal fusion enthalpy is shown by the dashed line. Data are plotted so that negative deviations from ideality fall below the ideal enthalpy line. The excess enthalpy for the fusion event and its uncertainty are shown in the inset.
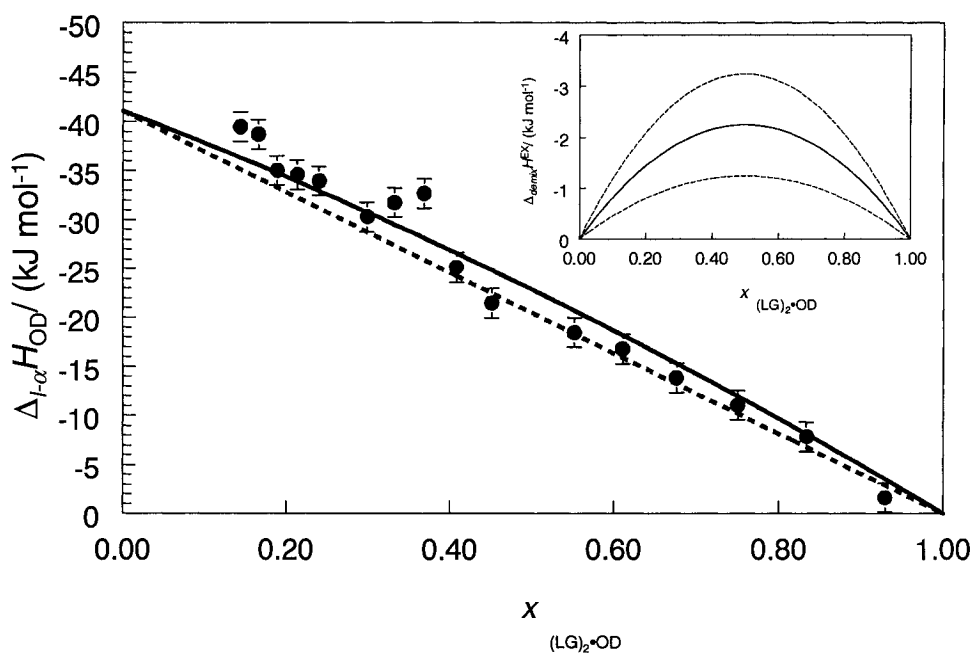
Figure 7.6. Experimental (points) and calculated (solid line) enthalpy changes for the liquid-α transition of 1-octadecanol within the lauryl gallate/1-octadecanol (LG/OD) binary mixture at 324 ± 1 K. $W^H_{OD}$ = -9 ± 3 kJ mol$^{-1}$ was found in agreement with experimental data. The ideal fusion enthalpy is shown by the dashed line. Data are plotted so that negative deviations from ideality fall below the ideal enthalpy line. The excess enthalpy for the fusion event and its uncertainty are shown in the inset.

$W^H_{alcohol}$ values determined from the liquid-α alcohol fusion data are shown in Table 7.4 and show a trend similar to $W^H_{alcohol}$ values determined from the liquidus data (Table 7.3): an attractive interaction when the alkyl chain is 14 carbons, and nearly ideal behaviour at longer chain lengths.

Table 7.4. $W^H_{alcohol}$ determined for the liquid-$\alpha$ alcohol fusion data in binary lauryl gallate/alcohol mixtures. Recall that the sign of $W^H$ is positive for attractive interaction and negative for repulsive interaction when considering the fusion event. $r^2$ is the statistical goodness-of-fit.

| System | $W^H_{alcohol}$/ $(kJ\ mol^{-1})$ | $r^2$ |
|---|---|---|
| LG/TD | $8 \pm 3$ | 0.917 |
| LG/HD | $-2 \pm 3$ | 0.940 |
| LG/OD | $-9 \pm 4$ | 0.915 |

The values of $W^H_{alcohol}$ determined by the two methods are in agreement; TD has a stronger attractive interaction with LG than either LG/HD or LG/OD. There is likely a sequential decrease in the attractive interaction between LG and the alcohols as the alcohol chain length is increased (*i.e.* attractive interaction of LG/TD > LG/HD > LG/OD). However, within experimental error, it can only be concluded that the attraction between LG/TD is the strongest of the three binary mixtures and that LG/HD and LG/OD display weaker interactions, near ideality.

### 7.1.4. Examination of the Lauryl Gallate Liquidus

The liquidus of pure LG was calculated using Eq. 7.11. Calculated and experimental LG liquidus data are shown in Figures 7.7, 7.8 and 7.9. $W^H_{LG}$ values represent the interaction between LG and the alcohol as they mix in the liquid state. (In the region of the phase diagram in the LG-rich side of the LG/(LG)$_2$•alcohol eutectic, (LG)$_2$•alcohol melts at the solidus, presumably decomposing to form LG and free alcohol.)

DSC thermograms of mixtures with $x_{LG} > 0.67$ displayed thermal events that were closely spaced and difficult to resolve on heating or cooling. The difficulty in separating the LG transition enthalpies from the $(LG)_2 \cdot$alcohol transition enthalpies made the uncertainty associated with a Margules type enthalpy large and a full analysis impractical. Calculated $W^H_{LG}$ values, shown in Table 7.5, are similar in all three binary mixtures.
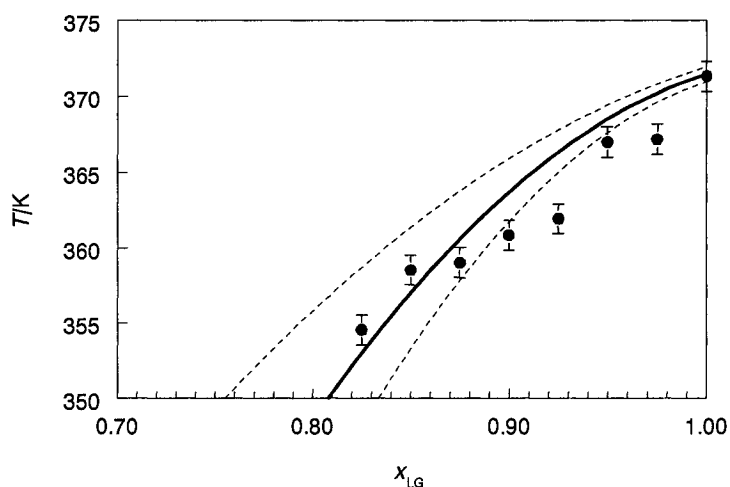


Figure 7.7. Calculated and experimental data for the lauryl gallate liquidus of the lauryl gallate/1-tetradecanol (LG/TD) binary phase diagram. An interaction parameter $W^H_{LG} = -29 \pm 5$ kJ mol$^{-1}$ produces a liquidus in reasonable agreement with experimental data. Dashed lines represent the range of uncertainties associated with $T_m$ and $\Delta_m H$ for lauryl gallate in Eq. 7.11.
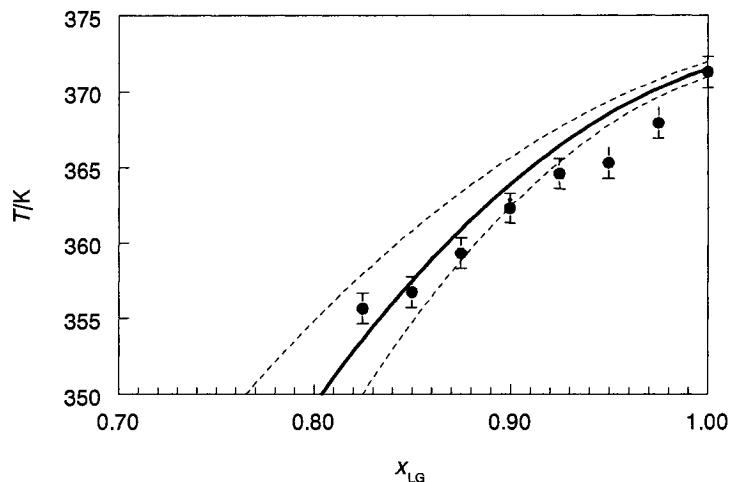
Figure 7.8. Calculated and experimental data for the lauryl gallate liquidus of the lauryl gallate/1-hexadecanol (LG/HD) binary phase diagram. An interaction parameter $W^H{}_{LG}$ = -27 ± 4 kJ mol$^{-1}$ produces a liquidus in reasonable agreement with experimental data. Dashed lines represent the range of uncertainties associated with $T_m$ and $\Delta_m H$ for lauryl gallate in Eq. 7.11.
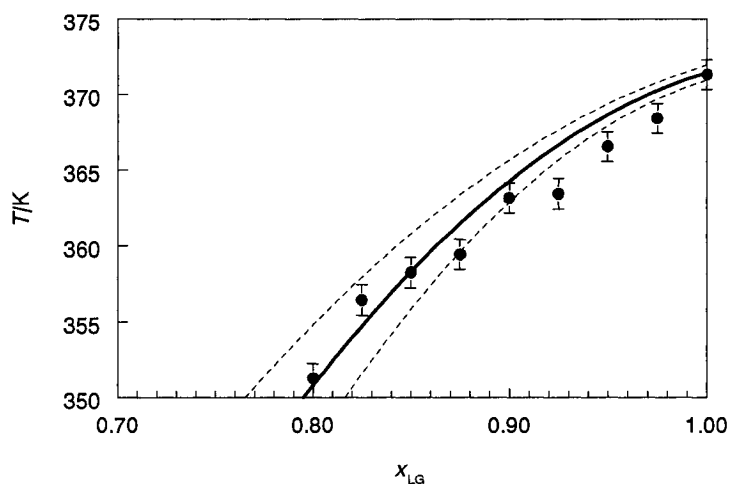


Figure 7.9. Calculated and experimental data for the lauryl gallate liquidus of the lauryl gallate/1-octadecanol (LG/OD) binary phase diagram. An interaction parameter $W^H{}_{LG}$ = -24 ± 3 kJ mol$^{-1}$ produces a liquidus in reasonable agreement with experimental data. Dashed lines represent the range of uncertainties associated with $T_m$ and $\Delta_m H$ for lauryl gallate in Eq. 7.11.

Table 7.5. Interaction parameters determined from the lauryl gallate liquidus of lauryl gallate/alcohol phase diagrams. $r^2$ is the statistical goodness-of-fit.

| System | $W^H{}_{LG}/$ (kJ mol$^{-1}$) | $r^2$ |
|--------|-------------------------------|-------|
| LG/TD  | -29 $\pm$ 5                    | 0.845 |
| LG/HD  | -27 $\pm$ 4                    | 0.910 |
| LG/OD  | -24 $\pm$ 3                    | 0.864 |

### 7.1.5. Examination of the Liquidus and Transition Enthalpies of (LG)$_2$•Alcohol

Calculation of the compound liquidus is not as straightforward as liquidus calculations for pure alcohols and LG. Kuznetsov et al. derived a general expression for calculating the liquidus for the equilibrium of an A$_m$B$_n$ compound with its liquid mixture in a binary AB system where it was assumed that A$_m$B$_n$ completely dissociates upon melting[201] (the zero slope of the liquidus of the LG/alcohol binary phase diagrams at the compound composition verifies this assumption).[192] The liquidus expression is given by:

$$\Delta_m H_{AB_2}\left[\frac{1}{T_{m,AB_2}} - \frac{1}{T}\right] = R \ln\left[\left(\frac{(1-x_B)(m+n)}{m}\right)^m \left(\frac{(x_B)(m+n)}{n}\right)^n\right]$$

$$+ \frac{W^H}{T}\left[m x_B^2 + n(1-x_B)^2 - \left(\frac{mn}{m+n}\right)\right]. \qquad 7.14$$

Since (LG)$_2$•alcohol is of the form AB$_2$ ($m = 1$, $n = 2$), Eq. 7.14 can be expressed as:[191,201]

$$\Delta_m H_{AB_2}\left[\frac{1}{T_{m,AB_2}} - \frac{1}{T}\right] = R\ln\left[[3 - 3x_B]\left[\left(\frac{3}{2}\right)x_B\right]^2\right]$$

$$+ \frac{W^H}{T}\left[x_B^2 + 2(1 - x_B)^2 - \left(\frac{2}{3}\right)\right], \qquad 7.15$$

where $\Delta_m H_{AB_2}$ and $T_{m,AB_2}$ are the enthalpy of melting and melting temperature of the pure

compound, $AB_2$. Eq. 7.14 can be rearranged and expressed in terms of $T(x_B)$, the liquidus

temperature, where $AB_2$ is in equilibrium with an A and B mixture:[191,201]

$$T(x_B) = \frac{\left[W^H\left[x_B^2 + 2(1 - x_B)^2 - \left(\frac{2}{3}\right)\right] + \Delta_m H_{AB_2}\right]}{\dfrac{\Delta_m H_{AB_2}}{T_{m,AB_2}} - R\ln\left[[3 - 3x_B]\left[\left(\frac{3}{2}\right)x_B\right]^2\right]}. \qquad 7.16$$

Eq. 7.16 produces the temperature of the liquidus of the $AB_2$ system as a function

of $x_B$, the mole fraction of B in the system, with a single fitting parameter, $W^H_B$.

A close examination of the LG/alcohol binary phase diagrams (Figures 5.4-5.6)

shows that the curvature of the $(LG)_2$•alcohol is not constant. In the calculation of LG

and alcohol liquidus curves in the previous sections, constant $W^H$ values produced

liquidus curves in good agreement with experimental data. Change in liquidus curvature

can occur when $W^H$ varies significantly as a function of temperature and mole fraction.

In the simplest case, Eq. 7.16 can be expressed in terms of $W^H(T, x_B)$:[191,201]

$$W^H(T, x_B) = \frac{T\Delta_m H_{AB_2}\left[\dfrac{1}{T_{m,AB_2}} - \dfrac{1}{T}\right] - R\ln\left[[3 - 3x_B]\left[\left(\frac{3}{2}\right)x_B\right]^2\right]}{\left[x_B^2 + 2(1 - x_B)^2 - \left(\frac{2}{3}\right)\right]}, \qquad 7.17$$

and can be used to calculate $W^H(T, x_B)$ for every experimental liquidus point. From Eq.

7.17, the relationship between $W^H$ (and subsequently $H^{EX}$) and $x_B$ can be determined.

It was found that the data below $x_{LG} = 0.50$ gave results that were distinguishable from experimental error in the temperature measurements. First, the interaction potential, $W^H$, was calculated for each $(T, x_{LG})$ value using Eq. 7.17. Next, a function for $W^H(x_{LG})$ was determined by linear regression of the data. The curves of $W^H(x_{LG})$ are shown in Figure 7.10 for LG/TD, LG/HD, and LG/OD mixtures.
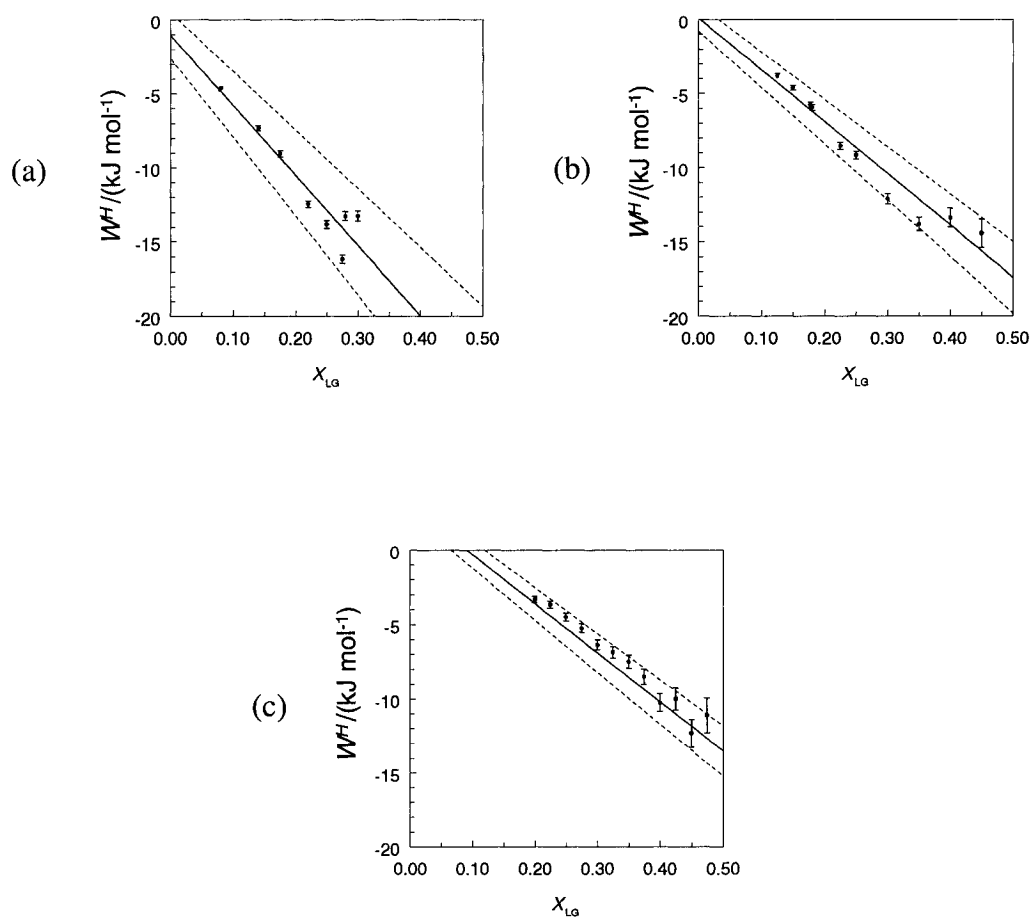


Figure 7.10. Experimental $W^H(x_{LG})$ values (points) are shown with their linear fit for the liquidus of (a) (LG)$_2$•TD (b) (LG)$_2$•HD and (c) (LG)$_2$•OD. Dashed lines represent the uncertainty in $W^H(x_{LG})$.

The fit parameters for $W^H_{LG} = L + Mx_{LG}$ are shown in Table 7.6. The $(LG)_2$•alcohol

liquidus can be calculated in the $x_{LG} = 0$ to 0.67 region by placing the expression for

$W^H(x_{LG})$ into Eq. 7.16. Calculated and experimental liquidus data for $(LG)_2$•TD,

$(LG)_2$•HD, and $(LG)_2$•OD (Figure 7.11) are in good agreement with experimental liquidus

values. The excess enthalpy of mixing, $\Delta_{mix}H^{EX}$, is shown for the three systems in Figure

7.12 . $\Delta H^{EX}$ for the fusion and dissociation of $(LG)_2$•alcohol becomes more negative as

the concentration of $(LG)_2$•alcohol in the mixture increases. $W^H_{(LG)_2•alcohol}$ (and $\Delta H^{EX}$ for

$(LG)_2$•alcohol) represent a more attractive interaction as the chain length of the alcohol

component is lengthened.

Table 7.6. The fit parameters for $W^H(x_{LG})$ = $L + M(x_{LG})$ for the liquidus of $(LG)_2$•alcohol. Standard deviations are shown in parenthesis. $r^2$ is the statistical goodness-of-fit.

| System | $L/(kJ\ mol^{-1})$ | $M/(kJ\ mol^{-1})$ | $r^2$ |
|--------|--------------------|--------------------|-------|
| LG/TD  | $-1 \pm 1.5$       | $-47 \pm 6$        | 0.890 |
| LG/HD  | $+0.1 \pm 0.9$     | $-35 \pm 3$        | 0.970 |
| LG/OD  | $+3 \pm 0.7$       | $-33 \pm 2$        | 0.968 |
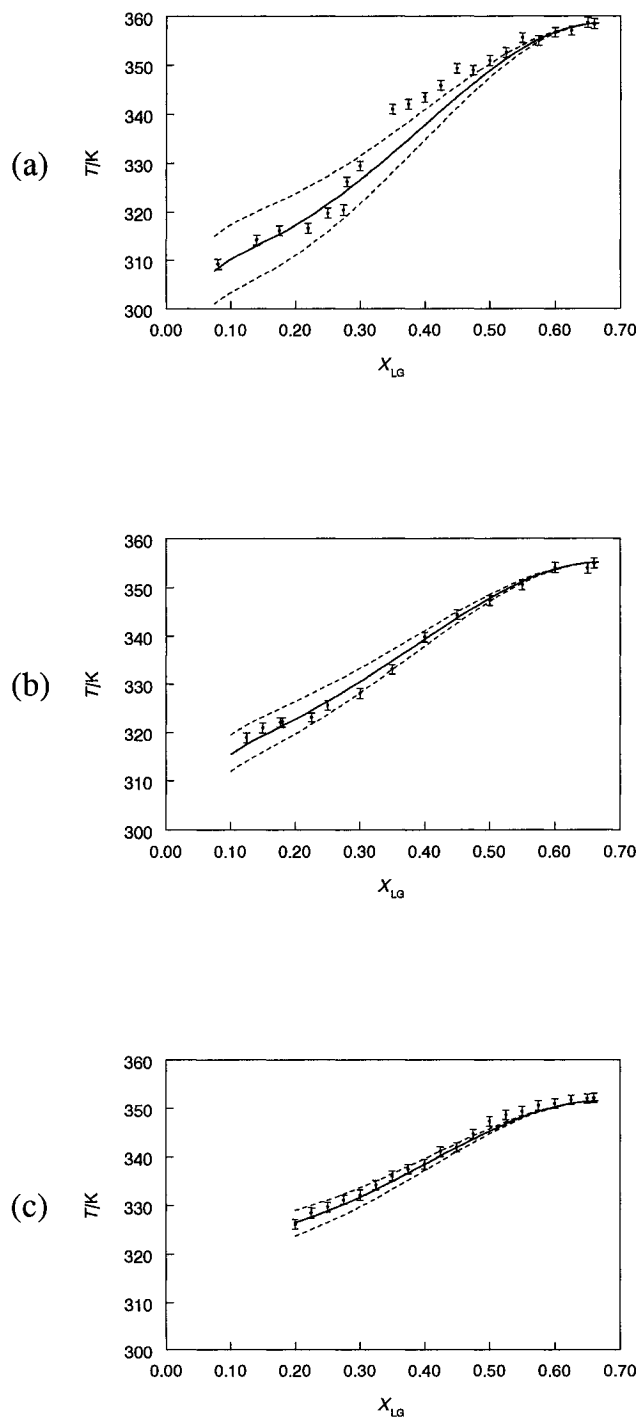
Figure 7.11. Experimental liquidus data points are shown with the calculated liquidus data (solid line) of (a) (LG)$_2$•TD (b) (LG)$_2$•HD and (c) (LG)$_2$•OD. Dashed lines represent the range of uncertainties associated $W^H(x_{LG})$.
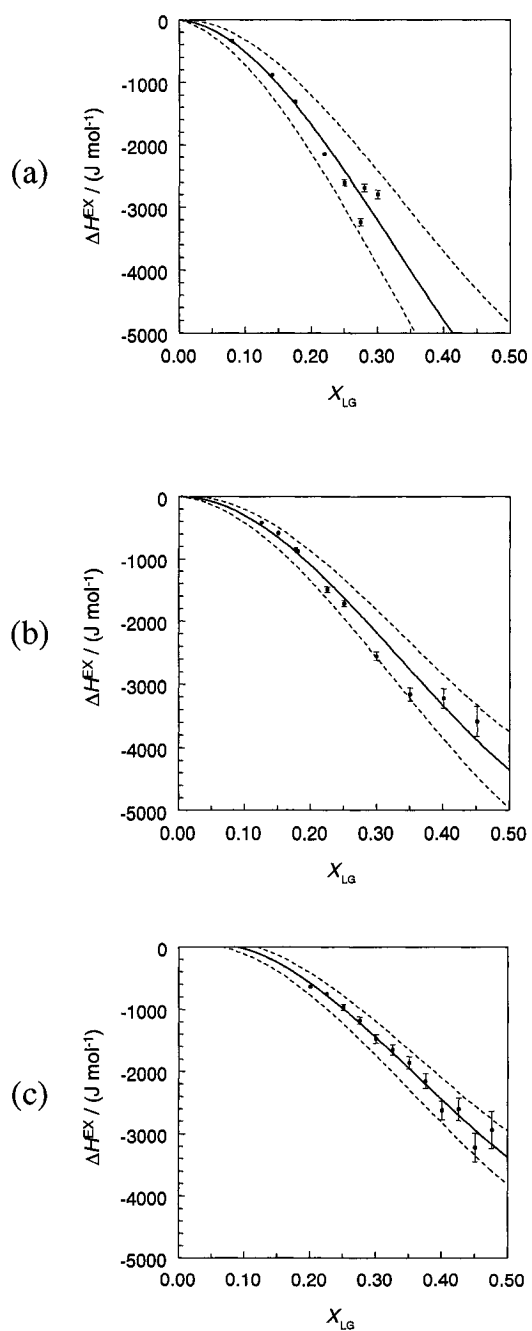
Figure 7.12. Experimental $\Delta_{mix}H^{EX}$ data are shown with their fit (solid line) for (a) $(LG)_2 \bullet TD$ (b) $(LG)_2 \bullet HD$ and (c) $(LG)_2 \bullet OD$. Dashed lines represent the range of uncertainties associated $W^H(x_{LG})$.

Differences in $W^H_{(LG)_2 \cdot alcohol}$ are more pronounced below $x_{LG} = 0.20$ (the region of $x_{LG}$ composition of interest to the present study). The increase of attractive interaction for $(LG)_2 \cdot TD$, compared with $(LG)_2 \cdot HD$ and $(LG)_2 \cdot OD$ follows the same trend as the change in attractive interaction observed for the pure alcohol components observed earlier in the chapter.

### 7.2. Significance of Lauryl Gallate/1-Alcohol Interaction on Time-Resolved Raman Data

The discussion at the end of Chapter 6 and the results from the first portion of this chapter show that the competition between CVL and alcohol for interaction with lauryl gallate will favour the alcohol such that: 1-tetradecanol $>>$ 1-hexadecanol $\geq$ 1-octadecanol. Increased LG/alcohol attraction results in a decrease in the amount of coloured complex (represented by Raman Peak I at 1584 $cm^{-1}$) observed immediately upon quenching. Rates of $(LG)_2 \cdot alcohol$ formation (represented by Raman Peak II at 1683 $cm^{-1}$) are faster in binary and ternary mixtures as the attractive interaction between LG and alcohol increases. Only the presence of the rotational alcohol phase (represented by Raman Peak III at 1710 $cm^{-1}$) is not fully explained by the LG/alcohol interaction.

### 7.3. Isothermal DSC of Thermochromic Mixtures

Detailed information concerning the behaviour of ternary thermochromic mixtures and their binary developer-solvent counterparts has been determined using spectroscopic techniques (Chapter 6). In this section thermal analysis of thermochromic mixtures will help to correlate structural changes to observed enthalpy changes.

### 7.3.1. Crystal Violet Lactone/Lauryl Gallate/1-Tetradecanol

The Cryofill™ cooling apparatus on the Pyris 1 DSC allows rapid cooling and equilibration of samples. This instrumentation was used to simulate the thermal conditions required for colour development and equilibration of thermochromic mixtures observed in the diffuse reflectance and Raman spectroscopic analyses. Samples of CVL/LG/TD were heated to well above their melting temperatures (373 K) and cooled at a rate of 300 K min$^{-1}$ to several isotherms: 288 K, 293 K, 298 K, and 303 K. The same experiment was also performed on various LG/TD mixtures to compare the thermal properties of the developer-solvent matrix to the ternary dye/developer/solvent mixture. Differential heat flow was measured for 30 min following quenching. Two major thermal events were observed for all samples examined. Figure 7.13 shows a representative sample of the isothermal DSC thermogram of a CVL/LG/TD mixture following rapid quenching. A large peak is observed with maximum heat flow of approximately -20 to -40 J g$^{-1}$ observed at 20 to 30 s following the quenching: this peak is designated the *fast event*. A second, smaller peak is observed after 30 s to 10 min following quenching. This broad peak is designated the *slow event*, and shows considerable overlap with the fast event.
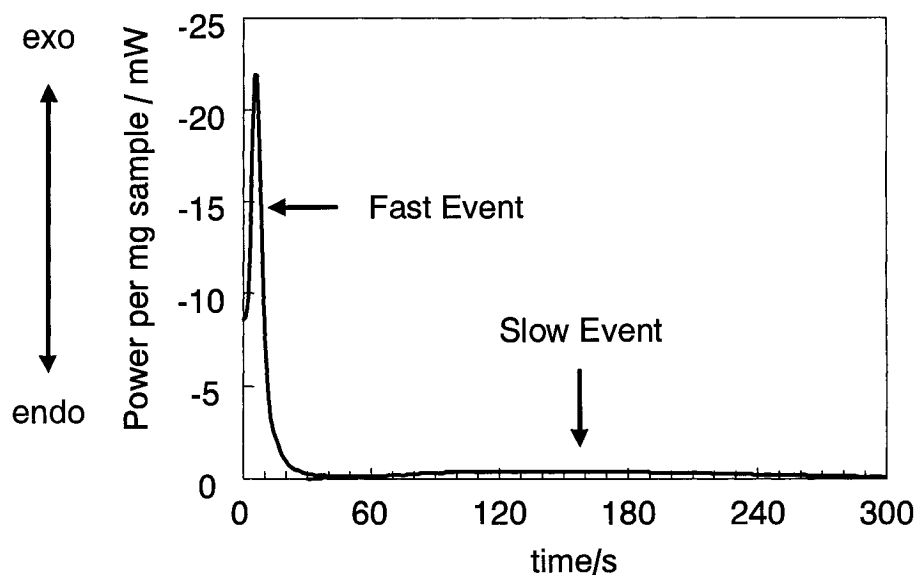
Figure 7.13. An isothermal (298 K) DSC thermogram of a crystal violet lactone/lauryl gallate/1-tetradecanol (CVL/LG/TD, 1:6:50 mole ratio) mixture following quenching from the melt shows two major thermal events. The *fast event* occurs within 0 to 20 s after cooling and the *slow event* occurs 2 to 10 min after cooling.

In order to assign specific thermal events to these peaks a reasonably accurate separation of their areas is required. Integration of the total area (fast event + slow event) was performed using the integration software of the Perkin Elmer Pyris 1™ DSC software. Separation of peak areas within the Pyris 1™ software is limited so the area of the slow event was calculated numerically. Although there was significant peak overlap between the two events, fast event peak maxima were generally resolved. The peak shape of the slow event was assumed to be symmetric about its maximum and the area was determined by numerically integrating the slow event from the peak maximum time to a longer time where the baseline was invariant. Doubling this peak area provided an estimate of the enthalpy change for the slow event which was then subtracted from the total area to provide the enthalpy change of the fast event. Numerical integration was performed on raw heat flow data with a Microsoft Excel spreadsheet using the Trapezoid Rule with $n$ = 3000 to 5000 and $\Delta x$ = 1 s :[202]

$$\int_a^b f(x)dx \approx \Delta x\left(\sum_i^n \frac{f(x_i)+f(x_{i+1})}{2}\right). \qquad 7.18$$

Figures 7.14 and 7.15 show DSC thermograms for the fast event and slow event

for selected CVL/LG/TD mixtures. The fast event displays a large peak that reaches

baseline power values within 30 s. The slow event shows variation in peak time, ranging

from 30 s to 10 min following rapid quenching. Both the fast and slow events vary with

composition.
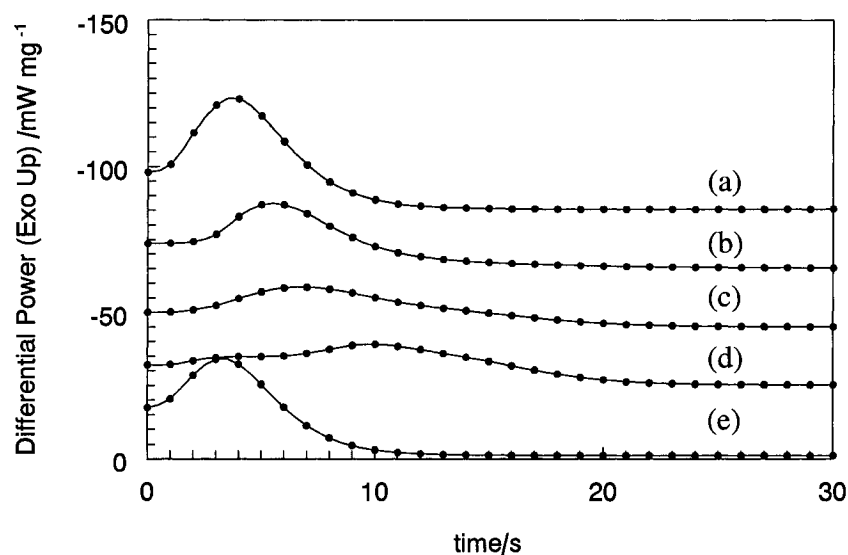


Figure 7.14. DSC thermogram data (points) for the fast event observed in crystal violet lactone/lauryl gallate/1-tetradecanol (CVL/LG/TD) mixtures of mole ratio (a) 1:3:50 (b) 1:6:50 (c) 1:9:50 (d) 1:12:50 and (e) 1:24:50 held at 298 K isotherms following quenching from the melt at 300 K min$^{-1}$.
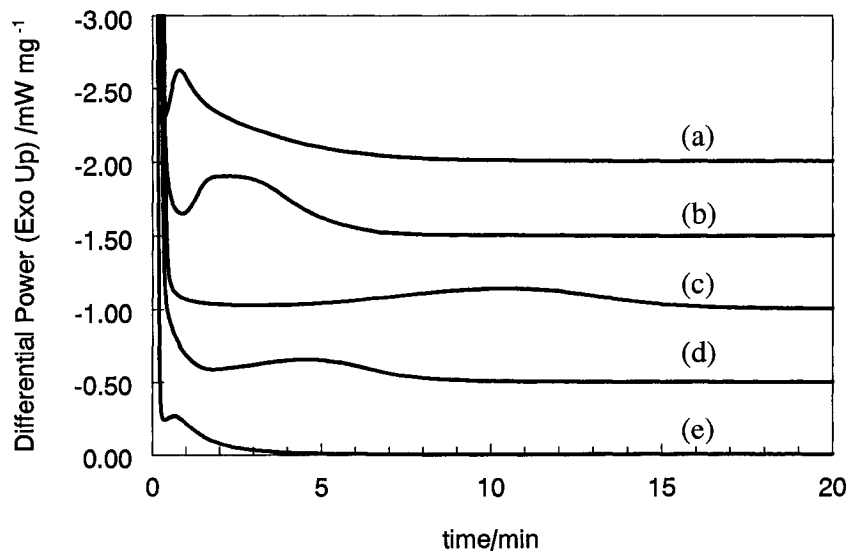
Figure 7.15. DSC thermograms of the slow event observed in crystal violet lactone/lauryl gallate/1-tetradecanol (CVL/LG/TD) mixtures of mole ratio (a) 1:3:50 (b) 1:6:50 (c) 1:9:50 (d) 1:12:50 and (e) 1:24:50 held at 298 K isotherms following quenching from the melt at 300 K min$^{-1}$.

Similar thermal events (Figures 7.16 and 7.17) were observed in binary LG/TD mixtures with compositions corresponding to the ternary mixtures. Figure 7.16 shows that the fast event occurs in approximately the same time as in CVL/LG/TD mixtures, equilibrating in less than 30 s. The slow event in binary LG/TD (Figure 7.17) mixtures has a peak at about 1 to 2 min and equilibrates in less than 5 min. The variation in peak time as a function of LG composition observed in ternary CVL/LG/TD mixtures was not observed in the binary LG/TD mixtures.
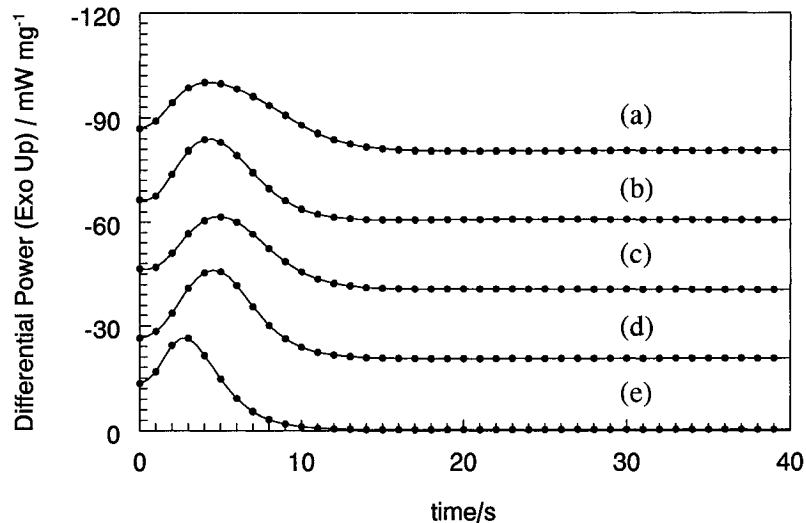
Figure 7.16. DSC thermogram data for the fast event observed in lauryl gallate/1-tetradecanol (LG/TD) mixtures of mole ratio (a) 3:50 (b) 6:50 (c) 9:50 (d) 12:50 and (e) 24:50 held at 298 K isotherms following quenching from the melt at 300 K min$^{-1}$.
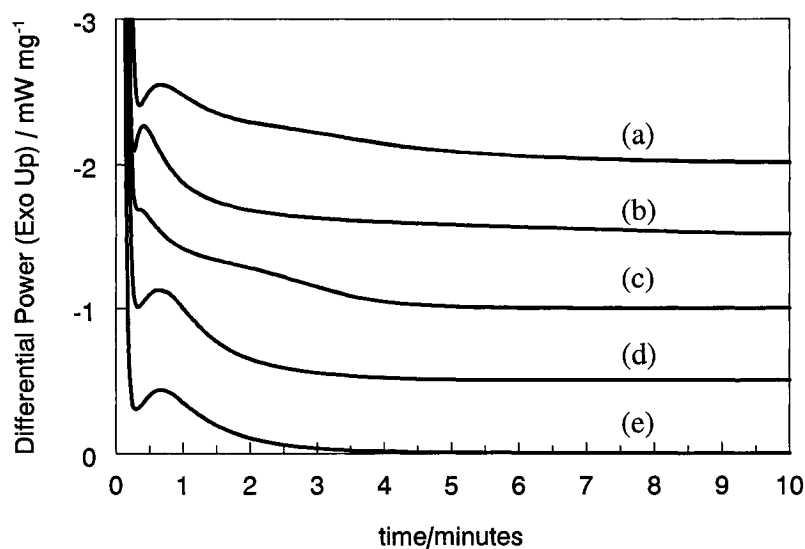


Figure 7.17. DSC thermograms of the slow event observed in lauryl gallate/1-tetradecanol (LG/TD) mixtures of mole ratio (a) 3:50 (b) 6:50 (c) 9:50 (d) 12:50 and (e) 24:50 held at 298 K isotherms following quenching from the melt at 300 K min$^{-1}$.

### 7.3.2. Assignment of Thermal Events

The total enthalpy change of both thermal events (fast + slow) in CVL/LG/TD is

shown in Figure 7.18 as a function of $x_{(LG)_2 \cdot TD}$. The summed ideal fusion enthalpy for the

transitions observed in the Raman analysis (liquid → $(LG)_2 \cdot TD_{solid}$ + $\alpha$-$TD_{solid}$) and ($\alpha$-

$TD_{solid}$ → $\beta$-$TD_{solid}$) is compared with the experimental points and shows that the data are

consistent with these processes. Data points represent the average values of events

observed at 293, 298, and 303 K isotherms.

Figure 7.19 compares the enthalpy changes for the

CVL/LG/TD slow event with the ideal enthalpy of the $\alpha$-$\beta$ TD transition. Again, the

average values of events observed at 293, 298, and 303 K isotherms are presented.
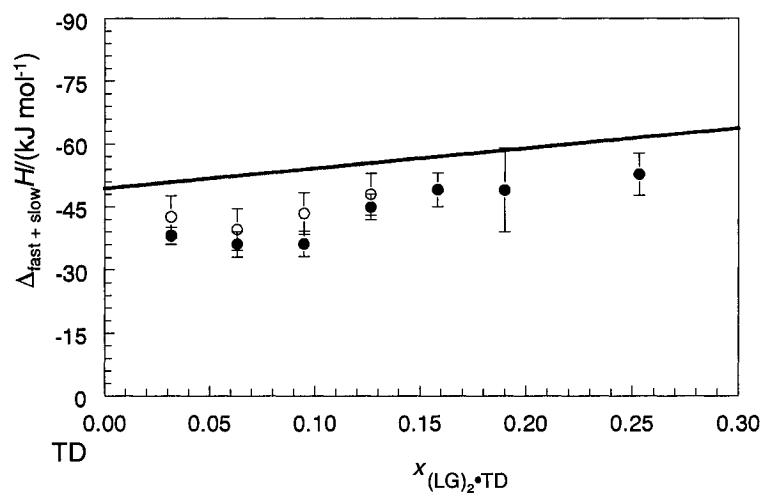


Figure 7.18. Total enthalpy changes for both thermal events (fast + slow) in (●) crystal violet lactone/lauryl gallate/1-tetradecanol (CVL/LG/TD) and (○) lauryl gallate/1-tetradecanol (LG/TD) mixtures were measured using Pyris DSC software. Data are compared with the summed ideal enthalpy changes for the fusion of 1-tetradecanol to the $\alpha$-phase, the fusion of $(LG)_2 \cdot TD$, and the transition of $\alpha$-tetradecanol to $\beta$-tetradecanol (solid line).
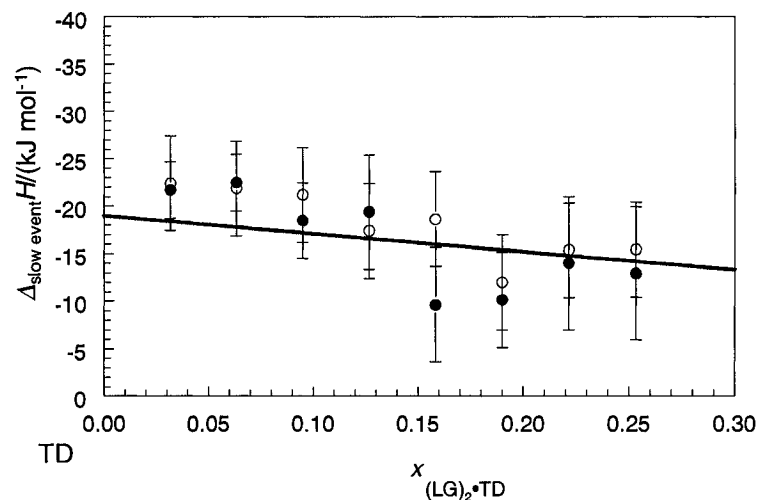
Figure 7.19. Enthalpy changes of the slow event observed in (●) crystal violet lactone/lauryl gallate/1-tetradecanol (CVL/LG/TD) and (○) lauryl gallate/1-tetradecanol (LG/TD) mixtures were integrated numerically from raw DSC data and are compared with the ideal enthalpy for the $\alpha$-$\beta$ phase transition of 1-tetradecanol in the solid mixture (solid line).

The enthalpy changes of the CVL/LG/TD fast event were estimated by subtracting the calculated enthalpy of the slow event from the total experimental enthalpy (fast + slow event). Fast event enthalpy changes are compared with the ideal transition enthalpy changes for the fusion of the molten mixture to a mixture of solid $(LG)_2\bullet TD$ and $\alpha$-TD in Figure 7.20.
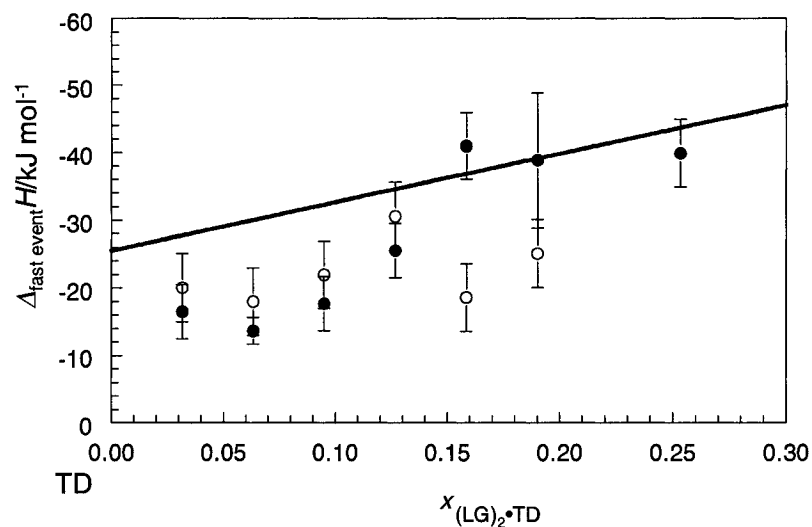
Figure 7.20. Enthalpy changes of the fast event observed in (●) crystal violet lactone/lauryl gallate/1-tetradecanol (CVL/LG/TD) and (○) lauryl gallate/1-tetradecanol (LG/TD) mixtures were determined by subtracting the numerically integrated slow event enthalpy changes from the total enthalpy obtained from the DSC software. Data are compared with the summed ideal enthalpy changes for the fusion of 1-tetradecanol to the $\alpha$-phase and the fusion of (LG)$_2$•TD (solid line).

Figure 7.21 shows the cooling and isothermal (298 K) steps of the differential heat flow data for the DSC thermograms of a CVL/LG/TD (mole ratio 1:15:50) mixture at a series of cooling rates ranging from 300 K min$^{-1}$ to 50 K min$^{-1}$. At rapid cooling rates, all thermal events were observed during the isotherm. As the cooling rate is decreased, the large, fast peak splits into two separate events consistent with the observed phase diagram of the binary LG/TD mixture: and corresponding to the solidification of the (LG)$_2$•TD compound followed by the conversion of TD from the liquid to the $\alpha$-phase.
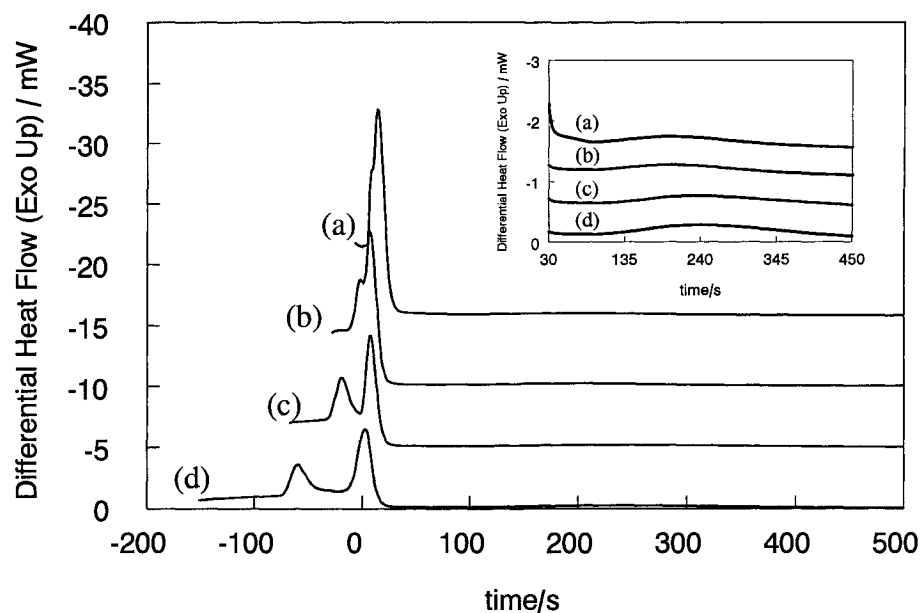
Figure 7.21. Cooling and isothermal (298 K) steps in the differential heat flow data for the DSC thermograms of crystal violet lactone/lauryl gallate/1-tetradecanol (CVL/LG/TD, at a 1:15:50 mole ratio) at cooling rates of (a) 300 K $\text{min}^{-1}$ (b) 200 K $\text{min}^{-1}$ (c) 100 K $\text{min}^{-1}$ and (d) 50 K $\text{min}^{-1}$. Time $= 0$ s is correlated with the beginning of the isothermal step. As the cooling rate decreases the fast thermal event divides into two separate events. The slow event is shown in the inset and is virtually invariant with the cooling rate.

Another interesting feature of Figure 7.21 is that all the thermograms for the slow event occur at approximately the same time (peak maximum ~ 240 s) following cooling of the mixture. This shows that the rate of quenching from the melt has little effect on the kinetics of the slow event of TD within the solid. This is of consequence to the time-resolved Raman experiments presented in Chapter 6; although care is taken to ensure consistent quenching in liquid nitrogen there is no way to accurately ascertain the actual cooling rates.

While the observed thermal events appear to be correlated with a rapid solidification of the mixture to $(\text{LG})_2 \cdot \text{TD}$ and $\alpha$-TD followed by the slow conversion of

α-TD to β-TD, it is important to note the structural changes observed in the Raman analysis. Peaks consistent with the presence of $(LG)_2 \cdot TD$ (Peak II) and α-TD (Peak III) are observed immediately upon quenching. As time passes, Peak II (1683 cm$^{-1}$) increases and Peak III (1710 cm$^{-1}$) decreases in intensity. Therefore, only a portion of the equilibrium amount of $(LG)_2 \cdot TD$ is formed in the solid on quenching. In the case of CVL/LG/TD mixtures the formation of $(LG)_2 \cdot TD$ and conversion of α- to β-TD appear to occur simultaneously. With this in mind the assignment of the thermal events observed in the isothermal DSC experiment is as follows: the fast event consists of the fusion of α-TD and a large portion of $(LG)_2 \cdot TD$ from the liquid mixture and the slow event is a combination of α to β-TD conversion and the formation of the remainder of $(LG)_2 \cdot TD$. The intensity of Peak II in CVL/LG/TD (1:6:40 mole ratio) in Figure 6.26 is 20-60% of equilibrium intensity immediately after quenching. It is important to note that the quenching rates in the Raman experiments are significantly faster than in the DSC experiment and that the amount of $(LG)_2 \cdot TD$ observed on quenching is not known for certain.

Combination of the small concentrations of $(LG)_2 \cdot TD$ (< 25mol%) and the large uncertainty in the enthalpies it is not possible to determine the relative amounts of $(LG)_2 \cdot TD$ formed in the fast and slow events. For example, for a mixture of composition $x_{(LG)_2 \cdot TD} = 0.10$ the enthalpy for complete $(LG)_2 \cdot TD$ formation is ~17% of the total enthalpy expected for the formation of $(LG)_2 \cdot TD$ + β-TD. Regardless of the proportion of $(LG)_2 \cdot TD$ formation compared with the slow event, the enthalpy of $(LG)_2 \cdot TD$ would be comparable to the uncertainty in the measured enthalpies due to the limitations of the thermogram peak separations.

### 7.3.3. Kinetics of Observed Thermal Events

Figures 7.14 and 7.15 show little variation in peak times for the fast event as a function of LG concentration or the concentration of CVL. While there is some broadening of the peaks for CVL/LG/TD relative to the corresponding LG/TD mixtures, all thermal events appear to be complete within 20 s of the start of the isotherm. Within experimental error, the enthalpy changes of the fast event are the same in the LG/TD and CVL/LG/TD mixtures.

The slow event in LG/TD mixtures, assigned to $\alpha$-$\beta$ TD plus $(LG)_2$•TD conversion, appears invariant to LG concentration; peak maximum times are approximately 30 to 45 s for all mixtures studied. However, addition of CVL to the mixture has a significant effect on the kinetics of this transition. While CVL/LG/TD 1:3:50 and 1:24:50 show peak maxima comparable to those observed in LG/TD 3:50 and 24:50 (at about 1 min), peak times for intermediate LG concentrations increase to a maximum of 10 min for CVL/LG/TD 1:9:50. This is consistent with the Raman data that showed a significant change in the rate of $(LG)_2$•TD formation (Peak II, Figure 6.26) and $\alpha$-$\beta$ TD (Peak III, Figure 6.24) in the ternary mixture relative to the corresponding binary mixture. However, separation of the two thermal events is not possible within the uncertainty of the measurement.

### 7.3.4. Comparison With Time-Resolved Data

Time-resolved Raman data for CVL/LG/TD predict the destruction of a coloured complex $((LG)_x$•CVL$)$ followed by the formation of $(LG)_2$•TD and the $\alpha$-$\beta$ TD phase transition. Enthalpy data for CVL/LG/TD and LG/TD are comparable within experimental error, so any enthalpy change associated with the destruction of $(LG)_x$•CVL

and formation of $(LG)_2 \bullet TD$ is not resolved. Based on Raman Peak I (1584 cm$^{-1}$) data, $(LG)_x \bullet CVL$ destruction occurs on the same time scale of the fast thermal event.

It is important to note that the $\alpha$-$\beta$ TD phase transition is a significant factor and that its rate appears to be dependent on the presence of CVL. The DSC slow event peak maximum time (300 s) of CVL/LG/TD 1:6:50 is comparable with the Raman Peak III (1710 cm$^{-1}$) equilibration (240 to 300 s) observed in CVL/LG/TD (mole ratio 1:6:40) (Figure 6.24). Binary LG/TD mixtures display the $\alpha$-$\beta$ TD phase transition in less than 60 s, consistent with the absence of Raman Peak III (1710 cm$^{-1}$) in the spectra of quenched LG/TD (mole ratio 6:40) (Figure 6.25). Comparison of the two sets of results shows that, in the case of CVL/LG/TD, formation of $(LG)_2 \bullet TD$ and the $\alpha$-$\beta$ TD phase transition appear to take place simultaneously.

Variation in the structural changes with $x_{LG}$ in CVL/LG/TD mixtures is not understood at present. The $\alpha$-$\beta$ TD phase transition, $(LG)_2 \bullet TD$ formation, and variations in decolourisation rates as a function of $x_{LG}$ could be related to microstructural features such as crystal size within the mixture. Another possibility to consider is the role of sample size in the observed behaviour of the mixture. Sample size can often play an important role in the phase transitions kinetics of solid-state processes because of the possibility that the material at the surface behaves differently than the bulk material.[123] The kinetics of solid phase reactions and solid-solid phase transitions are inherently more complicated than gas phase and liquid phase reactions.[123,203] The major difference is in the number of atoms involved. Classical kinetics is based on gas phase reactions (and can be extended to liquid phase systems) where reactants and products diffuse quickly through the reaction medium.[203] Solid phase reactions involve large numbers of atoms

that form a stable nucleus of product, generally on the surface of the reactant species. This mechanism, known as nucleation and growth, is strongly dependent on surface effects such as particle size, distribution of polymorphs, and bulk sample size.[123] The surface energy of the growing particle of product provides a positive contribution to the total Gibbs energy of the system. If the effect is large, it can offset the negative Gibbs energy contribution of the reaction (or phase transition) resulting in a halt of the reaction or instability of the product and reversal of the reaction.[123]

The sample masses used in the DSC experiments were generally between 10-15 mg (samples of similar mass were also used in the time-resolved Raman experiments) and uniform quenching conditions were used in the preparation of samples. Within the replicates of the experiments there was no significant variation in the peak times (Raman and DSC), but no specific experiment was performed to examine the role of sample size.

### 7.3.5. Crystal Violet Lactone/Lauryl Gallate/1-Hexadecanol and Crystal Violet Lactone/Lauryl Gallate/1-Octadecanol

Isothermal DSC experiments were attempted with little success for CVL/LG/HD and CVL/LG/OD mixtures. While fast event enthalpy changes were found to be comparable to those observed in the examination of CVL/LG/TD, the long time periods necessary for the phase transitions of $\alpha$-$\gamma$ HD and $\alpha$-$\gamma$ OD and conversions of $(LG)_2 \bullet$HD and $(LG)_2 \bullet$OD made the slow event enthalpies difficult to consistently and reliably resolve from the baseline.

Within CVL/LG/TD mixtures, where the thermal events are complete in 2 to 5 min, the maximum heat flow recorded was on the order of 0.25 to 0.50 W g$^{-1}$. For CVL/LG/HD and CVL/LG/OD, which have $\alpha$-$\gamma$ phase transition and $(LG)_2 \bullet$alcohol

enthalpy changes comparable to the CVL/LG/TD mixtures,[130,132] the equilibration times were 10 to 25 times longer. This produced theoretical peak power maxima of only 0.02 to 0.05 W g$^{-1}$. Since this was beyond the practical resolution of the Pyris 1 DSC, it was not possible to obtain consistent reliable data for CVL/LG/HD and CVL/LG/OD mixtures.

## 7.4. Discussion

Desirable thermochromic properties such as colour contrast, colour stability, and decolorization rates for these three-component thermochromic mixtures degrade as the alkyl-chain length of the solvent increases. The present thermodynamic analysis shows that the increase in alcohol chain length is reflected in a decrease in the attractive interaction between LG and the alcohol.

Increased attraction between LG and alcohol as the alkyl chain length of the alcohol is changed from 18 carbons to 14 carbons implies that the solubility of LG is probably higher in TD than it is in HD and OD. Solvation of colour developer in the molten mixture has been described as a means of achieving liquids with low colour density in conventional reversible thermochromic mixtures.[89] The more LG is solvated the less is available to interact with CVL. If TD solvates more LG than HD and OD in the melt than this could explain the increased liquid colour density of CVL/LG/HD and CVL/LG/OD mixtures relative to CVL/LG/TD mixtures (cf. Figures 6.15-6.17). This also could explain why the initial metastable colour densities attributed to ring-opened CVL are higher in CVL/LG/HD and CVL/LG/OD mixtures relative to CVL/LG/TD mixtures.

Events governed by Raman Peak I (1584 cm$^{-1}$, destruction and stability of (LG)$_x$•CVL) and Raman Peak II (1683 cm$^{-1}$, formation of (LG)$_2$•alcohol in the time-

resolved Raman experiments from Chapter 6) appear to be strongly correlated to changes in attractive interaction between LG and the respective alcohol.

The role of the $\alpha$-phase of the alcohol is not entirely clear; studies of CVL/LG/TD and LG/TD show that the presence of CVL has an effect on the equilibration time of the TD $\alpha$-phase. However, the rate of $\alpha$-phase conversion does not appear to change, within experimental error, for CVL/LG/HD and LG/HD mixtures or for CVL/LG/OD and LG/OD mixtures. Finally, enhanced $\alpha$-phase stability of HD relative to OD does not appear to significantly influence the trend in thermochromic properties dictated by the interaction.

Since Raman Peak III (1710 cm$^{-1}$) decay occurs at the same rate (in CVL/LG/TD mixtures) or faster (in CVL/LG/HD and CVL/LG/OD mixtures) than Raman Peak II (1683 cm$^{-1}$) formation, the following hypothesis is proposed. Free alcohol in the metastable ternary mixture converts to its low-temperature phase prior to interaction with LG freed from the destruction of LG/CVL complex. In all cases, the driving force for the transitions is the attractive interaction between the components. The relationship between the rates of $\alpha$-$\beta$/$\alpha$-$\gamma$ alcohol transitions and the formation of (LG)$_2$•alcohol are shown in Tables 7.7, 7.8, and 7.9.

An important caveat to consider is the lack of understanding of the effect of sample size and surface effects on the kinetics of the phase transitions observed in the DSC and Raman experiment. Although the samples examined were in a similar mass range (10-15 mg) there was no matching of sample masses between the two experiments (isothermal DSC and time-resolved Raman).

Table 7.7. Observed times of thermal events in crystal violet lactone/lauryl gallate/1-tetradecanol (mole ratio 1:6:40) and lauryl gallate/1-tetradecanol (mole ratio 6:40).

| Sample | α-β TD transition time/ s | (LG)₂•TD formation/ s |
|---|---|---|
| CVL/LG/TD 1:6:40 | 250-300 | 360-450 |
| LG/TD 6:40 | < 60 | 120-180 |

Table 7.8. Observed times of thermal events in crystal violet lactone/lauryl gallate/1-hexadecanol (mole ratio 1:6:40) and lauryl gallate/1-hexadecanol (mole ratio 6:40).

| Sample | α-γ HD transition time/ min | (LG)₂•HD formation/ min |
|---|---|---|
| CVL/LG/HD 1:6:40 | ~60 | 120-150 |
| LG/HD 6:40 | ~60 | ~60 |

Table 7.9. Observed times of thermal events in crystal violet lactone/lauryl gallate/1-octadecanol (mole ratio 1:6:40) and lauryl gallate/1-octadecanol (mole ratio 6:40).

| Sample | α-γ OD transition time/ min | (LG)₂•OD formation/ min |
|---|---|---|
| CVL/LG/OD 1:6:40 | ~30 | 120-150 |
| LG/OD 6:40 | ~30 | 45-60 |

In CVL/LG/TD mixtures, the α-β phase transition occurs quickly after quenching. Since the LG/TD attractive interaction is strong, concomitant formation of $(LG)_2$•TD occurs almost simultaneously. Raman Peak III ($1710$ cm$^{-1}$) equilibrates in 250 to 300 s in CVL/LG/TD 1:6:40 (Figure 6.24) while Raman Peak II ($1683$ cm$^{-1}$) equilibrates in about 360 s (Figure 6.26). This is consistent with the α-β phase transition in TD followed by

the formation of (LG)$_2$•TD. Since there is overlap of the two processes, only one thermal event is observed in the isothermal DSC experiment.

In CVL/LG/HD of mole ratio 1:6:40, metastable α-HD undergoes transformation to γ-HD within 60 min (Figure 6.32) while Raman Peak II (1683 cm$^{-1}$) intensity (corresponding to the formation of (LG)$_2$•HD) does not equilibrate for about 120 to 150 min (Figure 6.31). This indicates that, even after a significant amount of α-HD has transformed to γ-HD, excess LG and HD do not fully interact for nearly 60-90 min. This could be a result of a decrease in attractive interaction between the components. In binary LG/HD (mole ratio 6:40) Raman Peak II (1683 cm$^{-1}$) equilibrates at about the same rate as Raman Peak III (1710 cm$^{-1}$), *i.e.* within 60 min, indicating that the α-γ HD phase transition and (LG)$_2$•HD formation occur almost simultaneously.

CVL/LG/OD of mole ratio 1:6:40 displays the effect of decreased LG/alcohol interaction better than CVL/LG/HD of mole ratio 1:6:40. Mixtures display less α-OD metastability than comparable CVL/LG/HD mixtures, showing nearly full α–γ conversion in about 30 minutes (Figure 6.38). However, CVL/LG/OD at mole ratio 1:6:40 does not display full Raman Peak II (1683 cm$^{-1}$, due to (LG)$_2$•OD) equilibration for about 120 min (Figure 6.37). This result implies that excess γ-OD and LG do not fully interact to form (LG)$_2$•OD for 60-90 min following the α-γ phase transition of OD.

A decreased rate of (LG)$_2$•OD formation (relative to (LG)$_2$•TD and (LG)$_2$•HD formation) also is observed in the binary LG/OD mixture at mole ratio 6:40. While the rate of the α-γ phase transition is approximately the same in the binary (LG/OD) and ternary (CVL/LG/OD) mixture, (LG)$_2$•OD reaches equilibrium concentration after about

45 to 60 min in the binary (LG/OD) mixture, implying that excess $\gamma$-OD and LG do not fully interact to form $(LG)_2 \bullet OD$ for 15 to 30 min following the $\alpha$-$\gamma$ conversion of OD.

Another important factor affecting the kinetics of nucleation and growth in the solid phase mixture could be the presence of different 1-alcohol polymorphs.[123] CVL/LG/TD mixtures have TD in its $\beta$-phase in the equilibriun solid mixture, whereas CVL/LG/HD and CVL/LG/OD have HD and OD in their respective $\gamma$-phases at equilibrium. Since the alcohol component comprises the majority of the mixture it is not unreasonable to presume that the two low temperature polymorphs ($\beta$ and $\gamma$) have a role in altering the kinetics of the transitions observed in the mixtures, including: the destruction of $(LG)_x \bullet CVL$, the $\alpha$-$\beta$ (or $\alpha$-$\gamma$) alcohol phase transitions, and the formation of $(LG)_2 \bullet$alcohol. This could explain the significant differences in reaction rates observed in CVL/LG/TD mixtures (where all three reactions occur quickly) compared with CVL/LG/HD and CVL/LG/OD mixtures where the rates of all three reactions are slower.

In conclusion, the findings presented in this chapter indicate that changes in the attractive interaction between the solvent and developer components play an important role in the observed colour density, contrast and decolourisation rates of these rewritable thermochromic mixtures. Time resolved Raman and isothermal DSC experiments identify three major events occuring as quenched ternary mixtures equilibrate. Decreased rates of most of these three reactions as the solvent alkyl-chain length increases are correlated with a decrease in attractive interaction between the developer and solvent. However, detailed kinetics of these mixtures cannot be fully explained without further examination of the surface properties of the mixture, more specifically the role of sample

size and the surface effects associated with β- versus γ-alcohol phases in the developer-

solvent matrix.

# Chapter 8. Other Thermochromic Mixtures

## 8.1. Introduction

Chapters 6 and 7 presented examinations of crystal violet lactone/lauryl gallate/alcohol mixtures and showed how attractive interactions between solvent and developer components influenced the rapid destruction of metastable coloured complexes. Decreased attractive interaction between solvent and developer components resulted in enhanced colour density, poor colour contrast, and slower decolourisation rates.

In this chapter similar ternary thermochromic mixtures, where lauryl gallate is replaced with other alkyl gallate developers, are presented. The first section outlines binary interactions between dye/developer and developer/solvent in the ternary mixtures. The second section shows that the attractive interaction between propyl gallate and alcohol in the propyl gallate/alcohol mixture is weaker than the attractive interaction between octyl gallate and alcohol in the octyl gallate/alcohol mixture. Both systems display less attractive propyl gallate/alcohol and octyl gallate/alcohol interaction than the corresponding attractive interaction in lauryl gallate/alcohol mixtures. Decreased attractive interaction between alkyl gallate/alcohol is reflected in the observed thermochromic properties, most notably in equilibrium colour density of the mixtures. (*N.B.* attractive interactions between alkyl gallate and alcohols imply that the alkyl gallate/alcohol interaction is more attractive than respective alkyl gallate/alkyl gallate and alcohol/alcohol interactions.)

## 8.2. Thermal Analysis of Alkyl Gallate/Crystal Violet Lactone Interactions

Propyl gallate (PG) and octyl gallate (OG) were chosen because they have the same acidic functional groups and potential to interact with CVL to form complexes with similar structural features (Chapter 4). Interaction parameters for the interaction of PG, OG and LG with CVL are compared here using the methods described in Chapter 7.

### 8.2.1. Phase Diagrams of Propyl Gallate/Crystal Violet Lactone, Octyl Gallate/ Crystal Violet Lactone, and Lauryl Gallate/Crystal Violet Lactone

Onset temperatures for the melting of free alkyl gallate formed after annealing were used for the calculation of the alkyl gallate liquidus of the alkyl gallate/crystal violet lactone phase diagram using Eq. 7.11. Experimental and calculated alkyl gallate liquidus data obtained upon heating for PG/CVL, OG/CVL, and LG/CVL are shown in Figures 8.1, 8.2, and 8.3.
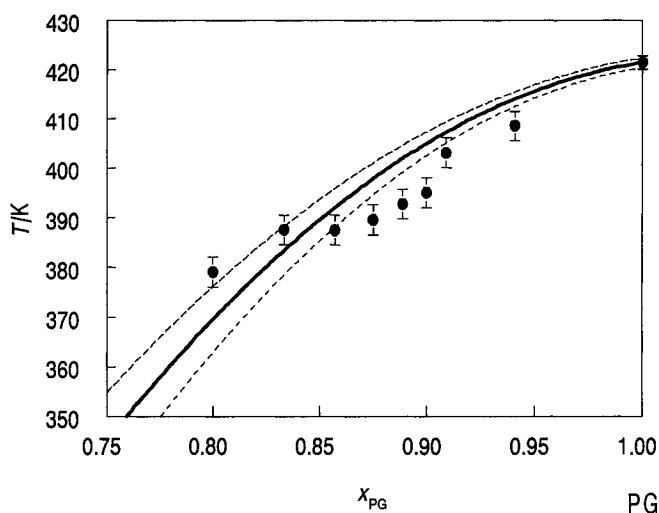


Figure 8.1. The solid line shows the calculated liquidus of propyl gallate in propyl gallate/crystal violet lactone (PG/CVL) mixtures calculated using Eq. 7.11, where the symbols with error bars correspond to the experimental data. The fit gave an interaction parameter, $W^H_{PG}$, of -52 ± 10 kJ mol$^{-1}$. Dashed lines indicate the melting point for the maximum and minimum fit values of $W^H_{PG}$ and incorporate the uncertainties in both $T_{m,PG}$ and $\Delta_m H_{PG}°$.
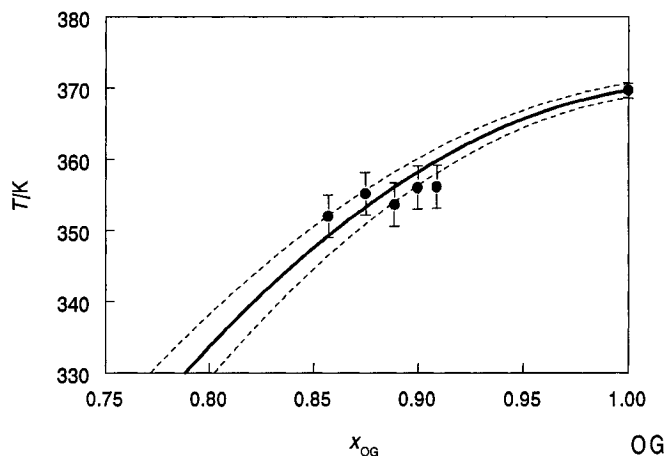
Figure 8.2. The solid line shows the calculated liquidus of octyl gallate in octyl gallate/crystal violet lactone (OG/CVL) mixtures calculated using Eq. 7.11, where the symbols with error bars correspond to the experimental data. The fit gave an interaction parameter, $W^H_{OG}$, of -44 ± 6 kJ mol$^{-1}$. Dashed lines indicate the melting point for the maximum and minimum fit values of $W^H_{OG}$ and incorporate the uncertainties in both $T_{m,PG}$ and $\Delta_m H_{OG}°$.
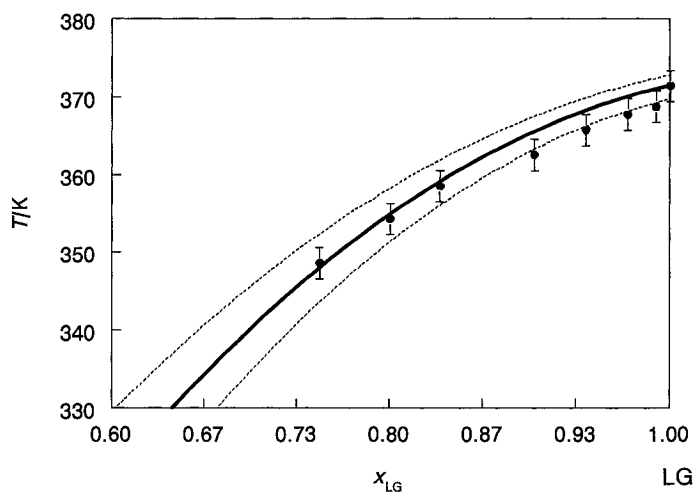


Figure 8.3. The solid line shows the calculated liquidus of lauryl gallate in lauryl gallate/crystal violet lactone (LG/CVL) mixtures calculated using Eq. 7.11, where the symbols with error bars correspond to the experimental data. The fit gave an interaction parameter, $W^H_{LG}$, of -30 ± 8 kJ mol$^{-1}$. Dashed lines indicate the melting point for the maximum and minimum fit values of $W^H_{LG}$ and incorporate the uncertainties in both $T_{m,LG}$ and $\Delta_m H_{LG}°$.

Observed melting enthalpies of pure alkyl gallate from the binary CVL/alkyl

gallate mixtures obtained after annealing (Chapter 5) were used to determine excess

mixing enthalpies and interaction parameters incorporating the Margules equation (Eq.

7.12 and 7.13). For this calculation the mole fraction of free alkyl gallate relative to its

equilibrium (alkyl gallate)$_x$•CVL complex were used. Stoichiometries of 2:1, 4:1 and 3:1

(determined in Chapter 4) were used for PG/CVL, CVL/OG, and LG/CVL mixtures

respectively. Observed and calculated melting enthalpy changes for pure alkyl gallate in

alkyl gallate/CVL mixtures are shown in Figures 8.4, 8.5, and 8.6.
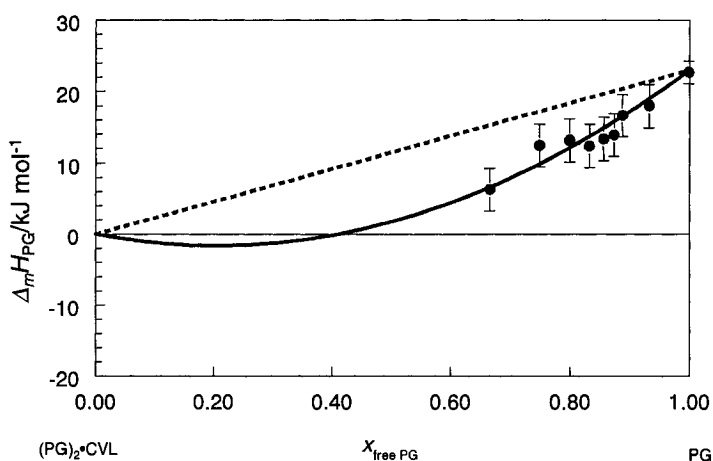


Figure 8.4. The enthalpy of melting as a function of the mole fraction of free propyl gallate in annealed propyl gallate-rich propyl gallate/crystal violet lactone (PG/CVL) mixtures. Observed enthalpy changes (symbols with error bars) deviate negatively from the ideal melting enthalpy (broken line). The observed enthalpy (solid line) was determined by a fit to the one-parameter Margules equation (Eq. 7.12), with an interaction parameter, $W^H_{PG}$, of -39 ± 4 kJ mol$^{-1}$.
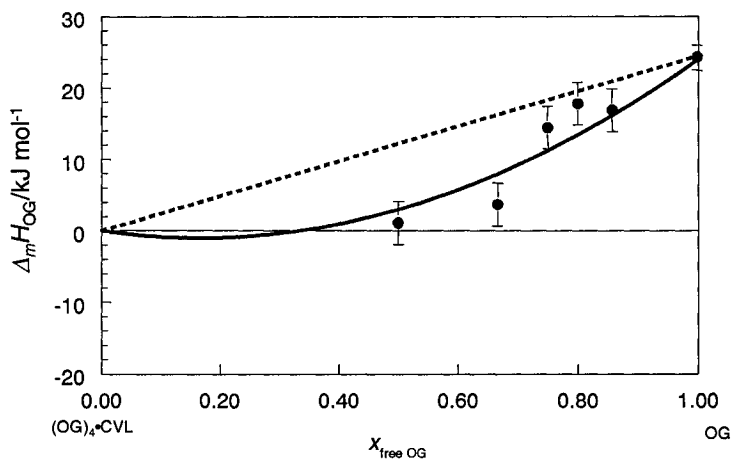
Figure 8.5. The enthalpy of melting as a function of the mole fraction of free octyl gallate in annealed octyl gallate-rich octyl gallate/crystal violet lactone (OG/CVL) mixtures. Observed enthalpy changes (symbols with error bars) deviate negatively from the ideal melting enthalpy (broken line). The observed enthalpy (solid line) was determined by a fit to the one-parameter Margules equation (Eq. 7.12), $W^H_{OG}$, of -36 ± 8 kJ mol$^{-1}$.
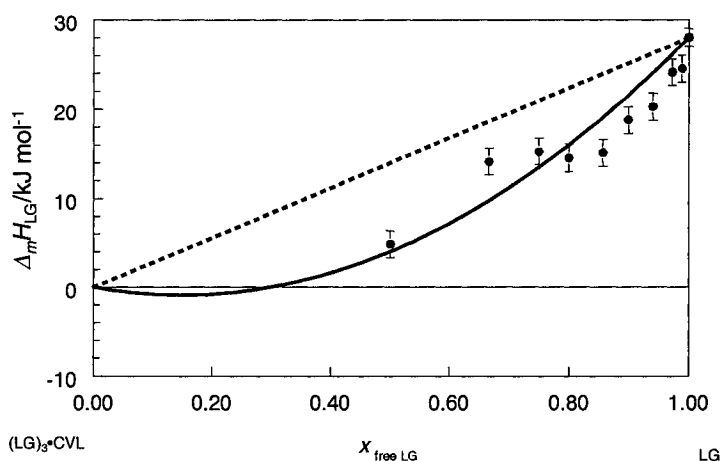


Figure 8.6. The enthalpy of melting as a function of the mole fraction of free lauryl gallate in annealed lauryl gallate-rich lauryl gallate/crystal violet lactone (LG/CVL) mixtures. Observed enthalpy changes (symbols with error bars) deviate negatively from the ideal melting enthalpy (broken line). The observed enthalpy (solid line) was determined by a fit to the one-parameter Margules equation (Eq. 7.12), $W^H_{LG}$, of -40 ± 7 kJ mol$^{-1}$.

$W^{H}_{\text{alkyl gallate}}$ values determined from both methods, shown in Table 8.1 and 8.2 represent significant attractive interactions consistent with the observed formation of strong CVL/alkyl gallate complexes within the mixture.

Table 8.1. $W^{H}_{\text{alkyl gallate}}$ values determined from liquidus calculation (Eq. 7.11).

| System | $W^{H}_{\text{alkyl gallate}} / (kJ \ mol^{-1})$ |
|--------|--------------------------------------------------|
| PG/CVL | $-52 \pm 10$ |
| OG/CVL | $-44 \pm 6$ |
| LG/CVL | $-30 \pm 8$ |

Table 8.2. $W^{H}_{\text{alkyl gallate}}$ values determined from excess enthalpy calculation (Eq. 7.12).

| System | $W^{H}_{\text{alkyl gallate}} / (kJ \ mol^{-1})$ |
|--------|--------------------------------------------------|
| PG/CVL | $-39 \pm 4$ |
| OG/CVL | $-36 \pm 8$ |
| LG/CVL | $-40 \pm 7$ |

### 8.2.2. Structure of Alkyl Gallate/Crystal Violet Lactone Mixtures

Figure 8.7 compares the Raman spectra of PG/CVL, OG/CVL, and LG/CVL at 6:1 mole ratios. Stoichiometries of equilibrium complexes $(PG)_x \cdot CVL$, $(OG)_x \cdot CVL$, and $(LG)_x \cdot CVL$ ranged from $x = 2$ to 4, however metastable stoichiometries of up to $x = 9$ were observed for all three binary mixtures (Chapter 4).
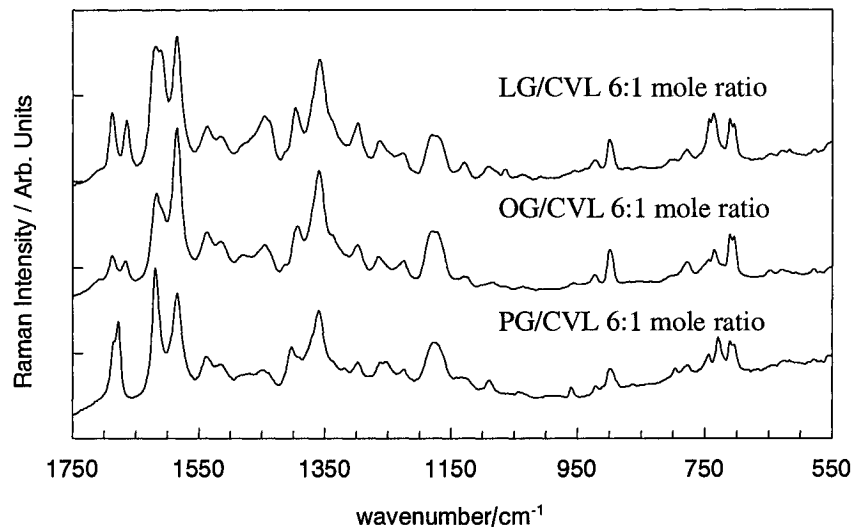
Figure 8.7. Comparison of the Raman spectra of propyl gallate/crystal violet lactone (PG/CVL), octyl gallate/crystal violet lactone (OG/CVL) , and lauryl gallate/crystal violet lactone (LG/CVL) in 6:1 mole ratios. Peaks corresponding to the ring-opened form of crystal violet lactone were observed in all three mixtures.

Below 1600 cm$^{-1}$ in the Raman spectra the spectral features are nearly identical and consistent with the presence of ring-opened CVL. Peaks between 1700 and 1650 cm$^{-1}$ represent the interaction of free alkyl gallate with the coloured, alkyl gallate/CVL complex. (Recall that free LG displays two carbonyl peaks indicating that a layering of free LG molecules in slightly different environments occurs near the coloured complex.) Doubling of carbonyl peaks is also observed in the OG/CVL mixture, but not to the same extent in the PG/CVL mixture. This leads to speculation that the multiple carbonyl environments might arise through a layering of OG and LG around the (OG)$_x$•CVL and (LG)$_x$•CVL complexes.

## 8.3. Phase Diagrams of Propyl Gallate/1-Alcohol and Octyl Gallate/1-Alcohol Mixtures

While propyl gallate and octyl gallate interact with crystal violet lactone in a manner similar to lauryl gallate with crystal violet lactone, the shorter-chain alkyl gallates differ significantly in their interaction with the 1-alcohols used in the present study, as follows.

Binary PG/alcohol and OG/alcohol phase diagrams in Chapter 5 (Figures 5.18-5.20 and Figures 5.24-5.26) showed no compound formation occuring between PG or OG and any of the alcohols examined. This fact alone demonstrates that the strength of the attractive interaction between the developer and solvent is much lower in PG/alcohol and OG/alcohol than in the corresponding LG/alcohol, where $(LG)_2 \bullet$alcohol compounds are formed.

Binary mixtures of PG/alcohol and OG/alcohol did not display significant increases in the stability of their $\alpha$-alcohol phases at alcohol-rich compositions. It is possible that the relatively short alkyl-chains of PG and OG are not able to interact with the free alcohol to stabilize the alcohol $\alpha$-phases at room temperature.[167,168,193] Studies by Al-Mamun[193] and Sirota et al.[167] of binary mixtures of 1-alcohols have shown that minimizing chain length differences between the two components tends to provide enhanced support to the rotational phases. If the chain length of the stabilizing component becomes short relative to that of the major component, the enhancement effect is weakened.[167,168,193] The lower room-temperature stability of $\alpha$-alcohol phases in PG/alcohol and OG/alcohol mixtures simplified the examination of interactions between the developer and the solvent, free of the presence of metastable $\alpha$-alcohol phases.

### 8.3.1. Interaction Parameters for Propyl Gallate/1-Alcohol Mixtures

Interaction parameters, $W^{H}_{alcohol}$, describing the melting and mixing of the alcohol

component in the PG/alcohol mixture were obtained using the Margules equation (Eq.

7.12). In most mixtures, melts and ($\beta$- or $\gamma$-)-$\alpha$ and $\alpha$-liquid alcohol transitions are

separated by only a few degrees. To simplify the analysis, the enthalpy change of the

entire transition from ($\beta$- or $\gamma$-)- to alcohol was used. For all mixtures, a one-parameter fit

was in good agreement with experimental data. Figures 8.8, 8.9, and 8.10 show

experimental and calculated enthalpy changes for PG/alcohol mixtures obtained upon

heating the mixtures.
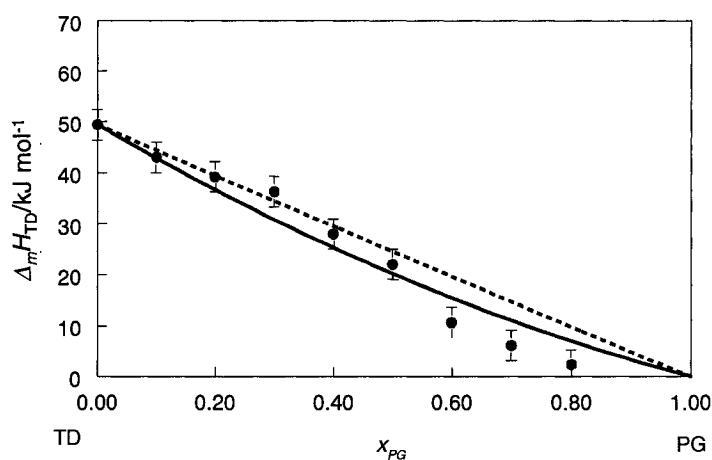


Figure 8.8. Calculated and experimental (data with error bars) enthalpy changes for the melting of 1-tetradecanol in binary propyl gallate/1-tetradecanol (PG/TD) mixtures. $W^{H}_{TD}$ =$-18 \pm 6$ kJ mol$^{-1}$ was determined to describe the excess enthalpy within the system. The ideal melting enthalpy is shown as a broken line with the fit to the experimental enthalpy change shown as a heavy curved line.
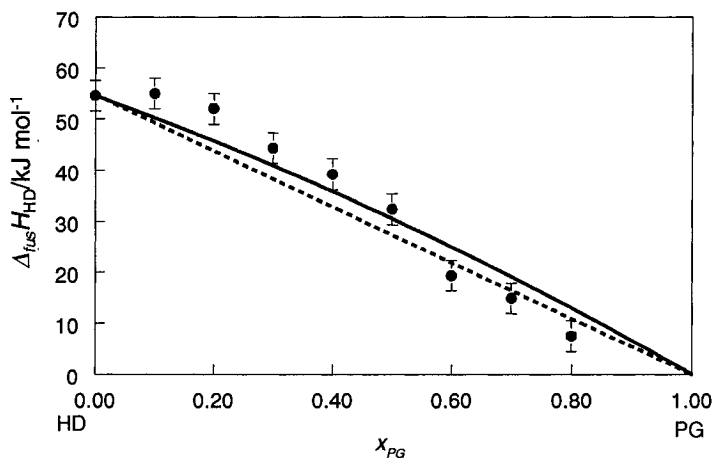
Figure 8.9. Calculated and experimental (data with error bars) enthalpy changes for the melting of 1-hexadecanol in binary propyl gallate/1-hexadecanol (PG/HD) mixtures. $W^H{}_{HD}$= +13 ± 8 kJ mol$^{-1}$ was determined to describe the excess enthalpy within the system. The ideal melting enthalpy is shown as a broken line with the fit to the experimental enthalpy change shown as a heavy curved line.
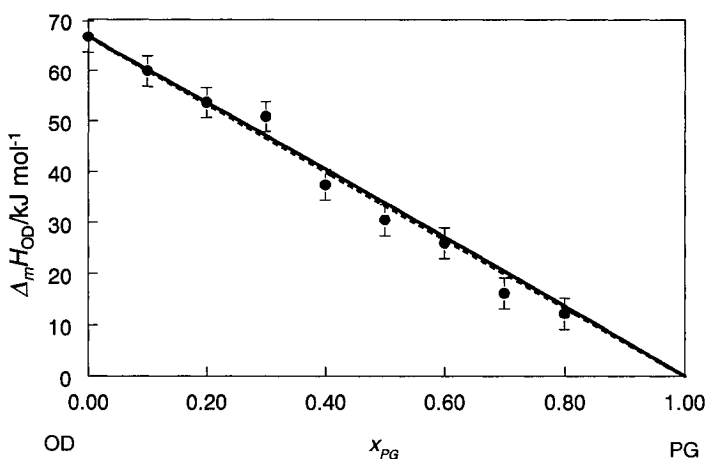


Figure 8.10. Calculated and experimental (data with error bars) enthalpy changes for the melting of 1-octadecanol in binary propyl gallate/1-octadecanol (PG/OD) mixtures. $W^H{}_{OD}$ = +2 ± 2 kJ mol$^{-1}$ was determined to describe the excess enthalpy within the system. The ideal melting enthalpy is shown as a broken line with the fit to the experimental enthalpy change shown as a heavy curved line.

$W^H{}_{PG}$ values were determined by calculating the liquidus of each phase diagram obtained upon heating using Eq. 7.11. For some PG/alcohol mixtures the phase behaviour was consistent with a composition-dependent interaction parameter similar to that observed for LG₂•alcohol (Chapter 7). The calculated liquidus data for the PG liquidus of PG/TD, PG/HD, and PG/OD are shown in Figures 8.11, 8.12, and 8.13. In PG/TD and PG/OD $W^H{}_{PG}$ is composition dependent and becomes more negative in compositions rich in alcohol.
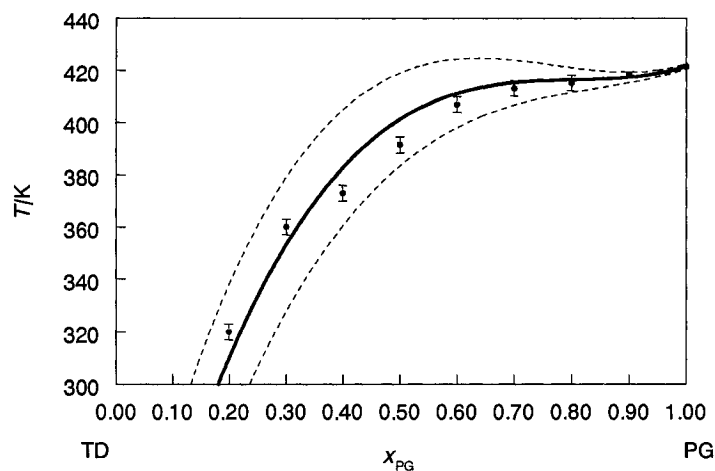


Figure 8.11. Calculated and experimental (data with error bars) liquidus data for the propyl gallate liquidus of propyl gallate/1-tetradecanol (PG/TD). A composition dependent interaction parameter of $W^H{}_{PG}$ = -8(±3) + 25(±4)$x_{PG}$ produces a liquidus in good agreement with the experimental values. Dashed lines represent the uncertainty associated with $T_m$ and $\Delta_m H$ for propyl gallate in Eq. 7.11.
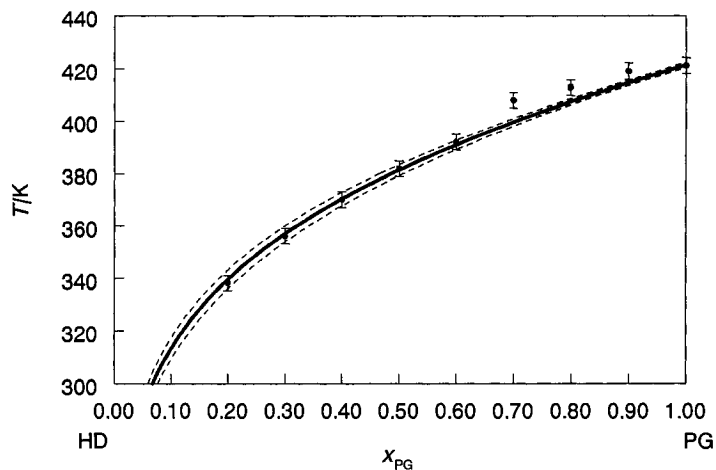
Figure 8.12. Calculated and experimental (data with error bars) liquidus data for the propyl gallate liquidus of propyl gallate/1-hexadecanol (PG/HD). An interaction parameter of $W^H_{PG} = 0.3 \pm 0.2$ produces a liquidus in good agreement with the experimental values. Dashed lines represent the uncertainty associated with $T_m$ and $\Delta_m H$ for propyl gallate in Eq. 7.11.
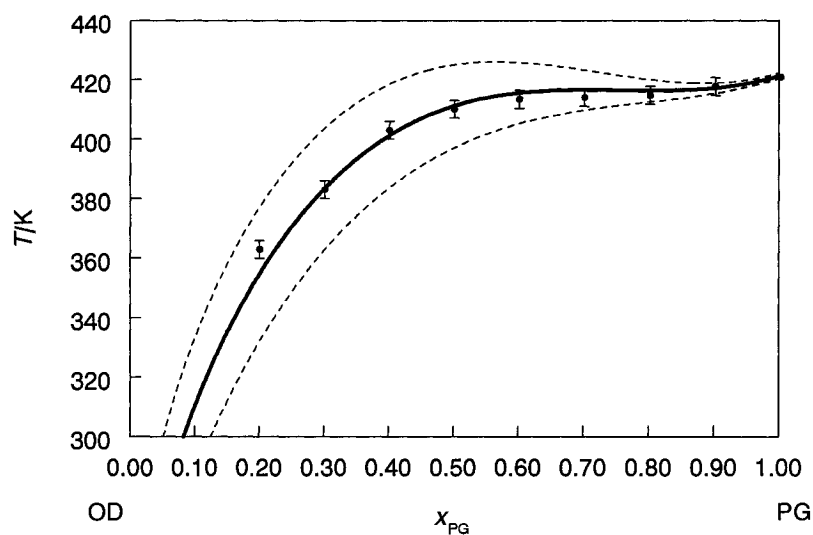


Figure 8.13. Calculated and experimental (data with error bars) liquidus data for the propyl gallate liquidus of propyl gallate/1-octadecanol (PG/OD). A composition dependent interaction parameter of $W^H_{PG} = -1.8(\pm1.6) + 18(\pm3)x_{PG}$ produces a liquidus in good agreement with the experimental values. Dashed lines represent the uncertainty associated with $T_m$ and $\Delta_m H$ for propyl gallate in Eq. 7.11.

## 8.3.2. Interaction Parameters for Octyl Gallate/1-Alcohol Mixtures

Figures 8.14, 8.15, and 8.16 show the experimental and calculated melting

enthalpies for TD, HD, and OD in TD/OG, HD/OG, and OD/OG mixtures when heated.

Closely spaced transitions from ($\beta$- or $\gamma$-)- $\alpha$ alcohol and $\alpha$-liquid alcohol phases makes it

difficult to resolve the enthalpy changes of two transitions in the DSC thermogram. With

this in mind, the enthalpy for the conversion of the low-T ($\beta$- or $\gamma$-) alcohol phase to the

liquid phase was considered. As is the case in the PG/alcohol mixtures, the observed

enthalpy changes were consistent with a full transition of the ($\beta$- or $\gamma$-) alcohol to liquid

phase upon heating the solid mixture. $W^H_{alcohol}$ values predict significant decreases in

alcohol attraction to OG as the chain length of the alcohol is increased.
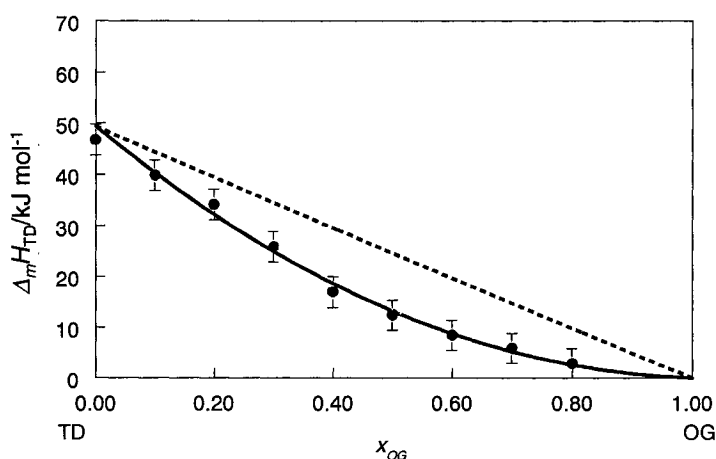


Figure 8.14. Calculated and experimental (data with error bars) enthalpy changes for the melting of 1-tetradecanol in binary octyl gallate/1-tetradecanol (OG/TD) mixtures. From a fit to Eq. 7.12, a $W^H_{TD}$ value of –46 ± 2 kJ mol⁻¹ was determined to describe the excess enthalpy within the system. The ideal melting enthalpy is shown as a broken line with the enthalpy change calculated from the fit shown as a heavy curved line.
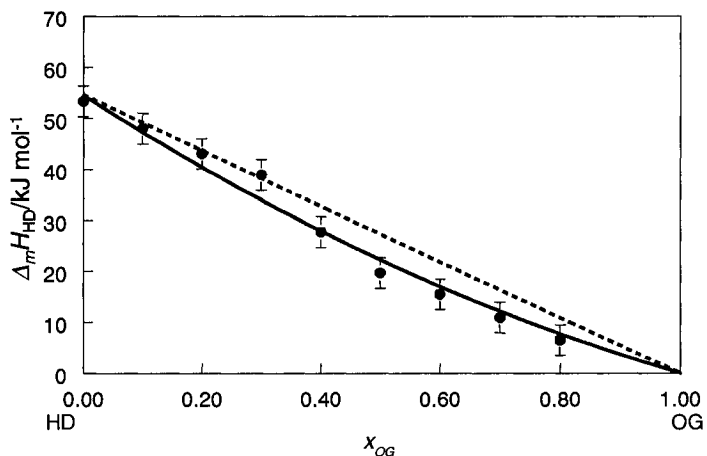
Figure 8.15. Calculated and experimental (data with error bars) enthalpy changes for the melting of 1-hexadecanol in binary octyl gallate/1-hexadecanol (OG/HD) mixtures. From a fit to Eq. 7.12, a $W^H_{HD}$ value of -20 ± 4 kJ mol$^{-1}$ was determined to describe the excess enthalpy within the system. The ideal melting enthalpy is shown as a broken line with the enthalpy change calculated from the fit shown as a heavy curved line.
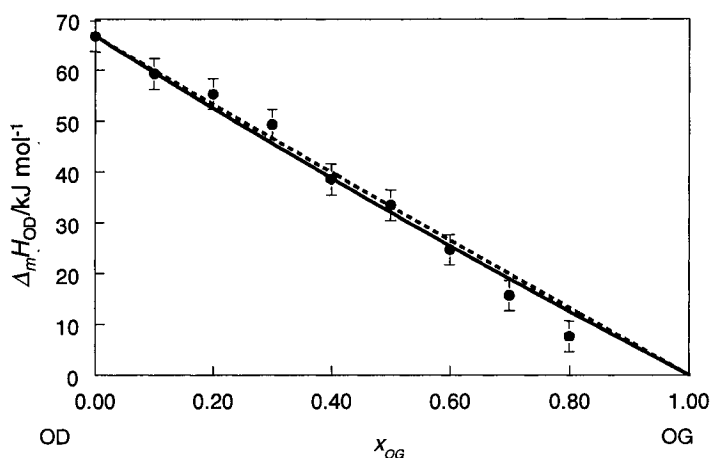


Figure 8.16. Calculated and experimental (data with error bars) enthalpy changes for the melting of 1-octadecanol in binary octyl gallate/1-octadecanol (OG/OD) mixtures. From a fit to Eq. 7.12, a $W^H_{OD}$ value of -5 ± 5 kJ mol$^{-1}$ was determined to describe the excess enthalpy within the system. The ideal melting enthalpy is shown as a broken line with the enthalpy change calculated from the fit shown as a heavy curved line.

The OG liquidus of the OG/TD, OG/HD, and OG/OD phase diagrams were also calculated using Eq. 7.11 and fit to experimental data (Figures 8.17, 8.18, and 8.19).
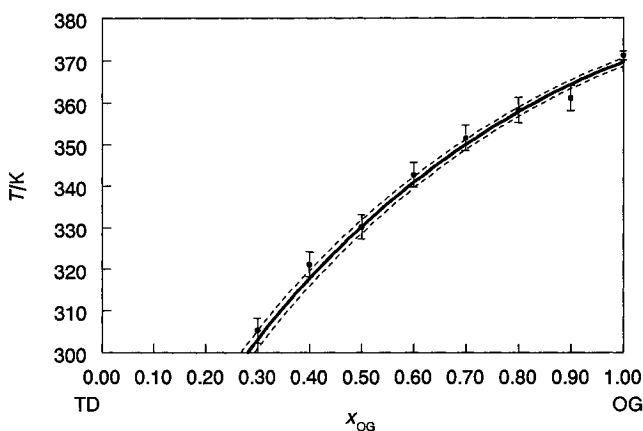


Figure 8.17. Calculated and experimental (data with error bars) liquidus data for the octyl gallate liquidus of octyl gallate/1-tetradecanol (OG/TD), as fit to Eq. 7.11. The fit gave $W^H_{OG} = -2.8 + 2$, which produces a liquidus (solid line) in good agreement with the experimental values. Dashed lines represent the uncertainty associated with $T_m$ and $\Delta_m H$ for octyl gallate.
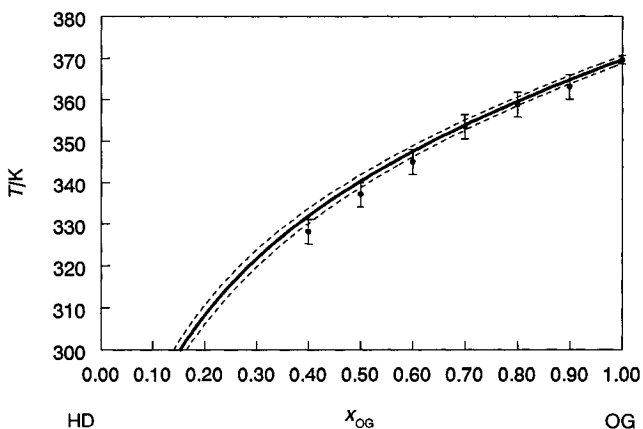


Figure 8.18. Calculated and experimental (data with error bars) liquidus data for the octyl gallate liquidus of octyl gallate/1-hexadecanol (OG/HD). The fit gave $W^H_{OG} = 0.7 \pm 0.1$, which produces a liquidus (solid line) in good agreement with the experimental values. Dashed lines represent the uncertainty associated with $T_m$ and $\Delta_m H$ for octyl gallate.
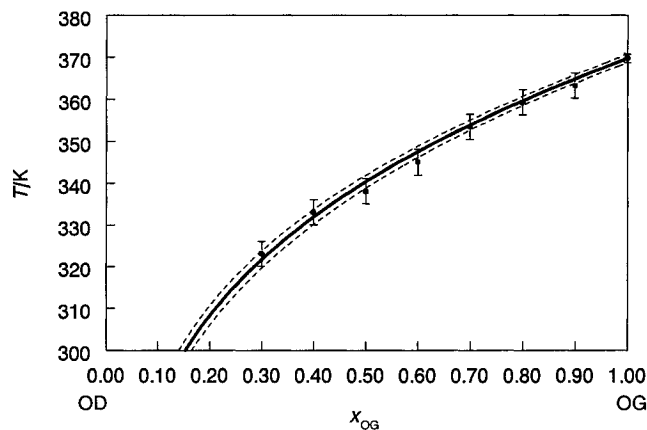
Figure 8.19. Calculated and experimental (data with error bars) liquidus data for the octyl gallate liquidus of octyl gallate/1-octadecanol (OG/OD). The fit gave $W^H_{OG} = 0.09 \pm 0.2$, which produces a liquidus (solid line) in good agreement with the experimental values. Dashed lines represent the uncertainty associated with $T_m$ and $\Delta_m H$ for octyl gallate.

### 8.3.3. Comparison of Propyl Gallate/1-Alcohol and Octyl Gallate/1-Alcohol Interactions

Interaction parameters determined for the alcohol component of PG/alcohol and OG/alcohol mixtures determined by the examination of excess enthalpy of mixing are summarized in Table 8.3.

Table 8.3. $W^H_{alcohol}$ values for the interaction of alcohols with propyl gallate and octyl gallate determined through an examination of the excess enthalpy of melting of the pure alcohol phases.

| System | $W^H_{alcohol}/(kJ\ mol^{-1})$ |
|--------|--------------------------------|
| PG/TD | $-18 \pm 6$ |
| PG/HD | $+13 \pm 8$ |
| PG/OD | $+2 \pm 2$ |
| OG/TD | $-46 \pm 2$ |
| OG/HD | $-20 \pm 4$ |
| OG/OD | $-5 \pm 5$ |

$W^H_{alcohol}$ values show two trends within these data. First, more negative $W^H_{alcohol}$ values are observed in OG/alcohol mixtures relative to PG/alcohol mixtures. This indicates that, for a given alkyl gallate/alcohol combination, the alcohol will be more attracted to OG than to PG. However, although OG is more strongly attracted to the alcohols than in PG, the attraction is not strong enough for compound formation. Second, within a given alkyl gallate/alcohol system $W^H_{alkyl\ gallate}$ values show that increasing the alkyl-chain length of the alcohol component decreases the attractive interaction between components, i.e. the attraction between alkyl gallate/TD is stronger than alkyl gallate/HD and alkyl gallate/OD.

$W^H_{PG}$ and $W^H_{OG}$ values, shown in Table 8.4, display only small deviations from ideal behaviour.

Table 8.4. $W^H_{alkyl\ gallate}$ values for the interaction of propyl gallate and octyl gallate with alcohols determined through an examination of the liquidus of the propyl gallate/alcohol and octyl gallate/alcohol phase diagrams.

| System | $W^H_{alkyl\ gallate}$ / (kJ mol$^{-1}$) |
|--------|------------------------------------------|
| PG/TD  | $-8(\pm3) + 25(\pm4)x_{PG}$ |
| PG/HD  | $0.3 \pm 0.2$ |
| PG/OD  | $-1.8(\pm1.6) + 18(\pm3)x_{PG}$ |
| OG/TD  | $-2.8 \pm 0.2$ |
| OG/HD  | $-0.7 \pm 0.1$ |
| OG/OD  | $0.09 \pm 0.2$ |

In composition regions of interest to thermochromic mixtures ($x_{alkyl\ gallate} < 0.20$), $W^H_{PG}$ values moved from small negative values in the alcohol rich compositions of PG/TD and PG/OD mixtures (indicating a weak attractive interaction) to nearly ideal values as $x_{PG}$ increased. (PG/HD mixtures displayed constant, negative interaction parameters). A similar trend was observed in the OG/alcohol mixtures where negative $W^H_{OG}$ values decreased in magnitude (implying an movement toward ideal behaviour) as the alkyl-chain length of the alcohol was increased.

## 8.4. Thermochromic Properties of Crystal Violet Lactone/Propyl Gallate/1-Alcohol and Crystal Violet Lactone/Octyl Gallate/1-Alcohol Mixtures

The thermochromic properties of crystal violet lactone/propyl gallate/alcohol (CVL/PG/alcohol) and crystal violet lactone/octyl gallate/alcohol (CVL/OG/alcohol) mixtures are presented here and compared with crystal violet lactone/lauryl gallate/alcohol (CVL/LG/alcohol). The changes in thermochromic behaviour are

correlated with the changes in interaction between the developer and solvent components discussed in the previous section.

### 8.4.1. Images of Crystal Violet Lactone/Propyl Gallate/1-Alcohol Mixtures

Figures 8.20 and 8.21 show some images of selected CVL/PG/alcohol mixtures taken 30 min and 1 week after slow cooling from the melt. These mixtures were highly coloured solids regardless of cooling rate (slow and rapid cooling produced indistinguishable colour density) and showed little change of colour over extended periods of time. Figure 8.22 compares the colour density of CVL/PG/TD, CVL/PG/HD and CVL/PG/OD (1:6:40) at 30 min and at one week after cooling from the melt.
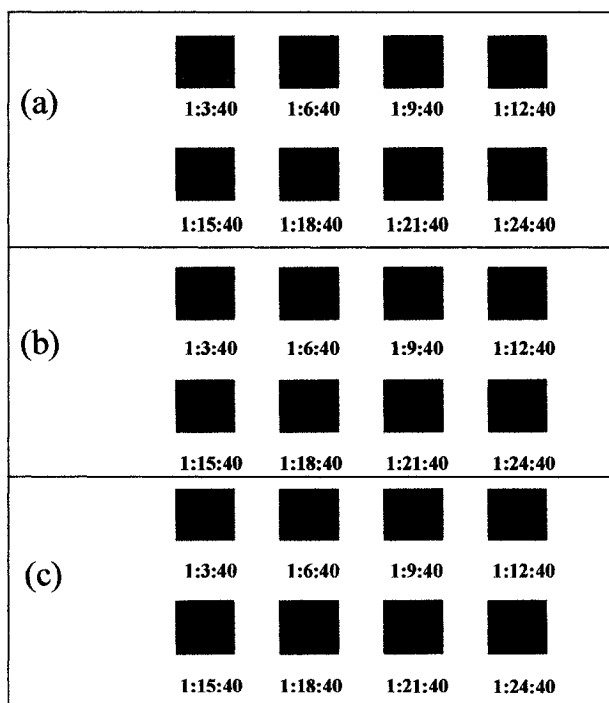


Figure 8.20. Images of selected (a) crystal violet lactone/propyl gallate/1-tetradecanol (CVL/PG/TD) (b) crystal violet lactone/propyl gallate/1-hexadecanol (CVL/PG/HD) and (c) crystal violet lactone/propyl gallate/1-octadecanol (CVL/PG/OD) mixtures obtained after 30 min of equilibration at 25 °C following slow cooling from the melt. Ratios given are CVL/PG/alcohol mole ratios.
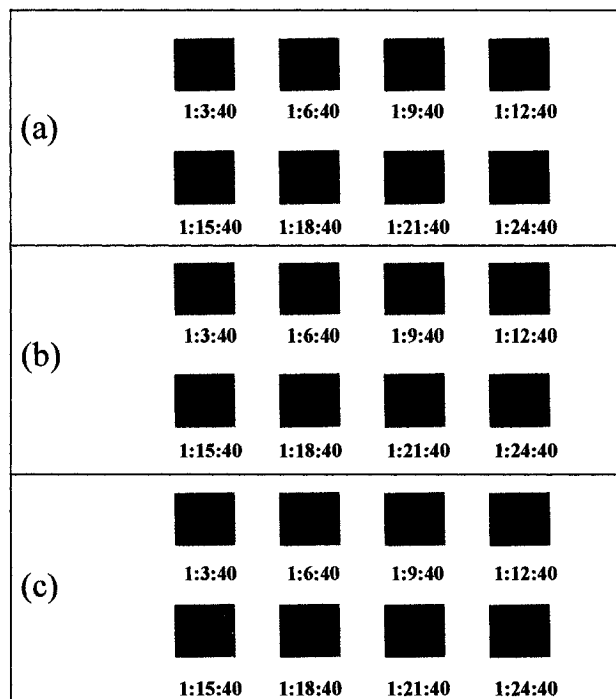
Figure 8.21. Images of selected (a) crystal violet lactone/propyl gallate/1-tetradecanol (CVL/PG/TD) (b) crystal violet lactone/propyl gallate/1-hexadecanol (CVL/PG/HD) and (c) crystal violet lactone/propyl gallate/1-octadecanol (CVL/PG/OD) mixtures obtained after one week of equilibration at 25 °C following slow cooling from the melt. Ratios given are CVL/PG/alcohol mole ratios.

Figure 8.22. Images of (a) crystal violet lactone/propyl gallate/1-tetradecanol (CVL/PG/TD, 1:6:40 mole ratio) (b) crystal violet lactone/propyl gallate/1-hexadecanol (CVL/PG/HD, 1:6:40 mole ratio) and (c) crystal violet lactone/propyl gallate/1-octadecanol (CVL/PG/OD,1:6:40 mole ratio) obtained after 30 min and after one week of equilibration at 25 °C following slow cooling from the melt.

While all three systems displayed high equilibrium colour density, CVL/PG/TD mixtures showed the greatest change in colour density as a function of time. The colour density of CVL/PG/HD and CVL/PG/OD mixtures remained virtually unchanged after 1 week.

With little or no solid-state colour contrast, combined with negligible decolourisation rates, none of these mixtures displayed rewritable thermochromic properties. However, some of these compositions can be used to produce conventional reversible thermochromic behaviour. PG is listed as a "good developer" for conventional rewritable thermochromic applications (cf. Figure 1.9).[85,88,103,104] If a mixture is prepared with high proportions of alcohol solvent relative to PG (PG:alcohol < 1:10 mole ratio) the resulting liquid has reduced colour density relative to the solid. This mechanism for reversible thermochromism has been addressed by Burkinshaw et. al.[89] and Luthern and Peredes[125] and requires a mixture with a highly stable coloured solid state with a solvent

able to dissolve a significant portion of the developer in the molten state. If amounts of developer in excess of its equilibrium solubility in the solvent are used the excess developer interacts with the dye, the liquid state develops high colour density, and the thermochromic effect is lost.

### 8.4.2. Raman Spectroscopy of Crystal Violet Lactone/Propyl Gallate/1-Alcohol Mixtures

Time-resolved Raman spectroscopy experiments were performed on selected mixtures within three systems: CVL/PG/TD, CVL/PG/HD, and CVL/PG/OD. Figures 8.23, 8.24, and 8.25 show the Raman spectra of quenched CVL/PG/TD (1:6:40), CVL/PG/HD (1:6:40), and CVL/PG/OD (1:6:40) obtained after 1 min, 30 min, and 24 hr of equilibration at 25 °C.
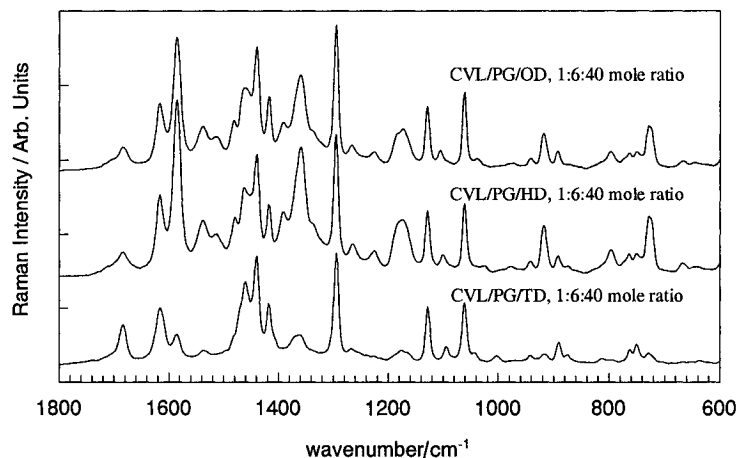


Figure 8.23. Raman spectra of selected crystal violet lactone/propyl gallate/alcohol (CVL/PG/alcohol) mixtures obtained after 1 min of equilibration at 25 °C following rapid quenching in liquid nitrogen. Peaks corresponding to the ring-open form of crystal violet lactone are present in all three mixtures but are more pronounced in crystal violet lactone/propyl gallate/1-hexadecanol (CVL/PG/HD, 1:6:40 mole ratio) and crystal violet lactone/propyl gallate/1-octadecanol (CVL/PG/OD, 1:6:40 mole ratio).
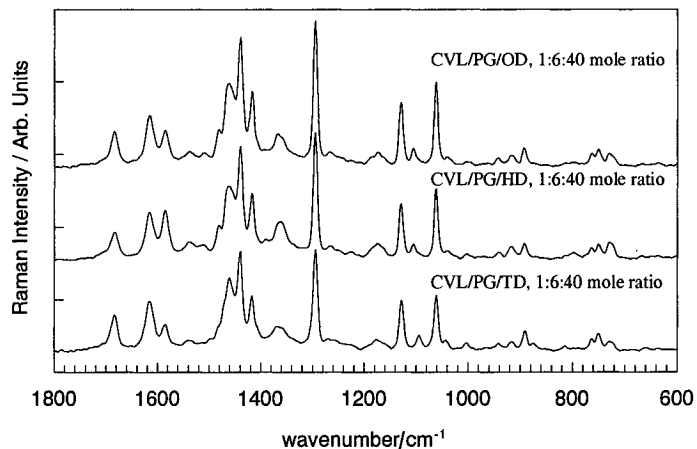
Figure 8.24. Raman spectra of selected crystal violet lactone/propyl gallate/alcohol (CVL/PG/alcohol) mixtures obtained after 30 min of equilibration at 25 °C following rapid quenching in liquid nitrogen. Peaks corresponding to ring-open form of crystal violet lactone in all three mixtures have diminished but are still visible in all three mixtures.
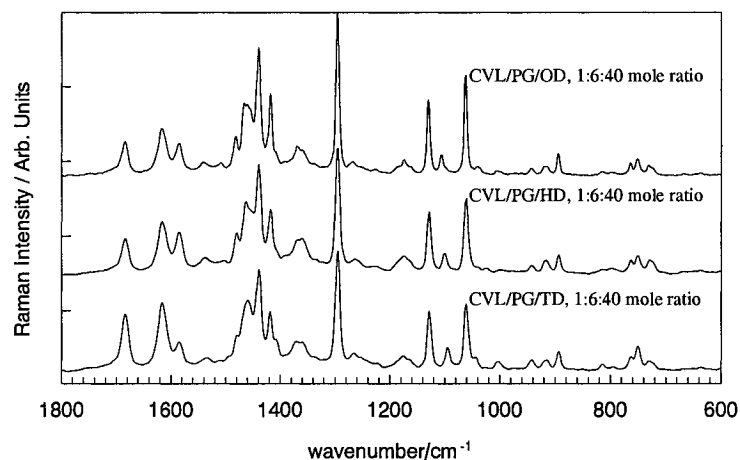


Figure 8.25. Raman spectra of selected crystal violet lactone/propyl gallate/alcohol (CVL/PG/alcohol) mixtures obtained after 24 hr of equilibration at 25 °C following rapid quenching in liquid nitrogen. Peaks corresponding to ring-open form of crystal violet lactone observed in the mixture have diminished slightly from the intensities observed after 30 min.

Peaks due to the strong interaction of CVL and PG appeared in the mixtures upon quenching and are very similar to those observed in quenched CVL/LG/alcohol mixtures (Figure 6.19). Peaks with carbon-nitrogen bond character characteristic of ring-opened CVL were observed at 1584 cm$^{-1}$ ($\upsilon$(C=N)) and 920 cm$^{-1}$ ($\beta$(C=NR$_2$)) with the asymmetric and symmetric bending modes ($\beta$(N$^+$C$_4$)) appearing as weak peaks at 940 and 790 cm$^{-1}$. Peaks assigned to the carboxylate moiety of ring-opened CVL were observed at 1359 cm$^{-1}$ ($\upsilon$(CO-)$_{sym.}$) and 730 cm$^{-1}$ ($\gamma$(CO-)$_{sym}$). These peaks decreased in intensity as the sample equilibrated but were still very prominent after 1 week. It is important to note that the intensity of ring-opened CVL peaks observed after 1 week in CVL/PG/alcohol mixtures was almost as prominent as those seen in CVL/LG/alcohol mixtures in the minutes following rapid quenching (Figure 6.19).

Figure 8.26 shows a small peak at 1710 cm$^{-1}$ appearing as a shoulder in the quenched mixtures of CVL/PG/alcohol This could be related to the presence of some $\alpha$-alcohol in the mixtures in the quenched solid and be due to an interaction between the carbonyl of PG and the alcohol. At equilibrium the weak shoulder was not observed.
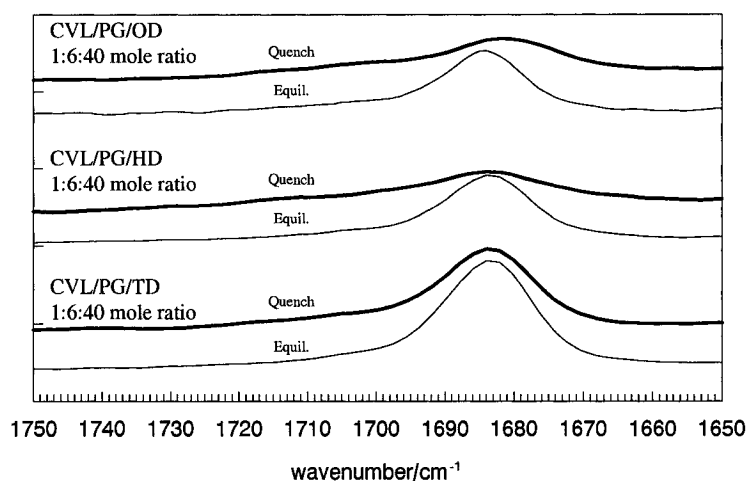
Figure 8.26. Comparison of the Raman spectra in the 1750 to 1650 cm$^{-1}$ region of crystal violet lactone/propyl gallate/alcohol (CVL/PG/alcohol, 1:6:40 mole ratio) mixtures 1 min after rapid quenching from the melt and at equilibrium. A small, broad peak at approximately 1720 to 1710 cm$^{-1}$, comparable to that observed in metastable crystal violet lactone/lauryl gallate/alcohol mixtures, could be associated with alcohol in its α-phase interacting with propyl gallate in the metastable phase. This peak is not a prominent feature of the spectrum and fades within seconds.

### 8.4.3. Images of Crystal Violet Lactone/Octyl Gallate/1-Alcohol Mixtures

Figures 8.27 and 8.28 show images of selected CVL/OG/alcohol mixtures obtained 30 min and at 1 week after slow cooling from the melt, displaying high colour density in the solid state over long time periods. Cooling rate did not appear to make a significant difference in the initial colour density of CVL/OG/alcohol mixtures. However, the colour stability was not as high as that observed in CVL/PG/alcohol mixtures and noticeable colour density was lost as the mixtures equilibrated. Mixtures with high concentrations of solvent relative to developer components (OG:alcohol < 1:10 mole ratio) displayed low colour density in the liquid state and are amenable to conventional reversible thermochromism. As $x_{OG}$ increased the colour density of the liquid become high and there was little contrast between the solid and liquid states. Figure 8.29

compares the colour density of CVL/OG/TD, CVL/OG/HD and CVL/OG/OD (1:6:40 mole ratio) at 30 min and one week after cooling from the melt.
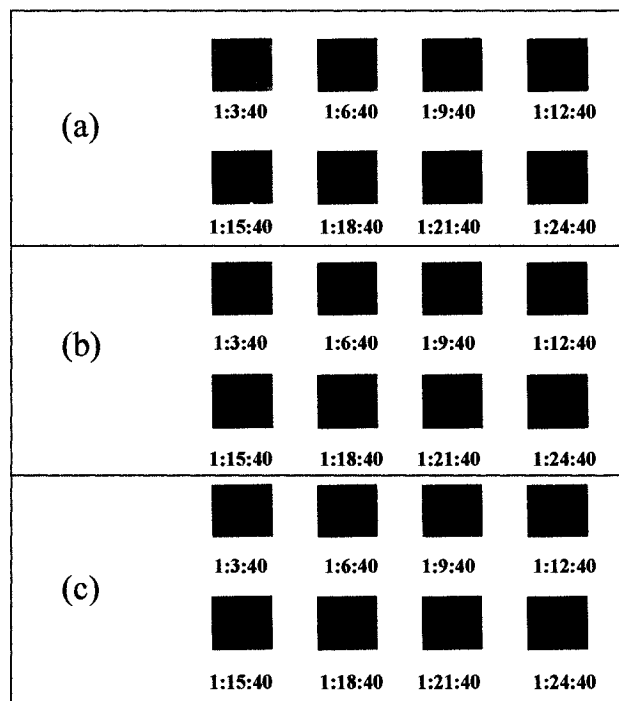
Figure 8.27. Images of selected (a) crystal violet lactone/octyl gallate/1-tetradecanol (CVL/OG/TD) (b) crystal violet lactone/octyl gallate/1-hexadecanol (CVL/OG/HD) and (c) CVL/octyl gallate/1-octadecanol (CVL/OG/OD) mixtures obtained after 30 min of equilibration at 25 °C following slow cooling from the melt. Ratios shown are CVL/OG/alcohol mole ratios.
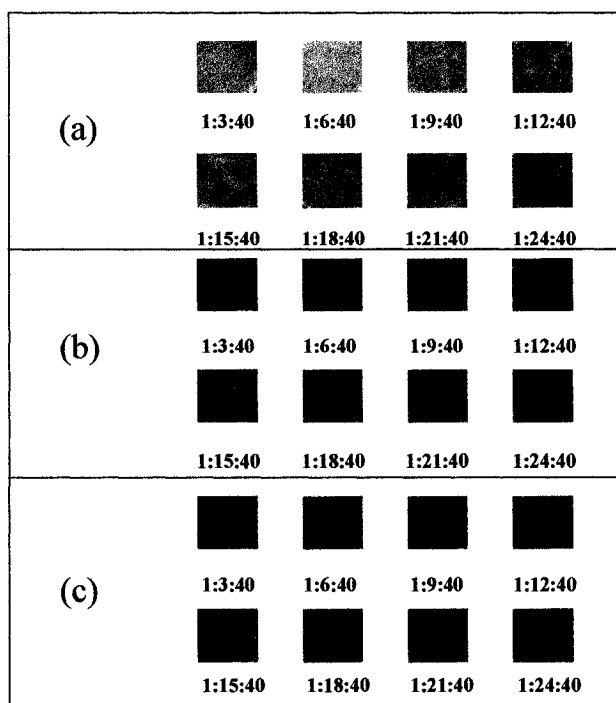
Figure 8.28. Images of selected (a) crystal violet lactone/octyl gallate/1-tetradecanol (CVL/OG/TD)  (b) CVL/octyl gallate/1-hexadecanol (CVL/OG/HD) and (c) crystal violet lactone/octyl gallate/1-octadecanol (CVL/OG/OD)  mixtures obtained after one week of equilibration at 25 °C following slow cooling from the melt. Ratios shown are CVL/OG/alcohol mole ratios.
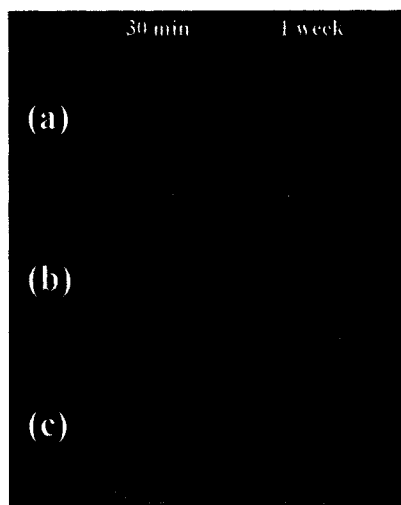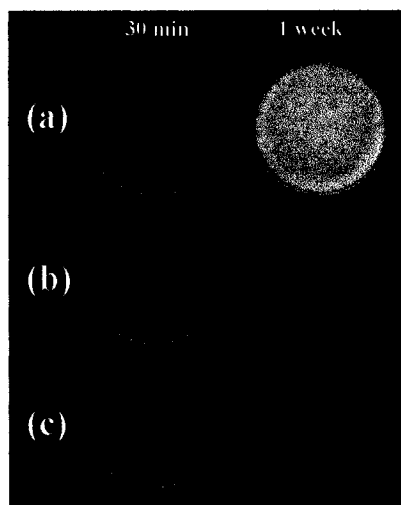


Figure 8.29. Images of (a) crystal violet lactone/octyl gallate/1-tetradecanol (CVL/OG/TD, 1:6:40 mole ratio) (b) CVL/octyl gallate/1-hexadecanol (CVL/OG/HD, 1:6:40 mole ratio) and (c) crystal violet lactone/octyl gallate/1-octadecanol (CVL/OG/OD, 1:6:40 mole ratio) obtained after 30 min and after one week of equilibration at 25 °C following slow cooling from the melt.

High colour density is observed in the time immediately following solidification of the mixtures. As the mixtures equilibrated they lost some colour density. CVL/OG/HD and CVL/OG/OD mixtures still showed high colour density at equilibrium, but CVL/OG/TD mixtures displayed significant decolourisation at equilibrium.

### 8.4.4. Raman Spectroscopy of Crystal Violet Lactone/Octyl Gallate/1-Alcohol Mixtures

Raman spectra of three CVL/OG/alcohol systems (CVL/OG/TD, CVL/OG/HD, and CVL/OG/OD) were obtained after 1 min, 30 min and 24 hr of equilibration at 25 °C following rapid quenching in liquid nitrogen, and are shown in Figures 8.30, 8.31, and 8.32.
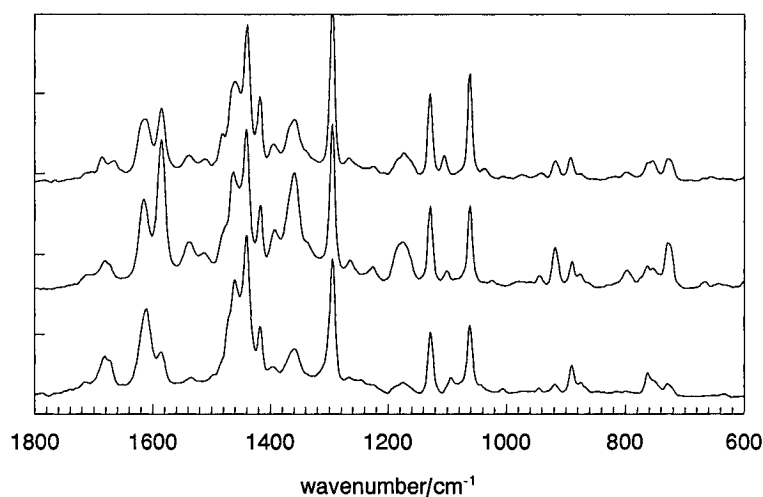


Figure 8.30. Raman spectra of selected crystal violet lactone/octyl gallate/alcohol (CVL/OG/alcohol) mixtures obtained after 1 min of equilibration at 25 °C following rapid quenching in liquid nitrogen. Peaks corresponding to the ring-open form of crystal violet lactone are present in all three mixtures but are more pronounced in crystal violet lactone/octyl gallate/1-hexadecanol (CVL/OG/HD, 1:6:40 mole ratio) and crystal violet lactone/octyl gallate/1-octadecanol (CVL/OG/OD, 1:6:40 mole ratio).
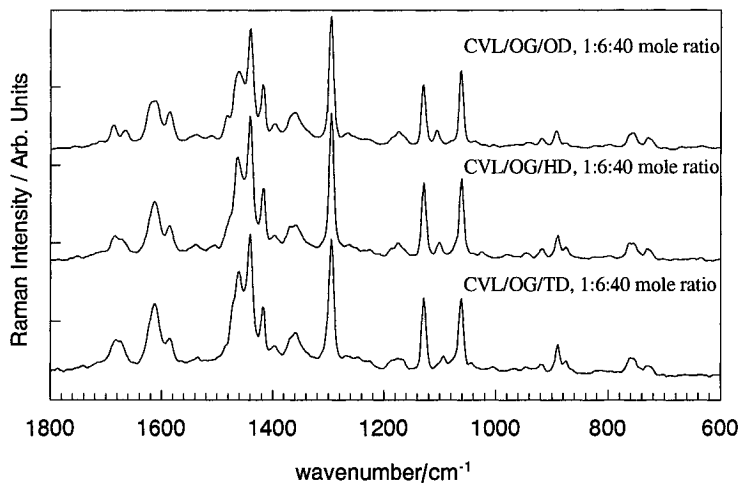
Figure 8.31. Raman spectra of selected crystal violet lactone/octyl gallate/alcohol (CVL/OG/alcohol) mixtures obtained after 30 min of equilibration at 25 °C following rapid quenching in liquid nitrogen. Peaks corresponding to the ring-open form of crystal violet lactone in all three mixtures diminish, but are still visible in all three mixtures.
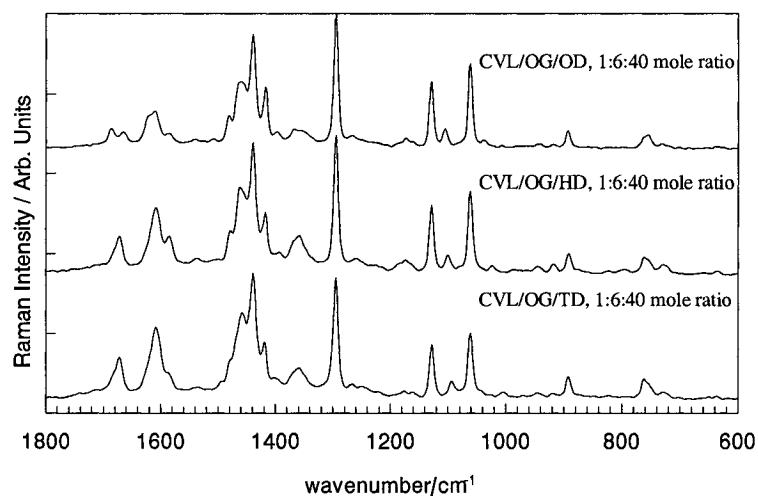


Figure 8.32. Raman spectra of selected crystal violet lactone/octyl gallate/alcohol (CVL/OG/alcohol) mixtures obtained after 24 hr of equilibration at 25 °C following rapid quenching in liquid nitrogen. Peaks corresponding to the ring-open form of crystal violet lactone observed in the mixture diminish somewhat from the intensities observed after 30 min.

Peaks due to the interaction of CVL and OG, similar to those observed in CVL/PG/alcohol and CVL/LG/alcohol systems, are present upon quenching. Over time these peaks lose intensity, but are still visible at equilibrium. Peaks with carbon-nitrogen bond character characteristic of ring-opened CVL are observed at 1584 cm$^{-1}$ ($\upsilon$(C=N)), 920 cm$^{-1}$ ($\beta$(C=NR$_2$)) and 940 and 790 cm$^{-1}$ ($\beta$(N$^+$C$_4$)). Peaks assigned to the carboxylate moiety of ring-opened CVL are observed at 1359 cm$^{-1}$ ($\upsilon$(CO-)$_{sym.}$) and 730 cm$^{-1}$ ($\gamma$(CO-)$_{sym}$). The intensities of these peaks decrease significantly as the mixtures equilibrate, but are still observed after 24 hr.

A small peak at 1710 cm$^{-1}$ (shown in Figure 8.33) is present immediately after quenching. Again, this could be related to the presence of some $\alpha$-alcohol in the mixtures in the quenched solid and be due to an interaction between the carbonyl of OG and the alcohol. At equilibrium the weak shoulder is not observed.
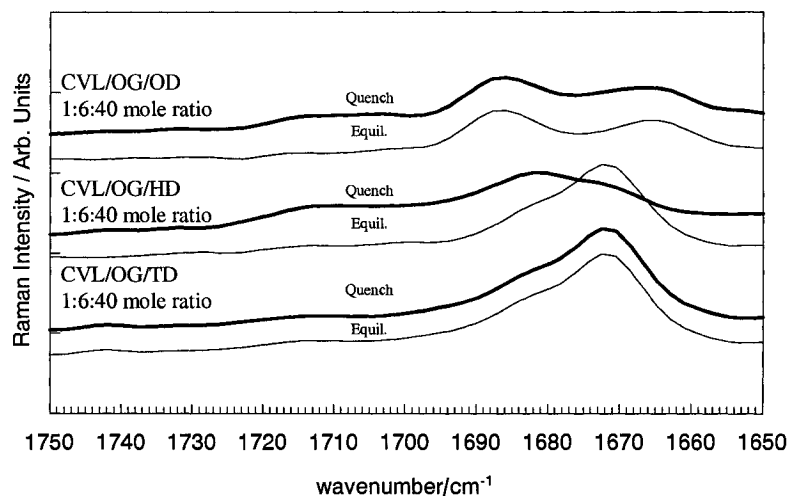
Figure 8.33. Comparison of the Raman spectra in the 1750 to 1650 cm$^{-1}$ region of crystal violet lactone/octyl gallate/alcohol (CVL/OG/alcohol, 1:6:40 mole ratio) mixtures 1 min after rapid quenching from the melt and at equilibrium. A small, broad peak at approximately 1720 to 1710 cm$^{-1}$ comparable to that observed in metastable crystal violet lactone/lauryl gallate/alcohol mixtures could be associated with alcohol in its α-phase interacting with octyl gallate in the metastable phase. This peak is more prominent than observed in the crystal violet lactone/propyl gallate/alcohol mixtures shown in Figure 8.26 and might be an indication that, in the metastable phase, octyl gallate is better than propyl gallate at stabilizing the alcohol α-phase.

## 8.5. Further Discussion of Crystal Violet Lactone/Propyl Gallate/1-Alcohol and Crystal Violet Lactone/Octyl Gallate/1-Alcohol

Examination of the interaction of binary PG/alcohol and OG/alcohol mixtures shows that the developer/solvent attractive interaction (relative to ideal) between PG/alcohol was greater than the attractive developer/solvent interaction between OG/alcohol Since none of the binary mixtures displayed compound formation, it is concluded that both the PG/alcohol and OG/alcohol systems have weaker developer-solvent interactions than the corresponding LG/alcohol mixtures. Both PG/TD and OG/TD mixtures showed the strongest developer-solvent interaction with slight decreases

as the alkyl-chain length of the alcohol is increased. The trend was more apparent in the OG/alcohol mixtures than in the PG/alcohol mixtures.

Introduction of CVL into the PG/alcohol and OG/alcohol mixtures resulted in the development of solids with high colour density and colour stability. Molten CVL/PG/alcohol mixtures that had been cooled to room temperature showed little loss of colour as they equilirated. CVL/OG/alcohol mixtures also displayed high colour density but lost observable amounts of colour density as they equilibrated.

# Chapter 9. Summary, Conclusions, and Future Work

## 9.1. Summary of Rewritable Thermochromic Behaviour as a Function of Developer and Solvent Composition

Through the previous three chapters, nine variations of an archetypal dye/developer/solvent rewritable thermochromic system have been presented, where both the solvent and developer components were varied. The following section briefly summarizes the most important results of this body of research to give the reader a quick overview of the outcomes.

### 9.1.1. Stability of Ring-Opened Crystal Violet Lactone

The presence of ring-opened crystal violet lactone (CVL) in the ternary mixtures was represented by a prominent peak in the Raman spectrum at 1584 cm$^{-1}$ (designated Peak I in Chapter 6). The intensity of this peak was correlated to the observed colour density of the mixture. Table 9.1 shows the ratio of the Raman intensities of Peak I (1584 cm$^{-1}$) and the aromatic $\upsilon$(C=C) of the alkyl gallates at 1616 cm$^{-1}$ ($I_{1584}/I_{1616}$) obtained at 25 °C, 60 s after quenching the melt in liquid nitrogen. (The peak at 1616 cm$^{-1}$ was observed in all three alkyl gallates examined and showed insignificant change in intensity in the time-resolved Raman experiments presented in Chapter 6.) Table 9.2 shows $I_{1584}/I_{1616}$ obtained at 25°C, 24 hr after quenching the melt in liquid nitrogen.

278

Table 9.1. The ratios of the Raman intensities of the $\upsilon$(C=N) mode in ring-opened crystal violet lactone (at 1584 cm$^{-1}$) to the aromatic $\upsilon$(C=C) mode of propyl gallate, octyl gallate, and lauryl gallate at (1616 cm$^{-1}$) in crystal violet lactone/alkyl gallate/1-alcohol mixtures (1:6:40 mole ratio) obtained 60 s after quenching in liquid nitrogen and equilibrating at 25 °C. All intensities are taken from data presented in Chapters 6 and 7.

|                    | 1-tetradecanol | 1-hexadecanol | 1-octadecanol |
|--------------------|----------------|---------------|---------------|
| *propyl gallate*   | 0.5 ± 0.2      | 2 ± 0.2       | 1.9 ± 0.2     |
| *octyl gallate*    | 0.5 ± 0.2      | 1.9 ± 0.2     | 1.4 ± 0.2     |
| *lauryl gallate*   | 0              | 0.8 ± 0.2     | 1.3 ± 0.2     |

Table 9.2. The ratios of the Raman intensities of the $\upsilon$(C=N) mode in ring-opened crystal violet lactone (at 1584 cm$^{-1}$) to the aromatic $\upsilon$(C=C) mode of propyl gallate, octyl gallate, and lauryl gallate at (1616 cm$^{-1}$) in crystal violet lactone/alkyl gallate/1-alcohol mixtures (1:6:40 mole ratio) obtained 24 hr after quenching in liquid nitrogen and equilibrating at 25 °C. All intensities are taken from data presented in Chapters 6 and 7.

|                    | 1-tetradecanol | 1-hexadecanol | 1-octadecanol |
|--------------------|----------------|---------------|---------------|
| *propyl gallate*   | 0.4 ± 0.2      | 0.8 ± 0.2     | 0.7 ± 0.2     |
| *octyl gallate*    | 0.3 ± 0.2      | 0.5 ± 0.2     | 0.4 ± 0.2     |
| *lauryl gallate*   | 0              | 0             | 0.1 ± 0.2     |

In general, mixtures containing propyl gallate (PG) had the most prominent Peak I (1584 cm$^{-1}$) intensities in both the metastable (after quenching) and equilibrium states of all the systems examined. Mixtures containing lauryl gallate (LG) had the weakest Peak I (1584 cm$^{-1}$) intensities in the metastable and equilibrium states. In all systems examined the Peak I (1584 cm$^{-1}$) intensities are weakest when 1-tetradecanol was used as the solvent component.

The changes in intensity ratio of Peak I (1584 cm$^{-1}$) compared with the peak at 1616 cm$^{-1}$, $\Delta(I_{1584}/I_{1616})$, are shown in Table 9.3 for the nine systems examined.

Table 9.3. The changes in intensity ratios of Peak I (1584 cm$^{-1}$) and the $\upsilon$(C=C) peak at 1616 cm$^{-1}$, $\Delta(I_{1584}/I_{1616})$, in crystal violet lactone/alkyl gallate/1-alcohol mixtures (1:6:40 mole ratio) obtained 60 s and 24 hr after quenching in liquid nitrogen and equilibrating at 25 °C. All intensities are taken from data presented in Chapters 6 and 7.

|  | 1-tetradecanol | 1-hexadecanol | 1-octadecanol |
|---|---|---|---|
| *propyl gallate* | $0.1 \pm 0.2$ | $1.2 \pm 0.2$ | $1.2 \pm 0.2$ |
| *octyl gallate* | $0.2 \pm 0.2$ | $1.4 \pm 0.2$ | $1.0 \pm 0.2$ |
| *lauryl gallate* | 0 | $0.8 \pm 0.2$ | $1.2 \pm 0.2$ |

The $\Delta(I_{1584}/I_{1616})$ values were smallest for systems containing 1-tetradecanol as the solvent and significantly larger when 1-hexadecanol and 1-octadecanol were used as solvents. Based on the time-resolved Raman data collected for CVL/LG/alcohol mixtures it is speculated that the large $\Delta(I_{1584}/I_{1616})$ values seen in mixtures containing 1-octadecanol and 1-hexadecanol are due to an enhanced stability of ring-opened CVL in the solid mixture, relative to mixtures containing 1-tetradecanol as the solvent. The small $\Delta(I_{1584}/I_{1616})$ in CVL/LG/TD may also be affected by rapid conversion from metastable to equilibrium coloured states in the mixtures, *i.e.* the measurements do not account for any Peak I (1584 cm$^{-1}$) decay occurring in the first 45 to 60 s of equilibration following quenching, so the actual $\Delta(I_{1584}/I_{1616})$ for the systems containing 1-tetradecanol may be higher than reported in Table 9.3.

### 9.1.2. Interaction Between Alkyl Gallate Developers and 1-Alcohol Solvents

Interactions between CVL/PG, CVL/OG, and CVL/LG were shown to be in line with thermodynamic interaction parameters and Raman structural data (Chapter 8). With this in mind, the change in the stability of ring-opened CVL was attributed to changes in

the attractive interaction between the developer and solvent components as the solvent component was changed in the rewritable thermochromic mixtures. Tables 9.4 and 9.5 summarize the interaction between PG, OG, and LG with the three alcohol solvents examined (TD, HD, and OD).

Table 9.4. Summary of overall features of the alkyl gallate/alcohol binary phase diagrams, as determined in Chapter 5. Propyl gallate/alcohol and octyl gallate/alcohol form simple eutectic mixtures with no compound formation. Lauryl gallate/alcohol mixtures display stronger alkyl gallate/alcohol attractive interaction through the formation of congruently melting compounds of the form (lauryl gallate)$_2$•alcohol.

| | *1-tetradecanol* | *1-hexadecanol* | *1-octadecanol* |
|---|---|---|---|
| *propyl gallate* | Eutectic mixture | Eutectic mixture | Eutectic mixture |
| *octyl gallate* | Eutectic mixture | Eutectic mixture | Eutectic mixture |
| *lauryl gallate* | Congruently melting compound: (LG)$_2$•TD | Congruently melting compound: (LG)$_2$•HD | Congruently melting compound: (LG)$_2$•OD |

Table 9.5. Summary of the interaction parameters determined for the alcohol component ($W^H{}_{alcohol}$) of alkyl gallate/alcohol binary mixtures. All data are from Chapters 7 and 8 and were determined by fitting Eq. 7.12 to experimental alcohol fusion and melting enthalpies. (*N.B.* the signs of $W^H{}_{alcohol}$ for lauryl gallate/alcohol mixtures have been reversed relative to their values in Table 7.4 so they compare better with the sign of $W^H{}_{alcohol}$ obtained for propyl gallate/alcohol and octyl gallate/alcohol mixtures from Table 8.3, *i.e.* a negative $W^H{}_{alcohol}$ value implies attractive interaction and *vice versa*.)

| | *1-tetradecanol* $W^H{}_{TD}/(kJ\ mol^{-1})$ | *1-hexadecanol* $W^H{}_{HD}/(kJ\ mol^{-1})$ | *1-octadecanol* $W^H{}_{OD}/(kJ\ mol^{-1})$ |
|---|---|---|---|
| *propyl gallate* | -18 ± 6 | +13 ± 8 | +2 ± 2 |
| *octyl gallate* | -46 ± 2 | -20 ± 4 | -5 ± 5 |
| *lauryl gallate* | -8 ± 3† | +2 ± 2† | +9 ± 4† |

† $W^H{}_{alcohol}$ values are determined for the interaction of the alcohol with (LG)$_2$•alcohol. These values cannot be compared directly with the $W^H{}_{alcohol}$ values determined for PG/alcohol and OG/alcohol mixtures.

The attractive interaction between developer and solvent was always strongest in the alkyl gallate/1-tetradecanol mixtures. As the alkyl-chain length of the alcohol was increased above 14 carbons the attractive interaction between the alkyl gallate and the alcohol weakened and/or became nearly ideal. Changing the alkyl-chain length of the developer from 3 carbons (propyl gallate, PG) to 8 carbons (octyl gallate, OG) resulted in a significant strengthening of the attractive interaction between the alkyl gallate and the alcohol for all alcohols examined. While the interaction parameters for lauryl gallate/alcohol (LG/alcohol) mixtures do not compare directly with those determined for PG/alcohol and OG/alcohol mixtures (*cf.* footnote on Figure 7.5), LG/alcohol was the only binary system examined found to form a binary compound ((LG)$_2$•alcohol). With this in mind, the attractive interaction between LG and the alcohols in LG/alcohol mixtures is considered much stronger than the attractive interaction between PG and alcohols and OG and alcohols in their respective binary mixtures.

In summary, within the systems examined, increasing the alkyl-chain length of the alkyl gallate developer and decreasing the alkyl-chain length of the alcohol solvent resulted in the strongest alkyl gallate/alcohol attractive interactions. It is important to note that long alkyl chains in both the developer and solvent molecules are necessary to achieve compound formation.

### 9.1.3. Effect of Developer/Solvent Interactions on Observed Thermochromic Behaviour

Results from Chapters 6 and 8 showed that changing the alkyl gallate/alcohol attractive interactions had a significant effect on thermochromic behaviour. Table 9.6

compares the quality of two rewritable thermochromic properties (colour contrast and

decolourisation rate) for the nine systems examined.

Table 9.6. Comparison of the quality of colour contrast and decolourisation rates for the nine crystal violet lactone/alkyl gallate/alcohol systems examined. A system is considered good if it displays optimal behaviour for both properties. If one, or both, of these properties not optimal, the system is considered poor.

|  | *1-tetradecanol* | *1-hexadecanol* | *1-octadecanol* |
|---|---|---|---|
| *propyl gallate* | Very Poor | Very Poor | Very Poor |
| *octyl gallate* | Poor | Very Poor | Very Poor |
| *lauryl gallate* | Good | Poor | Poor |

CVL/PG/alcohol and CVL/OG/alcohol mixtures display, for the most part, very

poor rewritable thermochromic properties. The most serious problem is the effective lack

of colour contrast between the metastable and equilibrium mixtures (these mixtures also

show the weakest attractive developer/solvent interactions.) Only CVL/LG/alcohol

mixtures display rewritable thermochromic properties and, within this system, only

CVL/LG/TD mixtures display good rewritable thermochromic properties. Comparison of

Tables 9.5 and 9.6 shows that rewritable thermochromic properties improve as the

attractive interaction between the alkyl gallate developer and the alkyl gallate solvent

increases. This has been proposed to be the result of the competition between the

developer/dye and developer/solvent (as outlined in Chapter 7). The greater the

developer/solvent attractive interaction, the greater the thermodynamic driving force to

overcome the developer/dye attractive interaction. Stronger developer/solvent

interactions result in higher colour contrast and faster declourization rates.[197]

Table 9.7 summarizes the rewritable thermochromic properties observed in

CVL/LG/alcohol mixtures and shows how the thermochromic properties improve as the

alkyl-chain length of the alcohol solvent is lowered from 18 carbons to 14 carbons (resulting in enhanced LG/alcohol attraction).

Table 9.7. Colour densities of thermochromic mixtures are expressed in % reflectance intensity at 620 nm (the $\lambda_{max}$ of ring-opened CVL). Reflectance data are from Chapter 6 and are the average values of a range of crystal violet lactone/lauryl gallate/alcohol mixtures with mole ratios ranging from 1:(1-20):(40-50). *N.B.* High values of reflectance intensity correspond to low colour density and *vice versa*.

| Rewritable Thermochromic Properties | CVL/LG/TD | CVL/LG/HD | CVL/LG/OD |
|---|---|---|---|
| Colour density in the melt as measured by % reflectance at 620 nm | 15-70 | 5-35 | 15-35 |
| Metastable colour density as measured by % reflectance at 620 nm | 5-20 | 5-10 | 5-10 |
| Equilibrium colour density as measured by % reflectance at 620 nm | 75-90 | 30-50 | 30-35 |
| Contrast (metastable colour density/equilibrium colour density) | 4-18 | 3-10 | 3-7 |
| Decolourisation time | seconds | minutes | hours |

The colour density of the molten mixtures is highest in the crystal violet lactone/lauryl gallate/1-octadecanol (CVL/LG/OD) and crystal violet lactone/lauryl gallate/1-hexadecanol (CVL/LG/HD) mixtures relative to crystal violet lactone/lauryl gallate/1-tetradecanol (CVL/LG/TD) mixtures. This probably reflects the enhanced LG/TD attractive interaction relative to LG/HD and LG/OD, resulting in an increased

solubility of LG in molten TD. Higher solubility of the developer in the molten solvent results in a lower coloour-developing interaction between the developer and the dye.

Metastable colour densities obtained from reflectance data are similar, within experimental error. Comparison of the reflectance data and the Peak I (1584 cm$^{-1}$) Raman data from Table 9.1 shows that the metastable colour density increases as the alkyl-chain length of the solvent increases from 14 carbons. This trend is also consistent with the increased colour density of the molten mixtures and reflects the increased stability of CVL in its ring-opened form as the attractive interaction between LG and the alcohols decreases.

The relative stability of the coloured form of CVL is also reflected in the equilibrium colour densities, which show an increasing trend within this data set as the alkyl-chain length of the solvent increases (also see Figures 6.6, 6.8, and 6.10). The colour contrast of the mixtures is a direct result of the metastable and equilibrium colour densities and shows the same trend as the solvent component is changed.

In general, increasing the concentration of LG within each system results in increased colour density in the melt, the metastable solid, and equilibrium solid states. This accounts for the variation in the reflectance intensities shown in Table 9.7. As $x_{LG}$ increases excess LG exists in the melt to interact with CVL, resulting in higher colour densities upon quenching. The cause of increased colour densities at equilibrium as $x_{LG}$ increases is not as easily explained. Larger amounts of LG presumably result in larger amounts of coloured (LG)$_x$•CVL complex. Colour density is lost as the LG migrates from (LG)$_x$•CVL to the more stable (LG)$_2$•alcohol. It is reasonable to assume that this conversion does not necessarily go to completion in the solid state and that small amounts

of free LG might exist at equilibrium that could interact with CVL. (The high molar extinction coefficient of ring-opened CVL[122] could explain observable colour density with only small amounts of LG present.)

The most prominent difference in the three thermochromic systems presented in Table 9.7 is the rate at which they change from their metastable to equilibrium solid states. Time-resolved Raman data presented in Chapter 6 showed that (LG)$_x$•CVL destruction, (LG)$_2$•alcohol formation, and $\alpha$-$\beta$ (or $\alpha$-$\gamma$) alcohol phase transitions occur in the quenched metastable solid mixtures as they equilibrate. In general, the rate of decolourisation correlated with these observed events.

## 9.2. Proposed Design Rules

The observation, characterization, and thermal analysis of developer/solvent compounds are the most interesting and useful results of this research. This is the first time that the aspect of competition within rewritable thermochromic mixtures has been quantitatively examined.[197] Desirable rewritable thermochromic properties could be improved by using developer-solvent combinations which possess strong attractive interactions that can compete with attractive dye-developer interactions in the solid state. Therefore, a potential design rule is proposed for the optimization of rewritable thermochromic properties: *high colour contrast, low equilibrium colour density, and rapid decolourisation rates could be optimized by selecting developer-solvent combinations that show strong attractive interactions, preferably displaying binary compound formation in the solid state.*

A schematic of optimal rewritable thermochromic mechanism is shown in Figure 9.1 for the CVL/LG/alcohol system.
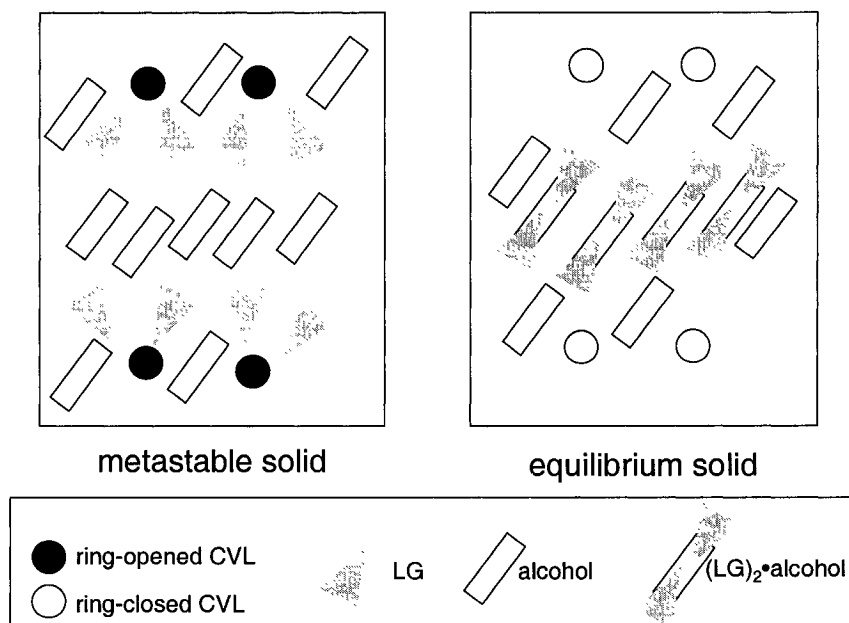


Figure 9.1 A schematic of optimal thermochromic mechanism based on the observations of the CVL/LG/alchol mixture. The metastable solid mixture is coloured and characterized by a strong dye-developer interaction. Strong developer-solvent attractive interactions result in the formation and phase separation of a $(LG)_2 \bullet OD$ in the equilibrium, non-coloured solid.

The metastable solid is characterized by strong dye-developer interactions resulting in high colour density. If the developer-solvent attractive interactions are significantly greater than the developer-dye attractive interactions (as in CVL/LG/alcohol mixtures) the equilibrium mixture will favour the destruction of the developer-dye compound, formation of developer-solvent compound, and subsequent decolourisation. If the developer-solvent attractive interactions are comparable to or weaker than the developer-dye attractive interactions the mixture will decolour slowly, if at all (CVL/PG/alcohol and CVL/OG/alcohol mixtures).

Application of the proposed design rules would involve a search for developer/solvent combinations that display compound formation. In the case of the alkyl gallate and alcohol combinations examined, two features were required to achieve compound formation. Raman and NMR data confirmed the presence of H-bonds between the phenol group (or groups) of the alkyl gallate and the hydroxy group of the alcohol. However, this interaction alone was not sufficient to result in compound formation. The extension of the alkyl-chain of the gallate molecule was necessary to produce a stable binary compound. This phenomenon highlights the importance of interchain van der Waals interactions in the development of stable molecular compounds.

A reasonable first step in a future search for optimal developer/solvent combinations would begin with developer molecules with long-chain alkyl groups that are known to produce coloured complexes with leuco dyes such as CVL. Examples of these materials include common organic acids such as: alkyl phosphonic acids, alkyl carboxylic acids, and acidic derivatives of alkyl benzoates. For example, the mixtures of octadecylgallate (ODG) and docosylphosphonic acid (P20) shown in Figures 2.7 through 2.9 display alkyl gallate bonding comparable to that observed in lauryl gallate/1-alcohol mixtures.[85] Next, solvent components with alkyl-chain lengths comparable to the developer molecules, such as alcohols, parrafins, and esters, would be selected. Analysis of the developer/solvent combinations using the techniques outlined in this thesis could provide the researcher with more developer/solvent combinations that posseses the attractive interactions required to produce optimal rewritable thermochromic behaviour.

Once a series of developer/solvent compounds is prepared, a series of design rules could be developed to predict and explain compound formation within developer/solvent

mixtures, such as the optimal H-bond donor and acceptor combinations, the optimal differences in alkyl chain length, and the role of rotational or disordered phases in one or both components.

Finally, a thermochromic leuco dye could be incorporated into promising developer/solvent systems to produce ternary rewritable thermochromic mixtures with optimal colour contrast and decolourisation rates.

### 9.3. Future Work

This research has provided a general overview of several thermochromic systems and their properties, but it is by no means complete. The following section outlines a number of potentially fruitful future directions for this research.

### 9.3.1. Extension of Design Rules Using Combinatorial Techniques

Full examination of the structural, thermal, and thermochromic properties of even a small group of developers and solvents, such as those in the present study, is a labour-intensive process. A typical thermochromic patent[60,64,85,92,108,112] shows thousands of potential developer/solvent combinations. Screening of all potential candidates in the manner used in this study would be a tedious, and potentially fruitless undertaking. The development of a combinatorial approach could be the best avenue to approach this aspect of the study.

In the last several years, combinatorial techniques have become important in synthetic and pharmaceutical chemistry.[204-206] Recently, advances have been made in applying combinatorial techniques to materials science. In solid-state applications these

combinatorial techniques are limited to reactions that occur by mixing various ratios of components together and heating (*e.g.* superconductors, advanced battery materials, and electroluminescent phosphors).[204-206] Since the process of thermochromic sample preparation involves a simple mixing and heating of components, a combinatorial approach might be relatively straightforward to develop.

While some combinatorial approaches are expensive to prepare and analyze there have been some notable and ingenious exceptions. In 1998 Reddington *et al.* modified a standard inkjet printer to deposit known quantities of dissolved solute to a substrate.[206] Since the printer is programmed to deposit specific volumes of ink for the desired output it could be modified to deliver known volumes of separate dye, developer, and solvent solutions. Deposition of the solutions into a pit or depression within a substrate, followed by solvent evaporation, could reproduce the manual mixing of the components. Subsequent heating and fusion of the remaining solids could produce the desired binary or ternary mixture. Arrays of sample compositions within a substrate could be quickly and easily prepared. Micro-Raman spectroscopy equipment could be used to raster the laser across samples and obtain spectra at various positions. In principle, Raman spectra of each individual sample within an array could be obtained in an automated process. Examination of the Raman data of various compositions of a binary solvent-developer mixture would allow a quick screen for compound formation. The solid-liquid equilibrium phase diagrams of binary mixtures showing promise could be examined in greater detail using DSC.

### 9.3.2. Enhanced Thermal Analysis

Thermal analysis has proven to be a powerful tool in the examination and understanding of thermochromic mixtures. For the purposes in the present study the Pyris-1 DSC has been extremely useful and productive. However, its limited sensitivity precludes detailed isothermal DSC studies of CVL/LG/HD and CVL/LG/OD mixtures. Information on the thermal events occurring during the equilibration of these mixtures would be useful in comparing with the behaviour of CVL/LG/TD mixture and in the confirmation of the events predicted by the time-resolved Raman experiments. Isothermal DSC using a nano-DSC instrument with enhanced sensitivity might be best way to examine the small enthalpy changes observed in these mixtures.

A detailed comparison of the strength of binary compounds formed requires knowledge of the heat capacities of the compounds and their individual components. Use of a PPMS (Physical Properties Measurement System, Quantum Design) would allow for a rapid determination of the heat capacities, and other thermal properties of samples from 0.5 K to 350 K.

### 9.3.3. Microstructural Analysis

While Raman spectroscopy and thermal analysis give insight into the possible processes occurring within the mixtures and their thermodynamic barriers, there is still limited information on the detailed structures of these systems.

In CVL/LG/alcohol mixtures, the thermodynamic analysis indicates that the developer-solvent complex is more stable than the dye-developer complex in the solid state and that the developer will migrate to the solvent. Raman spectroscopy confirms the

rapid destruction of coloured complex, transition of $\alpha$-alcohol to the $\beta$- or $\gamma$-alcohol phase, and formation of $(LG)_2$•alcohol.

Examination of the microstructure of quenched materials as a function of time using techniques such as X-ray diffraction or transmission electron microscopy could provide more information to supplement these observations and provide insight into how they take place. Microstructural examination could also explain some of the variation in the rate of the processes observed as a function of LG concentration, sample size, and alcohol morphology within a given CVL/LG/alcohol mixture. For instance, why do the rates of the $\alpha$-$\beta$ TD and $(LG)_2$•TD transitions in CVL/LG/TD decrease and then increase as $x_{LG}$ is increased? Could the molar composition and/or sample size play a role in the size or distribution of crystals formed in the mixture? Do different quenching rates produce changes in the microcrystalline structure and the way in which the phases nucleate and separate? How significant are the structural differences between $\beta$- and $\gamma$-alcohol phases in the solid state and how do they influence the stability of $\alpha$-phases and/or the kinetics of decolourisation? Resolution of some of these questions could provide even greater understanding of the mechanisms of these interesting materials.

### 9.3.4. Application

The research presented in this thesis provides fundamental data on rewritable thermochromic mixtures that is missing from the open literature. It is the first body of research that provides evidence for the competition between components in a ternary dye/developer/solvent mixture. While this research begins to fill important gaps in the knowledge of these materials there are still considerable obstacles to be understood and

overcome before rewritable thermochromic materials can be commercially applied. These obstacles are associated with the industrial preparation of these materials outlined in Chapters 1 and 2.

First, these materials are generally microencapsulated prior to application to a substrate.[7,95,96] The first barrier to application of an optimal mixture would be to develop a microencapsulation technique that reproduces the benchtop composition within the microcapsule structure. The present research has shown that rewritable thermochromic systems are highly sensitive to subtle changes in interactions between individual components, and therefore it would be necessary to probe the interaction of the thermochromic system with the microcapsule material. The effect of sample size could become significant in the production of microcapsules; instead of a bulk homogeneous mixture, the mixture would consist of tiny encapsulated domains on the order of 5 to 50 $\mu$m.[7,41,84] A full understanding and optimization of the effect of sample size would be necessary to reproduce the behaviour designed on the benchtop.

Second, thermochromic materials are often combined with small amounts anti-oxidants and photo-stabilizers to enhance the colour density and lifetime of the material. Once optimal dye/developer/solvent mixtures are developed they must be combined with these stabilizing materials to see if the properties remain the same. The selection of developer and/or solvent components that also act as photostabilizers might be a way of avoiding this problem.

## 9.4. Final Thoughts

This project has shown the utility of fundamental research in addressing problems in interesting industrial applications. Many of the problems within the field of rewritable thermochromism can be attributed to a lack of understanding of the way the components interact at the molecular level. The research presented has shows that the properties of rewritable thermochromic systems are governed by a complex balance of interactions between dye, developer, and solvent components. While this research does not provide a definitive understanding of all rewritable thermochromic mixtures, it outlines an approach for examining new systems that considers and assesses the importance of competition of intermolecular interactions between mixture components.

# References

1. M.A. White, *Properties of Materials*, Oxford University Press: Oxford, **1999**.

2. K. Nassau, *The Physics and Chemistry of Colour*, 2$^{nd}$ Edition, John Wiley and Sons: New York, **2001**.

3. D. N. Batchelder, *Contemporary Physics*, **1988**, *29*, 31-36.

4. F.A. Cotton and G. Wilkinson, *Advanced Inorganic Chemistry*, 5$^{th}$ Edition, John Wiley and Sons: New York, **1988**.

5. J.H. Day, *Chem. Rev.*, **1968**, *68*, 649-657.

6. T.H. Lowry and K.H. Richardson, *Mechanism and Theory in Organic Chemistry*, 3$^{rd}$ Edition, Harper Collins: New York, **1987**.

7. D. Aitken, S.M. Burkinshaw, J. Griffiths, and A.D. Towns, *Rev. Prog. Coloration*, **1996**, *26*, 1-8.

8. N. Sekar, *Colourage*, May 1998, 45-52.

9. D.A. McQuarrie, *Quantum Chemistry*, University Science Books: Sausalito, **1983**.

10. J.H. Day, *Chem Rev.*, **1963**, *63*, 65-80.

11. C.B. Greenberg, "Chromogenic Materials (Thermochromism)" in *Kirk-Othmer Encyc. of Chem. Tech.* 4$^{th}$ ed., Vol. 6, 337-343, John-Wiley & Sons: New York, **1993**.

12. C. Lampert, *IEEE Circuits and Devices Magazine*, **1997**, *8*, 19-26.

13. M. Marinovic, R. Nikolic, J. Savovic, S. Gadzuric, and I. Zsigrai, *Solar Energy Materials and Solar Cells*, **1998**, *51*, 401-411.

14. R. M. Podhajny, *Paper Film Foil Converter*, June 1999, 24.

15. M. Tanaka, H. Hayashi, S. Matsonoto, S. Kashino, and K. Mogi, *Bull. Chem. Soc. Jpn.* , **1997**, *70*, 329-337.

16. J. Stasiek, *Heat and Mass Transfer*, **1997**, *33*, 27.

17. J.H. Sun, K.C. Leong, and C.Y. Liu, *Heat and Mass Transfer*, **1997**, *33*, 121.

18. B.M. Christie and D. Bryant, *Surface Coatings International*, **1995**, *8*, 332.

19. T. Sugawara and I. Takasu, *Advances in Physical Organic Chemistry*, **1999**, *32*, 219-264.

20. H. Meyer, *Chem. Berichte*, **1909**, *42*, 143-145.

21. A. Schönberg and O. Schutz, *Chem. Berichte*, **1928**, *61*, 478-479.

22. E.D. Bergmann and H. Corte, *Chem. Berichte*, **1933**, *66*, 39-43.

23. M. Tanaka, *Bull. Chem. Soc. Jpn.*, **1993**, *70*, 3171-3174.

24. M. Leclerc, M. Fréchette, J.-Y. Bergeron, M. Ranger, I. Lévesque, and Karim Faid, *Macromol. Chem. Phys.*, **1996**, *197*, 2077-2087.

25. H. Tachibana, R. Kumai, N. Hosaka, and Y. Tokura, *Chem. Mater.*, **2001**, *13*, 155-158.

26. T. Kanai, H. Ishibashi, Y. Hayashi, T. Ogawa, S. Furukawa, R. West, T. Dohmaru, and K. Oka, *Chem. Lett.*, **2000**, 650-651.

27. B. Chu and R. Xu, *Acc. Chem. Res.*, **1991**, *24*, 384-389.

28. M. Wenzel and G.H. Atkinson, *J. Am. Chem. Soc.*, **1989**, *111*, 6123-6127.

29. T. Gahimer and W.J. Welsh, *Polymer*, **1996**, *10*, 1815-1823.

30. C.Yang, F.P. Orfino, and S. Holdcroft, *Macromolecules*, **1996**, *29*, 6510-6517.

31. T. Sanji, K. Sakamoto, and H. Saurai, *Chem. Lett.*, **1998**, 255-256.

32. C.-H. Yuan and R. West, *Macromolecules*, **1998**, *31*, 1087-1092.

33. T. Mino, H. Tamura, and K. Ogawa, *Langmuir*, **1991**, *7*, 2336-2341.

34. A. Lio, A. Reichert, D.J. Ahn, J.O. Nagy, M. Salmeron, and D.H. Charych, *Langmuir*, **1997**, *13*, 6524-6532.

35. I. Levesque and M. LeClerc, *Chem. Mater.*, **1996**, *8*, 2843-2849.

36. D.-C. Lee, S.K. Sahoo, A.L. Choll, and D.J. Sandman, *Macromolecules*, **2002**, *35*, 4347-4355.

37. N. Hirota, N. Hisamatsu, S. Maeda, H. Tsukashara, and K. Hyodo, *Synthetic Metals*, **1996**, *67*, 67-72.

38. D.H. Charych, W. Spevak, J.O. Nagy, and M.D. Bednarski, *Mat. Res. Soc. Symp. Proc.*, **1993**, *292*, 153-161.

39. S. Okada, S. Peng, W. Spevak, and D. Charych, *Acc. Chem. Res.*, **1998**, *31*, 229-239.

40. A. Mills and A. Lepre, *Analyst*, **1999**, *124*, 685-689.

41. M.A. White and M. LeBlanc, *J. Chem. Ed.*, **1999**, *76*, 1201-1204.

42. C.R. Smith, D.R. Sabatino, and T.J. Praisner, *Experiments in Fluids*, **2001**, *30*, 190-201.

43. S. Slade, *Engineering Digest*, **1987**, *33*, 24.

44. L. Wenge, Z. Changzhong, W. Wenfen, and W. Jinping, *Gongneng Caliao*, **1997**, *28*, 337-341.

45. S. Slade, *Surface Coatings Australia*, Jan/Feb 1987, 8-9.

46. T.J. Homola, *Screenprinting*, Nov. 1998, 12-20.

47. K. Ogawa, J. Harada, T. Fujiwara, and S. Yoshida, *J. Phys. Chem. A*, **2001**, *105*, 3425-3427.

48. R. M. Christie, *Colour Chemistry*, Royal Society of Chemistry: Cambridge, **2001**.

49. S. Glasstone, *Text Book of Physical Chemistry*, G.Van Norstrand: New York, **1940**.

50. T. Sekikawa, T. Kobayashi, and T. Inabe, *J. Phys. Chem. B*, **1997**, *101*, 10645-10652.

51. T. Sekikawa, T. Kobayashi, and T. Inabe, *J. Phys. Chem. A*, **1997**, *101*, 644-649.

52. C. Benedict, U. Langer, H.-H. Limbach, H. Ogata, and S. Takeda, *Ber. Bunsenges. Phys. Chem.*, **1998**, *102*, 355-339.

53. H. Gorner, *Chem. Phys.*, **1997**, *222*, 315-329.

54. G. Favaro, F. Masetti, U. Mazzucato, G. Ottavi, P. Allegrini, and V. Malatesta, *J. Chem. Soc. Faraday Trans.*, **1994**, *90*, 333.

55. S.-K. Keum, M.-S. Hur, P.M. Kazmaier, and E. Buncel, *Can. J. Chem.*, **1991**, *69*, 1941-1947.

56. G. Favaro, F. Ortica, and V. Malatesta, *J. Chem. Soc. Faraday Trans.*, **1995**, *91*, 333-4103.

57. R. Dickinson and I.M. Heilbron, *J. Chem. Soc.*, **1927**, 1699-1705.

58. Y.S. Lee, J.G. Kim, Y.D. Huh, and H.K. Kim, *J. Korean Chem. Soc.*, **1994**, *38*, 864-872.

59. M.A. White, *J. Chem. Ed.*, **1998**, *9*, 1119-1120.

60. K. Tsutsui, T. Yamaguchi, and K. Sato, *Jpn. J. Appl. Phys.*, **1994**, *33*, 5925-5928.

61. K. Tsutsui, T. Yamaguchi, and K. Sato, *Ranilao Gongye*, **1995**, *1*, 68-73.

62. D.G. Hafeman, K.L. Crawford, and L.J. Bousse, *J. Phys. Chem.*, **1993**, *97*, 3058.

63. P.J. Sadkowski and G. R. Flemming, *J. Phys. Chem.*, **1972**, *5*, 762.

64. M. Yanagita, S. Kanda, K. Ito, R. Shibuya, and S. Tokita, *Mol. Cryst. Liq. Cryst.*. **1999**, *327*, 53-56.

65. D.A. Hinckley, P.G. Seyfold, and D.P. Berris, *Spectrochimica Acta*, **1986**, *42A*, 747-754.

66. D.A. Hinckley and P.G. Seyfold, *Spectrochimica Acta*, **1988**, *44A*, 1053-1059

67. M. Tremayne, B.M. Karuki, and K.D.M. Harris, *Angew. Chem. Int. Ed. Engl.*, **1997**, *36*, 770-772.

68. D.A. Brown and M.J.S. Dewar, *J. Chem. Soc.*, **1954**, 2134-2136.

69. R. Markuszewski and H. Diehl, *Talanta*, **1980**, *27*, 937-946.

70. K. Takaoka, S. Maeda, H. Miura, K. Endo, and D. P. Chong, *Bull. Chem. Soc. Jpn.*, **1998**, *71*, 807-816.

71. M. Yanagita, S. Kanda, and S. Tokita, *Mol. Cryst. Liq. Cryst.*, **1999**, *327*, 49-52.

72. I. Rosenthal, P. Peretz, and K.A. Muszkat, *Chem. Phys. Lett.*, **1978**, *57*, 526-528.

73. I. Rosenthal, P. Peretz, and K.A. Muszkat, *J. Phys. Chem.*, **1979**, *83*, 350-353.

74. M. Matsuoka, "Molecular Orbital Design, Synthesis, and Characteristics of Functional Dyes for Electo-Optical Application" in *Chemistry of Functional Dyes*, Vol.1, Z. Yoshida and T. Kitao eds. p.9, Mita Press: Tokyo, **1992**.

75. J. Griffiths, "The MO Design and Development of Functonal Dye Materials" in *Chemistry of Functional Dyes*, Vol.2, Z. Yoshida and Y. Shirota eds. p.1, Mita Press: Tokyo, **1993**.

76. P. Gregory, "High Technology Applications of Functional Dye Materials" in *Chemistry of Functional Dyes*, Vol.2, Z. Yoshida and Y. Shirota eds. p.656, Mita Press: Tokyo, **1993**.

77. N. Sekar, *Colourage*, July 1998, 39.

78. P. Engleeinne, *J. Mater. Chem.*, **1999**, *9*, 1043-1054.

79. R.R. Mather, *Rev. Prog. Color.*, **2001**, *31*, 36-41.

80. B.K. Green, *National Cash Register Co.* US Patent 2,800,457, **1957**.

81. Y. Abe, K. Kawashima, and S. Suzuki, *J. Am. Ceramic Soc.*, **1981**, *64*, 206-208.

82. A. Beck, T. Hoffman, W. Körner, and J. Fricke, *Solar Energy*, **1993**, *50*, 407-414.

83. O. Faran and E. Natan, *PCT Int. Appl.* WO 208,821, **2002**.

84. P. Whitehead, *Polymers Paint Colour Journal (PPCJ)*, August 1995, 22.

85. K. Hideaki, K. Keishi, K. Tsutsui, H. Goto, E. Kawamura, H. Kuboyama, S. Maruyama, I. Sawamura, M. Shimada, and T. Yamaguchi, *Ricoh Co. Ltd.*, European Patent EP 576,015, **1994**.

86. S. Takayama, F. Sawoko, T. Okuyama, H. Nishizawa, H. Miyamoto, and M. Sugiuchi, *Kabushiki Kaisha Toshiba*, U.S. Patent 5,849,651, **1998**.

87. K. Senga and T. Kito, *The Pilot Ink Co., Ltd.*, U.S. Patent 5,879,443, **1999.**

88. K. Yammane and M. Nishioka., *OJI Paper Co.*, U.S. Patent 5,928,988, **1999**.

89. S.M. Burkinshaw, J. Griffiths, and A.D. Towns, *J. Mater. Chem.*, **1998**, *8*, 2677-2683.

90. K. Sano, K. Naito, S. Takayama, S. Fujioka, and T. Okuyama, *Kabushiki Kaisha Toshiba*, U.S. Patent 5,922,115, **1999**.

91. K. Naito, *Kabushiki Kaisha Toshiba*, U.S. Patent 5,869,420, **1999**.

92. S. Maruyama, H. Goto, E. Kawamura, M. Shimada, K. Kubo, K. Tsutsui, H. Ema, T.Yamaguchi, H. Kuboyama, I. Sawamura, and K. Taniguchi, *Ricoh Co. Ltd.*, U.S. Patent 5,395,433, **1995.**

93. K. Fujita and Y. Ono, *Pilot Ink Co., Ltd.*, U.S. Patent 5,919,404, **1999**.

94. Y. Ma, B. Zhu, and K. Wu, *J. Coatings Tech.*, **2000**, *72*, 67-71.

95. C. Thies, "Microencapsulation" in *Kirk-Othmer Encyc. of Chem. Tech.*, 4th Edition, Vol.16, 628-651, John-Wiley & Sons: New York, **1993**.

96. G. Nelson, *Rev. Prog. Color.*, **2001**, *31*, 57-64.

97. K. Ito, M. Kuwabara, K. Fukunishi, and Y. Fujiwara, *Dyes and Pigments*, **1997**, *34*, 297-306.

98. K. Okada and S. Okada, *J. Molecular Structure*, **1999**, *484*, 161-179.

99. H. Oda and T. Kitao, *Dyes and Pigments*, **1991**, *16*, 1-10.

100. K. Ito and K. Fukunishi, *Chem. Lett.*, **1997**, 357.

101. G. Rihs and C.D. Weis, *Dyes and Pigments*, **1991**, *15*, 107-127.

102. G. Rihs and C.D. Weis, *Dyes and Pigments*, **1991**, *15*, 165-173.

103. H.Yamamoto, T. Shiono, and T. Saimi, U.S. Pat. Appl. Publ. 122,374 A1 **2002**.

104. G.D. White, D. A. Zartman, and J.M. Bonicamp, *Chem. Educator*, **2000**, *5*, 2-7.

105. M. Bide, *Chemmatters*, October 1992, 8-11.

106. G. Sacripante and S. Kittelberger, *Chemistry in Britain*, April 2001, 52-54.

107. J. Nicholls, *Materials World*, **1996**, *4*, 19-21.

108. K. Tsutsui and T.Yamaguchi, *Ricoh Co. Ltd.*, US Patent 5,552,364, **1999**.

109. H. Furuya, M. Torii, K. Tsutsui, and M. Shimada, *Ricoh Co. Ltd.*, US Patent 5,866,505, **1999**.

110. H. Furuya, M. Torii, K. Tsutsui, and M. Shimada, *Ricoh Co. Ltd.*, US Patent 6,001,159, **1999**.

111. S. Maruyama, H. Goto, E. Kawamura, M. Shimada, K. Kubo, K. Tsutsui, H. Ema, T. Yamaguchi, H. Kuboyama, I. Sawamura, and K. Taniguchi, *Ricoh Co. Ltd.*, U.S. Patent 5,296,439, **1994**.

112. K. Fujita and K. Senga, *Matsushita Electric Industrial Co.,* European Patent Application EP 1,084,860, **2001**.

113. J. Maruyama and H. Sano, *Mitsubishi Paper Mills Ltd.,* U.S. Patent 6,184,180 B1, **2001**.

114. Y. Yokota, *Chromic Co. Ltd.,* European Patent Application EP 999,071, **2000**.

115. S. Yukata and S. Jun, *Pilot Ink Co. Ltd.,* European Patent Application EP 908,501, **1999**.

116. K. Tsutsui and T. Yamaguchi, *Ricoh Co. Ltd.,* US Patent 5,534,907, **1996**.

117. K. Tsutsui and T. Yamaguchi, *Ricoh Co. Ltd.,* US Patent 5,547,500, **1996**.

118. J. M. Jacobsom and V.M. Bove Jr., *MIT,* US Patent 6,022,648, **2000**.

119. K.Sano, K.Naito, S. Takayama, S. Fujioka, T. Okuyama, *Kabushiki Kaisha Toshiba,* U.S. Patent 5,663,115, **1997**.

120. M. Tajima, M. Sugai, K. Matsunaga, T. Yamashita, H. Inoue, and M. Hida, *Dyes and Pigments,* **1998**, *39,* 97-109.

121. H. Oda, *J. Chem. Tech. Biotechnol.,* **1995**, *63,* 223-228.

122. N.S. Allen, N. Hughes, and P. Mahon, *J. Photochem.,* **1987**, *37,* 379-390.

123. A.D. West, *Solid state Chemistry,* John Wiley and Sons: New York, **1984**.

124. P.C. Schulz, M. Abrameto, J.E. Puig, and F.A. Soltero-Martinez, *Langmuir,* **1996**, *12,* 3082-3088.

125. J. Luthern and A. Peredes, *J. Mater. Sci. Lett.,* **2000**, *19,* 185-188.

126. C.R. Theocharis and W. Jones, *J. Cryst. and Spec. Res.,* **1984**, *4,* 121-128.

127. S.G. Morris and R.W. Riemenschneider, *J. Am. Chem. Soc.,* **1946**, *68,* 500.

128. G.A. Jeffrey and Y. Yeon, *Acta Cryst.,* **1990**, *B46,* 519-524.

129. J. Reuter and A. Würflinger, *Ber. Bunsenges. Phys. Chem.,* **1995**, *99,* 1247-1251.

130. C. Mosselman, J. Mourik, and H. Dekker, *J. Chem. Thermodynamics,* **1974**, *6,* 477-487.

131. M. Tasumi, T. Shimanouchi, A. Watanabe, and R. Goto, *Spectrochimica Acta*, **1964**, *20*, 629-666.

132. J.C. van Miltenburg, H.A.J. Oonk, and L. Ventola, *J. Chem. Eng. Data*, **2001**, *46*, 90-97.

133. M. Windholz, S. Budavari, R.F. Blumetti, and E. S. Otterbein eds. *The Merck Index*, 10th ed., Merck & Co.: Rahway, N.J., **1983**.

134. M.A. White, " Thermal Analysis and Calorimetry" Chapter 4 in Volume 8 (*Physical Methods in Supramolecular Chemistry* , Eds. J. Ripmeester and J.E. Davies) in *Comprehensive Supramolecular Chemistry* , Eds. J.-M.Lehn, J.L. Atwood, D.D. MacNicol, J.E.D. Davies and F. Vogtle, Pergamon: Oxford, **1996.**

135. V.J. Griffin and P.G. Laye, "Differential Thermal Analysis and Differential Scanning Calorimetry" Chapter 2 in *Thermal Analysis Techniques and Applications*, Eds. E.L.Charsley and S.B. Warrington, Royal Society of Chemistry: Cambridge, **1992.**

136. B. Wunderlich, *Thermal Analysis*, Academic Press Inc.: Boston, **1990**.

137. M.A. White and M.J.M. Van Oort, *Ber. Bunsenges. Phys. Chem.*, **1988**, *92*, 168-176.

138. D.L. Pavia, G.M. Lampman, and G.S. Kriz, *Introduction to Spectroscopy – A Guide for Students of Organic Chemistry*, 2nd Ed., Harcourt Brace College Publishers:Fort Worth, **1996**.

139. J.R. Ferraro and K. Nakamoto, *Introductory Raman Spectroscopy*, Academic Press Inc.: Boston, **1994**.

140. D. Lin-Vlen, N.B. Colthup, W.G. Fateley, and J.G. Grasselli, *The Handbook of Infrared and Raman Characteristic Frequencies of Organic Molecules*, Academic Press: Boston, **1991**.

141. G. Kortüm, *Reflectance Spectroscopy – Priciples, Methods, Applications*, Springer-Verlag: New York, **1969**.

142. W.W. Wendlandt and H.G. Hecht, *Reflectance Spectroscopy*, John Wiley & Sons: New York, **1966**.

143. D. Fassler and R. Gade, *J. Molecular Spectroscopy*, **1991**, *246*, 145-153.

144. H.S. Shah, P.R. Desai, and M.S. Roy, *Applied Optics*, **1997**, *36*, 3538-3546.

145. T. Nagano and S. Nakashima, *Geochemical Journal*, **1989**, *23*, 75-83.

146. A. Springsteen, *Anal. Chim. Acta.*, **1999**, *380*, 379-390.

147. P.J. Hore, *Nuclear Magnetic Resonance*, Oxford Univerity Press: Oxford,**1995**.

148. R.K. Harris, *Nuclear Magnetic Resonance Spectroscopy:A Physiochemical View*, John Wiley & Sons: New York, **1986**.

149. L.L. Koh and K. Eriks, *Acta Crystallographica*, **1971**, *B27*, 1405-1413.

150. D.W.A. Sharp and N. Sheppard, *J. Chem. Soc.*, **1957**, 674-681.

151. M. Yanagita, I. Aoki, and S. Tokita, *Bull. Chem. Soc. Jpn.*, **1997**, *70*, 2757-2763.

152. Y. Sueishi, Y. Sugiyama, S. Yammamoto, and N. Nishwmura, *Bull. Chem. Soc. Jpn.*, **1994**, *67*, 572-574.

153. G. Lingjie, Z. Tianzeng, Q. Hailin, and F. Jingguo, *Chinese Journal of Magnetic Resonance*, **1995**, *12*, 607-611.

154. L. Angeloni, G. Smulevich, and M.P. Marzocchi, *J. Raman Spec.*, **1979**, *8*, 305-310.

155. E.J. Liang, X.L. Ye, and W. Kiefer, *J. Phys. Chem. A*, **1997**, *101*, 7330-7335.

156. K.Ibata, K.Oriishi, T.Otsuka, and S. Saito, *IS&T's Eighth International Congress on Advances in Non-Impact Printing Technologies*, **1992**, 376-383.

157. A.A. Hasanein, M.S. Masoud, and M.M. Habeeb, *Spectroscopy Letters*, **1988**, 21, 481-83.

158. J.-M. Yan and D.-Y. Yan, *Chinese Science Bulletin*, **1994**, *39*, 1448-1451.

159. J. S. Wright, E. R. Johnson, and G.A. DiLabio, *J. Am. Chem. Soc.*, **2001**, *123*, 1173-1183.

160. L.S. Vartanyan and E.M. Gonikberg, *Izv. Akad. Nauk. SSSR Ser. Khim.*, **1963**, 11, 2047-2049.

161. Advanced Chemistry Development (ACD) Software Solaris Calculation of the pKa values of alkyl gallates (CAS Scifinder Scholar)

162. B. Sas, B. Coppens, and J. Van hemel, U.S. Patent 6,297,396, **2001**.

163. N. Okabe and H. Kyoyama, *Acta Cryst.*, **2002**, *E58*, o245-o247.

164. D.C. MacLaren and M.A. White, *J. Mater. Chem.*, *13*, **2003**, *13*, 1695-1700.

165. G. Varsanyi, *Assignments for Vibrational Spectra of Seven Hundred Benzene Derivatives*, Vol. 1, John Wiley & Sons: New York, **1974**.

166. C.D. Chriswell and A.A. Schilt, *Anal. Chem.*, **1975**, *47*, 1623-1629.

167. E.B. Sirota and X.Z. Wu, *J. Chem. Phys.*, **1996**, *105*, 7763-7773.

168. T. Yamamoto, K. Nozaki, and T. Hara, *J. Chem. Phys.*, **1990**, *92*, 631-641.

169. D.F.R. Gilson, A.S. Kertes, R. St. J. Manley, J. Tsau, and G. Donnay, *Can. J. Chem.*, **1976**, *54*, 765-8.

170. Y.K. Kuchhal, R.N. Shukla, and A.B. Biswas *Spectrochimica Acta*, **1979**, *31*, 61-70.

171. L. Ventolà, M. Ramirez, T. Calvet, X. Solans, M.A. Cuevas-Diarte, P. Negrier, D. Mondieig, J.C. van Miltenburg and H.A.J. Oonk, *Chem. Mater.*, **2002**, *14*, 508-517.

172. A. Watanabe, *Bull. Chem. Soc. Jpn.*, **1961**, *34*, 1728-1734.

173. K. Tanaka, T. Sato, and T. Hayashida, *Bull. Inst. Chem. Res. Kyoto Univ.*, **1957**, *35*, 123-138.

174. K. Tanaka, T. Sato, A. Watanabe, and T. Hayashida, *Bull. Res. Kyoto Univ.*, **1959**, *39*, 281-293.

175. M. Soutzidou, V.-A. Glezakou, K. Viras, M. Helliwell, A.J. Masters, and M.A. Vincent, *J. Phys. Chem. B*, **2002**, *106*, 4405-4411.

176. S. Ishikawa and I. Ando, *J. Molecular Structure*, **1993**, *291*, 183-190.

177. F. Michaud, L. Ventolá, M.T. Calvet, M.A. Cuevas-Diarte, X. Solans, and M. Font-Bardía, *Acta Cryst.*, **2000**, *C56*, 219-221.

178. S. Abhrahamson, G. Larrson, and E. von Sydow, *Acta Cryst.*, **1960**, *13*, 770-774.

179. Y. Kakiuchi, H. Komatsu, and S. Kyoya, *J. Phys. Soc. Jpn.*, **1951**, *6*, 321-328.

180. J.D. Hoffman and C.P. Smyth, *J. Am. Chem. Soc.*, **1949**, *71*, 431-439.

180. H.F. Hanna and I.K. Hakim, *Z. Naturforsch.*, **1971**, *26A*, 1194-1198.

182. N. Murase, T. Fujita, N. Morikawa, and S. Koga, *Bull. Chem. Soc. Jpn.*, **1978**, *51*, 2836-2837.

183. N.G. Parsonage and L.A.K. Staveley, *Disorder in Crystals*, Oxford University Press: Oxford, **1978**.

184. A. Ammar and D.A. Young, *Mol. Cryst. Liq. Cryst.*, **1974**, *27*, 207-215.

185. M.G. Broadhurst, *J. Res. Nat. Bur. Standards A.*, **1962**, *66A*, 241-249.

186. Y.K. Kuchhal R.N. Shukla, and A.B. Biswas, *Ind. J. Chem.*, **1981**, *20A*, 837-839.

187. A.A. Trapeznikov and T.A. Lomonosova, *Russ. J. Phys. Chem.*, **1967**, *41*, 139-144.

188. T. Seto, *Mem. Coll. Sci., Kyoto Univ., Ser. A*, **1962**, *30*, 89-107.

189. G.M. Anderson and D.A. Crerar, *Thermodynamics in Geochemistry-The Equilibrium Model*, Oxford University Press: Oxford, **1993**.

190. I. Prigogine and R. Defay, *Chemical Thermodynamics*, Longmans:London, **1965**.

191. H.A.J. Oonk, *Phase Theory: The Thermodynamics of Heterogeneous Equilibria*, Elsevier: Amsterdam, **1981**.

192. A. Findlay and A.N. Campbell, *The Phase Rule And Its Applications, 8th Ed.* Longmans: London, **1940**.

193. M.A. Al-Mamun, *J. Am. Oil Chem. Soc.*, **1974**, *51*, 234-237.

194. SDBS No. 7442CDS-06-135 SDBSWeb:http://www.aist.go.jp/RIODB/SDBS/ 100102

195. SDBS No. 7689CDS-10-219 SDBSWeb:http://www.aist.go.jp/RIODB/SDBS/ 100102

196. T.T. Nakashima and G.E. Maciel, *Appl. Spec.*, **1972**, *26*, 220-223.

197. D.C. MacLaren and M.A. White, *J. Mater. Chem.*, **2003**, *13*, 1701-1704.

198. G.D. Rockwell, T.B. Grindley, K.C. Smith, and M.A. White, *J. Phys. Chem. B*, **2002**, *106*, 12311-12316.

199. D.F.R. Gilson, *J. Chem. Educ.*, **1992**, *69*, 23-25.

200. M. Farina, G. DiSilvestro, and A. Columbo, A. *Mol. Cryst. Liq. Cryst.*, **1986**, *137*, 265-277.

201. G.M. Kuznetsov, M.P. Leonov, A.S. Kuk'yanov, V.A. Kovaleva, and M.P. Shopavalov *Dokl. Akad. Nauk. SSSR*, **1975**, *223*, 124-125.

202. D. Hughes-Hallet, A.M. Gleason, D.E. Flath, S.P. Gordon, D.O. Lomen, D. Lovelock, W.G. McCallum, B.G. Osgood, A. Pasquale, J. Tecosky-Feldman, J.B. Thrash, K.R. Trash, T.W. Tucker, and O.K. Bretsher, *Calculus*, John Wiley and Sons: New York, **1994**.

203. K.J. Laidler, *Chemical Kinetics*, 3rd Ed., Harper Collins: New York, **1987**.

204. R.F. Service, *Science*, **1997**, *277*, 474.

205. R.F. Service, *Science*, **1998**, *280*, 1690.

206. R. E. Reddington, A. Sapienza, B. Gurau, R. Viswanathan, S. Saragapani, E.S. Smotkin, and T.E. Mallouk, *Science*, **1998**, *280*, 1735-1737.